BEILSTEIN JOURNAL OF NANOTECHNOLOGY

Low-dimensional materials and systems

Edited by Sumeet Walia and Jianzhen Ou

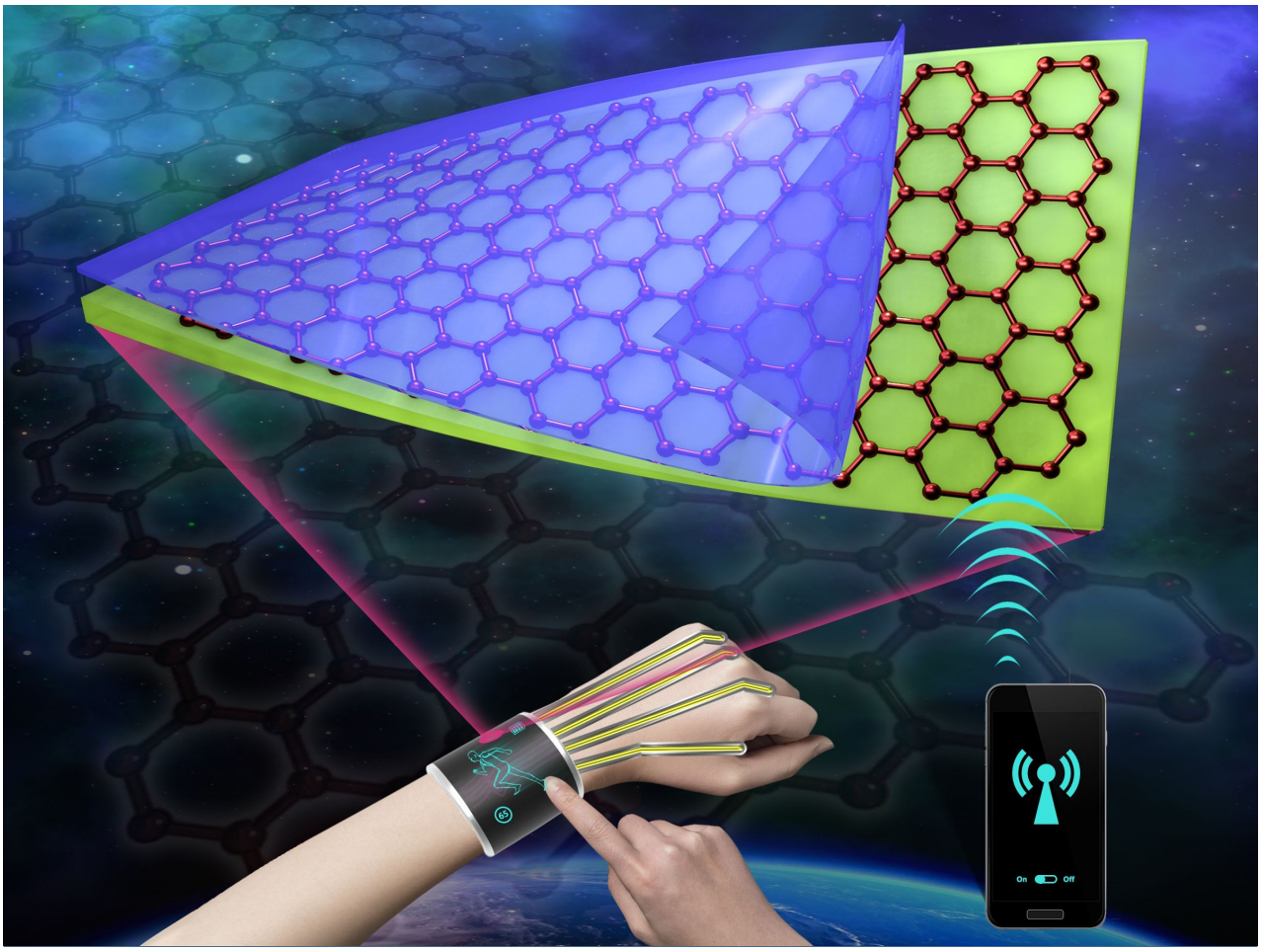

Imprint

Beilstein Journal of Nanotechnology
www.bjnano.org
ISSN 2190-4286
Email: journals-support@beilstein-institut.de

The *Beilstein Journal of Nanotechnology* is published by the Beilstein-Institut zur Förderung der Chemischen Wissenschaften.

Beilstein-Institut zur Förderung der Chemischen Wissenschaften
Trakehner Straße 7–9
60487 Frankfurt am Main
Germany
www.beilstein-institut.de

BEILSTEIN JOURNAL OF NANOTECHNOLOGY

Nanostructure-induced performance degradation of $WO_3 \cdot nH_2O$ for energy conversion and storage devices

Zhenyin Hai[*1,2], Mohammad Karbalaei Akbari[1,2], Zihan Wei[1,2], Danfeng Cui[3], Chenyang Xue[3], Hongyan Xu[4], Philippe M. Heynderickx[1,2], Francis Verpoort[1,5,6] and Serge Zhuiykov[*1,2]

Full Research Paper

Open Access

Address:
[1]Center for Environmental and Energy Research, Ghent University Global Campus, Yeonsu-gu, Incheon 21985, South Korea, [2]Department of Green Chemistry and Technology, Faculty of Bioscience Engineering, Ghent University, Coupure Links 653, 9000 Ghent, Belgium, [3]Science and Technology on Electronic Test and Measurement Laboratory, North University of China, Taiyuan, Shanxi 030051, P.R. China, [4]School of Materials Science and Engineering, North University of China, Shanxi 030051, P.R. China, [5]National Research Tomsk Polytechnic University, Lenin Avenue 30, Tomsk 634050, Russian Federation and [6]Laboratory of Organometallics, Catalysis and Ordered Materials, State Key Laboratory of Advanced Technology for Materials Synthesis and Processing, Center for Chemical and Material Engineering, Wuhan University of Technology, Wuhan, P.R. China

Email:
Zhenyin Hai[*] - zhenyin.hai@ugent.be; Serge Zhuiykov[*] - serge.zhuiykov@ugent.be

* Corresponding author

Keywords:
2D layered oxides; interlayer water; van der Waals interaction; $WO_3 \cdot nH_2O$

Beilstein J. Nanotechnol. **2018,** *9,* 2845–2854.
doi:10.3762/bjnano.9.265

Received: 03 September 2018
Accepted: 26 October 2018
Published: 12 November 2018

This article is part of the thematic issue "Low-dimensional materials and systems".

Guest Editor: S. Walia

Abstract

Although 2D layered nanomaterials have been intensively investigated towards their application in energy conversion and storage devices, their disadvantages have rarely been explored so far especially compared to their 3D counterparts. Herein, $WO_3 \cdot nH_2O$ (n = 0, 1, 2), as the most common and important electrochemical and electrochromic active nanomaterial, is synthesized in 3D and 2D structures through a facile hydrothermal method, and the disadvantages of the corresponding 2D structures are examined. The weakness of 2D $WO_3 \cdot nH_2O$ originates from its layered structure. X-ray diffraction and scanning electron microscopy analyses of as-grown $WO_3 \cdot nH_2O$ samples suggest a structural transition from 2D to 3D upon temperature increase. 2D $WO_3 \cdot nH_2O$ easily generates structural instabilities by 2D intercalation, resulting in a faster performance degradation, due to its weak interlayer van der Waals forces, even though it outranks the 3D network structure in terms of improved electronic properties. The structural transformation of 2D layered $WO_3 \cdot nH_2O$ into 3D nanostructures is observed via ex situ Raman measurements under electrochemical cycling experiments. The proposed degradation mechanism is confirmed by the morphology changes. The work provides strong ev-

idence for and in-depth understanding of the weakness of 2D layered nanomaterials and paves the way for further interlayer reinforcement, especially for 2D layered transition metal oxides.

Introduction

Within the less than 20 years since the successful exfoliation of atomically thin graphene, 2D layered nanomaterials have been contributing greatly to the advances of nanoscience and nanotechnology with their exotic properties and versatility of applications [1-10]. Among all 2D nanomaterials, 2D transition metal oxides (TMOs) are the group with the highest electrochemical activities for energy conversion and storage [11-15]. As the energy-related field is rapidly developing, the limits of 2D TMOs began to come clear and ways of chemical functionalization were developed to make them more suitable for practical applications [16-18]. However, comparably less attention has been paid to the comprehensive investigation of the disadvantage of 2D TMOs and their failure mechanism.

Tungsten trioxide (WO_3) is one of the few TMOs with both excellent electrochemical and electrochromic properties [19-23]. It has a three-dimensional (3D) network lattice structure consisting of corner-sharing or edge-sharing WO_6 octahedra [24-26]. Its phases (monoclinic, triclinic, orthorhombic and tetragonal) form trigonal, quadrangular, pentagonal, and hexagonal tunnels and cavities for 3D electrochemcial intercalation [27-29]. In contrast, its hydrates exhibit a 2D layered strcuture composed of $WO_5(OH_2)$ single sheets in a corner-sharing arrangement with additional water molecules between layers, which is suitable for 2D intercalation chemistry [30-32].

Both WO_3 and its hydrates have been fabricated via different methods and analyzed with regard to electrochemical, photocatalysis, sensing and electrochromic applications [24,33,34]. Oriented $WO_3{\cdot}H_2O$ sheets were hydrothermally grown in mixed acids at 80 °C for 17 h, followed by sintering at 500 °C in order to obtain crystalline WO_3 for the photoelectrochemical water oxidation [35]. A 2D WO_3 nanosheet sensor fabricated by high-temperature anodization of tungsten thin films displayed a maximum response of 80% for 1% of hydrogen gas at 250 °C [36]. 2D $WO_3{\cdot}2H_2O$ films developed by a facile dipping process exhibited a significantly improved response time as electrochromic electrodes compared to WO_3 thin films [37]. The acidic precipitation reaction was also adopted to fabricate $WO_3{\cdot}2H_2O$ electrochemical energy storage electrodes with a higher rate capability than annealed WO_3 [38]. The investigation of 2D sheets of WO_3 and a rGO–WO_3 composite prepared via a one-pot hydrothermal method suggested that the rGO–WO_3 composite could be a promising material for photocatalytic and antibacterial applications [39]. Unfortunately, despite the great number of 2D WO_3 compounds and their hydrates synthesized and utilized for energy conversion and storage applications, their weakness has not yet been investigated thoroughly.

In this study, $WO_3{\cdot}nH_2O$ (n = 0, 1, 2) was fabricated by a facile hydrothermal method for the first time at the different termperatures to investigate the disadvantages of 2D structures. The growth mechanism analyzed by X-ray diffraction (XRD) and scanning electron microscopy (SEM) suggested a 2D to 3D structural transition upon temperature increment, revealing that the weakness of layered 2D $WO_3{\cdot}nH_2O$ originates from weak interlayer van der Waals interactions. The faster performance degradation in electrochemical tests of 2D layered $WO_3{\cdot}nH_2O$ further indicated the structural instability of 2D nanostructures compared to 3D nanostructures. The structural transformation of 2D layered $WO_3{\cdot}nH_2O$ to 3D structures was observed via ex situ Raman measurements under electrochemical cycling experiments. The morphology change confirmed the degradation mechanism proposed in this work. Consequently, this work provides an in-depth understanding of the weakness of 2D layered nanomaterials and paves the way for the interlayer reinforcement of 2D TMOs.

Experimental

All nanostructured WO_3 and their hydrates in this work were prepared on FTO/glass substrates through a facile hydrothermal reaction at different temperatures. All chemicals were purchased from chemical suppliers and were used without further purification.

Before the hydrothermal reaction, the seed solution was first spin-coated on the FTO/glass and annealed at 350 °C for 20 min. To prepare the seed solution, 0.824 g of sodium tungstate dihydrate ($Na_2WO_4{\cdot}2H_2O$) was initially dissolved into 10 mL deionized water under continuous stirring. After complete dissolution of the $Na_2WO_4{\cdot}2H_2O$ powder, 0.416 mL of hydrochloric acid (HCl, 36–38 wt %) solution was added dropwise while stirring for 15 min at room temperature. Subsequently, 0.2241 g of oxalic acid ($C_2H_2O_4$) was added to the solution and the solution was then diluted with deionized water to a total volume of 12.5 mL accompanied by another 15 min of stirring. The prepared seed solution was spin-coated onto FTO/glass at 3000 rpm for four times with each step consisting of 40 s spin-coating at room temperature followed by annealing at 350 °C for 20 min.

The as-prepared FTO/glasses were sealed in 25 mL Teflon-lined stainless autoclaves filled with 15 mL solution that was prepared by the same procedures as the seed solution mentioned above. However, its concentration was ten times lower than that of the the seed solution. Then the autoclaves were heated at temperatures of 80, 100, 120, 150 or 180 °C for 2 h. After heating, the autoclaves cooled down to the room temperature naturally. The FTO/glass substrates were taken out from autoclaves and dried at 60 °C for 1 h. Subsequently, the as-grown WO_3 and its hydrates were measured and analyzed.

The crystal structures of the samples were identified with a high-resolution X-ray diffractometer (HR-XRD, SmartLab, Rigaku). The morphology of samples was investigated by field-emission scanning electron microscopy (FE-SEM, JSM-7100F, Jeol) together with energy-dispersive spectroscopy (EDS). Information about chemical composition and bonding was collected by X-ray photoelectron spectrometry (XPS, K-Alpha, Thermo Scientific) and Raman spectroscopy (EZRaman-N-785, TSI. Inc.), respectively.

Electrochemical characterization of the samples was performed using an Autolab PGSTAT204 (Metrohm Autolab B.V.) with a three-electrode configuration in 1.0 M H_2SO_4 aqueous solution. The as-prepared sample, a Pt wire and a Ag/AgCl electrode acted as working, counter and reference electrode, respectively. Cyclic voltammetry (CV) was conducted in the potential range from −0.8 V to +0.8 V (vs Ag/AgCl).

Results and Discussion

The crystal structure of the as-prepared samples was initially investigated by XRD. As shown in the XRD patterns from the top to bottom of Figure 1a, the samples display different phase compositions depending on the synthesis temperature. The samples synthesized at 80 °C is composed of monoclinic $WO_3{\cdot}2H_2O$ (JCPDS No. 18-1420) [40] and orthorhombic $WO_3{\cdot}H_2O$ (JCPDS No. 43-0679) [41], which are both layered structures as illustrated in Figure 1b and Figure 1c, respectively. The structural difference between these two components is the number of interlayer water molecules. For the samples synthesized at 100 and 120 °C, only $WO_3{\cdot}H_2O$ (JCPDS no. 43-0679) was measured with two main peaks corresponding to (020) and (111) as some of the interlayer water disappeared [41]. However, the dominant facet changed from (020) to (111) as the synthesis temperature increased. Moreover, for the samples synthesized at 150 °C, the full width at half maximum (FWHM) of the (111) reflection of the main component $WO_3{\cdot}H_2O$ broadened, which indicates the instability of $WO_3{\cdot}H_2O$ at such a high temperature. A small hump on the left side of the (111) peak of $WO_3{\cdot}H_2O$ clearly shows the appearance of monoclinic WO_3 (JCPDS no. 43-1035) [42,43], which also supports the dehydration tendency of $WO_3{\cdot}H_2O$. When the samples were grown at 180 °C, only monoclinic WO_3 (JCPDS no. 43-1035) with its dominant (002) facet existed in the sample. The crystal structure of monoclinic WO_3 presented in Figure 1d displays 3D covalent bonding structures compared to the stacked 2D layers of $WO_3{\cdot}2H_2O$ and $WO_3{\cdot}H_2O$ with only weak interlayer van der Waals forces. It is also noteworthy that at temperatures lower than 80 °C, neither $WO_3{\cdot}2H_2O$ nor $WO_3{\cdot}H_2O$ could be synthesized using the hydrothermal process presented in this work. Both experimental results and the theoretical models mentioned above suggested that the layered WO_3 hydrates are relatively unstable compared to WO_3.

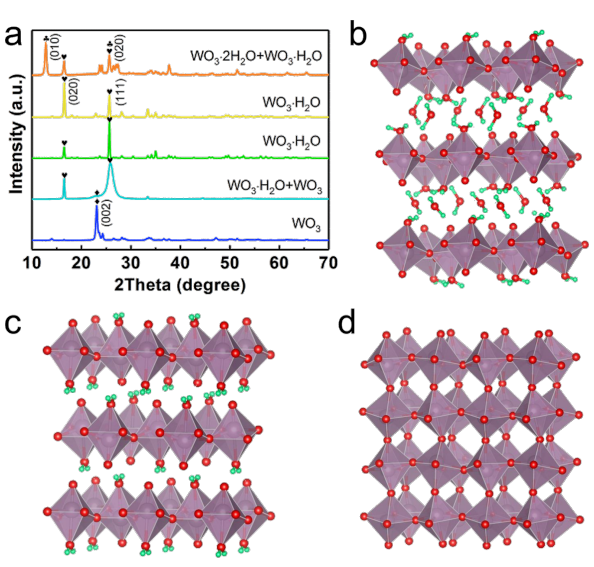

Figure 1: a) XRD patterns of the as-prepared samples at 80, 100, 120, 150 and 180 °C from top to bottom. Schematic illustration of the crystal structures: b) monoclinic $WO_3{\cdot}2H_2O$, c) orthorhombic $WO_3{\cdot}H_2O$ and d) monoclinic WO_3.

The following figures (Figures 2–4) show the morphology of the three typical samples synthesized at 80, 120 and 180 °C, examined by SEM. Figure 2a,b shows the relatively uniform growth of WO_3 hydrates with flower-like balls on the upper layer and nanosheets beneath them as represented in Figure 2c. The nanosheets were ca. 1.3 μm square-shaped and almost vertically aligned on the substrate (Figure 2d,e). The image of a typical nanosheet shows the very low thickness of ca. 27 nm (Figure 2f). The upper layer with grouped flower-like balls is highlighted in Figure 2g,h. The images show that the flower-like balls have a diameter of ca. 2.5 μm and are composed of self-assembled square nanosheets with similar sizes as the nanosheets in the layer grown beneath. The magnified image in Figure 2i displays nanosheets with average thickness of ca. 37 nm in a flower-like ball crossing each other.

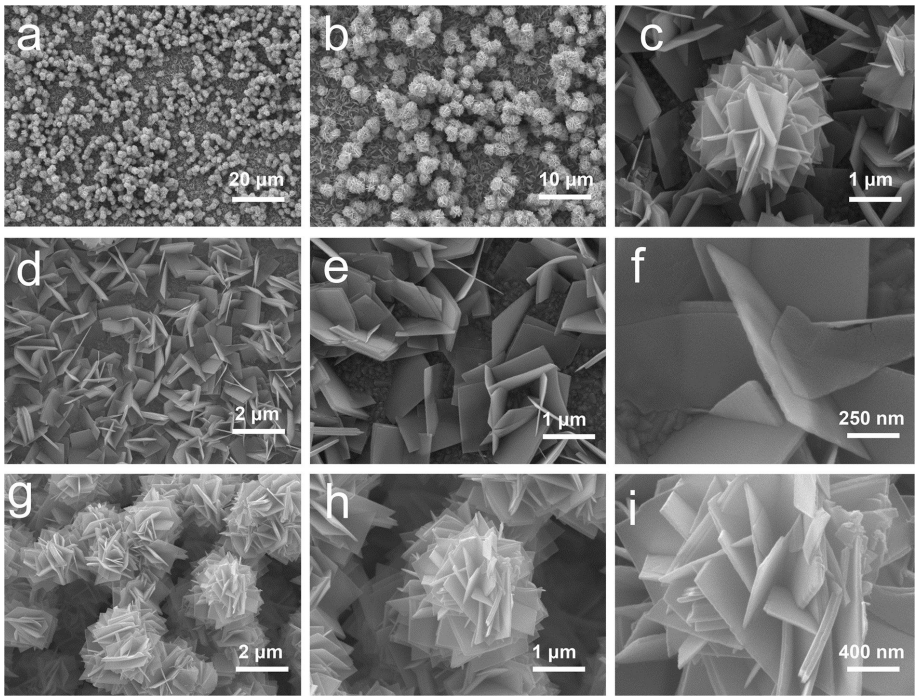

Figure 2: SEM images of the sample synthesized at 80 °C. a) Overview and b) magnified images of the WO_3 hydrates grown on the substrate; c) image of a representative area; d) typical image of nanosheets and e) magnified view; f) image of a typical nanosheet; g) grouped flower-like balls; h) typical flower-like ball with i) magnified image.

Figure 3 shows SEM images of the sample synthesized at 120 °C. The as-grown pure $WO_3{\cdot}H_2O$ existed in form of square sheets and hexagonal plates as displayed in Figure 3a–c. The square sheets were measured to be ca. 6 µm long and ca. 1.5 µm thick, while the hexagonal plates were 0.5 µm thick with diagonal length of ca. 2.9 µm. Figure 3d,e shows the square sheets with opened layers, indicating the layered crystal structure of the as-grown material. The magnified image of the opened layers in Figure 3f clearly demonstrated the 2D layered nature of $WO_3{\cdot}H_2O$. In addition to the square sheets, the hexagonal plates were stacked by nanoribbons in the direction parallel to the diagonals of the hexagons (Figure 3g). As shown in Figure 3g,h, the nanoribbons were wider (ca. 400 nm) at the center and narrower (ca. 100 nm) near the two ends, forming tips at their very ends (Figure 3i).

The SEM images of the sample synthesized at 180 °C are presented in Figure 4. The WO_3 structures are assembled from square sheets with a few individual sheets beneath as indicated in Figure 4a and Figure 4b. The square sheets with a length of ca. 2.8 µm and a thickness of ca. 0.4 µm grew crossed with each other at all angles, forming a network structure (Figure 4c,d). Figure 4e clearly displays the crossed square nanosheets in the network structure. The individual square sheets were measured to be ca. 3.5 µm long and ca. 0.7 µm thick (Figure 4f,g). The EDS element mapping in Figure 4h,i demonstrates a homogeneous elemental distribution in the sheet and confirms the formation of WO_3. The oxygen appearing outside the square comes from the substrate.

Three typical sample structures acquired with SEM are presented in Figure 5a. It clearly shows that the feature structure size of the nanostructures synthesized at 80 °C are much smaller compared to similar feature structures obtained in the other two samples, especially in terms of the longitudinal size. Besides the lower synthesis temperature, this could be mainly due to the interlayer water molecules in $WO_3{\cdot}2H_2O$, which caused the slow growth of the samples. The structural features of the WO_3 sample synthesized at 180 °C are also smaller than those of the $WO_3{\cdot}H_2O$ sample synthesized at 120 °C. Although a higher synthesis temperature produces more energy for the sample growth, the layered $WO_3{\cdot}H_2O$ still grew faster than the 3D WO_3, as the formation of van der Waals interactions consumes less energy than the formation of covalent bonds. From both the structural and energy consumption point of view, $WO_3{\cdot}2H_2O$ and $WO_3{\cdot}H_2O$ are kinetically and thermodynamically less stable than WO_3.

Figure 5b,c depicts the high-resolution XPS core-level W4f and O1s spectra, respectively. The W 4f orbitals in Figure 5b are almost identical in the three samples and can be resolved into W $4f_{5/2}$ and W $4f_{7/2}$. The two main peaks correspond to the

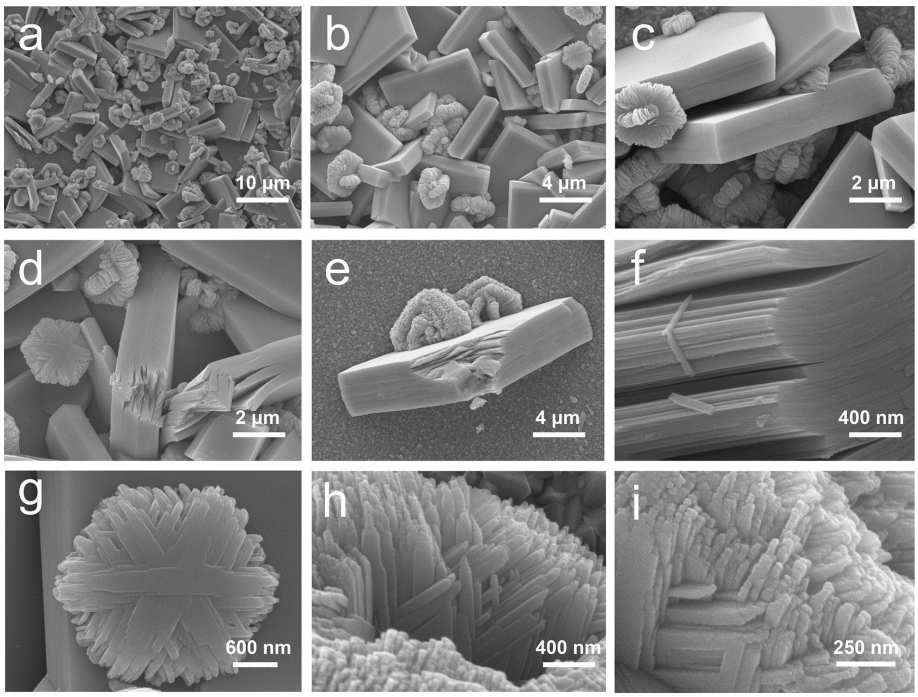

Figure 3: SEM images of the sample synthesized at 120 °C. a) Overview and b) magnified images of $WO_3 \cdot H_2O$ grown on the substrate; c) image of a representative area; d) square sheets with opened layers; e) a typical square sheet with opened layers and f) its magnified view at the opened layers; g) a typical hexagonal plate; magnified views of h) the edge and i) the side face of a hexagonal plate.

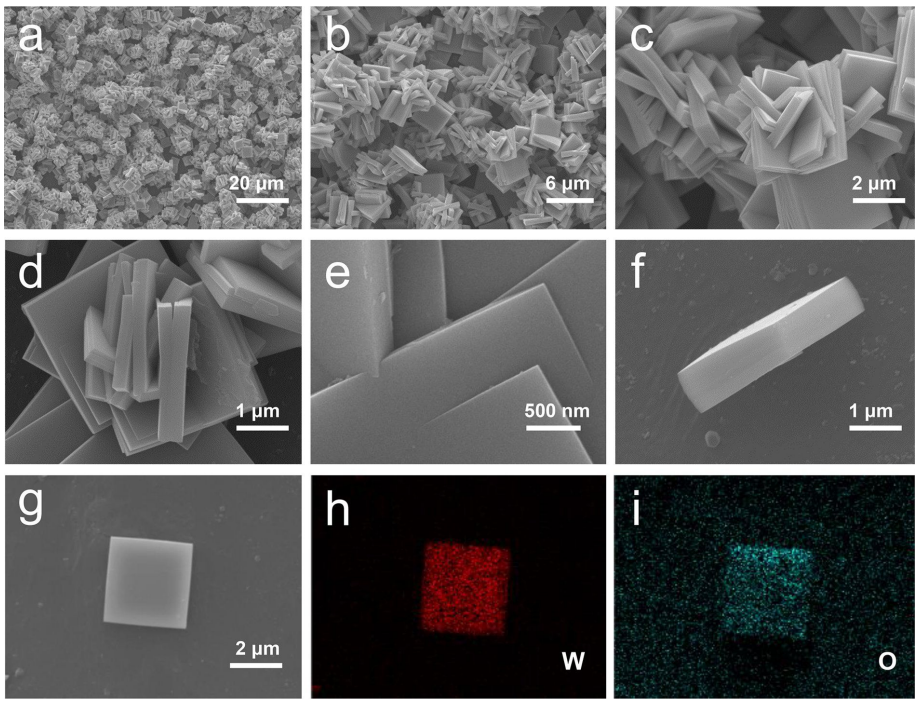

Figure 4: SEM images of the sample synthesized at 180 °C. a) Overview and b) magnified images of WO_3 grown on the substrate; images of c) one part of the network structure and d) the magnified view; e) image of the crossed nanosheets; f) vertically standing and g) flat laying square sheets. EDS element mapping of the flat laying square sheet: h) W and i) O.

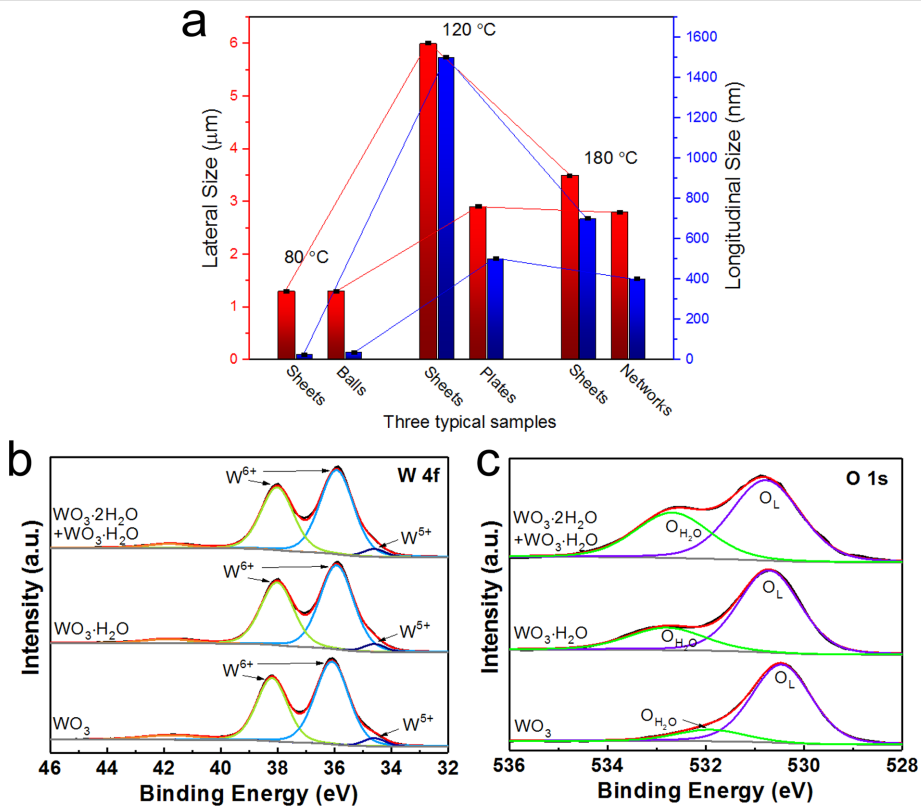

Figure 5: a) The structural feature sizes of three typical samples synthesized at 80, 120 and 180 °C, respectively. High-resolution XPS core-level b) W4f and c) O1s spectra of the three as-synthesized samples.

$W4f_{7/2}$ and $W4f_{5/2}$ of the tungsten atoms in a +6 oxidation state [44,45]. The two peaks from the two samples synthesized with lower temperatures are both located at 35.9 eV and 38.0 eV, which is ca. 0.2 eV lower than the peak locations (ca. 36.1 eV and ca. 38.2 eV) in the WO_3 sample synthesized at 180 °C. The very small peaks at ca. 34.6 eV in all three samples originate from W^{5+} ions in the lattice, which reveals the formation of a few oxygen vacancies [29,46]. The O 1s spectra for all samples in Figure 5c depict two peaks with one main peak from the lattice oxygen, O_L, and another from the oxygen in water molecules, O_{H2O} [47,48]. With increasing temperature, the lattice oxygen in the three as-synthesized samples shifts to lower binding energies from 530.8 eV over 530.6 eV to 520.3 eV. The area of the O_{H2O} peaks indicates the structural difference between layered $WO_3{\cdot}2H_2O$, layered $WO_3{\cdot}H_2O$ and 3D WO_3. The decreasing area of O_{H2O} peaks with higher synthesis temperature demonstrated the increasing stability of the samples as the interlayer water and coordinated water molecules disappeared successively with only a few unavoidable surface-absorbed water molecules left [49,50]. The above XPS results confirm the SEM analysis.

To get further inside of the electrochemical performance degradation of the three samples, CV tests were carried out at a scan rate of 50 $mV{\cdot}s^{-1}$ within the potential range from −0.8 V to +0.8 V (vs Ag/AgCl). The electrochemical energy conversion and storage of $WO_3{\cdot}nH_2O$ in H_2SO_4 electrolyte are based on the intercalation of protons and injection of electrons as described in the following equation [38]:

$$WO_3{\cdot}nH_2O + xH^+ + xe^- \longleftrightarrow H_xWO_3{\cdot}nH_2O\ (0 \le x \le 1).$$

The transition of W between the valence states of W^{6+} and W^{5+} is the basis of both electrochemical energy storage and electrochromic behavior. As shown in Figure 6a, in all cases the cathodic current rises when the potential was scanned to negative values because of the intercalation of protons into the samples. Figure 6c–e illustrates the intercalation of ions into $WO_3{\cdot}nH_2O$. The reduction of W^{6+} to W^{5+} in the process also resulted in coloration. In the reverse process, the rise of anodic current indicates the deintercalation of protons and oxidation of tungsten ions with concomitant bleaching. The video presented in Supporting Information File 1 shows the coloration/bleaching processes of the samples during cycling. With a growing number of cycles, the samples exhibited a strong performance degradation as displayed in Figure 6b. The integrated areas of the CV curves in Figure 6b suggested much larger drops of the specific capacitance of the WO_3 hydrates compared to those of

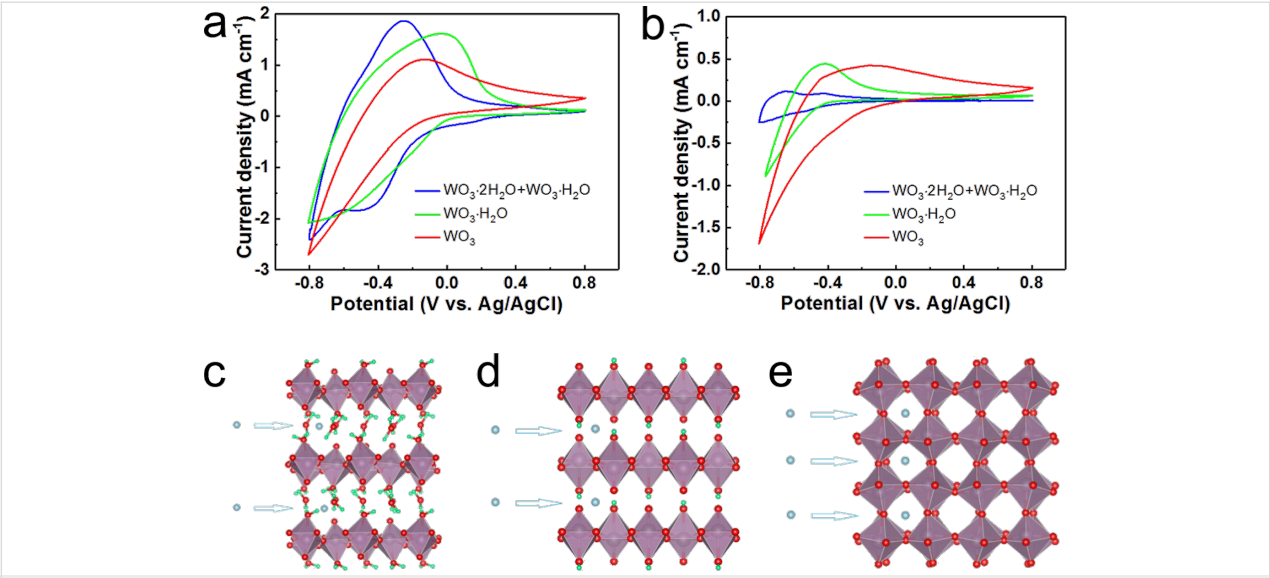

Figure 6: CV curves of the three samples at a) the 1st cycle and b) the 500th cycle; schematic illustration of ion intercalation into c) $WO_3·2H_2O$, d) $WO_3·H_2O$, and e) WO_3.

WO_3. As shown in Figure 6c–e, the intercalated ions in WO_3 hydrates are surrounded by weak hydrogen bonds, coordination bonds, and van der Waals forces, while the ions in WO_3 are surrounded by a strong 3D covalent bond network. The intercalation/deintercalation process in WO_3 may cause less distortions and destructions of the structure than in WO_3 hydrates, leading to a better electrochemical stability.

The SEM images of the samples taken after 500 cycles of CV support the performance degradation. Specifically, the nanostructured flower-like balls and the nanosheets in the samples synthesized at 80 °C seem to be glued together in Figure 7a, forming a thin film-like structure as indicated in the inset of Figure 7a, which could be a result of strong reaction between the interlayer water molecules and the electrolyte. For the $WO_3·H_2O$ sample synthesized at 120 °C (Figure 7b), the sheets were found to swell heavily due to the 2D intercalation/deintercalation processes in the CV cycles, turning almost twice as thick as their original thickness. Under the strong effect of 2D intercalation/deintercalation, the hexagonal plates were transformed into very thin nanosheets, which were composed of nanoribbons (Inset of Figure 7b). In contrast to the two samples mentioned above, the WO_3 sample synthesized at 180 °C still kept some of the features from the original sample, as depicted in Figure 7c. Although the original network was broken, a considerable number of the sheet components in the samples remained almost unchanged in their original shape (Inset of Figure 7c).

Figure 8 compares the Raman spectra of the three samples before and after CV tests. As displayed in Figure 8a, the initial WO_3 sample is characterized by two main peaks at ca. 713 and ca. 807 cm^{-1}, which are associated with two types of W–O–W stretching vibration modes [51,52]. The ν_1(W–O–W) mode also appeared in the other two initial samples. The Raman spectra of the initial $WO_3·H_2O$ and $WO_3·2H_2O$ samples were characterized by the stretching vibration mode of their terminal W=O bonds [53,54]. In spite of their high similarity, the peaks of $WO_3·2H_2O$ are shifted slightly to higher wavenumbers compared to those of $WO_3·H_2O$ as indicated in the sample containing both $WO_3·2H_2O$ and $WO_3·H_2O$. The Raman spectra presented in Figure 8b reflect the structural transformation of the samples after CV tests. The Raman spectra of both the samples synthesized at 80 and 120 °C showed a new peak from the W–O–W stretching vibration mode (ν_2(W–O–W)), while the other peaks were broadened. The peaks of the ν_1(W–O–W) modes in these two samples shifted to higher wavenumbers and became relatively stronger in comparison to the W=O peaks. These results clearly suggest the break of W=O bonds and the formation of W–O–W bonds, which leads to dehydration of WO_3 hydrates. In contrast, the Raman spectra of the WO_3 samples synthesized at 180 °C remains almost unaffected after CV tests. The investigation of Raman spectra further supports the relative electrochemical instability of $WO_3·2H_2O$ and $WO_3·H_2O$ compared to WO_3.

Conclusion

In summary, $WO_3·nH_2O$ (n = 0, 1, 2) synthesized in 2D and 3D nanostructures by a facile hydrothermal method, and the disadvantages of the 2D structures were thoroughly examined. The weakness of 2D $WO_3·nH_2O$ originates from the layered structure. XRD and SEM characterizations of the as-grown

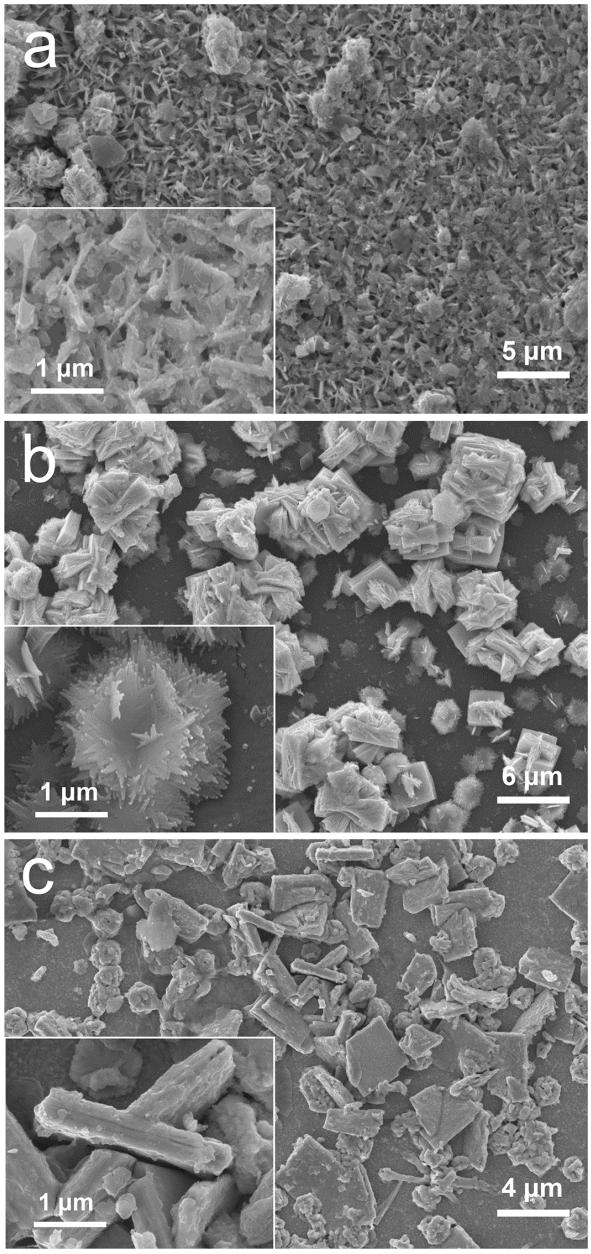

Figure 7: SEM images of the three typical samples synthesized at a) 80 °C, b) 120 °C and c) 180 °C after 500 CV cycles.

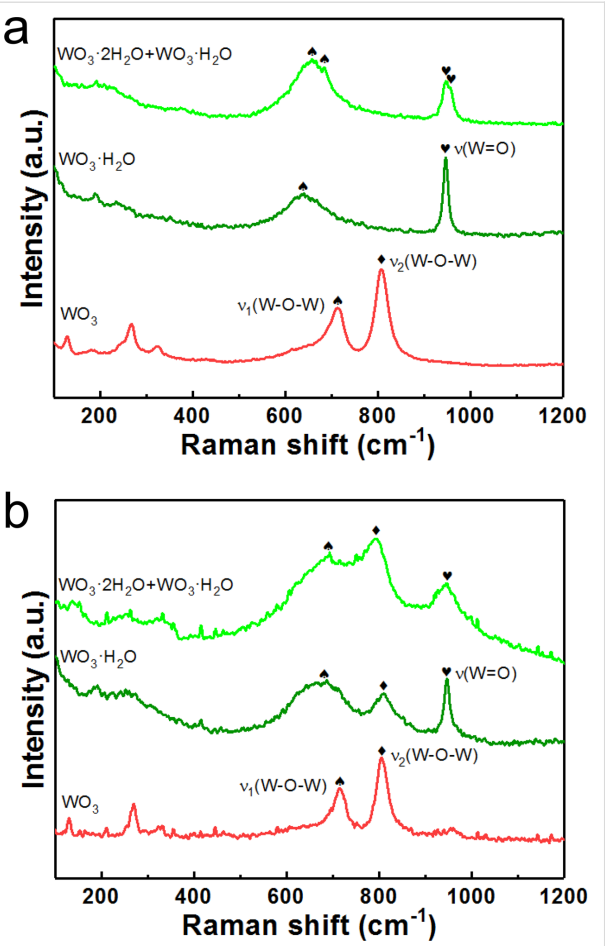

Figure 8: Raman spectra of the three samples a) before and b) after the CV tests.

$WO_3{\cdot}nH_2O$ samples suggested a structural transition from 2D to 3D upon temperature increase. The independent electrochemical tests of three typical samples confirmed a faster performance degradation in the 2D nanostructures compared to 3D nanostructures, supported by the SEM investigation and further explained by subsequent ex situ Raman measurements. Although 2D layered $WO_3{\cdot}nH_2O$ nanostructures outranks the 3D network counterparts in terms of the improved electronic properties, they can easily generate the structural instability by 2D intercalation owing to its weak interlayer van der Waals interactions. Their morphology change confirms the degradation mechanism proposed in this work. Consequently, this work provides in-depth understanding the weakness of 2D layered nanomaterials and paves the way for further interlayer reinforcement of 2D TMOs.

Supporting Information

The video shows the typical coloration/bleaching process of the samples during electrochemical cycling.

Supporting Information File 1

Coloration/bleaching during electrochemical cycling.
[https://www.beilstein-journals.org/bjnano/content/supplementary/2190-4286-9-265-S1.mp4]

Acknowledgements

The work was supported by the Research and Development Program of the Ghent University Global Campus, South Korea. This work was supported in part by the Melbourne Centre for

Nanofabrication (MCN) in the Victoria Node of the Australian National Fabrication Facility (ANFF). F.V. acknowledges the support from the Tomsk Polytechnic University Competitiveness Enhancement Program grant (VIU-316/2017). S.Z. acknowledges the support from the "100 Talents Program" of Shanxi Province, P.R. China.

ORCID® iDs

Zhenyin Hai - https://orcid.org/0000-0002-7821-4274
Philippe M. Heynderickx - https://orcid.org/0000-0002-6376-5890
Francis Verpoort - https://orcid.org/0000-0002-5184-5500

References

1. Xia, F.; Wang, H.; Xiao, D.; Dubey, M.; Ramasubramaniam, A. *Nat. Photonics* **2014,** *8,* 899–907. doi:10.1038/nphoton.2014.271
2. Niu, T.; Li, A. *Prog. Surf. Sci.* **2015,** *90,* 21–45. doi:10.1016/j.progsurf.2014.11.001
3. Li, H.; Shi, Y.; Chiu, M.-H.; Li, L.-J. *Nano Energy* **2015,** *18,* 293–305. doi:10.1016/j.nanoen.2015.10.023
4. Di, J.; Xia, J.; Li, H.; Liu, Z. *Nano Energy* **2017,** *35,* 79–91. doi:10.1016/j.nanoen.2017.03.030
5. Chakravarty, D.; Late, D. J. *Eur. J. Inorg. Chem.* **2015,** 1973–1980. doi:10.1002/ejic.201500039
6. Li, Z.-F.; Liu, Q.; Liu, Y.; Yang, F.; Xin, L.; Zhou, Y.; Zhang, H.; Stanciu, L.; Xie, J. *ACS Appl. Mater. Interfaces* **2015,** *7,* 27087–27095. doi:10.1021/acsami.5b05819
7. Khandare, L.; Late, D. J. *Appl. Surf. Sci.* **2017,** *418,* 2–8. doi:10.1016/j.apsusc.2016.11.199
8. Suryawanshi, S. R.; Kaware, V.; Chakravarty, D.; Walke, P. S.; More, M. A.; Joshi, K.; Rout, C. S.; Late, D. J. *RSC Adv.* **2015,** *5,* 80990–80997. doi:10.1039/C5RA12364J
9. Sahoo, S.; Mondal, R.; Late, D. J.; Rout, C. S. *Microporous Mesoporous Mater.* **2017,** *244,* 101–108. doi:10.1016/j.micromeso.2017.02.043
10. Sahoo, S.; Naik, K. K.; Late, D. J.; Rout, C. S. *J. Alloys Compd.* **2017,** *695,* 154–161. doi:10.1016/j.jallcom.2016.10.163
11. Kalantar-zadeh, K.; Ou, J. Z.; Daeneke, T.; Mitchell, A.; Sasaki, T.; Fuhrer, M. S. *Appl. Mater. Today* **2016,** *5,* 73–89. doi:10.1016/j.apmt.2016.09.012
12. Salanne, M.; Rotenberg, B.; Naoi, K.; Kaneko, K.; Taberna, P.-L.; Grey, C. P.; Dunn, B.; Simon, P. *Nat. Energy* **2016,** *1,* No. 16070. doi:10.1038/nenergy.2016.70
13. Haque, F.; Daeneke, T.; Kalantar-zadeh, K.; Ou, J. Z. *Nano-Micro Lett.* **2018,** *10,* No. 23. doi:10.1007/s40820-017-0176-y
14. Osada, M.; Sasaki, T. *J. Mater. Chem.* **2009,** *19,* 2503–2511. doi:10.1039/b820160a
15. Kisu, K.; Iijima, M.; Iwama, E.; Saito, M.; Orikasa, Y.; Naoi, W.; Naoi, K. *J. Mater. Chem. A* **2014,** *2,* 13058–13068. doi:10.1039/C4TA01994F
16. Peng, L.; Zhu, Y.; Chen, D.; Ruoff, R. S.; Yu, G. *Adv. Energy Mater.* **2016,** *6,* 1600025. doi:10.1002/aenm.201600025
17. Wang, D.; Li, X.-B.; Han, D.; Tian, W. Q.; Sun, H.-B. *Nano Today* **2017,** *16,* 30–45. doi:10.1016/j.nantod.2017.07.001
18. Hai, Z.; Zhuiykov, S. *Adv. Mater. Interfaces* **2018,** *5,* 1701385. doi:10.1002/admi.201701385
19. Zheng, H.; Ou, J. Z.; Strano, M. S.; Kaner, R. B.; Mitchell, A.; Kalantar-zadeh, K. *Adv. Funct. Mater.* **2011,** *21,* 2175–2196. doi:10.1002/adfm.201002477
20. Yan, C.; Kang, W.; Wang, J.; Cui, M.; Wang, X.; Foo, C. Y.; Chee, K. J.; Lee, P. S. *ACS Nano* **2014,** *8,* 316–322. doi:10.1021/nn404061g
21. Yang, P.; Sun, P.; Chai, Z.; Huang, L.; Cai, X.; Tan, S.; Song, J.; Mai, W. *Angew. Chem., Int. Ed.* **2014,** *53,* 11935–11939. doi:10.1002/anie.201407365
22. Yuan, S.-J.; Li, W.-W.; Cheng, Y.-Y.; He, H.; Chen, J.-J.; Tong, Z.-H.; Lin, Z.-Q.; Zhang, F.; Sheng, G.-P.; Yu, H.-Q. *Nat. Protoc.* **2014,** *9,* 112–119. doi:10.1038/nprot.2013.173
23. Baeck, S.-H.; Choi, K.-S.; Jaramillo, T. F.; Stucky, G. D.; McFarland, E. W. *Adv. Mater.* **2003,** *15,* 1269–1273. doi:10.1002/adma.200304669
24. Wang, J.; Liu, C.-j. *ChemBioEng Rev.* **2015,** *2,* 335–350. doi:10.1002/cben.201500014
25. Zhang, J.; Zhang, P.; Wang, T.; Gong, J. *Nano Energy* **2015,** *11,* 189–195. doi:10.1016/j.nanoen.2014.10.021
26. Sasidharan, M.; Gunawardhana, N.; Yoshio, M.; Nakashima, K. *Nano Energy* **2012,** *1,* 503–508. doi:10.1016/j.nanoen.2012.03.003
27. Cong, S.; Geng, F.; Zhao, Z. *Adv. Mater.* **2016,** *28,* 10518–10528. doi:10.1002/adma.201601109
28. Sun, W.; Yeung, M. T.; Lech, A. T.; Lin, C.-W.; Lee, C.; Li, T.; Duan, X.; Zhou, J.; Kaner, R. B. *Nano Lett.* **2015,** *15,* 4834–4838. doi:10.1021/acs.nanolett.5b02013
29. Wu, X.; Yao, S. *Nano Energy* **2017,** *42,* 143–150. doi:10.1016/j.nanoen.2017.10.058
30. Kuti, L. M.; Bhella, S. S.; Thangadurai, V. *Inorg. Chem.* **2009,** *48,* 6804–6811. doi:10.1021/ic900738m
31. Amano, F.; Tian, M.; Wu, G.; Ohtani, B.; Chen, A. *ACS Appl. Mater. Interfaces* **2011,** *3,* 4047–4052. doi:10.1021/am200897n
32. Chen, D.; Gao, L.; Yasumori, A.; Kuroda, K.; Sugahara, Y. *Small* **2008,** *4,* 1813–1822. doi:10.1002/smll.200800205
33. Jadkar, V.; Pawbake, A.; Waykar, R.; Jadhavar, A.; Date, A.; Late, D.; Pathan, H.; Gosavi, S.; Jadkar, S. *Phys. Status Solidi A* **2017,** *214,* 1600717. doi:10.1002/pssa.201600717
34. Late, D. J.; Kashid, R. V.; Rout, C. S.; More, M. A.; Joag, D. S. *Appl. Phys. A: Mater. Sci. Process.* **2010,** *98,* 751–756. doi:10.1007/s00339-009-5536-0
35. Qin, D.-D.; Tao, C.-L.; Friesen, S. A.; Wang, T.-H.; Varghese, O. K.; Bao, N.-Z.; Yang, Z.-Y.; Mallouk, T. E.; Grimes, C. A. *Chem. Commun.* **2012,** *48,* 729–731. doi:10.1039/C1CC15691H
36. Rahmani, M. B.; Yaacob, M. H.; Sabri, Y. M. *Sens. Actuators, B* **2017,** *251,* 57–64. doi:10.1016/j.snb.2017.05.029
37. Xie, Z.; Gao, L.; Liang, B.; Wang, X.; Chen, G.; Liu, Z.; Chao, J.; Chen, D.; Shen, G. *J. Mater. Chem.* **2012,** *22,* 19904–19910. doi:10.1039/c2jm33622g
38. Mitchell, J. B.; Lo, W. C.; Genc, A.; Lebeau, J.; Augustyn, V. *Chem. Mater.* **2017,** *29,* 3928–3937. doi:10.1021/acs.chemmater.6b05485
39. Ahmed, B.; Ojha, A. K.; Singh, A.; Hirsch, F.; Fischer, I.; Patrice, D.; Materny, A. *J. Hazard. Mater.* **2018,** *347,* 266–278. doi:10.1016/j.jhazmat.2017.12.069
40. Liang, L.; Zhang, J.; Zhou, Y.; Xie, J.; Zhang, X.; Guan, M.; Pan, B.; Xie, Y. *Sci. Rep.* **2013,** *3,* No. 1936. doi:10.1038/srep01936
41. Zheng, J. Y.; Haider, Z.; Van, T. K.; Pawar, A. U.; Kang, M. J.; Kim, C. W.; Kang, Y. S. *CrystEngComm* **2015,** *17,* 6070–6093. doi:10.1039/C5CE00900F
42. Zheng, J. Y.; Song, G.; Kim, C. W.; Kang, Y. S. *Nanoscale* **2013,** *5,* 5279–5282. doi:10.1039/c3nr00964e

43. Hai, Z.; Karbalaei Akbari, M.; Xue, C.; Xu, H.; Solano, E.; Detavernier, C.; Hu, J.; Zhuiykov, S. *Compos. Commun.* **2017,** *5,* 31–35. doi:10.1016/j.coco.2017.06.001
44. Bai, S.; Zhang, K.; Wang, L.; Sun, J.; Luo, R.; Li, D.; Chen, A. *J. Mater. Chem. A* **2014,** *2,* 7927–7934. doi:10.1039/C4TA00053F
45. Hai, Z.; Akbari, M. K.; Xue, C.; Xu, H.; Hyde, L.; Zhuiykov, S. *Appl. Surf. Sci.* **2017,** *405,* 169–177. doi:10.1016/j.apsusc.2017.02.031
46. Qiu, M.; Zhu, D.; Bao, X.; Wang, J.; Wang, X.; Yang, R. *J. Mater. Chem. A* **2016,** *4,* 894–900. doi:10.1039/C5TA08898D
47. Khan, H.; Zavabeti, A.; Wang, Y.; Harrison, C. J.; Carey, B. J.; Mohiuddin, M.; Chrimes, A. F.; Alves De Castro, I.; Zhang, B. Y.; Sabri, Y. M.; Bhargava, S. K.; Ou, J. Z.; Daeneke, T.; Russo, S. P.; Li, Y.; Kalantar-zadeh, K. *Nanoscale* **2017,** *9,* 19161–19175. doi:10.1039/C7NR05403C
48. Hai, Z.; Karbalaei Akbari, M.; Wei, Z.; Xue, C.; Xu, H.; Hu, J.; Hyde, L.; Zhuiykov, S. *Mater. Today Commun.* **2017,** *12,* 55–62. doi:10.1016/j.mtcomm.2017.06.006
49. Salmaoui, S.; Sediri, F.; Gharbi, N.; Perruchot, C.; Jouini, M. *Electrochim. Acta* **2013,** *108,* 634–643. doi:10.1016/j.electacta.2013.07.086
50. Hai, Z.; Karbalaei Akbari, M.; Wei, Z.; Xue, C.; Xu, H.; Hu, J.; Zhuiykov, S. *Electrochim. Acta* **2017,** *246,* 625–633. doi:10.1016/j.electacta.2017.06.095
51. Wang, R.; Chung, C. C.; Liu, Y.; Jones, J. L.; Augustyn, V. *Langmuir* **2017,** *33,* 9314–9323. doi:10.1021/acs.langmuir.7b00705
52. Zhuiykov, S.; Hyde, L.; Hai, Z.; Karbalaei Akbari, M.; Kats, E.; Detavernier, C.; Xue, C.; Xu, H. *Appl. Mater. Today* **2017,** *6,* 44–53. doi:10.1016/j.apmt.2016.12.004
53. He, Y.; Zhao, Y. *J. Phys. Chem. C* **2008,** *112,* 61–68. doi:10.1021/jp076898x
54. Nayak, A. K.; Lee, S.; Choi, Y. I.; Yoon, H. J.; Sohn, Y.; Pradhan, D. *ACS Sustainable Chem. Eng.* **2017,** *5,* 2741–2750. doi:10.1021/acssuschemeng.6b03084

License and Terms

BEILSTEIN JOURNAL OF NANOTECHNOLOGY

Amorphous Ni_xCo_yP-supported TiO_2 nanotube arrays as an efficient hydrogen evolution reaction electrocatalyst in acidic solution

Yong Li[1], Peng Yang[1], Bin Wang[2] and Zhongqing Liu[*1]

Full Research Paper

Open Access

Address:
[1]School of Chemical Engineering, Sichuan University, Chengdu 610065, Sichuan, P. R. China and [2]Engineered Multifunctional Composites (EMC), Knoxville, Tennessee 37934, USA

Email:
Zhongqing Liu[*] - liuzq_hgxy@scu.edu.cn

* Corresponding author

Keywords:
electrocatalysis; electrodeposition; HER; NiCoP bimetallic phosphides

Beilstein J. Nanotechnol. **2019,** *10,* 62–70.
doi:10.3762/bjnano.10.6

Received: 15 September 2018
Accepted: 20 November 2018
Published: 07 January 2019

This article is part of the thematic issue "Low-dimensional materials and systems".

Guest Editor: S. Walia

Abstract

Bimetallic phosphides have been attracting increasing attention due to their synergistic effect for improving the hydrogen evolution reaction as compared to monometallic phosphides. In this work, NiCoP modified hybrid electrodes were fabricated by a one-step electrodeposition process with TiO_2 nanotube arrays (TNAs) as a carrier. X-ray diffraction, transmission electron microscopy, UV–vis diffuse reflection spectroscopy, X-ray photoelectron spectroscopy and scanning transmission electron microscopy/energy-dispersive X-ray spectroscopy were used to characterize the physiochemical properties of the samples. The electrochemical performance was investigated by cyclic voltammetry, linear sweep voltammetry, and electrochemical impedance spectroscopy. We show that after incorporating Co into Ni–P, the resulting Ni_xCo_yP/TNAs present enhanced electrocatalytic activity due to the improved electron transfer and increased electrochemically active surface area (ECSA). In 0.5 mol L^{-1} H_2SO_4 electrolyte, the Ni_xCo_yP/TNAs (x = 3.84, y = 0.78) demonstrated an ECSA value of 52.1 mF cm^{-2}, which is 3.8 times that of Ni–P/TNAs (13.7 mF cm^{-2}). In a two-electrode system with a Pt sheet as the anode, the Ni_xCo_yP/TNAs presented a bath voltage of 1.92 V at 100 mA cm^{-2}, which is an improvment of 79% over that of 1.07 V at 10 mA cm^{-2}.

Introduction

Significant research efforts have been invested in the electrochemical splitting of water using renewable energy to attempt to overcome the growing energy demands and associated environmental crisis [1-3]. In water splitting, the hydrogen evolution reaction (HER) is a fundamentally important process. This process involves the reduction of protons to form dihydrogen ($2H^+ + 2e \rightarrow H_2$) with a thermodynamic potential of 0 V vs SHE. A major bottleneck for HER is the high overpotential associated with the process that takes place at a significant rate due to the high activation barrier and the sluggish multiple-

proton-coupled electron transfer [4-6]. Noble metal Pt-based catalysts are widely used for HER to circumvent the overpotential hurdle, but their exorbitant cost and scarcity seriously limit their large-scale application. Hence, it is quite appealing to develop inexpensive and earth-abundance electrocatalysts with higher electrolytic efficiency and lower dynamic overpotential [7,8].

More recently, transition-metal phosphides (TMPs) have attracted great interest as efficient HER electrocatalysts, including Ni_xP, MoP, CoP, FeP and Cu_3P. These materials are significantly promising because of their abundance, remarkable stability and activity derived from their hydrogenase-like catalytic mechanism [9-14]. By adding an additional metal element to these mono-metal posphides, the electronic structure and surface properties of the phosphides can be intrinsically altered that may greatly improve the catalytic performance. Compared to mono-metal phosphides, some binary metal phosphides (MgFeP, FeNiP, NiCoP, etc.) demonstrate a superior electrochemical performance. Because the ternary phases provide a synergistic effect, these bi-metal phosphides provide good electrical conductivity and electronic structure [15-17]. Among the bi-metal phosphides, Ni–Co–P catalysts have been intensively investigated. The similar radii of Co and Ni have been shown to be favorable to form ternary TMPs rather than secondary-metal doped phosphides [18-20]. As exemplified by Fu et al., hierarchical whisker-on-sheet nanostructures of NiCoP/nickel foam presented a superior performance, giving overpotentials of 59 mV and 220 mV to obtain current densities of 10 mA cm^{-2} and 100 mA cm^{-2} in alkaline electrolyte for HER, respectively [21]. However, the preparation procedure is more complicated and not environmentally friendly and includes a hydrothermal reaction, phosphorization step and KOH activation. This brings some difficulties to large-scale industrial application.

Amorphous catalysts intrinsically contain more defect sites which probably work as active centers compared to the crystalline counterparts. A representative work is that by Zhang et al. where they synthesized Ni–Co–P/nickel foam electrodes via a facile electroless deposition [22]. The as-prepared electrode requires only a small overpotential of 107 mV and 125 mV to achieve current densities of 10 and 20 mA cm^{-2}, respectively. Unfortunately, although the TMPs present excellent electrocatalytic activity in alkaline electrolytes [21-23], they are very unstable under acidic conditions. One effective way to improve their stability is with an appropriate support material. Compared to the nickel foam or other substrates [19,23,24], TiO_2 nanotube arrays prepared by anodization are favorable for the loading of catalysts and the fast transfer of electrons from the electrode to the active sites owing to the large surface area and distinctive 3D well-ordered nanotube structure. Furthermore, the curved interface and confined space facilitate the formation of amorphous phases with more active catalytic sites and contribute to the stability of active components [25,26]. Accordingly, in this study, the TNAs work as the support material in the preparation of Ni_xCo_yP/TNA hybrid electrodes by a one-step electrodeposition process. The physiochemical and electrochemical properties of as-prepared Ni_xCo_yP/TNAs electrodes were investigated in detail. In acidic aqueous solution, the Ni_xCo_yP/TNAs electrodes presented enhanced electrocatalytic activity and robust stability after incorporating Co into NiP.

Experimental

Preparation of Ni_xCo_yP/TNA electrodes

The TiO_2 nanotube arrays used here were prepared using an electrochemical anodization technique according to our previous work [25,26]. In a three-electrode system, the TNAs act as the working electrode, Pt as the counter electrode, Ag/AgCl (saturated KCl) as the reference, and a constant voltage (−1.2 V vs Ag/AgCl) was applied to the system and the duration of the electrodeposition was 200 s. The electrolyte (0.05 mol L^{-1} $Ni(NO_3)_2$ + 0.05 mol L^{-1} $Co(NO_3)_2$ + 0.1 mol L^{-1} NaH_2PO_2) pH was adjusted with 5% HCl to about 1.0. After electrodeposition, the working electrode was rinsed with deionized water, absolute ethanol, and then deionized water, and dried under blowing air. The sample was named Ni_xCo_yP/TNAs. A control sample Ni–P/TNAs was prepared in a similar fashion without adding $Co(NO_3)_2$ in the electrolyte.

Sample characterization

The following analytic methods were applied to provide structural information on the Ni_xCo_yP/TNA samples: X-ray diffraction (XRD, X'Pert pro MPD, Philips) for crystallographic texture, scanning electron microscopy (SEM, JSM-5900 LV, JEOV) for micro-morphology, transmission electron microscopy (TEM, Tecnai G2 F20 S-TWIN) for microstructure, UV–vis diffuse reflectance spectroscopy (UV2100) for photoabsorption properties, X-ray photoelectron spectroscopy (XPS, Escalab 250Xi, Thermo Fisher, Al Ka X-ray source generated at 12 kV and 15 mA) for chemical composition, and energy dispersive spectroscopy (EDS, JSM-7500F) for single nanotube chemical composition.

Electrochemical measurements

The electrochemical characteristics of the samples were evaluated using a CHI650E electrochemical workstation (Chenhua, Shanghai) including linear sweep voltammetry (LSV), cyclic voltammetry (CV), electrochemical impedance spectroscopy (EIS), and Tafel analysis at 25 °C. The three electrode system was constituted of the sample working electrode, a platinum counter electrode, a Ag/AgCl (saturated KCl) reference elec-

trode, and 0.5 mol L^{-1} H_2SO_4 as the electrolyte. During the LSV, CV, and Tafel experiments, the scan rate was 5 mV s^{-1}. During the EIS experiment, the frequency range was 10^{-2}–10^5 Hz and the applied bias was the open-circuit potential of the samples. The measured current was normalized by the geometrical area of the cathodes immersed in electrolyte solution. The obtained potential (vs Ag/AgCl) was converted RHE after imposing iR_s correction, using the following Equation 1:

$$E_{RHE} = E_{Ag/AgCl} + 0.059 \times pH + E^0_{Ag/AgCl}(0.197) \quad (1)$$

Results and Discussion

Characterization of electrocatalysts

Figure 1 shows the wide-angle XRD patterns of the samples. All three samples displayed characteristic anatase TiO_2 diffraction peaks of (101), (004), (200), (105), (211), (204), (116), and (215) (JCPDS card No. 21-1272) and the Ti peak at (101) [27]. No diffraction peaks related to Ni–P or NiCoP crystallites was found, illustrating that the crystallographic texture of the electrode samples was not altered by the electrodeposition of Ni–P or NiCoP. The intensity of the diffraction peaks follow the order: TNAs > Ni–P/TNAs > Ni_xCo_yP/TNAs. It is suggested that after electrodeposition, there was an amorphous deposit covering the TiO_2 surface to dampen the anatase peak intensities. The top-view FE-SEM images of TNAs and Ni_xCo_yP/TNAs are shown in Figure 2. It is obvious that the openings of the TNAs were smooth with even wall thickness. After electrodeposition of NiCoP, the openings of sample Ni_xCo_yP/TNAs were coarse with apparent deposit attached. Figure 3 demonstrates the TEM and HR-TEM images of Ni_xCo_yP/TNAs. The lattice spacing of 0.35 nm is ascribed to anatase TiO_2 (101) plane [28], and no lattice fringe that corresponds to NiCoP can be finely resolved. Combining the XRD and SEM results, we conclude that amorphous NiCoP particles of ≈6 nm were attached to TiO_2 (101) phase, as shown in the upper left and square areas. The STEM-HAADF and corresponding EDS maps of single tube Ni_xCo_yP/TNAs are revealed in Figure 4. From the figure, the diameter of the TiO_2 nanotube was determined to be about 150 nm with a chemical composition of Ti, O, Ni, Co, and P evenly distributed on the whole tube. The elemental intensity distributions of Ti and O were similar to one another, however the combinations Ni and P, Co and P, and Ni and Co did not have similar distributions. The distribution intensity of Ni is obviously higher than that of Co. It is possible that in addition to NiCoP, there might be other phases of Ni, Co, or P.

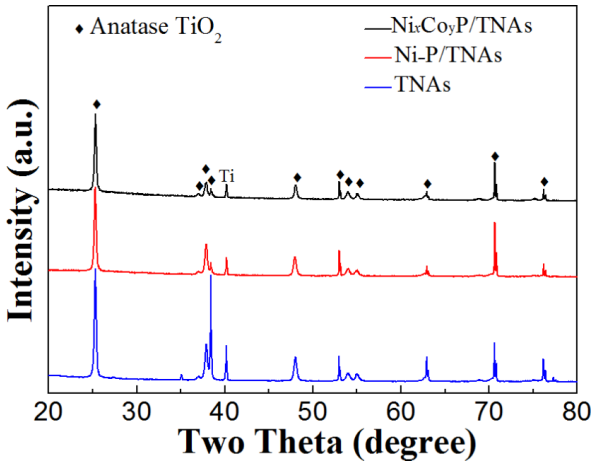

Figure 1: XRD patterns of the samples.

To further probe the surface chemical composition and valence states in the Ni_xCo_yP/TNAs, we conducted X-ray photoelectron spectroscopy measurements. In Figure 5a, TiO_2 shows two peaks, the Ti $2p_{3/2}$ peak at 458.3 eV and Ti $2p_{1/2}$ at 464.1 eV, along with a satellite peak at 460.1 eV. The O 1s peaks at 531.5 and 529.6.5 eV are assigned to O in O_2 and TiO_2, respectively. The peak at 855.3 eV for Ni $2p_{3/2}$ can be ascribed to $Ni^{\delta+}$ in

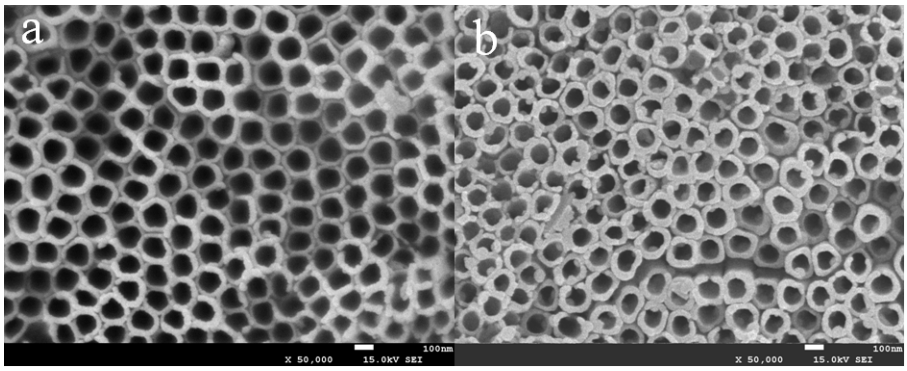

Figure 2: Top-view FE-SEM images of the samples. (a) TNAs, (b) Ni_xCo_yP/TNAs.

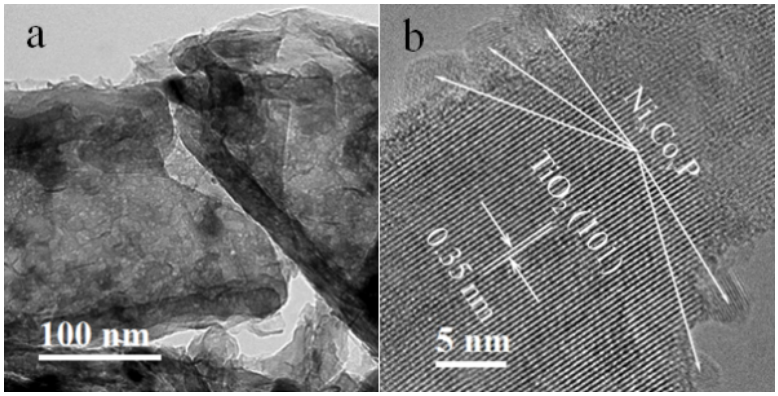

Figure 3: (a) TEM and (b) HR-TEM images of the Ni_xCo_yP/TNAs.

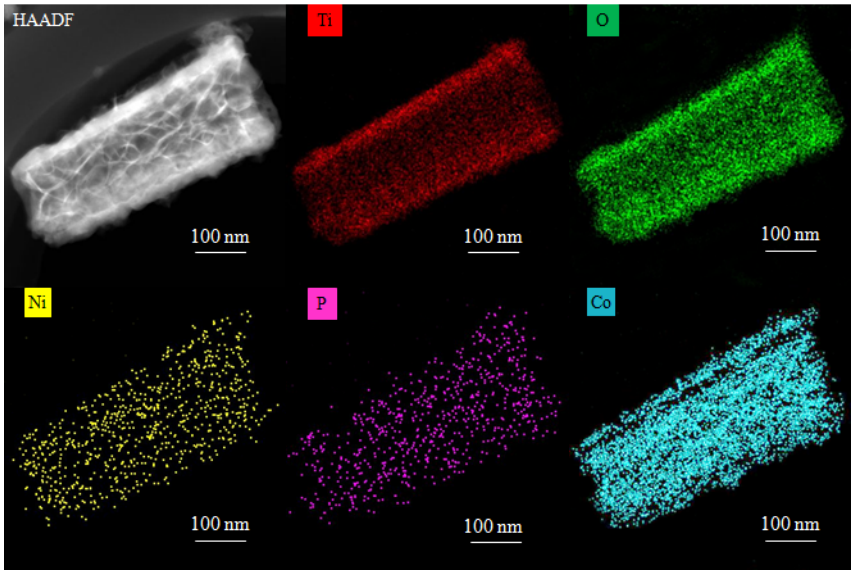

Figure 4: HAADF STEM image and EDS elemental maps of the Ni_xCo_yP/TNAs.

Ni−P bonds, positively shifted relative to that of metallic Ni (852.3 eV) (Figure 5c). The Ni $2p_{3/2}$ peak at 861.5 and Ni $2p_{1/2}$ peak at 879.3 eV are assigned to the Ni 2p satellite peaks [15,29-31]. In Figure 5d, the Co $2p_{3/2}$ peak at 778.2 is assigned to metallic Co, and the Co $2p_{3/2}$ peak at 781.5 and Co $2p_{1/2}$ peak at 797.2 eV can be ascribed to $Co^{\delta+}$ and Co^{3+} ions in NiCoP, respectively. The broad peaks at 786.2 ($2p_{3/2}$) and 803.5 eV ($2p_{1/2}$) are assigned to the Co 2p satellite peaks [21,32]. In the high-resolution P 2p spectrum of Figure 5e, the binding energy at 129.6 eV is close to the binding energy of P $2p_{3/2}$, assigned to metal–P bonds in NiCoP. The peak at 133.1eV can be ascribed to the oxidized phosphorus species by contact with air [21,33-35]. The binding energy of 129.6 eV is slightly lower than that of elemental P (130.0 eV), which suggests the P is partially negatively charged ($P^{\delta-}$) [36]. Given the probing depth of 3 nm for XPS measurements, the NiCoP amorphous phase in Ni_xCo_yP/TNAs presents a molar mole ratio of 10.82: 2.21:2.82, giving $x = 3.84$ and $y = 0.78$. According to the XPS results, polyvalent interactions of Ni, Co and P heteroatoms are suggested. In this complex material, both Ni and Co carry a partially positive charge (δ^+) whereas P carries a partially negative charge (δ^-), suggesting a small electron density transfer from Ni and Co to P [37]. This charged structure is very beneficial for improving surface activity toward HER.

A critical means to improve the charge transfer of HER is to enhance the conductivity of the electrocatalysts. Doping or hybridization to form a heterojunction can lower the band gap of the material thus augment the conductivity. The material band gap can be calculated by measuring the optical absorption edge in UV–vis DRS, shown in Figure 5f. It is observed that the absorption edge showed a red shift after electrodeposition of

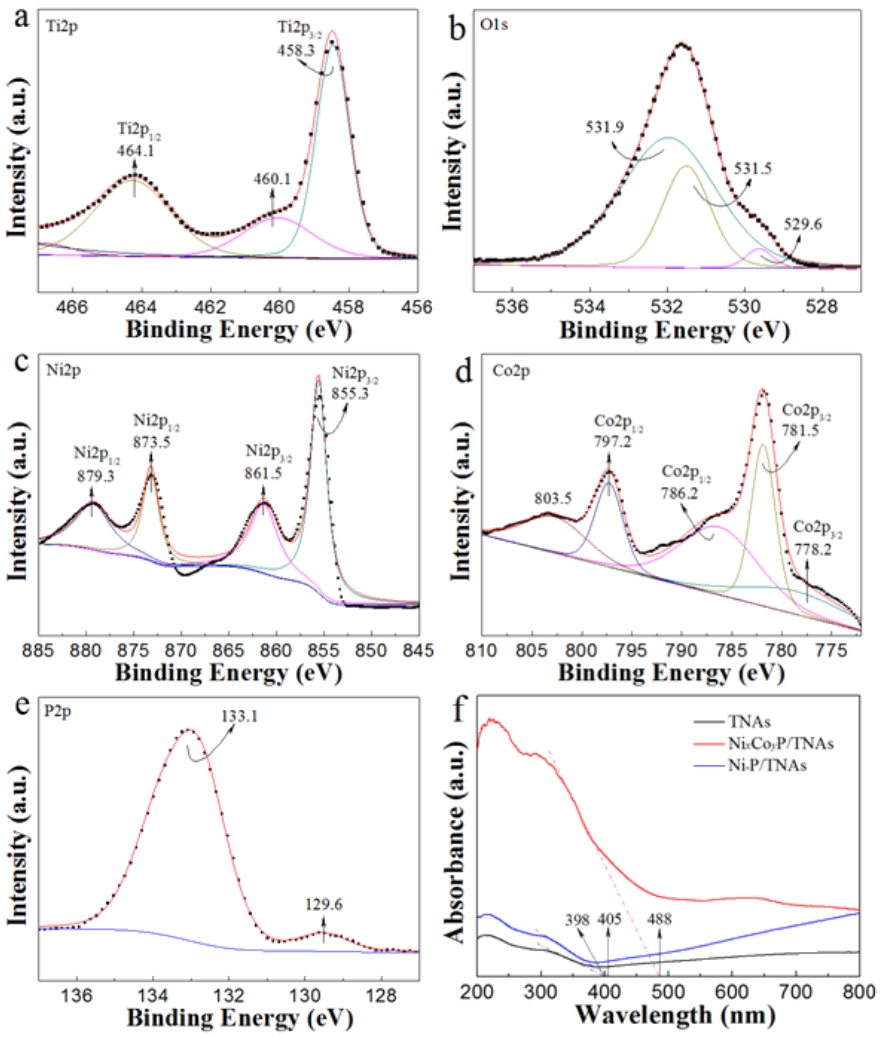

Figure 5: High-resolution XPS spectra of (a) Ti 2p, (b) O 1s, (c) Ni 2p, (d) Co 2p and (e) P 2p of the Ni_xCo_yP/TNAs. (f) UV–vis diffuse reflection absorbance spectra of the samples.

Ni–P and NiCoP. The absorption edges are 398, 405, and 488 nm for TNAs, Ni–P/TNAS, and Ni_xCo_yP/TNAs, corresponding the band gaps of 3.12, 3.06, and 2.54 eV, respectively. Sample Ni_xCo_yP/TNAs had a band gap 0.52 eV lower than that of Ni–P/TNAs. This indicates that the binary-metal phosphides synthesized via electrodeposition provide a higher conductivity in the material.

Electrochemical activity

The electrochemical properties of the samples are shown in Figure 6, including LSV, CV, Tafel curves, bath voltage histograms, and cycling stability characteristics. In Figure 6a, the activity of Ni_xCo_yP/TNAs is much higher than that of Ni–P/TNAs. The onset hydrogen evolution potential (defined as the potential at a current density of −0.1 mA cm^{-2}) at −10 and −20 mA cm^{-2} of Ni_xCo_yP/TNAs were −65, −209, and −257 mV, respectively. These values are 235, 363, and 359 mV lower than that of Ni–P/TNAs of −300, −572, and −616 mV, respectively. It should be noted that the hydrogen doping may occur due to the small radius of the hydrogen atom when measuring the electrocatalytic activity of Ni_xCo_yP/TNAs. Generally speaking, hydrogen doping increases electrical conductivity and enhances electron transfer. Thus the electrocatalytic activity is improved to some extent. Figure 6b illustrates the Tafel curves of the Ni_xCo_yP/TNAs electrode. The Tafel slope of this electrode is 46.6 mV dec^{-1}, which is 40.3 mV dec^{-1} lower than that of Ni–P/TNAs at 86.9 mV dec^{-1}. For HER in acidic electrolyte, the theoretical Tafel slopes are 120, 40, and 30 mV dec^{-1}, corresponding to the Volmer step, Heyrovsky step, and Tafel step, respectively. A Tafel slope of 46.6 mV dec^{-1} indicates that hydrogen evolution occurred via a fast discharge reaction ($H_3O^+ + e^- + cat = cat\text{-}H + H_2O$)

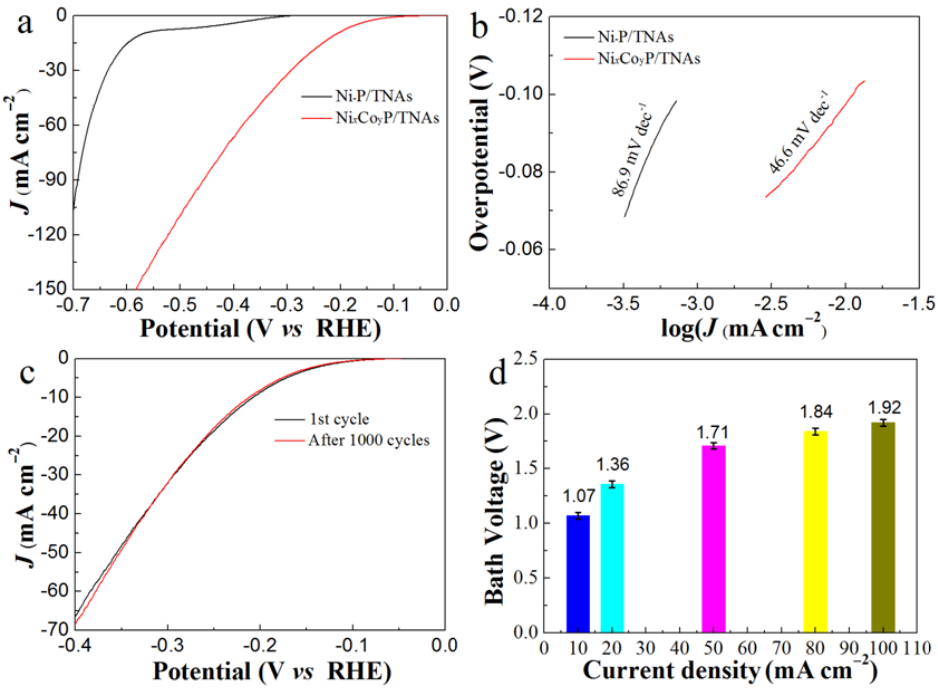

Figure 6: (a) Current–voltage characteristic plots and (b) Tafel plots of the samples. (c) Current–voltage characteristics during durability tests and (d) bath voltages at various current densities for the two-electrode system with Ni_xCo_yP/TNAs as a cathode.

and thereafter a rate determining (ion + atom) reaction ($H_3O^+ + e^- + cat\text{-}H = cat + H_2 + H_2O$), that is, the Volmer–Heyrovsky mechanism [38,39]. A comparison was given with published data in Supporting Information File 1, where Table S1 and shows that NiCoP catalysts present lower overpotentials in alkaline electrolyte than those in acidic solution. The Ni_xCo_yP/TNAs electrode gives a lower activity than the electrode without the titanium dioxide carrier, which may be related to the low conductivity of titanium dioxide. Thus the electrocatalytic activity can be improved effectively by improving the conductivity of the TNA support.

In electrochemical HER, the bath voltage is an important parameter determining the energy consumption of the process. At a certain current density, the bath voltage is proportional to the electric energy consumption. In Figure 6d, the bath voltage was only 1.07 ± 0.03 V at hydrogen evolution current density of −10 mA cm^{-2} in the two-electrode system of Ni_xCo_yP/TNAs as the cathode and Pt sheet as the anode. A bath voltage of 1.71 V at a current density of 50 mA cm^{-2} is comparable to that of the NiCoP/foam nickel electrode [21]. It is noticeable that with increasing current density, the bath voltage does not rise in a linear pattern. A bath voltage of 1.92 V at 100 mA cm^{-2} is only 79% higher than that of 1.07 V at 10 mA cm^{-2}. This demonstrates the excellent electrocatalytic activity of Ni_xCo_yP/TNA electrodes in acidic conditions. Other than the high electrocatalytic activity, the electrochemical stability is another critical parameter for electrodes in practical applications. The electrochemical activity of the Ni_xCo_yP/TNAs suffered a negligible decrease after 1000 cycles at a scan rate of 100 mV s^{-1} (Figure 6d). This shows a high stability of this electrode.

For electrocatalytic reactions, the active site density is proportional to the reaction rate under certain conditions. The higher the density of exposed active sites, the faster the reaction rate. The active site density is related to the double-layer capacitance of the electrode surface without Faradic current and corresponds to the effective electrochemical surface area (ESA). Therefore the magnitude of the double-layer capacitance can be used to estimate the ESA. To estimate the effective ESA, we measured the electrochemical double-layer capacitances (C_{dl}) using the CV method [22,40,41]. The scan rates during the CV measurements were set in the range of 25–175 mV s^{-1} (step by 25 mV s^{-1}), electrode potential range of 0.1–0.2 V vs RHE. In Figure 7a–c, the CV curves are shown as zero-symmetric, rectangular curves against current density. This illustrates the double-layer capacitance nature of the electrode in this potential range and good reversibility. Figure 7d shows the double-layer capacitance of the Ni_xCo_yP/TNAs electrode to be 52.1 mF cm^{-2}, which is 2.8 and 5.6 times that of Ni–P/TNAs (13.7 mF cm^{-2}) and TNAs (7.9 mF cm^{-2}). The incorporation of Co into the Ni–P formed amorphous binary-metal phosphides that are beneficial for the improvement of the electrocatalytic active site density, and thus the electrocatalytic activity.

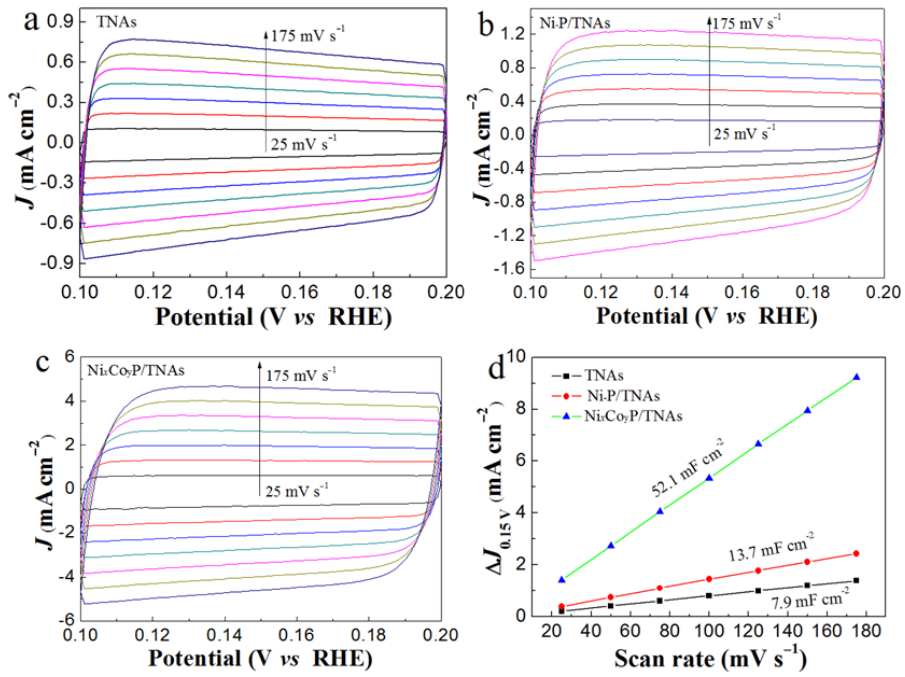

Figure 7: Cyclic voltammograms of (a) TNAs, (b) Ni–P/TNAs and (c) Ni_xCo_yP/TNAs at various scan rates (25–175 mV s^{-1}), and (d) corresponding current density scan rate curves to estimate the C_{dl} and relative electrochemically active surface area.

The Nyquist and Bode plots are displayed in Figure 8. In the Nyquist plot, the arc radius of the high-frequency section corresponds to the impedance of charge transfer between electrolyte and the catalyst surface, and the ones of the low-frequency area correspond to the impedance of charge transport inside the electrode [15,42-44]. In Figure 8a, the Nyquist curves are shown as two arcs with different radius in the high and low frequency, suggesting that the catalytic reaction was limited by the charge transfer step. The arc radii of the high and low frequency sections of sample Ni_xCo_yP/TNAs are smaller than that of Ni–P/TNAs, suggesting that the NiCoP hybrid enhanced the charge transfer inside the electrode and between the electrolyte and catalyst surface. The Bode plots (Figure 8b) show that for the two samples, the total impedance (|*Z*|) is nearly equivalent at high frequency, while at low frequency, the impedance of Ni_xCo_yP/TNAs is lower than that of Ni–P/TNAs. This indicates that after incorporating Co into Ni–P, the main contribution is to improve the transmission of electrons inside the electrode, in agreement with a higher conductivity of Ni_xCo_yP/TNA confirmed by UV–vis diffuse reflection spectra. Both the CV and EIS results exemplify the high electrocatalytic activity of the Ni_xCo_yP/TNAs electrode, in accordance with the aforementioned electrochemical experiment results.

Conclusion

The binary-metal phosphide hybrid electrode Ni_xCo_yP/TNAs was synthesized through the one-step electrodeposition of Ni, Co, and P under a constant voltage. Experimental results

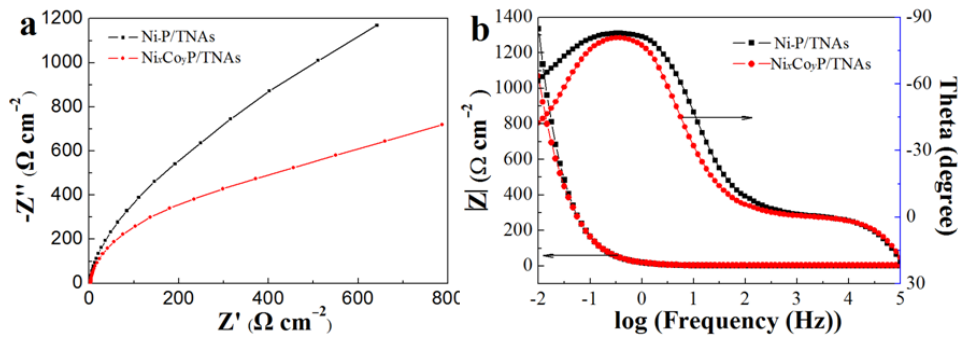

Figure 8: (a) Nyquist curves and (b) Bode plots of the samples.

demonstrate that the NiCoP deposit was in amorphous phase with a diameter of ≈6 nm. The incorporation of Co into the binary Ni–P system formed the amorphous ternary NiCoP HER electrocatalyst. The catalyst showed a high electrochemically active center density that benefited the electron transfer within the electrode and between electrolyte and electrode surface. The electrocatalytic activity of the HER was thus improved. In the two-electrode system using Ni_xCo_yP/TNAs as the cathode, the bath voltage was only 1.07 V at hydrogen evolution current density of −10 mA cm^{-2}, indicating superb electrocatalytic activity. The electrochemical stability of the electrode was proved via continuous cycling measurements.

Supporting Information

Supporting Information File 1

Comparison of the overpotentials (vs RHE) between the references and this work.
[https://www.beilstein-journals.org/bjnano/content/supplementary/2190-4286-10-6-S1.pdf]

Acknowledgements

This work was supported by the National Science Foundation of China (Grant no. 21376154). The authors would like to express their gratitude to Analytical and Test Center of Sichuan University.

ORCID® iDs

Zhongqing Liu - https://orcid.org/0000-0003-3019-2413

References

1. Walter, M. G.; Warren, E. L.; McKone, J. R.; Boettcher, S. W.; Mi, Q.; Santori, E. A.; Lewis, N. S. *Chem. Rev.* **2010,** *110,* 6446–6473. doi:10.1021/cr1002326
2. Joya, K. S.; Joya, Y. F.; Ocakoglu, K.; van de Krol, R. *Angew. Chem., Int. Ed.* **2013,** *52,* 10426–10437. doi:10.1002/anie.201300136
3. Cabán-Acevedo, M.; Stone, M. L.; Schmidt, J. R.; Thomas, J. G.; Ding, Q.; Chang, H.-C.; Tsai, M.-L.; He, J.-H.; Jin, S. *Nat. Mater.* **2015,** *14,* 1245–1251. doi:10.1038/nmat4410
4. Turner, J. A. *Science* **2004,** *305,* 972–974. doi:10.1126/science.1103197
5. Han, L.; Dong, S.; Wang, E. *Adv. Mater.* **2016,** *28,* 9266–9291. doi:10.1002/adma.201602270
6. Moniz, S. J. A.; Shevlin, S. A.; Martin, D. J.; Guo, Z.-X.; Tang, J. *Energy Environ. Sci.* **2015,** *8,* 731–759. doi:10.1039/c4ee03271c
7. Wang, Y.; Carey, B. J.; Zhang, W.; Chrimes, A. F.; Chen, L.; Kalantar-zadeh, K.; Ou, J. Z.; Daeneke, T. *J. Phys. Chem. C* **2016,** *120,* 2447–2455. doi:10.1021/acs.jpcc.5b10939
8. Wang, Y.; Della Gaspera, E.; Carey, B. J.; Atkin, P.; Berean, K. J.; Clark, R. M.; Cole, I. S.; Xu, Z.-Q.; Zhang, Y.; Bao, Q.; Ou, J. Z.; Daeneke, T.; Kalantar-zadeh, K. *Nanoscale* **2016,** *8,* 12258–12266. doi:10.1039/c6nr02197b
9. Lin, Y.; He, L.; Chen, T.; Zhou, D.; Wu, L.; Hou, X.; Zheng, C. *J. Mater. Chem. A* **2018,** *6,* 4088–4094. doi:10.1039/c7ta09524d
10. Zhou, L.; Shao, M.; Li, J.; Jiang, S.; Wei, M.; Duan, X. *Nano Energy* **2017,** *41,* 583–590. doi:10.1016/j.nanoen.2017.10.009
11. Wang, R.; Dong, X.-Y.; Du, J.; Zhao, J.-Y.; Zhang, S.-Q. *Adv. Mater.* **2018,** *30,* 1703711. doi:10.1002/adma.201703711
12. Schipper, D. E.; Zhao, Z.; Thirumalai, H.; Leitner, A. P.; Donaldson, S. L.; Kumar, A.; Qin, F.; Wang, Z.; Grabow, L. C.; Bao, J.; Whitmire, K. H. *Chem. Mater.* **2018,** *30,* 3588–3598. doi:10.1021/acs.chemmater.8b01624
13. Zhang, X.; Wu, Z.; Wang, D. *Electrochim. Acta* **2018,** *281,* 540–548. doi:10.1016/j.electacta.2018.05.176
14. Tang, W.; Wang, J.; Guo, L.; Teng, X.; Meyer, T. J.; Chen, Z. *ACS Appl. Mater. Interfaces* **2017,** *9,* 41347–41353. doi:10.1021/acsami.7b14466
15. Qin, Z.; Chen, Y.; Huang, Z.; Su, J.; Guo, L. *J. Mater. Chem. A* **2017,** *5,* 19025–19035. doi:10.1039/c7ta04434h
16. Costa, J. D.; Lado, J. L.; Carbó-Argibay, E.; Paz, E.; Gallo, J.; Cerqueira, M. F.; Rodríguez-Abreu, C.; Kovnir, K.; Kolen'ko, Y. V. *J. Phys. Chem. C* **2016,** *120,* 16537–16544. doi:10.1021/acs.jpcc.6b05783
17. Kibsgaard, J.; Tsai, C.; Chan, K.; Benck, J. D.; Nørskov, J. K.; Abild-Pedersen, F.; Jaramillo, T. F. *Energy Environ. Sci.* **2015,** *8,* 3022–3029. doi:10.1039/c5ee02179k
18. Li, J.; Yan, M.; Zhou, X.; Huang, Z.-Q.; Xia, Z.; Chang, C.-R.; Ma, Y.; Qu, Y. *Adv. Funct. Mater.* **2016,** *26,* 6785–6796. doi:10.1002/adfm.201601420
19. Du, C.; Yang, L.; Yang, F.; Cheng, G.; Luo, W. *ACS Catal.* **2017,** *7,* 4131–4137. doi:10.1021/acscatal.7b00662
20. Liang, H.; Gandi, A. N.; Anjum, D. H.; Wang, X.; Schwingenschlögl, U.; Alshareef, H. N. *Nano Lett.* **2016,** *16,* 7718–7725. doi:10.1021/acs.nanolett.6b03803
21. Cai, Z.; Wu, A.; Yan, H.; Xiao, Y.; Chen, C.; Tian, C.; Wang, L.; Wang, R.; Fu, H. *Nanoscale* **2018,** *10,* 7619–7629. doi:10.1039/c8nr01057a
22. Yang, Q.; Lv, C.; Huang, Z.; Zhang, C. *Int. J. Hydrogen Energy* **2018,** *43,* 7872–7880. doi:10.1016/j.ijhydene.2018.03.003
23. Ma, X.; Chang, Y.; Zhang, Z.; Tang, J. *J. Mater. Chem. A* **2018,** *6,* 2100–2106. doi:10.1039/c7ta09619d
24. Bai, Y.; Zhang, H.; Li, X.; Liu, L.; Xu, H.; Qiu, H.; Wang, Y. *Nanoscale* **2015,** *7,* 1446–1453. doi:10.1039/c4nr05862c
25. Liu, Z.; Zhang, X.; Wang, B.; Xia, M.; Gao, S.; Liu, X.; Zavabeti, A.; Ou, J. Z.; Kalantar-Zadeh, K.; Wang, Y. *J. Phys. Chem. C* **2018,** *122,* 12589–12597. doi:10.1021/acs.jpcc.8b01678
26. Gao, S.; Wang, B.; Liu, X.; Guo, Z.; Liu, Z.; Wang, Y. *Nanoscale* **2018,** *10,* 10288–10295. doi:10.1039/c8nr02532k
27. Zhang, P.; Tachikawa, T.; Fujitsuka, M.; Majima, T. *Chem. Commun.* **2015,** *51,* 7187–7190. doi:10.1039/c5cc01753j
28. Zheng, L.; Han, S.; Liu, H.; Yu, P.; Fang, X. *Small* **2016,** *12,* 1527–1536. doi:10.1002/smll.201503441
29. Yu, J.; Li, Q.; Li, Y.; Xu, C.-Y.; Zhen, L.; Dravid, V. P.; Wu, J. *Adv. Funct. Mater.* **2016,** *26,* 7644–7651. doi:10.1002/adfm.201603727
30. Bi, L.; Gao, X.; Zhang, L.; Wang, D.; Zou, X.; Xie, T. *ChemSusChem* **2018,** *11,* 276–284. doi:10.1002/cssc.201701574
31. Tian, J.; Cheng, N.; Liu, Q.; Xing, W.; Sun, X. *Angew. Chem., Int. Ed.* **2015,** *54,* 5493–5497. doi:10.1002/anie.201501237
32. Han, A.; Chen, H.; Zhang, H.; Sun, Z.; Du, P. *J. Mater. Chem. A* **2016,** *4,* 10195–10202. doi:10.1039/c6ta02297a
33. Liang, Y.; Li, Y.; Wang, H.; Dai, H. *J. Am. Chem. Soc.* **2013,** *135,* 2013–2036. doi:10.1021/ja3089923

34. Blanchard, P. E. R.; Grosvenor, A. P.; Cavell, R. G.; Mar, A. *Chem. Mater.* **2008,** *20,* 7081–7088. doi:10.1021/cm802123a
35. Li, Y.; Liu, J.; Chen, C.; Zhang, X.; Chen, J. *ACS Appl. Mater. Interfaces* **2017,** *9,* 5982–5991. doi:10.1021/acsami.6b14127
36. Wang, C.; Jiang, J.; Ding, T.; Chen, G.; Xu, W.; Yang, Q. *Adv. Mater. Interfaces* **2016,** *3,* 1500454. doi:10.1002/admi.201500454
37. Zhang, R.; Wang, X.; Yu, S.; Wen, T.; Zhu, X.; Yang, F.; Sun, X.; Wang, X.; Hu, W. *Adv. Mater.* **2017,** *29,* 1605502. doi:10.1002/adma.201605502
38. Merki, D.; Fierro, S.; Vrubel, H.; Hu, X. *Chem. Sci.* **2011,** *2,* 1262–1267. doi:10.1039/c1sc00117e
39. Zou, X.; Zhang, Y. *Chem. Soc. Rev.* **2015,** *44,* 5148–5180. doi:10.1039/c4cs00448e
40. Lukowski, M. A.; Daniel, A. S.; English, C. R.; Meng, F.; Forticaux, A.; Hamers, R. J.; Jin, S. *Energy Environ. Sci.* **2014,** *7,* 2608–2613. doi:10.1039/c4ee01329h
41. Pham, K.-C.; Chang, Y.-H.; McPhail, D. S.; Mattevi, C.; Wee, A. T. S.; Chua, D. H. C. *ACS Appl. Mater. Interfaces* **2016,** *8,* 5961–5971. doi:10.1021/acsami.5b09690
42. Li, X.; Wu, H.; Elshahawy, A. M.; Wang, L.; Pennycook, S. J.; Guan, C.; Wang, J. *Adv. Funct. Mater.* **2018,** *28,* 1800036. doi:10.1002/adfm.201800036
43. Ye, Z.; Yang, J.; Li, B.; Shi, L.; Ji, H.; Song, L.; Xu, H. *Small* **2017,** *13,* 1700111. doi:10.1002/smll.201700111
44. Liu, S.; Liu, Q.; Lv, Y.; Chen, B.; Zhou, Q.; Wang, L.; Zheng, Q.; Che, C.; Chen, C. *Chem. Commun.* **2017,** *53,* 13153–13156. doi:10.1039/c7cc08340h

License and Terms

BEILSTEIN JOURNAL OF NANOTECHNOLOGY

A $Ni(OH)_2$ nanopetals network for high-performance supercapacitors synthesized by immersing Ni nanofoam in water

Donghui Zheng[1], Man Li[1], Yongyan Li[1], Chunling Qin[*1], Yichao Wang[2] and Zhifeng Wang[*1]

Full Research Paper

Open Access

Address:
[1]School of Materials Science and Engineering, Hebei University of Technology, Tianjin 300130, China and [2]School of Life and Environmental Sciences, Deakin University, Waurn Ponds, VIC 3216, Australia

Email:
Chunling Qin* - clqin@hebut.edu.cn; Zhifeng Wang* - wangzf@hebut.edu.cn

* Corresponding author

Keywords:
dealloying; Ni nanofoam; $Ni(OH)_2$ nanopetals; metallic glass; supercapacitor

Beilstein J. Nanotechnol. **2019,** *10,* 281–293.
doi:10.3762/bjnano.10.27

Received: 01 November 2018
Accepted: 09 January 2019
Published: 25 January 2019

This article is part of the thematic issue "Low-dimensional materials and systems".

Guest Editor: S. Walia

Abstract

Developing a facile and environmentally friendly approach to the synthesis of nanostructured $Ni(OH)_2$ electrodes for high-performance supercapacitor applications is a great challenge. In this work, we report an extremely simple route to prepare a $Ni(OH)_2$ nanopetals network by immersing Ni nanofoam in water. A binder-free composite electrode, consisting of $Ni(OH)_2$ nanopetals network, Ni nanofoam interlayer and Ni-based metallic glass matrix ($Ni(OH)_2$/Ni-NF/MG) with sandwich structure and good flexibility, was designed and finally achieved. Microstructure and morphology of the $Ni(OH)_2$ nanopetals were characterized. It is found that the $Ni(OH)_2$ nanopetals interweave with each other and grow vertically on the surface of Ni nanofoam to form an "ion reservoir", which facilitates the ion diffusion in the electrode reaction. Electrochemical measurements show that the $Ni(OH)_2$/Ni-NF/MG electrode, after immersion in water for seven days, reveals a high volumetric capacitance of 966.4 F/cm^3 at a current density of 0.5 A/cm^3. The electrode immersed for five days exhibits an excellent cycling stability (83.7% of the initial capacity after 3000 cycles at a current density of 1 A/cm^3). Furthermore, symmetric supercapacitor (SC) devices were assembled using ribbons immersed for seven days and showed a maximum volumetric energy density of ca. 32.7 mWh/cm^3 at a power density of 0.8 W/cm^3, and of 13.7 mWh/cm^3 when the power density was increased to 2 W/cm^3. The fully charged SC devices could light up a red LED. The work provides a new idea for the synthesis of nanostructured $Ni(OH)_2$ by a simple approach and ultra-low cost, which largely extends the prospect of commercial application in flexible or wearable devices.

Introduction

Nowadays, environmental contamination and energy crisis require new energy storage devices. This leads to a considerable interest in the research of supercapacitors because of their higher power density, longer cycling stability and faster charge/discharge periods compared to batteries [1-4]. Generally speaking, supercapacitors fall into two categories with different energy storage mechanisms. One is electrical double-layer supercapacitors (EDLCs) dominated by the electrostatic adsorption/desorption of electrolyte ions on the electrode surfaces. In EDLCs carbonaceous materials and their derivatives, such as active carbon, porous carbon, graphene, carbon nanotubes with good electrical conductivity and high specific surface area, are most commonly employed as electrode materials [5-7]. The other category are pseudocapacitors governed by reversible faradic redox reactions at the interface between active materials and electrolyte, for which transition metal oxides/hydroxides with multiple valence are used as electrode materials [8,9]. EDLCs hold a high power density and long cycling stability, but their practical application is limited by the low energy density. In comparison, pseudo-capacitors possess a higher energy density and are regarded as promising candidates for energy storage systems [10]. Among the various transition metal oxides/hydroxides, $Ni(OH)_2$ is an ideal candidate for pseudocapacitors due to its unique features such as high theoretical capacity and outstanding redox performance. Moreover, they are environmentally friendly, easily available and inexpensive [11-14]. However, bulk $Ni(OH)_2$ is a semiconductor material with poor electrical conductivity [15], which leads to low capacity at a high scan rate and poor cycling stability. In order to overcome this shortcoming of bulk nickel hydroxide, various morphologies of $Ni(OH)_2$ with a large specific surface area have been developed.

The conventional preparation method of $Ni(OH)_2$ composite electrodes is to press a slurry of nickel hydroxide, conductive agents and binders on a conductive substrate (Ni foam, usually) [16-19]. However, this fabrication strategy is complicated and unsafely [20]. In addition, the presence of non-conductive binders not only increases the internal resistance but also the total mass of electrode, thus reducing the electrochemical performance. Therefore, the in situ synthesis of nickel hydroxide without binders has become a hot topic in recent years. For instance, $Ni(OH)_2$ active materials have been loaded on stainless steel [21], carbon foam [22] and three-dimensional (3D) graphite foam [23]. Furthermore, 3D porous nickel materials have been used extensively as conductive substrate for electroactive $Ni(OH)_2$ in supercapacitors because of the large surface area, good conductivity and compatibility with nickel hydroxide. Yuan et al. synthesized porous $Ni(OH)_2$/NiOOH net on Ni foam by a chemical bath deposition and the electrode showed good rate capability [24]. Ke et al. demonstrated a nickel hydroxide@nanoporous gold/Ni foam electrode, which was synthesized by electrodeposition of a Sn–Au alloy on nickel foam with subsequent dealloying of Sn and electrodepostion of $Ni(OH)_2$ on the nanoporous gold/Ni foam [25]. Liu et al. created $Ni(OH)_2/Cu_2O$ nanosheets on nanoporous NiCu alloy surfaces by a hydrothermal method in H_2O_2 solution [26]. However, all above syntheses of nickel hydroxides require high temperature, nickel salts or/and oxidants that are toxic and hard to clean up. Moreover, the use of noble metals also increases the synthesis cost. To the best of our knowledge, there is no report on the in situ synthesis of nickel hydroxide nanosheets on Ni nanofoam through a simple and environmentally friendly method.

In the present work, we propose a simple and environmentally friendly two-step preparation, including the dealloying of $Ni_{40}Zr_{20}Ti_{40}$ metallic glass in HF solutions and then immersing in deionized water for several days, to fabricate a binder-free, sandwich-like $Ni(OH)_2$ nanopetals/Ni nanofoam/metallic glass ($Ni(OH)_2$/Ni-NF/MG) electrode. $Ni(OH)_2$ nanopetals interconnected with each other grow uniformly on the surface of the Ni nanofoam, which shortens the ions diffusion distance and facilitates the electrolyte transport. The as-synthesized $Ni(OH)_2$/Ni-NF/MG electrodes demonstrate an excellent flexibility due to the ductile MG matrix and a good electrochemical performance. Moreover, the influence of immersion time in deionized water on the evolution of the $Ni(OH)_2$ nanopetals and the specific capacitance of $Ni(OH)_2$/Ni-NF/MG electrodes are investigated. Symmetric supercapacitor (SC) devices were also assembled and tested in this work.

Experimental

Synthesis

A general synthesis scheme is depicted in Figure 1a. Firstly, the $Ni_{40}Zr_{20}Ti_{40}$ (atom %) MG ribbons (2 mm wide and 20–30 μm thick) are fabricated by arc melting of the pure metals (99.99 wt %) followed by melt spinning [27,28]. Subsequently the dealloying process, as reported in our previous work [29,30], is carried out in 0.05 M HF solution for 4 h open to air at 298 K to form a Ni nanofoam layer on the MG surface. The dealloyed strips were washed with deionized water for three times and then immersed in deionized water for two, five or seven days at 298 K. Thereafter, the $Ni(OH)_2$ nanopetals network was grown in situ on the Ni nanofoam. As a result of this growing process $Ni(OH)_2$/Ni-NF/MG electrodes (ca. 2 mm wide and ca. 25 μm thick) were successfully obtained and were denoted as $Ni(OH)_2$/Ni-NF/MG-2, $Ni(OH)_2$/Ni-NF/MG-5, $Ni(OH)_2$/Ni-NF/MG-7, respectively, according to the number of days immersed.

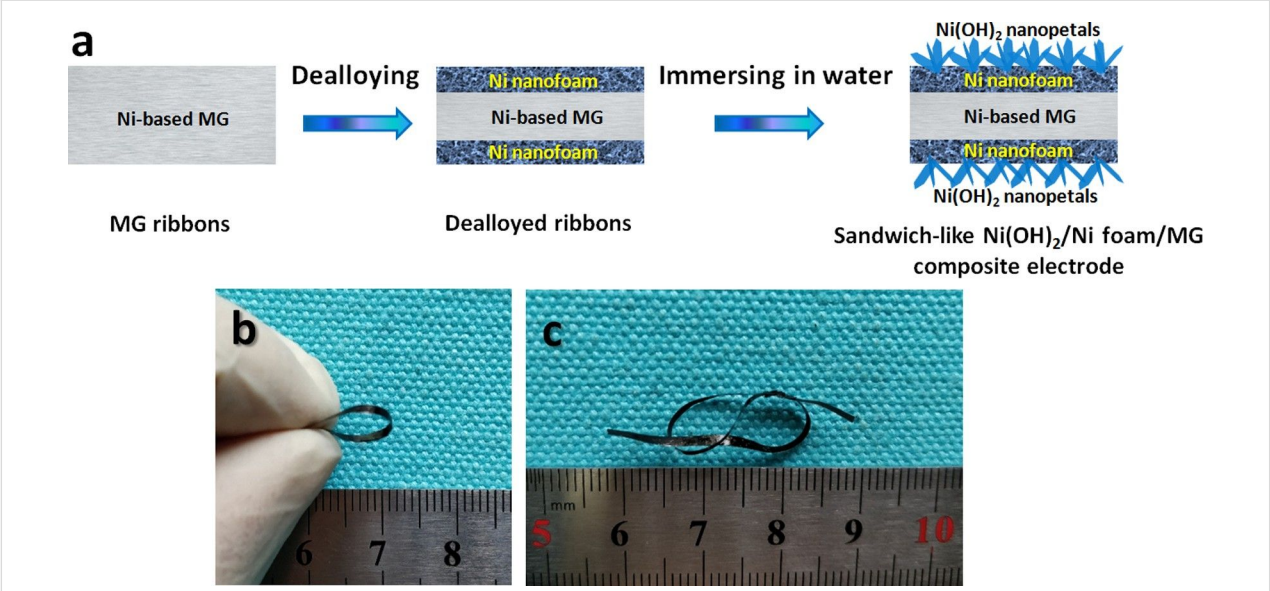

Figure 1: (a) Schematics of the fabrication process of the sandwich-like $Ni(OH)_2$/Ni-NF/MG composite electrodes; (b, c) photographs of the as-fabricated electrodes with excellent flexibility.

Instrumental methods

The phase structure of the as-obtained composites was measured by X-ray diffraction (XRD, Bruker D8) with Cu Kα radiation. Chemical composition and valence state of the products were studied using X-ray photoelectron spectroscopy (XPS, Thermo Fisher Scientific). The surface morphology of the samples was characterized using a scanning electron microscope (SEM, Nova nanoSEM 450) equipped with an X-ray energy dispersive spectroscope (EDS) and a transmission electron microscopy (TEM, JEOL JEM-2100). The preparation process of the TEM sample was as follows: Firstly, the active materials were scraped off with a knife. Then the materials were dispersed in ethanol with ultrasonic vibration. Finally, the dispersed materials were dripped on copper mesh supported carbon film.

Electrochemical measurements

The electrochemical tests of the $Ni(OH)_2$/Ni-NF/MG electrodes were carried out in a standard three-electrode cell. The $Ni(OH)_2$/Ni-NF/MG composites, a Pt net, and a Ag/AgCl electrode were employed as the working electrodes, the counter electrode and the reference electrode, respectively. Cyclic voltammograms (CV), galvanostatic charge/discharge curves (GCD) and electrochemical impedance spectroscopy (EIS) measurements were carried out using an electrochemical workstation (Chenhua CHI660D, China) in 1 M KOH aqueous solution at 298 K. The CV curves were examined in the voltage window of 0 to 0.5 V (vs Ag/AgCl) at scan rates of 2.5, 5, 10, 20, 50, 100 mV/s, and the GCD curves were collected at current densities of 0.5, 1, 2, 4, 8,12 A/cm^3. The volumetric capacitance, based on the whole volume of the electrode including Ni-NF, MG and active materials, was calculated by the following equations according to GCD curves [31]:

$$C_V = \frac{I \cdot \Delta t}{V \cdot \Delta V}, \quad (1)$$

where C_v is the volumetric capacitance, Δt is the discharge time, ΔV is the voltage range, I is the discharge current, and V is the nominal volume of the free-standing electrode. The volumetric capacitance can be also calculated by the following formula according to CV curves:

$$C_V = \frac{\int_{\varphi_i}^{\varphi_f} i d\varphi}{V \cdot v\left(\varphi_f - \varphi_i\right)}, \quad (2)$$

where φ_i and φ_f are initial and final potential, i is the current, $d\varphi$ is the potential differential, and v is the scan rate of CV curves. EIS tests were performed by applying an AC voltage with 5 mV amplitude within a frequency range of 0.01 to 1000 kHz under open-circuit potential conditions.

Assembly of symmetrical energy storage devices

The SC devices were assembled in a commercial 2032 button-cell shell, using $Ni(OH)_2$/Ni-NF/MG-7 as active material, non-woven fabrics as separator and 1 M KOH as electrolyte under the pressure of 60 kg/cm^2. The lengths of positive and negative

ribbon are both of 15 cm in total. The SC device was tested by a two-electrode cell system. The CV curves were obtained at scan rates of 10, 20, 50 and 100 mV/s and the GCD curves were examined at current densities of 0.5, 1, 1.5, 2 A/cm^3. The voltage of a fully charged SC device was further measured with a VC890C+ digital multimeter. The volumetric energy density (E_V, Wh/cm^3) and power density (P_V, W/cm^3) of a single SC device are calculated by the following equations:

$$E_V = \frac{C_{SC} \cdot \Delta V_{SC}^2}{2 \cdot 3600}, \quad (3)$$

$$P_V = \frac{3600 \cdot E_V}{\Delta t_{SC}}, \quad (4)$$

where C_{sc} is the specific capacitance, ΔV_{sc} is the potential range, and Δt is the discharge time of a single SC device.

Results and Discussion

Material structure

The sandwich-like Ni(OH)$_2$/Ni-NF/MG composite electrode inherits the excellent flexibility and ductility of $Ni_{40}Zr_{20}Ti_{40}$ MG after dealloying in 0.05 M HF solutions for 4 h and being immersed in deionized water for two to seven days. As depicted in Figure 1b and Figure 1c, the as-synthesized Ni(OH)$_2$/Ni-NF/MG electrodes can be bent into a small circle with a diameter of about 5 mm. Amazingly, it can be also tied into a small bowknot. Therefore, the as-prepared Ni(OH)$_2$ nanopetals composite can be directly used as electrode for a supercapacitor without any binders.

The morphologies of the as-dealloyed ribbons and as-prepared electrodes were examined by SEM, as shown in Figure 2a–h. The plane-view (Figure 2a) and the enlarged partial view (Figure 2e) show that the sample after dealloying possesses a 3D continuous pore structure with a ligament size of ca. 100 nm, which provides a path for the transportation of both electrons and ions in the electrolyte, resulting in the improved electrochemical performance. After immersing the dealloyed sample in water for two days, rose petal-like Ni(OH)$_2$ with network structure are formed, as seen in Figure 2b. From Figure 2c,d, it is found that some flower-like structures (marked by arrows) composed of Ni(OH)$_2$ nanopetals are formed upon the surface of the Ni(OH)$_2$ nanopetals network, and are becoming larger with longer immersion time. These over-

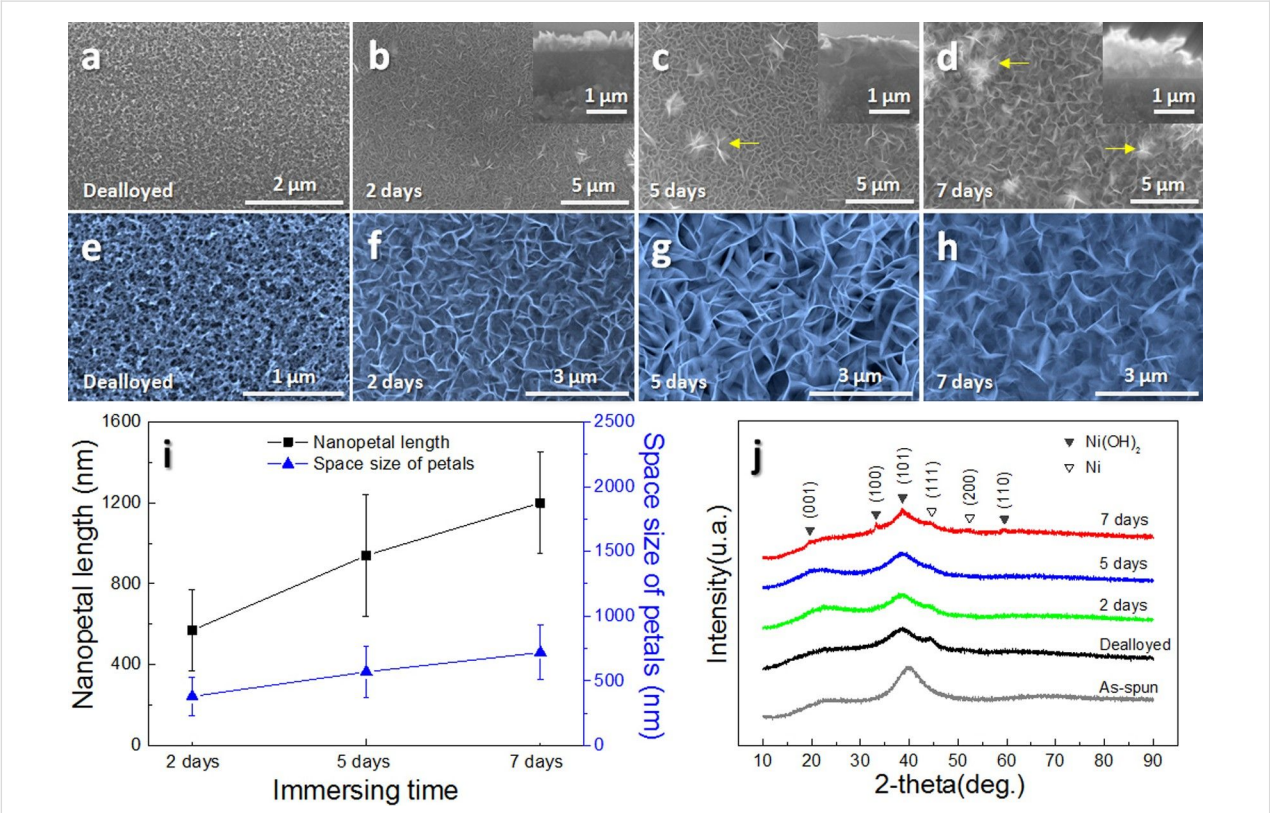

Figure 2: Low- and high-magnification SEM images of (a, e) the as-dealloyed ribbon, (b, f) Ni(OH)$_2$/Ni-NF/MG-2, (c, g) Ni(OH)$_2$/Ni-NF/MG-5, and (d, h) Ni(OH)$_2$/Ni-NF/MG-7; the insets are the corresponding cross-sectional views. (i) Nanopetals length and space size of petals as functions of the immersion time. (j) XRD patterns of the as-spun, as-dealloyed and Ni(OH)$_2$/Ni-NF/MG electrodes.

growths of flower-like structures may arise from nucleation and coalescence processes [32]. The thickness of the nanopetals rises with immersion time from 0.5 µm (inset of Figure 2b) over 1.0 µm (inset of Figure 2c) to 1.5 µm (inset of Figure 2c). We can see from Figure 2f–h that the curly $Ni(OH)_2$ nanopetals interweave and grow vertically on the surface of the Ni nanofoam, which forms an "ion reservoir". In addition, length and spacing of $Ni(OH)_2$ nanopetals grow with immersion time. The length of $Ni(OH)_2$ nanopetals changes from ca. 600 to ca. 1200 nm and the spacing between them changes from ca. 300 to ca. 550 nm, as plotted in Figure 2i. This structural characteristic of an "ion reservoir" would bring about fast ion/electron transfer, short ion transport distances and sufficient contact at active material/electrolyte interfaces, which might improve the electrochemical performance [33].

Figure 2j shows typical XRD patterns of the as-spun ribbon, the as-dealloyed ribbon and the as-synthesized $Ni(OH)_2$/Ni-NF/MG composites immersed in deionized water for different days. The original ribbon presents a characteristic broad halo peak of metallic glass without appreciable sharp crystalline peaks, indicating the formation of a single homogeneous metallic glassy structure. After dealloying, in addition to a broad halo peak, two peaks located at 44.5° and 51.8° can be assigned to the (111) and (200) planes of Ni metal (JCPDS no. 04–0850), respectively. This further confirmed the formation of the Ni nanofoam layer after dealloying of MG precursors. The other diffraction peaks at 19.2°, 33.1°, 38.5°, 59.1° can be attributed to the (001), (100), (101) and (110) planes of β-$Ni(OH)_2$ (JCPDS no. 14–0177), respectively, suggesting the successful synthesis of $Ni(OH)_2$ nanopetals upon the Ni nanofoam surface after immersing in deionized water for several days.

To understand the structure of the as-obtained electrode, the cross-sectional view of the sample immersed in deionized water for five days is investigated (Figure 3a). The sandwich-like $Ni(OH)_2$ composite electrode is successfully prepared after initially dealloying the MG precursor and subsequently immersing the dealloyed sample in deionized water. The layers of the structure are in close contact with each other, indicating the good integrity of the electrode. The inset is a locally magnified SEM image showing the structure of the "ion reservoir" and is in accordance with the SEM images in Figure 2c and Figure 2g. Morphology and structure of as-synthesized $Ni(OH)_2$ nanopetals are further observed by TEM. As seen from Figure 3b, the intersected nanopetals are loaded on the Ni nanofoam. Figure 3c shows the high electron transparency of the nanopetals with several layers stacked together, indicating an ultrathin nature [12,34]. The high-resolution TEM image in Figure 3d provides more detailed lattice structure information of the $Ni(OH)_2$ nanopetals. The interplanar distances of 0.156 nm and 0.234 nm are related to the (110) and (101) planes of the

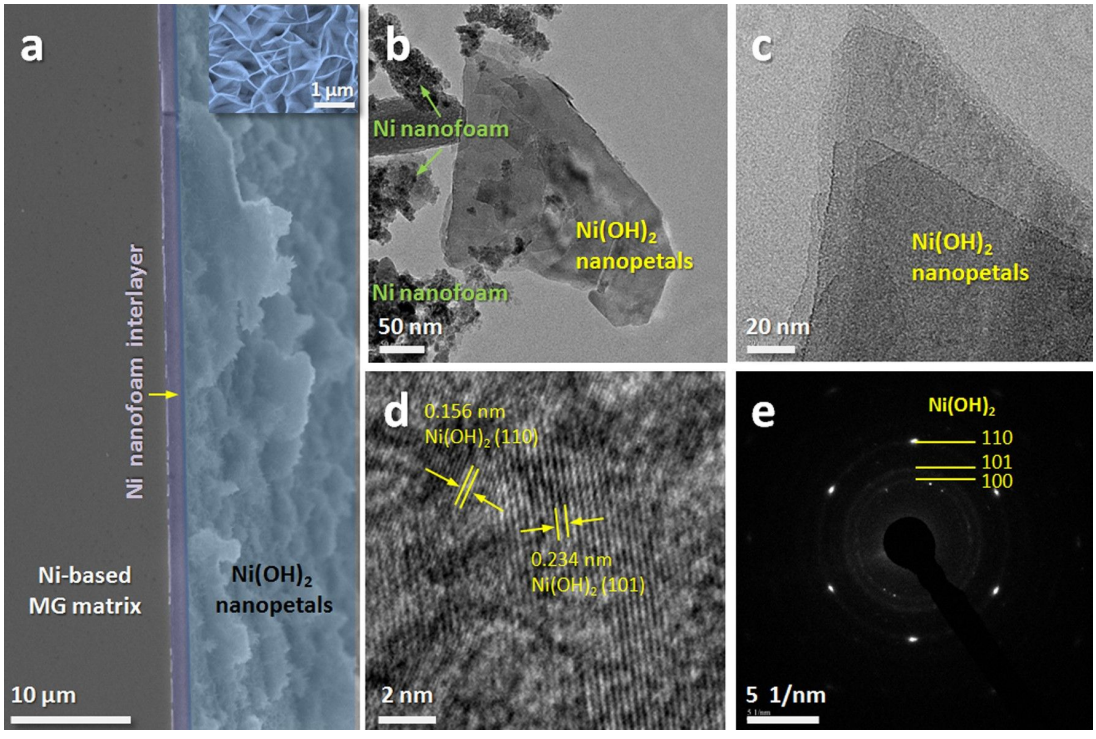

Figure 3: (a) Cross-sectional SEM images of the $Ni(OH)_2$/Ni-NF/MG-5, the inset is a local high-resolution image; (b, c) low- and high-magnification TEM images; (d) HRTEM image; (e) SAED pattern of $Ni(OH)_2$ nanopetals.

$Ni(OH)_2$, respectively. The SAED pattern taken from a single nanopetal shown in Figure 3e indicates that the $Ni(OH)_2$ nanopetals are polycrystalline. The diffraction rings belong to the (100), (101), and (110) planes of $Ni(OH)_2$, respectively, which is consistent with the XRD results and can further confirm the successful synthesis of $Ni(OH)_2$ nanopetals. It is worth noting that the sandwich-like $Ni(OH)_2$/Ni-NF/MG composite electrode exhibits excellent flexibility. This can be explained by the fact that the Ni-NF/MG substrate was obtained by dealloying ductile $Ni_{40}Zr_{20}Ti_{40}$ MG. The cross section (Figure 3a) shows that the Ni-NF layer smoothly adheres to the MG matrix. The thickness of the Ni-NF layer is ca. 1.5 μm; the $Ni_{40}Zr_{20}Ti_{40}$ MG is ca. 22 μm thick. It is well known that Ni-based MGs exhibit a much larger elasticity and ductility than their corresponding crystalline alloys. A sufficiently thick MG layer acts as a ductile support to the dealloyed Ni-NF/MG substrate. In additon, the in situ growth in deionized water offers a good connection between Ni-NF and $Ni(OH)_2$.

The growth mechanism of $Ni(OH)_2$ nanopetals

According to the SEM images (Figure 2b–d), $Ni(OH)_2$ nanopetals and flower-like microspheres grow on the surface of Ni-NF/MG after immersion in water. A possible growth mechanism of $Ni(OH)_2$ nanopetals is proposed in the following. A large amount of defects (twin boundaries, stack faults and/or dislocations) were generated in the nanoporous metal ligament surface after dealloying [35]. When the nanoporous Ni (Ni-NF) with many defects with higher distortion energy was placed in deionized water, many microgalvanic cells were formed at the surface of Ni-NF. Most likely, the following electrode reactions of a microgalvanic cell take place [36]:

$$\text{Anode: } 2Ni \rightarrow 2Ni^{2+} + 4e^{-}, \quad (5)$$

$$\text{Cathode: } O_2 + 2H_2O + 4e^{-} \rightarrow 4OH^{-}, \quad (6)$$

$$\text{Cell reaction: } 2Ni + O_2 + 2H_2O \rightarrow 2Ni(OH)_2. \quad (7)$$

Based on the above reactions, $Ni(OH)_2$ crystals nucleated and grew at the surface of 3D Ni-NF ligaments. The morphological change of $Ni(OH)_2$ nanopetals after different immersion times was shown in Figure 2. The pH value of deionized water is about 7.0. Research has shown that when the pH value is higher, the crystals tend to grow into a flake structure in the [100] or [010] directions [37]. The anisotropic growth leads to the formation of high-density crosslinked nanopetals. The flower-like structures composed of $Ni(OH)_2$ nanopetals are formed through Ostwald ripening [38]. Meanwhile, the dissolved tiny and unstable plates provide the source material for the growth of plates during the dissolution and recrystallization process. The dissolved nickel atoms may continuously attach and bond to the surface of larger nanopetals, and form flower-like structures in order to achieve a minimum total free energy.

Chemical characteristics of the composite surface

In order to clarify the changes in chemical state of the elements, XPS measurements are performed for the as-spun, as-dealloyed, and as-synthesized $Ni(OH)_2$ specimens. Figure 4a shows that the XPS spectra over a wide energy region exhibit the main peaks of Zr 3d, Ti 2p, O 1s, and C 1s for the as-spun Ni-Zr-Ti alloy, while large peaks of Ni 2p and O 1s appear for both the as-dealloyed alloy and as-synthesized $Ni(OH)_2$. It is found that the intensity of O 1s peak greatly increases for the as-dealloyed alloy immersed in deionized water for five and seven days. The deconvolution results of the Ti 2p and Zr 3d spectra measured for the as-spun and as-dealloyed alloy, respectively, are shown in Figure 4b and Figure 4c, respectively. For the as-spun alloy, it is found that the large peaks correspond to Ti^{4+} and Zr^{4+} on the alloy surface, whereas the minor peaks are associated to lower oxidation states. These phenomena can be explained through a preferential oxidation of Ti and Zr during the alloy fabrication and the subsequent oxidation exposed to the air. After immersion in 0.05 M HF for 4 h, the signals for Ti and Zr become very weak due to the dissolution of Ti and Zr. It is clarified that the surface film of as-spun alloy mainly consists of Ti^{4+} and Zr^{4+} oxides. On the other hand, Figure 4d and Figure 4e reveal the Ni $2p_{3/2}$ and O 1s peaks obtained from the as-spun alloy and as-dealloyed alloy before and after immersion in deionized water. The O 1s region analyzed by using a Gaussian fitting method (Figure 4e) shows three chemical states of oxygen. The strong peak at 531.1 eV is related to bound hydroxide groups (OH^-) and the peak at 529.9 eV is assigned to a typical metal–oxygen bond (O–M). Additionally, the peaks at 532.1 eV can be ascribed to water adsorbed at the material surface [39]. For the as-dealloyed sample before and after immersion in water, the Ni $2p_{3/2}$ spectrum (Figure 4d) consists of a major characteristic peak at 855.8 eV corresponding to $Ni(OH)_2$ and two satellite peaks (indicated as s.), which is in good agreement with previous reports [40,41]. It should be mentioned that the Ni hydroxide peak increases greatly with longer immersion times, indicating that the immersion facilitates the in situ growth of $Ni(OH)_2$ on the Ni nanofoam surface.

Supercapacitor performance

The electrochemical performance of the $Ni(OH)_2$ nanopetals on Ni nanofoam was evaluated systematically by CV and GCD measurements with a three-electrode cell in 1 M KOH aqueous solution at 298 K (Figure 5). The CV curves of the $Ni(OH)_2$/Ni-NF/MG-2, $Ni(OH)_2$/Ni-NF/MG-5, and $Ni(OH)_2$/Ni-NF/MG-7

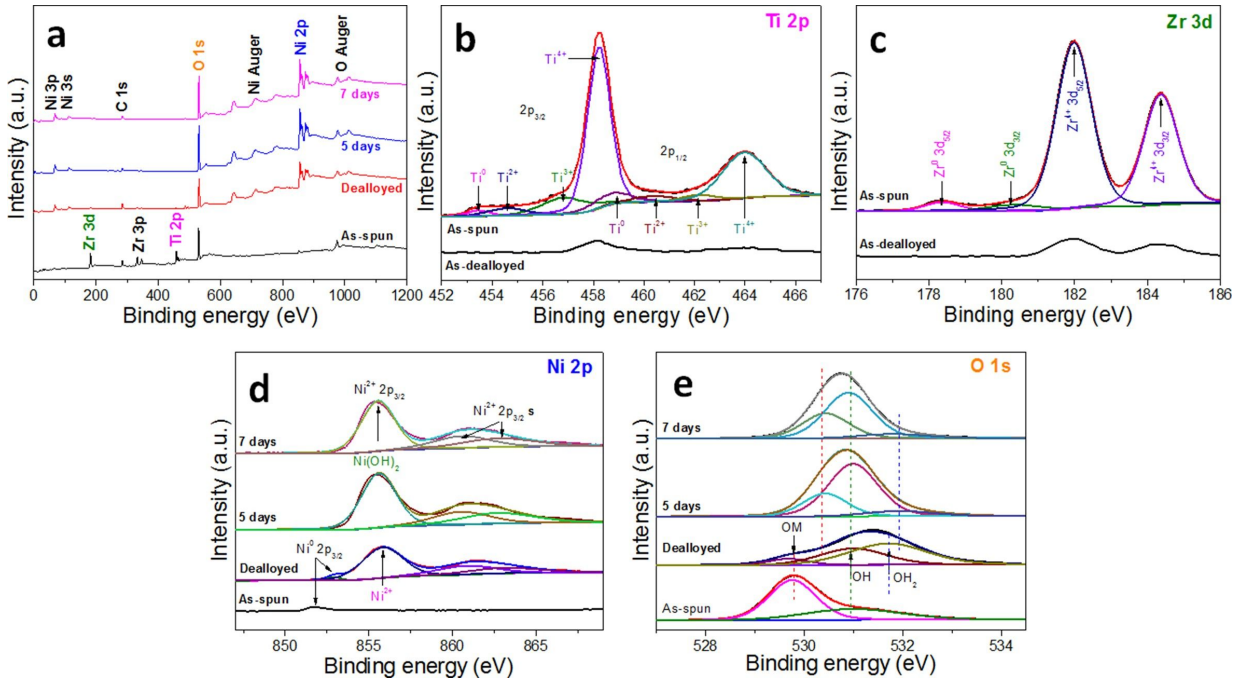

Figure 4: XPS spectra of the elements of the as-spun ribbon, as-dealloyed ribbon and as-synthesized electrode: (a) survey spectrum, (b) Ti 2p, (c) Zr 3d, (d) Ni 2p and (e) O 1s.

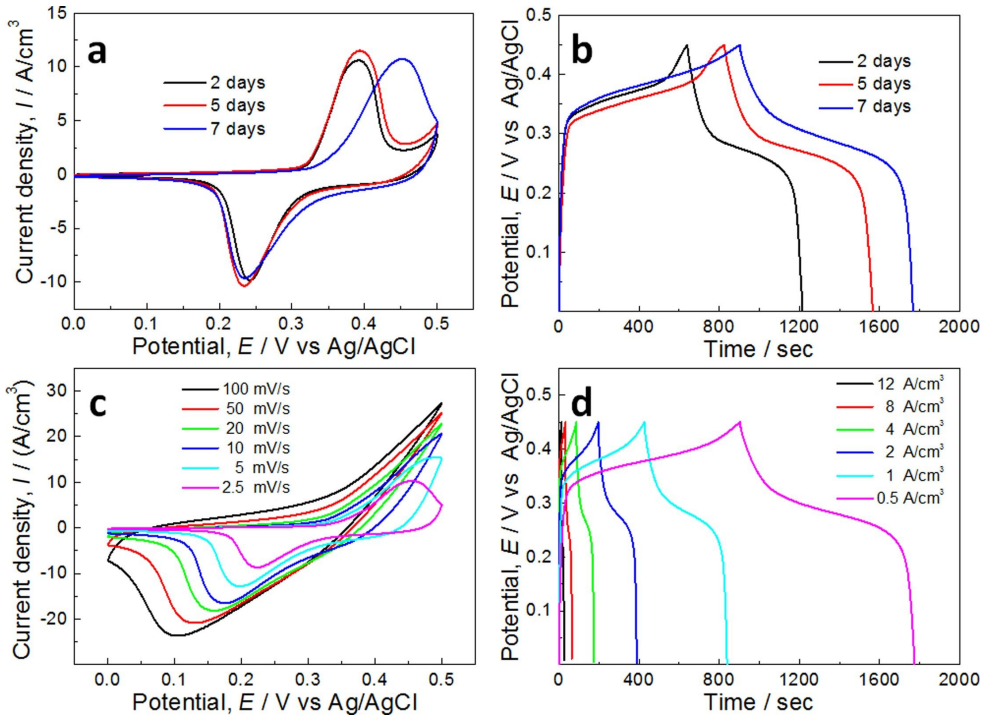

Figure 5: (a) CV curves of the $Ni(OH)_2$/Ni-NF/MG-2, $Ni(OH)_2$/Ni-NF/MG-5, $Ni(OH)_2$/Ni-NF/MG-7 electrodes at a scan rate of 0.5 mV/s in 1 M KOH solution; (b) GCD curves of the $Ni(OH)_2$/Ni-NF/MG-2, $Ni(OH)_2$/Ni-NF/MG-5, $Ni(OH)_2$/NiNF/MG-7 at a current density of 0.5 A/cm^3; (c) CV curves of the $Ni(OH)_2$/Ni-NF/MG-5 at different scan rates from 2.5 to 100 mV/s; (d) GCD curves of the $Ni(OH)_2$/Ni-NF/MG-5 at different current densities from 0.5 to 12 A/cm^3.

electrodes at the scan rate of 2.5 mV/s with the potential window from 0 to 0.5 V are shown in Figure 5a. A set of strong redox peaks can be clearly detected for the three electrodes, which corresponds to reversible reactions of $Ni^{2+} \leftrightarrow Ni^{3+}$. The redox peaks illustrate that pseudo-capacitive behavior occurred at the electrode/electrolyte interface. The corresponding kinetically reversible faradic redox reaction involved in the electrochemical process is [25,42]:

$$Ni(OH)_2 + OH^- \leftrightarrow NiOOH + H_2O + e^-. \quad (8)$$

The specific capacitance of $Ni(OH)_2$/Ni-NF/MG-2, $Ni(OH)_2$/Ni-NF/MG-5 and $Ni(OH)_2$/Ni-NF/MG-7 calculated from the CV curves are 728.1, 823.8 and 866.3 F/cm^3, respectively. It is notable that the anodic peak of the $Ni(OH)_2$/Ni-NF/MG-7 electrode is shifted to a more positive value than the other two peaks, which is related to the poor conductivity (larger ohmic resistance) of $Ni(OH)_2$ nanopetals [21,43]. Larger ohmic resistance leads to slow kinetics of charge transport and interfacial charge transfer of the material. Thus, the electrode reaction rate slows down, resulting in a reduced reversibility of the redox processes. This is consistent with the SEM images (Figure 2d and Figure 2h) of the samples immersed in deionized water for seven days showing the thickest $Ni(OH)_2$ nanopetals layer among the experimental samples. The GCD curves measured at current density of 0.5 A/cm^3 for the three $Ni(OH)_2$/Ni-NF/MG electrodes further elucidate the pseudo-capacitance characteristics, as shown in Figure 5b. Every GCD curve has an obvious charge–discharge plateau and the voltage position is in agreement with the CV curves, demonstrating that the faradic redox reactions mainly contribute to the capacitance. The specific capacitance values of the electrodes were calculated from Equation 1. The $Ni(OH)_2$/Ni-NF/MG-7 electrode presented the highest volumetric capacitance value of 966.4 F/cm^3. It is worth noting that the real value of the volumetric capacitance should be much higher, because the present volumetric capacitance is calculated by the total volume of the sandwich-structured electrode, and the volume of active $Ni(OH)_2$ accounts for only a small proportion of the whole electrode. Figure 5c discloses the CV response of $Ni(OH)_2$/Ni-NF/MG-7 at different scan rates ranging from 2.5 to 100 mV/s. The results indicate that the current response increases with an increase of the scan rate. Moreover, it is found that the reduction peaks are shifted to more negative values with the increase of the scan rate, whereas the anodic peaks are shifted to more positive values and finally disappear at scan rates above 20 mV/s. This phenomenon is related to electrochemical polarization, i.e., the electron flow rate not keeping pace with the electrode reaction [44]. The GCD (Figure 5d) was recorded at different current densities from 0.5 to 12 A/cm^3. The nonlinear GCD curves confirm typical pseudo-capacitive behavior, which is also in accord with Figure 5c.

Figure 6a shows the volumetric capacity of the three electrodes obtained from the GCD curves at different current densities according to Equation 1. As we can see, the volumetric capacitance of the three electrodes decreases when the current density is changed from 0.5 to 12 A/cm^3. This is the results of less electroactive materials being available because of limited ion diffusion when the discharge current density increases [45]. The volumetric capacitance values of $Ni(OH)_2$/Ni-NF/MG-7 are found to be 966.4, 915.1, 852.4, 761.8, 568.9 and 328 F/cm^3 at discharge current densities of 0.5 1, 2, 4, 8 and 12 A/cm^3 (retention ratio 34%), respectively, whereas for the $Ni(OH)_2$/Ni-NF/MG-5 electrode, it is 822.6, 798.7, 781.3, 758.2, 730.7 and 720 F/cm^3 (retention ratio 87.5%), respectively, and for $Ni(OH)_2$/Ni-NF/MG-2, it is 637.7, 628.9, 632.0, 629.3, 620.4 and 624.0 F/cm^3 (retention ratio 97.9%), respectively. Obviously, the rate performance of the $Ni(OH)_2$/Ni-NF/MG-2 electrode is the best, while that of $Ni(OH)_2$/Ni-NF/MG-7 is the

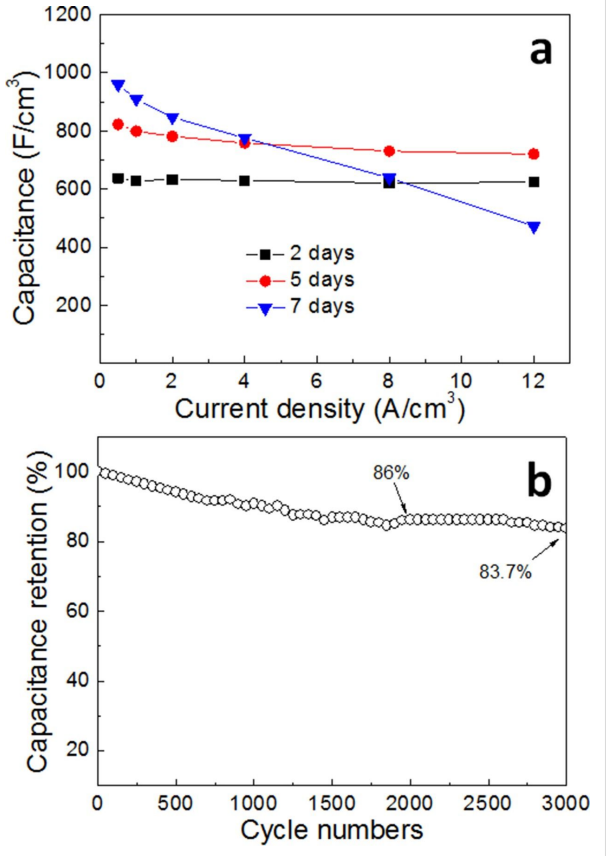

Figure 6: (a) Volumetric capacitance of the $Ni(OH)_2$/Ni-NF/MG-2, $Ni(OH)_2$/Ni-NF/MG-5, $Ni(OH)_2$/Ni-NF/MG-7 electrodes at different discharge current densities; (b) volumetric capacitance versus cycle number of $Ni(OH)_2$/Ni-NF/MG-5 at a galvanostatic charge and discharge current density of 1 A/cm^3.

worst. That is probably because the structural differences of the surface $Ni(OH)_2$. When the immersion time is short, the $Ni(OH)_2$ nanopetals exhibit a network shape. With increasing immersion time, clusters of nanopetals accumulate into a flower morphology upon the $Ni(OH)_2$ network layer, resulting in a thickness increase of the $Ni(OH)_2$ layer and a decline in conductivity. A higher conductivity of the electrode leads to a better rate performance. Good conductivity makes the electrode stand up the impact of higher currents. This is due to the fast electron transfer occurring at high current densities through which the minimum specific capacitance is reduced when compared to its initial value [46]. Cycle performance is another key factor affecting the practical application of electrode materials. The cycling stability (Figure 6b) of the $Ni(OH)_2$/Ni-NF/MG-5 electrode is evaluated by a continuous GCD test up to 3000 cycles at a current density of 1 A/cm^3. It is noticed that the capacitance of $Ni(OH)_2$/Ni-NF/MG-5 decreases gradually without an obvious activation process. The $Ni(OH)_2$/Ni-NF/MG-5 delivers a relatively high specific capacitance of 687.7 F/cm^3 with 86.1% retention of its initial capacitance after 2000 cycles, and even shows an excellent cycling stability of 83.7% after 3000 cycles. Although the capacitance retention of $Ni(OH)_2$/NiNF/MG-5 is not comparable to those of a 2D $MoSe_2$-$Ni(OH)_2$ nanohybrid electrode (90% retention after 3000 cycles at 2 A/g) [46] and a NiCo-LDH composite electrode (90% retention after 5000 cycles at 20 mA/cm^2) [47], it exceeds most of the $Ni(OH)_2$@Ni foam electrodes [14,42,48].

In order to explain the decline in the cycling performance of $Ni(OH)_2$/Ni-NF/MG-5, the microstructure of the electrode after 3000 cycles was observed by SEM (Figure 7a,b). It is found that $Ni(OH)_2$ nanopetals become thicker and interweave into a catkin-like morphology. Though a certain amount of nanopetals still remains, the "ion reservoir" structure is badly damaged. This results in a decrease in the surface area of active materials and subsequently leads to the decline in the volumetric capacitance of the electrode.

Impedance spectroscopy

To better understand the kinetics of the charge transfer within the electrodes, EIS measurements were also carried out. The impedance spectra (Nyquist plots) are shown in Figure 7c,d. The inset is the equivalent electrical circuit. The intersection with the Z'-axis represents the equivalent series resistance (R_s). All Nyquist plots exhibit a small semi-circle at high frequencies and a straight line at low frequencies. The semicircle repre-

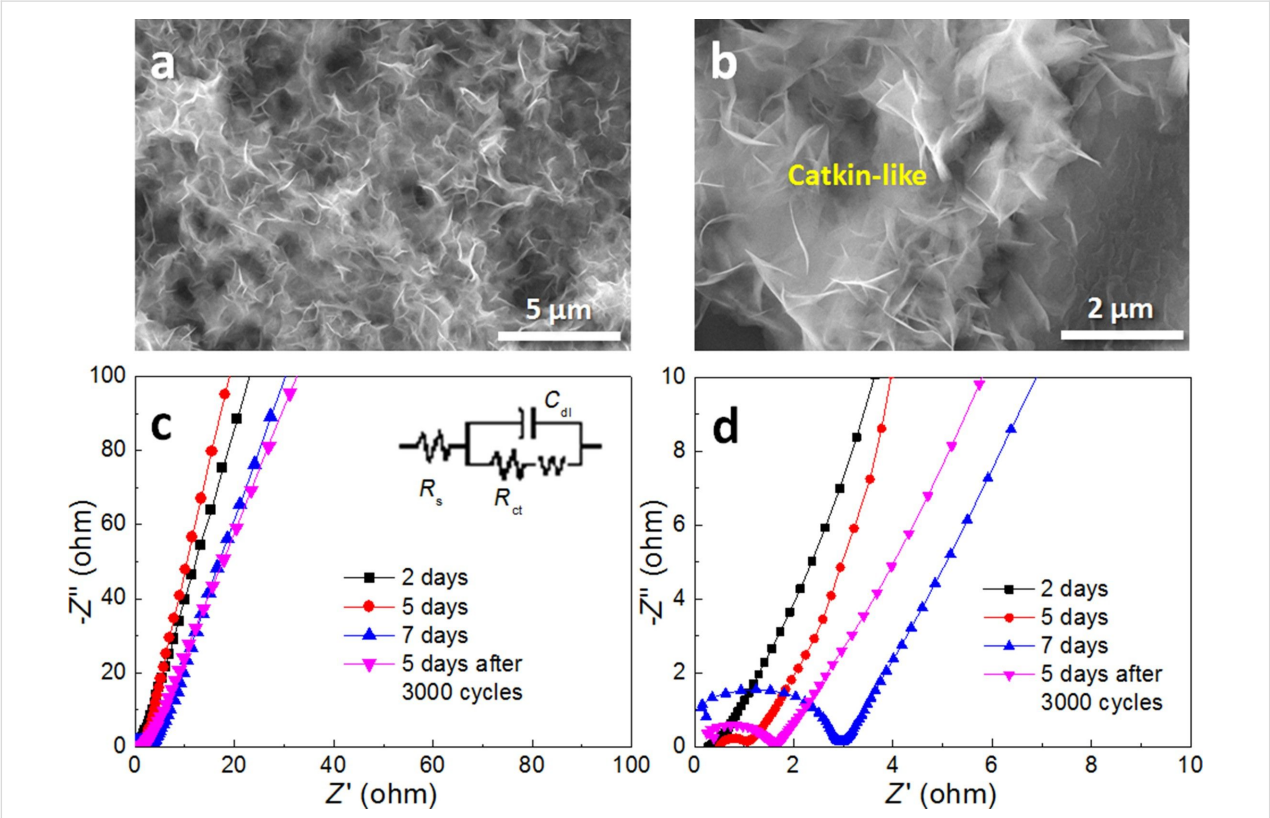

Figure 7: (a, b) Low- and high-magnification SEM images of $Ni(OH)_2$/Ni-NF/MG-5 after a 3000 cycles at a GCD current density of 1 A/cm^3; (c, d) Nyquist plots of $Ni(OH)_2$/Ni-NF/MG-2, $Ni(OH)_2$/Ni-NF/MG-5, $Ni(OH)_2$/Ni-NF/MG-7 and $Ni(OH)_2$/Ni-NF/MG-5 after 3000 cycles at a GCD current density of 1 A/cm^3.

sents the charge transfer impedance (R_{ct}) for the redox reaction of $Ni(OH)_2$/NiOOH at the electrode/electrolyte interface. The straight line at low frequencies indicates the diffusive resistance of the electrolyte ions (Warburg impedance) [49]. The simulated R_s values of the three electrodes are 1.27, 1.48 and 2.87 Ω/cm^2. Moreover, the $Ni(OH)_2$/Ni-NF/MG-2 exhibits the smallest R_{ct} value of 0.011 Ω/cm^2, indicating its lowest charge transfer resistance. This is why $Ni(OH)_2$/Ni-NF/MG-2 exhibits the best rate performance, whereas $Ni(OH)_2$/Ni-NF/MG-7 exhibits the worst (R_{ct} = 0.028 Ω/cm^2). Besides, $Ni(OH)_2$/Ni-NF/MG-5 with the maximum slope at low frequency has the fastest ion diffusion rate among the three electrodes. It is found that both charge transfer resistance and ion diffusion resistance of the $Ni(OH)_2$/Ni-NF/MG-5 increase after 3000 cycles, which is related to the agglomeration of $Ni(OH)_2$ nanopetals.

Performance of energy storage devices

In order to further show the good energy storage performance of the as-prepared sandwich-like electrodes, the SC devices were assembled using $Ni(OH)_2$/Ni-NF/MG-7. The CV and GCD curves of a single SC device are shown in Figure 8. CV and GCD curves present a higher voltage window of ca. 1.6 V. The calculated Ragone plot of a single SC device according to Equation 3 and Equation 4 is shown in Figure 8c. The volumetric energy densities are 32.7, 27.1, 17.3, 13.7 mWh/cm^3 at power densities of 0.8, 1.2, 1.6, 2.0 W/cm^3, respectively. The highest energy density in this work is comparable to that of a Ni@$Ni(OH)_2$//graphene-CNT hybrid SC device (33.9 mWh/cm^3 at a power density of 0.2 W/cm^3) [50] and better than that of our previous NiO/np-Ni/MG symmetric supercapacitor device (19.82 mWh/cm^3 at 0.4 W/cm^3) [51]. This volumetric energy density is approximately three times larger than that of a thin-film lithium ion battery (1–12 mW h/cm^3, 4 V/500 μAh) [52] and far exceeds that of a MnO_2-$Ni(OH)_2$/AB//active carbon asymmetric supercapacitor (3.62 mWh/cm^3 at 11 mW/cm^3) [39] and a NiCo-LDH//AC asymmetric capacitor (7.4 mWh/cm^3 at 103 mW/cm^3) [47]. After being fully charged, the voltage of a single SC device was measured with a digital multimeter. After a slow drop to 1.158 V, the voltage remains constant, as shown in Figure 8d.

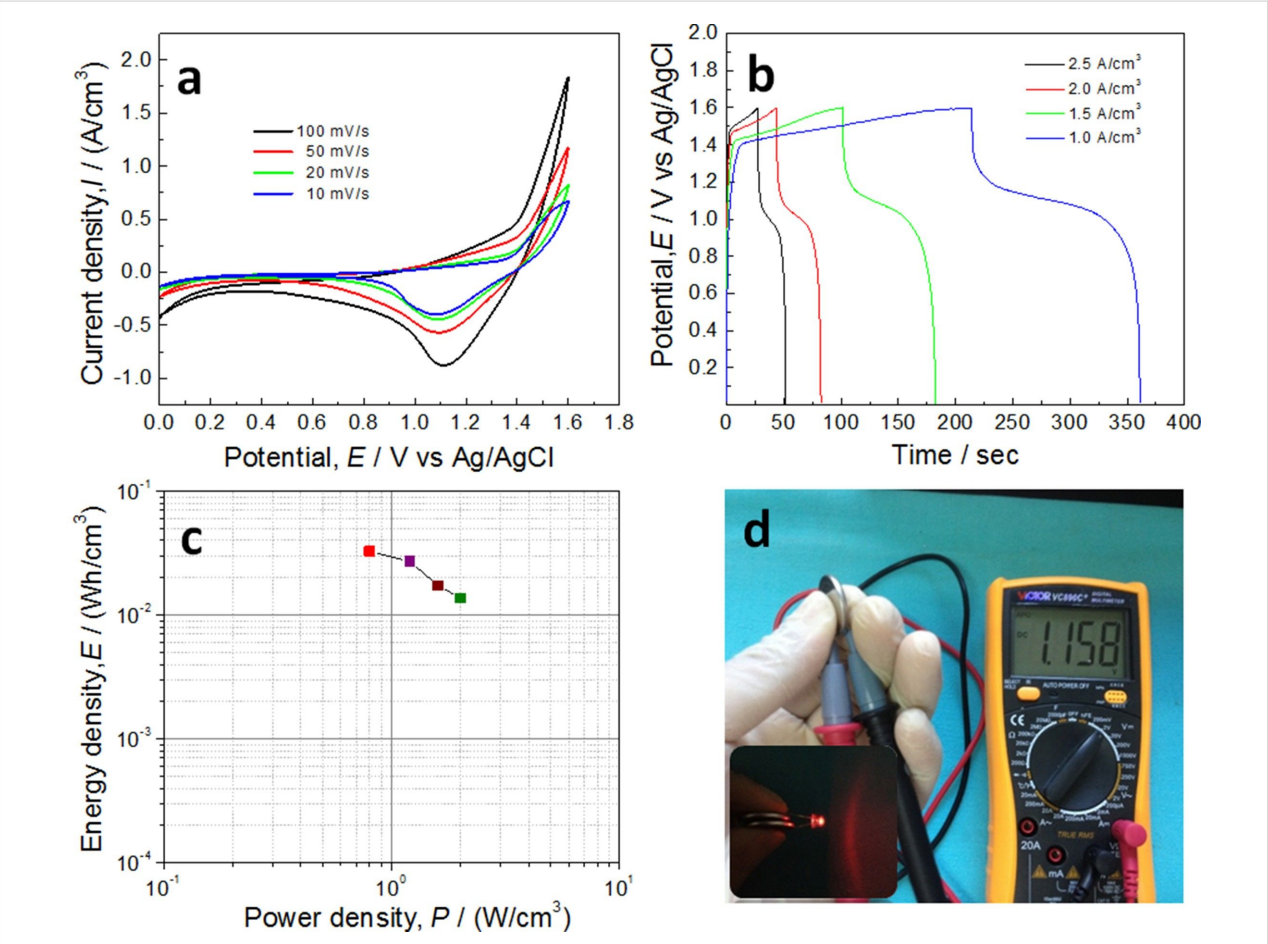

Figure 8: (a) CV curves and (b) GCD curves of a single SC device; (c) Ragone plot of the SC device; (d) voltage of a single fully charged device and a red LED bulb powered by two SC.

The two SC devices connected in series could power a red LED (1.8 V and 20 mA, inset of Figure 8d) for more than 2 min, which indicates that the as-prepared electrodes have a good energy storage performance.

Table 1 presents a summary of several electrode performance values compared with previous literature [40-42,46,48,53-55]. Although the cycling stability of the $Ni(OH)_2$/Ni-NF/MG electrode is not comparable to that of $Ni(OH)_2$/NF [41] and 2D $MoSe_2$-$Ni(OH)_2$ composite electrodes [46], the rate capability of $Ni(OH)_2$/Ni-NF/MG electrode is greater than that of the two latter electrodes. (The capacitance retention rate still reaches 87.5% with 24-fold increase in current density). Except for the higher rate capability of $NiCo_2S_4$@$Ni(OH)_2$ composite electrode with lower cycling stability [48], the present $Ni(OH)_2$/Ni-NF/MG electrodes, which were obtained by a much easier environmentally friendly and cost-effective method, exhibit comparable or much better electrochemical performance among the electrodes based on electro-active $Ni(OH)_2$. Besides, the key point is that $Ni(OH)_2$/Ni-NF/MG electrodes exhibit excellent flexibility, which is a prominent feature of $Ni(OH)_2$/Ni-NF/MG electrodes and meets the requirements of wearable devices. The outstanding electrochemical performance of $Ni(OH)_2$/Ni-NF/MG electrodes can be ascribed to the following analysis of its unique sandwich-like electrode structure: Firstly, the conductive ligaments of the 3D continuous Ni nanofoam together with Ni-based MG substrate can provide multidimensional electron and ion transport pathways during the reversible faradic redox processes. Remarkably, the $Ni(OH)_2$/Ni-NF/MG electrodes demonstrate an excellent flexibility and they can be bent into a circle with a diameter of ca. 5 mm and even be tied into a small bowknot, which indicates the integrated internal structure of the electrode. Secondly, the squiggly interconnected nanopetals grown on the 3D Ni nanofoam can play the role of an "ion reservoir", yielding fast ion transfer, short ion transport distances and sufficient contact at active material/electrolyte interfaces. Finally, a complete integrated electrode is formed by the close bonding between the $Ni(OH)_2$ nanopetals and the Ni nanofoam substrate, avoiding the addition of conductive agent and binder, resulting in highly efficient electron transfer and ion transport. Accordingly, the sandwich-like $Ni(OH)_2$/Ni-NF/MG electrodes with good energy storage performance, high cycling stability as well as excellent flexibility are a promising prospect in wearable energy storage devices.

Conclusion

In summary, a sandwich-like $Ni(OH)_2$/Ni-NF/MG electrode with good flexibility was synthesized through a two-step synthesis including the dealloying of ductile $Ni_{40}Zr_{20}Ti_{40}$ metallic glass to form a Ni nanofoam interlayer and subsequent immersion in water to create a $Ni(OH)_2$ nanopetal network on the Ni nanofoam surface. The $Ni(OH)_2$ nanopetals interweave with each other and grow vertically on the surface of Ni nanofoam to create an "ion reservoir", which facilitates the ion diffusion in the electrode reaction. Because of this unique structure, the $Ni(OH)_2$/Ni-NF/MG-7 electrode reveals a high volumetric capacitance of 966.4 F/cm^3 at a current density of 0.5 A/cm^3 and the $Ni(OH)_2$/Ni-NF/MG-5 electrode exhibits an excellent cycling stability (83.7% of the initial capacity after 3000 cycles at a current density of 1 A/cm^3). In addition, symmetric supercapacitor (SC) devices were assembled using $Ni(OH)_2$/Ni-NF/MG-7 and showed a maximum volumetric energy density of

Table 1: Comparison of $Ni(OH)_2$/Ni-NF/MG with other electrode materials.

electrodes	preparation method	C_{sp}[a]	rate capability	cycling stability	ref.
3D-porous $Ni(OH)_2$	solvothermal precipitation	2110 F/g at 1.0 A/g	55.5%, 10-fold	2000 cycles at 5 A/g, 53% retention	[40]
$Ni(OH)_2$/NF[b]	hydrothermal	3.51 F/cm^2 at 2 mA/cm^2	46.2%, 20-fold	7500 cycles at 20 mA/cm^2, 95.5% retention	[41]
$Ni(OH)_2$ nanosheets	hydrothermal	609.2 C/g at 1 A/g	62.4%, 20-fold	1000 cycles at 5 A/g, 83.3% retention	[42]
2D $MoSe_2$-$Ni(OH)_2$	hydrothermal	1175 F/g at 1 A/g	85.6%, 10-fold	3000 cycles at 2 A/g, 90% retention	[46]
$NiCo_2S_4$@$Ni(OH)_2$	hydrothermal and electrodeposition	680 F/g at 5 mA/cm^2	94.9%, 20-fold	2000 cycles at 40 mA/cm^2, 81.4% retention	[48]
$Ni(OH)_2$@ACMT[c]	acid treatment and hydrothermal	1568 F/g at 1 A/g	51.1%, 20-fold	3000 cycles at 5 A/g, 84.3% retention	[53]
$Ni(OH)_2$@NF[b]	hydrothermal	693 F/g at 4 A/g	34.8%, 3-fold	3000 cycles at 10 A/g, 77.3% retention	[54]
CNT[d]@$Ni(OH)_2$	chemical bath deposition	1136 F/g at 2 A/g	33.8%, 10-fold	1000 cycles at 8 A/g, 92% retention	[55]
$Ni(OH)_2$/Ni-NF[e]/MG[f]	dealloying and water-immersion	822.6 F/cm^3 at 0.5 A/cm^3	87.5%, 24-fold	3000 cycles at 1 A/cm^3, 83.7% retention	this work

[a]specific capacitance; [b]Ni foam; [c]acid-treated carbon microtubes; [d]carbon nanotubes; [e]nanofoam; [f]metallic glass.

ca. 32.7 mWh/cm^3 at a power density of 0.8 W/cm^3, and of 13.7 mWh/cm^3 when the power density increased to 2 W/cm^3. We proved for the first time that $Ni(OH)_2$ nanopetals were successfully prepared without elevated temperatures and nickel salt additives. This work may provide with a new idea for the synthesis of nanostructured $Ni(OH)_2$ by a simple and environmentally friendly approach.

Acknowledgements

This work is financially supported by the National Natural Science Foundation of China (51671077) and Natural Science Foundation of Hebei Province, China (E2016202212).

ORCID® iDs

Chunling Qin - https://orcid.org/0000-0003-3525-7802
Zhifeng Wang - https://orcid.org/0000-0003-3880-1957

References

1. González, A.; Goikolea, E.; Barrena, J. A.; Mysyk, R. *Renewable Sustainable Energy Rev.* **2016,** *58,* 1189–1206. doi:10.1016/j.rser.2015.12.249
2. Simon, P.; Gogotsi, Y.; Dunn, B. *Science* **2014,** *343,* 1210–1211. doi:10.1126/science.1249625
3. Winter, M.; Brodd, R. J. *Chem. Rev.* **2004,** *104,* 4245–4270. doi:10.1021/cr020730k
4. Simon, P.; Gogotsi, Y. *Nat. Mater.* **2008,** *7,* 845–854. doi:10.1038/nmat2297
5. Zhang, L. L.; Zhao, X. S. *Chem. Soc. Rev.* **2009,** *38,* 2520–2531. doi:10.1039/b813846j
6. Béguin, F.; Presser, V.; Balducci, A.; Frackowiak, E. *Adv. Mater. (Weinheim, Ger.)* **2014,** *26,* 2219–2251. doi:10.1002/adma.201304137
7. Zhu, Y.; Murali, S.; Stoller, M. D.; Ganesh, K. J.; Cai, W.; Ferreira, P. J.; Pirkle, A.; Wallace, R. M.; Cychosz, K. A.; Thommes, M.; Su, D.; Stach, E. A.; Ruoff, R. S. *Science* **2011,** *332,* 1537–1541. doi:10.1126/science.1200770
8. Lu, Z.; Wu, X.; Jiang, M.; Wang, J.; Liu, J.; Lei, X.; Sun, X. *Sci. China Mater.* **2014,** *57,* 59–69. doi:10.1007/s40843-014-0004-2
9. Faraji, S.; Ani, F. N. *J. Power Sources* **2014,** *263,* 338–360. doi:10.1016/j.jpowsour.2014.03.144
10. Yu, Z.; Tetard, L.; Zhai, L.; Thomas, J. *Energy Environ. Sci.* **2015,** *8,* 702–730. doi:10.1039/c4ee03229b
11. Le Comte, A.; Brousse, T.; Bélanger, D. *J. Power Sources* **2016,** *326,* 702–710. doi:10.1016/j.jpowsour.2016.03.065
12. Shi, D.; Zhang, L.; Yin, X.; Huang, T. J.; Gong, H. *J. Mater. Chem. A* **2016,** *4,* 12144–12151. doi:10.1039/c6ta03336a
13. Li, H. B.; Yu, M. H.; Wang, F. X.; Liu, P.; Liang, Y.; Xiao, J.; Wang, C. X.; Tong, Y. X.; Yang, G. W. *Nat. Commun.* **2013,** *4,* 1894. doi:10.1038/ncomms2932
14. Chen, H.; Hu, L.; Yan, Y.; Che, R.; Chen, M.; Wu, L. *Adv. Energy Mater.* **2013,** *3,* 1636–1646. doi:10.1002/aenm.201300580
15. Katić, J.; Metikoš–Huković, M.; Peter, R.; Petravić, M. *J. Power Sources* **2015,** *282,* 421–428. doi:10.1016/j.jpowsour.2015.02.063
16. Wang, H.; Casalongue, H. S.; Liang, Y.; Dai, H. *J. Am. Chem. Soc.* **2010,** *132,* 7472–7477. doi:10.1021/ja102267j
17. Yan, J.; Fan, Z.; Sun, W.; Ning, G.; Wei, T.; Zhang, Q.; Zhang, R.; Zhi, L.; Wei, F. *Adv. Funct. Mater.* **2012,** *22,* 2632–2641. doi:10.1002/adfm.201102839
18. Luo, Y.; Li, Y.; Wang, D.; Zhai, C.; Yang, T.; Zhang, M. *J. Alloys Compd.* **2018,** *743,* 1–10. doi:10.1016/j.jallcom.2018.01.341
19. Cui, H.; Xue, J.; Wang, M. *Adv. Powder Technol.* **2015,** *26,* 434–438. doi:10.1016/j.apt.2014.11.016
20. Xiao, Z.; Xu, B.; Zhang, S.; Yang, Z.; Mei, Y.; Fan, W.; Zhang, M.; Zhang, L.; Sun, D. *Electrochim. Acta* **2018,** *284,* 202–210. doi:10.1016/j.electacta.2018.07.173
21. Nguyen, T.; Boudard, M.; Carmezim, M. J.; Montemor, M. F. *Sci. Rep.* **2017,** *7,* 39980. doi:10.1038/srep39980
22. Nguyen, T.; Fátima Montemor, M. *J. Mater. Chem. A* **2018,** *6,* 2612–2624. doi:10.1039/c7ta05582j
23. Ji, J.; Zhang, L. L.; Ji, H.; Li, Y.; Zhao, X.; Bai, X.; Fan, X.; Zhang, F.; Ruoff, R. S. *ACS Nano* **2013,** *7,* 6237–6243. doi:10.1021/nn4021955
24. Yuan, Y. F.; Xia, X. H.; Wu, J. B.; Yang, J. L.; Chen, Y. B.; Guo, S. Y. *Electrochim. Acta* **2011,** *56,* 2627–2632. doi:10.1016/j.electacta.2010.12.001
25. Ke, X.; Zhang, Z.; Cheng, Y.; Liang, Y.; Tan, Z.; Liu, J.; Liu, L.; Shi, Z.; Guo, Z. *Sci. China Mater.* **2018,** *61,* 353–362. doi:10.1007/s40843-017-9144-8
26. Liu, P.; Qin, K.; Wen, S.; Wang, L.; He, F.; Liu, E.; He, C.; Shi, C.; Li, J.; Li, Q.; Ma, L.; Zhao, N. *Electrochim. Acta* **2018,** *283,* 970–978. doi:10.1016/j.electacta.2018.07.007
27. Wang, Z.; Liu, J.; Qin, C.; Liu, L.; Zhao, W.; Inoue, A. *Intermetallics* **2015,** *56,* 48–55. doi:10.1016/j.intermet.2014.09.002
28. Zhao, W.; Fei, P.; Zhang, X.; Zhang, Y.; Qin, C.; Wang, Z. *Mater. Lett.* **2018,** *211,* 254–257. doi:10.1016/j.matlet.2017.10.019
29. Wang, Z.; Fei, P.; Xiong, H.; Qin, C.; Zhao, W.; Liu, X. *Electrochim. Acta* **2017,** *252,* 295–305. doi:10.1016/j.electacta.2017.08.189
30. Liu, S.; Pang, F.; Zhang, Q.; Guo, R.; Wang, Z.; Wang, Y.; Zhang, W.; Ou, J. *Appl. Mater. Today* **2018,** *13,* 135–143. doi:10.1016/j.apmt.2018.08.014
31. Ma, W.; Chen, S.; Yang, S.; Chen, W.; Cheng, Y.; Guo, Y.; Peng, S.; Ramakrishna, S.; Zhu, M. *J. Power Sources* **2016,** *306,* 481–488. doi:10.1016/j.jpowsour.2015.12.063
32. Khan, Y.; Hussain, S.; Söderlind, F.; Käll, P.-O.; Abbasi, M. A.; Durrani, S. K. *Mater. Lett.* **2012,** *69,* 37–40. doi:10.1016/j.matlet.2011.11.058
33. Zhang, Y.; Yu, S.; Lou, G.; Shen, Y.; Chen, H.; Shen, Z.; Zhao, S.; Zhang, J.; Chai, S.; Zou, Q. *J. Mater. Sci.* **2017,** *52,* 11201–11228. doi:10.1007/s10853-017-0955-3
34. Yuan, C.; Li, J.; Hou, L.; Zhang, X.; Shen, L.; Lou, X. W. D. *Adv. Funct. Mater.* **2012,** *22,* 4592–4597. doi:10.1002/adfm.201200994
35. Dan, Z.; Lu, J.; Li, F.; Qin, F.; Chang, H. *Nanomaterials* **2018,** *8,* 18. doi:10.3390/nano8010018
36. Mao, W.; He, H.; Sun, P.; Ye, Z.; Huang, J. *ACS Appl. Mater. Interfaces* **2018,** *10,* 15088–15095. doi:10.1021/acsami.8b03433
37. Lu, Y.; Wang, H.; Gu, Y.; Xu, L.; Sun, X.; Deng, Y. *Acta Chim. Sin. (Chin. Ed.)* **2012,** *70,* 1731–1736. doi:10.6023/a12070376
38. Parveen, N.; Cho, M. H. *Sci. Rep.* **2016,** *6,* 27318. doi:10.1038/srep27318
39. Xi, Y.; Wei, G.; Li, J.; Liu, X.; Pang, M.; Yang, Y.; Ji, Y.; Izotov, V. Y.; Guo, Q.; Han, W. *Electrochim. Acta* **2017,** *233,* 26–35. doi:10.1016/j.electacta.2017.02.038

40. Liu, F.; Chu, X.; Zhang, H.; Zhang, B.; Su, H.; Jin, L.; Wang, Z.; Huang, H.; Yang, W. *Electrochim. Acta* **2018,** *269,* 102–110. doi:10.1016/j.electacta.2018.02.130
41. Li, K.; Li, S.; Huang, F.; Lu, Y.; Wang, L.; Chen, H.; Zhang, H. *Appl. Surf. Sci.* **2018,** *428,* 250–257. doi:10.1016/j.apsusc.2017.09.066
42. Mao, Y.; Li, T.; Guo, C.; Zhu, F.; Zhang, C.; Wei, Y.; Hou, L. *Electrochim. Acta* **2016,** *211,* 44–51. doi:10.1016/j.electacta.2016.06.027
43. Guo, J.; Zhao, Y.; Jiang, N.; Liu, A.; Gao, L.; Li, Y.; Wang, H.; Ma, T. *J. Electrochem. Soc.* **2018,** *165,* A882–A890. doi:10.1149/2.0411805jes
44. Zhang, L.; Song, S.; Shi, H. *J. Alloys Compd.* **2018,** *751,* 69–79. doi:10.1016/j.jallcom.2018.04.109
45. Li, L.; Xu, J.; Lei, J.; Zhang, J.; McLarnon, F.; Wei, Z.; Li, N.; Pan, F. *J. Mater. Chem. A* **2015,** *3,* 1953–1960. doi:10.1039/c4ta05156d
46. Kirubasankar, B.; Palanisamy, P.; Arunachalam, S.; Murugadoss, V.; Angaiah, S. *Chem. Eng. J.* **2019,** *355,* 881–890. doi:10.1016/j.cej.2018.08.185
47. Zhi, L.; Zhang, W.; Dang, L.; Sun, J.; Shi, F.; Xu, H.; Liu, Z.; Lei, Z. *J. Power Sources* **2018,** *387,* 108–116. doi:10.1016/j.jpowsour.2018.03.063
48. Yang, Y.; Cheng, D.; Chen, S.; Guan, Y.; Xiong, J. *Electrochim. Acta* **2016,** *193,* 116–127. doi:10.1016/j.electacta.2016.02.053
49. Lobiak, E. V.; Bulusheva, L. G.; Fedorovskaya, E. O.; Shubin, Y. V.; Plyusnin, P. E.; Lonchambon, P.; Senkovskiy, B. V.; Ismagilov, Z. R.; Flahaut, E.; Okotrub, A. V. *Beilstein J. Nanotechnol.* **2017,** *8,* 2669–2679. doi:10.3762/bjnano.8.267
50. Xu, S.; Li, X.; Yang, Z.; Wang, T.; Jiang, W.; Yang, C.; Wang, S.; Hu, N.; Wei, H.; Zhang, Y. *ACS Appl. Mater. Interfaces* **2016,** *8,* 27868–27876. doi:10.1021/acsami.6b10700
51. Zheng, D.; Zhao, F.; Li, Y.; Qin, C.; Zhu, J.; Hu, Q.; Wang, Z.; Inoue, A. *Electrochim. Acta* **2019,** *297,* 767–777. doi:10.1016/j.electacta.2018.12.035
52. Pech, D.; Brunet, M.; Durou, H.; Huang, P.; Mochalin, V.; Gogotsi, Y.; Taberna, P.-L.; Simon, P. *Nat. Nanotechnol.* **2010,** *5,* 651–654. doi:10.1038/nnano.2010.162
53. Li, Q.; Lu, C.; Xiao, D.; Zhang, H.; Chen, C.; Xie, L.; Liu, Y.; Yuan, S.; Kong, Q.; Zheng, K.; Yin, J. *ChemElectroChem* **2018,** *5,* 1279–1287. doi:10.1002/celc.201800024
54. Liu, X.; Yang, Y.; Xing, X.; Zou, T.; Wang, Z.; Wang, Y. *ChemElectroChem* **2018,** *5,* 434–444. doi:10.1002/celc.201701094
55. Yi, H.; Wang, H.; Jing, Y.; Peng, T.; Wang, Y.; Guo, J.; He, Q.; Guo, Z.; Wang, X. *J. Mater. Chem. A* **2015,** *3,* 19545–19555. doi:10.1039/c5ta06174a

License and Terms

BEILSTEIN JOURNAL OF NANOTECHNOLOGY

Temperature-dependent Raman spectroscopy and sensor applications of $PtSe_2$ nanosheets synthesized by wet chemistry

Mahendra S. Pawar[1,2] and Dattatray J. Late[*1,2]

Full Research Paper

Open Access

Address:
[1]Physical and Materials Chemistry Division, CSIR-National Chemical Laboratory, Dr. Homi Bhabha Road, Pune 411008, India and
[2]Academy of Scientific and Innovative Research (AcSIR), Ghaziabad 201002, India

Email:
Dattatray J. Late[*] - dj.late@ncl.res.in

* Corresponding author

Keywords:
nanosheets; $PtSe_2$; Raman spectroscopy; sensor; thermal effect

Beilstein J. Nanotechnol. **2019,** *10,* 467–474.
doi:10.3762/bjnano.10.46

Received: 01 November 2018
Accepted: 16 January 2019
Published: 13 February 2019

This article is part of the thematic issue "Low-dimensional materials and systems".

Guest Editor: S. Walia

Abstract

We report on a wet chemistry method used to grow $PtSe_2$ nanosheets followed by thermal annealing. The SEM and TEM analysis confirms the formation of $PtSe_2$ nanosheets. Furthermore, XRD, Raman, XPS and SAED patterns were used to analyze the crystal structure and to confirm the formation of the $PtSe_2$ phase. The temperature-dependent Raman spectroscopy investigations were carried out on $PtSe_2$ nanosheets deposited on Si substrates in the temperature range 100–506 K. The shifts in Raman active E_g and A_{1g} modes as a function of temperature were monitored. The temperature coefficient for both modes was calculated and was found to match well with the reported 2D transition metal dichalcogenides. A $PtSe_2$ nanosheet-based sensor device was tested for its applicability as a humidity sensor and photodetector. The humidity sensor based on $PtSe_2$ nanosheets showed an excellent recovery time of ≈5 s, indicating the great potential of $PtSe_2$ for future sensor devices.

Introduction

Graphene, the most well-studied example of the two-dimensional (2D) aromatic compounds, is the building block of all forms of carbon allotropes [1]. In recent years, it has been widely studied due to its extraordinary optical, electrical, mechanical, magnetic and chemical properties [2-5]. Like graphene and its organic analogues [6], inorganic 2D metal dichalcogenides also exhibit outstanding performance in many applications including transistors, sensors, photodetectors, solar cells, field emitters, battery materials, light harvesting and energy storage devices, catalyst for H_2 generation, and drug delivery applications [7-12]. Most of the transition metal dichalcogenides (TMDCs) are semiconducting in nature with MX_2 type – where M is a metal, M = W, Mo, Sn, Nb, V, etc. from group IV–V and X represents the chalcogenides family, X = S, Se, Te, etc. The metal atom M is sandwiched between layers of chalcogenide (X) atoms in the structure X–M–X. The

TMDCs show diverse functional properties at the monolayer level in contrast to bulk due to the quantum confinement effect. Apart from this, these TMDCs, for example MoS_2 and $MoSe_2$, show an indirect to direct band gap transition [13-17].

A 2D platinum diselenide ($PtSe_2$) material has recently joined the growing class of stable TMDCs due its promising applications. The 2D $PtSe_2$ has not been explored much to date due to difficulties in synthesis. It is well known that bulk $PtSe_2$ is a semimetal in nature with a nearly zero band gap [18,19]. With the help of theoretical calculations such as density functional theory (DFT) and local-density approximations (LDAs), it has been observed that bulk $PtSe_2$ shows a semimetallic nature and single-layer $PtSe_2$ has a semiconducting nature with a bandgap of 1.2 eV. Bilayer $PtSe_2$ is also a semiconducting material but with a slightly smaller band gap than the monolayer material [19]. This layer-dependent conversion of semimetal-to-semiconductor transition has potential for electronic device applications [20-22]. Bulk $PtSe_2$ was first prepared in 1909 by Minozzi from elements [23]. $PtSe_2$ nanosheets have been recently prepared by heating thin foils of platinum in selenium vapors at 400 °C [19,24]. In this paper we have synthesized few-layer-thick $PtSe_2$ nanosheets by a wet chemical method [25] at 90 °C using chloroplatinic acid (H_2PtCl_6) and Se powder as precursors followed by thermal annealing at 500 °C. Temperature-dependent Raman spectroscopic characterization was carried out on the materials.

Materials and Methods

All the chemicals such as chloroplatinic acid, Se powder, hexamethylenetetramine, and $NaBH_4$ were purchased from Sigma-Aldrich for the synthesis of $PtSe_2$ nanosheets.

Synthesis method

The $PtSe_2$ nanosheets were synthesized using a solvothermal method followed by annealing at 500 °C using a previously described method for $PtSe_2$ synthesis [25]. The $PtSe_2$ material was prepared in two steps. The first step is the formation of the PtSe complex on the wall of a container by a wet chemical method; the second step is the phase transformation of $PtSe_2$ by thermal annealing. 0.5 mL of a 0.015 M solution of H_2PtCl_6 was mixed with 0.5 mL of 0.5 M hexamethylenetetramine. In order to get a homogeneous solution, the mixture was carefully stirred for 15–20 s until the colour of the solution became slightly yellow; this is referred to as the Pt precursor. In another beaker 0.8 mg of Se powder was added into a 10 mL ice-cold solution of 0.1 M $NaBH_4$ which acts as a strong reducing agent for the reduction of Se powder. The solution of Se was then heated in an oil bath at 90 °C for ≈20 min in order to completely reduce the Se. After complete reduction, the colour of the solution became dark brown and is referred to as the Se precursor. The Pt precursor was then slowly added into the Se precursor. The colour of the solution was found to suddenly change to greenish brown. The mixture was then kept undisturbed for ≈20 min. After 20 min the complex of Pt and Se was formed on the wall of the beaker. The complex was then washed several times using deionized water. First complex was transferred onto a Si substrate and heated at 100 °C on a hot plate. After complete evaporation, the substrate was annealed in a chemical vapour deposition system at 500 °C in argon gas atmosphere for 5 h. Supporting Information File 1, Figure S1 shows the schematic of the $PtSe_2$ nanosheet synthesis steps.

Sensor device fabrication and testing

Sensor devices were fabricated on a tin-doped indium oxide (ITO) substrate with a channel length of ≈300 μm and width ≈5 mm. The $PtSe_2$ nanosheet powder was dispersed in *N*-methyl-2-pyrrolidone (NMP) solvent and then drop casted between the channels. The devices were further annealed in a vacuum furnace at 170 °C to improve the contact resistance and adhesion of the nanosheets with the substrate. The humidity sensing performance was investigated by exposing the sensor device to various relative humidity (RH) levels ranging from 11.3–97.3% as described in detail previously [26]. All of the electrical tests such as current–voltage (*I*–*V*) and current–time (*I*–*t*) measurements were carried out using a Keithley 2612A system source meter which was attached to a computer through a GPIB 488A interface. For the photodetection study, a green LED was used. All sensor experiments were carried out at ambient pressure and room temperature.

Results and Discussion

Structural characterization

The structural characterization was carried out using X-ray diffraction (XRD) and Raman spectroscopy. Figure 1a shows the typical XRD pattern of the as-prepared sample deposited on a Si substrate. XRD was performed on a PANalytical X'pert pro dual goniometer diffractometer using Cu Kα radiation. The samples were mounted flat and scanned between 10 to 60°. The XRD pattern of the as-prepared sample shows the strong characteristic peaks around $2\theta = 17.41°$ and 33.17° belonging to the (001) and (011) planes of $PtSe_2$. These values match well with the JCPDS data card number (88-2281) and as observed in a previous report [27]. Figure 1b shows the Raman spectra of the as-prepared few-layer $PtSe_2$ nanosheets. The Raman spectra were recorded using a Renishaw microscope at a wavelength of 532 nm with laser power ≈25 mW and laser spot diameter ≈1 μm. The typical Raman spectra recorded at room temperature consist of two distinct peaks, one at ≈176 cm^{-1} corresponding to the E_g mode and another slightly less intense peak at ≈205 cm^{-1} corresponding to the A_{1g} mode. The E_g mode in the Raman spectra corresponds to in-plane vibration due to the

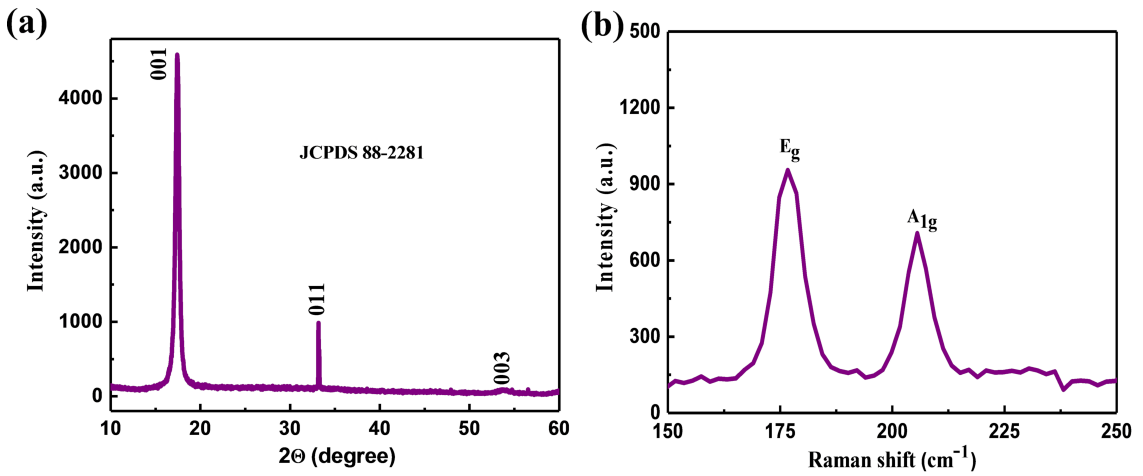

Figure 1: $PtSe_2$ nanosheets. (a) Typical XRD pattern and (b) Raman spectra recorded at room temperature.

opposite motion of the upper and lower Se atoms. The A_{1g} mode in the Raman spectra corresponds to the out-of-plane vibration of Se atoms [22,28].

Morphological investigations were carried out using scanning electron microscopy (SEM). Figure 2a–c shows SEM images of few-layer $PtSe_2$ with typical overlapping of multiple sheets on

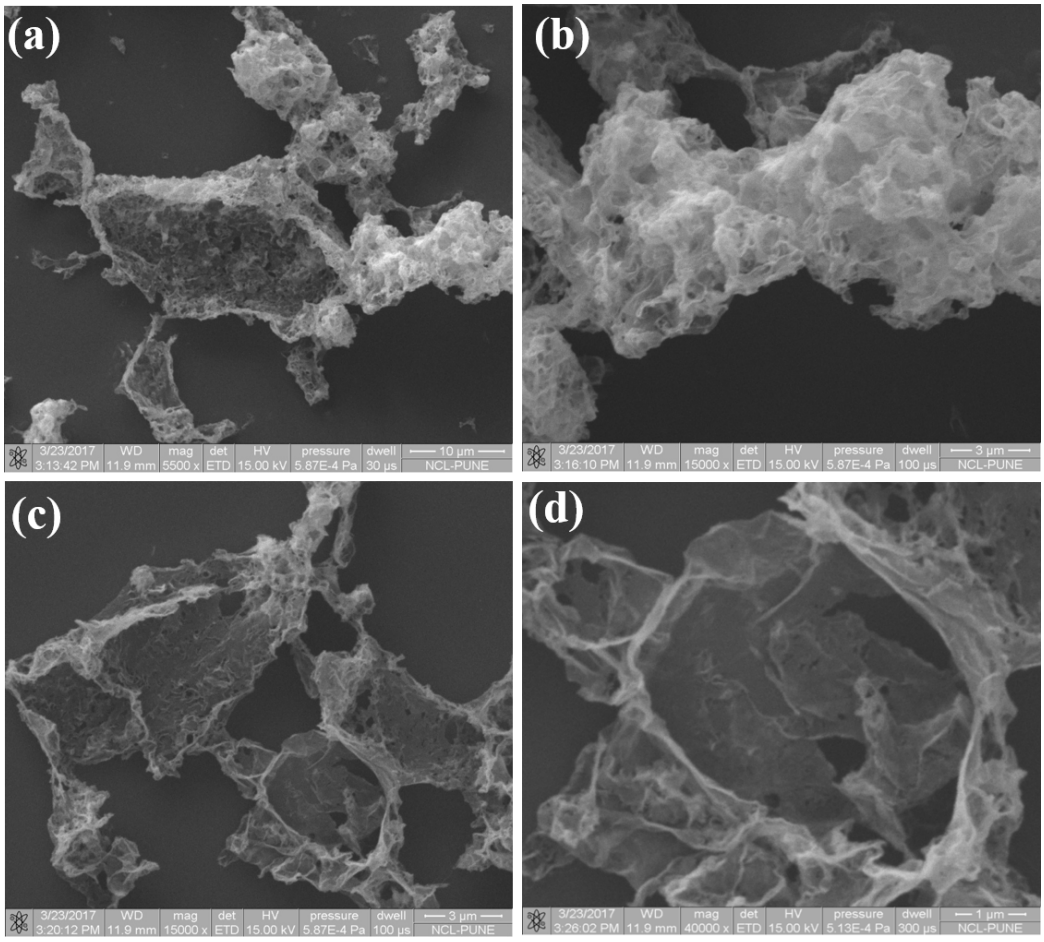

Figure 2: (a–d) Typical SEM images for $PtSe_2$ nanosheets synthesized using the wet chemistry method.

each other. Figure 2d shows an SEM image indicating a more transparent thin layer of $PtSe_2$ stacked on each other, exhibiting the few-layer nature of the as-synthesized $PtSe_2$ sample. Figure 3a–c shows the low-resolution TEM images of the as-synthesized $PtSe_2$ sample clearly showing the sheet-like morphology with lateral dimension of ≈700 nm. Figure 3d shows a high-resolution TEM image of the $PtSe_2$ nanosheets. The inset of Figure 3d shows the selected area electron diffraction pattern (SAED) which depicts the crystalline nature of the as-synthesized $PtSe_2$ sample. The X-ray photoelectron spectroscopy (XPS) spectra of the Pt 4f and Se 3d regions acquired on a $PtSe_2$ nanosheet sample were carried out on a film deposited on the Si substrate. The Figure 4a represents the fitted spectrum for Pt $4f_{7/2}$ and Pt $4f_{5/2}$ with binding energy 72.55 eV and 75.83 eV, respectively. Similarly, for Se, the binding energy spectrum can be fitted by Gaussian–Lorentzian curves shown in Figure 4b. The two peaks with binding energy 54.8 eV and 55.6 eV are observed for the $3d_{5/2}$ and $3d_{3/2}$ states, respectively. There is one more peak observed in the Se region with low intensity at 52.9 eV which corresponds to Pt $5d_{3/2}$ [24]. The thickness of the as-prepared $PtSe_2$ nanosheets was calculated using atomic force microscopy (AFM). Figure 5a shows the AFM image which clearly shows that the lateral dimensions of the nanosheets are ≈700 nm. Figure 5b represents the corresponding height profile plot for the $PtSe_2$ nanosheet with thickness found to be ≈47 nm.

Temperature-dependent Raman spectroscopy of few-layer $PtSe_2$ nanosheets

The temperature-dependent Raman spectroscopy investigations of few-layer $PtSe_2$ nanosheets were carried out between 100–506 K. The Raman spectra of the $PtSe_2$ nanosheets at different temperatures are provided in Supporting Information File 1, Figures S2 and S3. The Raman mode E_g and A_{1g} as a function of temperature is shown in Figure 6a,b. It can be clearly seen that the position of the A_{1g} and E_g modes shifts to

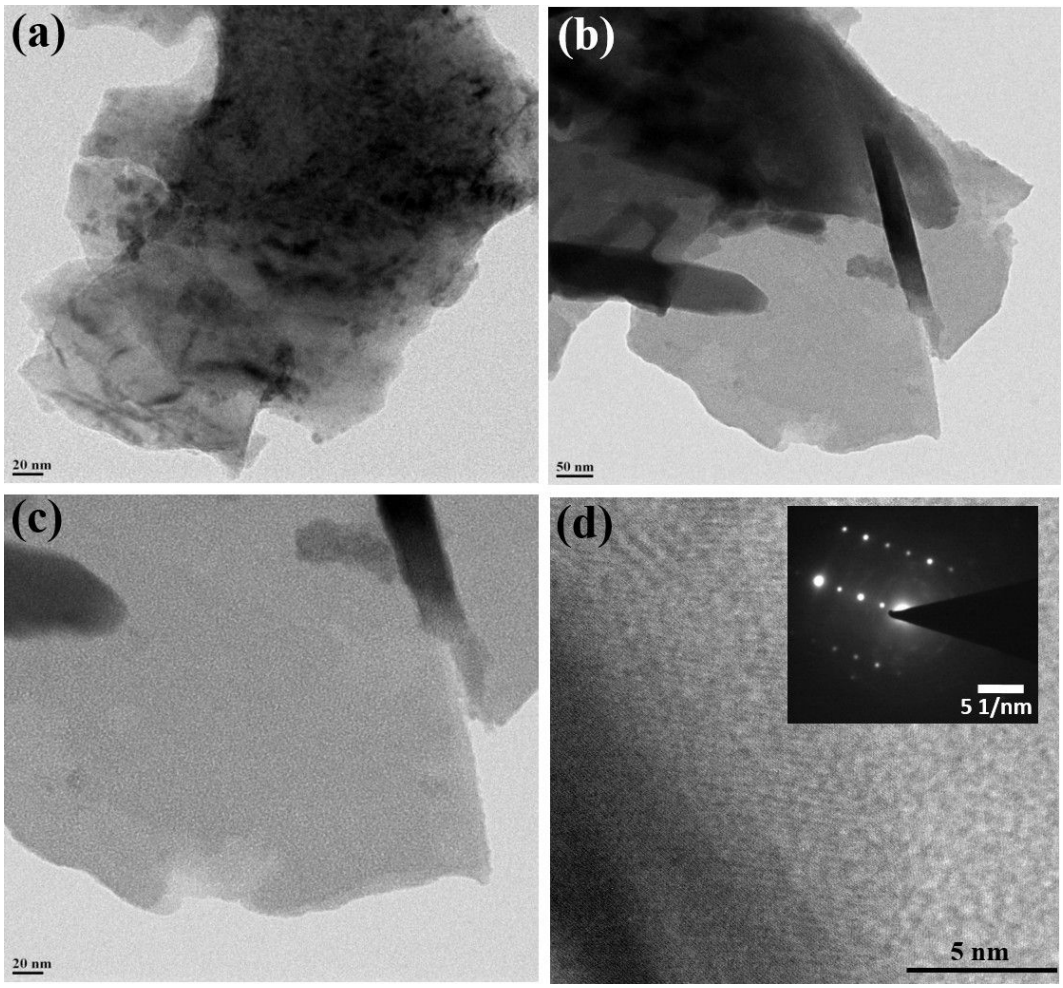

Figure 3: (a–c) Low-magnification TEM images and (d) a high-magnification TEM image, where the inset shows the selected area electron diffraction (SAED) pattern for the as-synthesized $PtSe_2$ nanosheets.

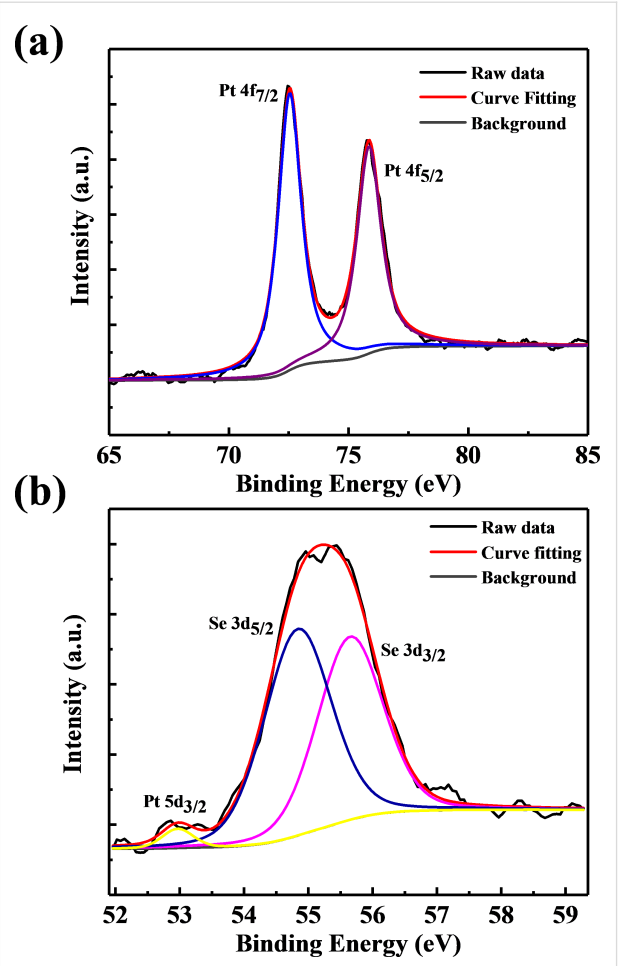

Figure 4: (a) Deconvoluted XPS spectra for Pt and (b) Se elements.

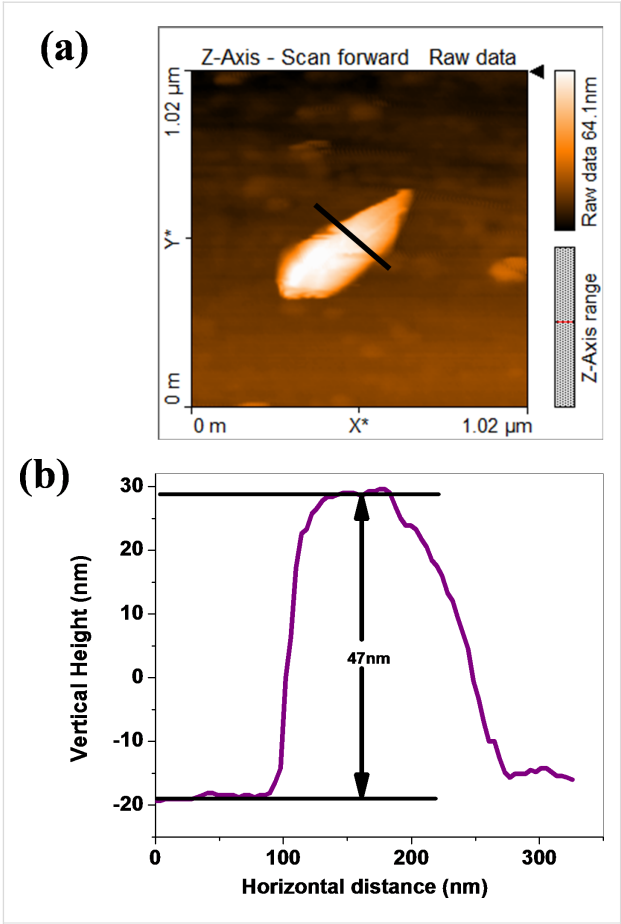

Figure 5: (a) AFM image and (b) AFM height profile plot for a $PtSe_2$ nanosheet.

lower wavenumbers as the temperature increases from 100 K to 506 K. The Raman modes E_g and A_{1g} for $PtSe_2$ behave linearly within the temperature range 100–506 K. Furthermore, it was observed that the full width half maximum (FWHM) increases with an increase in temperature. The peak positions in the Raman spectra were calculated by fitting the Lorentzian function to the A_{1g} and E_g modes. The temperature coefficient can be calculated by Equation 1 [29]:

$$\omega(T) = \omega_0 + \chi T\,, \tag{1}$$

where ω_0 is the peak position of the A_{1g} and E_g mode at zero Kelvin, χ is the temperature coefficient of the A_{1g} and E_g modes, and ω is a Raman phonon frequency. The slope of the Raman modes vs temperature plot directly gives the value of the temperature coefficient and is given in Table 1. Further, it was clearly seen that the Raman peak position and peak broadening was affected by temperature. This change in Raman modes is mainly due to the contribution from the thermal anharmonicity.

The Raman phonon frequency as a function of volume and temperature is given by Equation 2 [30]:

$$\left(\frac{\partial \ln\omega}{\partial T}\right)_P = \left(\frac{\partial \ln V}{\partial T}\right)_P \left(\frac{\partial \ln\omega}{\partial \ln V}\right)_T + \left(\frac{\partial \ln\omega}{\partial T}\right)_V$$
$$\left(\frac{\partial \ln\omega}{\partial T}\right)_P = -\frac{\gamma}{K}\left(\frac{\partial \ln\omega}{\partial P}\right)_T + \left(\frac{\partial \ln\omega}{\partial T}\right)_V \tag{2}$$

where γ is the volume thermal coefficient and K represents the isothermal volume compressibility. The first term on the right hand side, $-\gamma/K\,(\partial \ln\omega/\partial P)_T$, represents the volume contribution at a constant temperature. The second term, $(\partial \ln\omega/\partial T)_V$, represents the temperature contribution at constant volume. In single-layer TMDCs due to the direct band gap, the double resonance phenomenon is useful to explain the change in FWHM, intensity and the peak shift as a function of temperature. The double resonance phenomenon can be attributed to several process including absorption of an incident photon, creation of a hole pair,

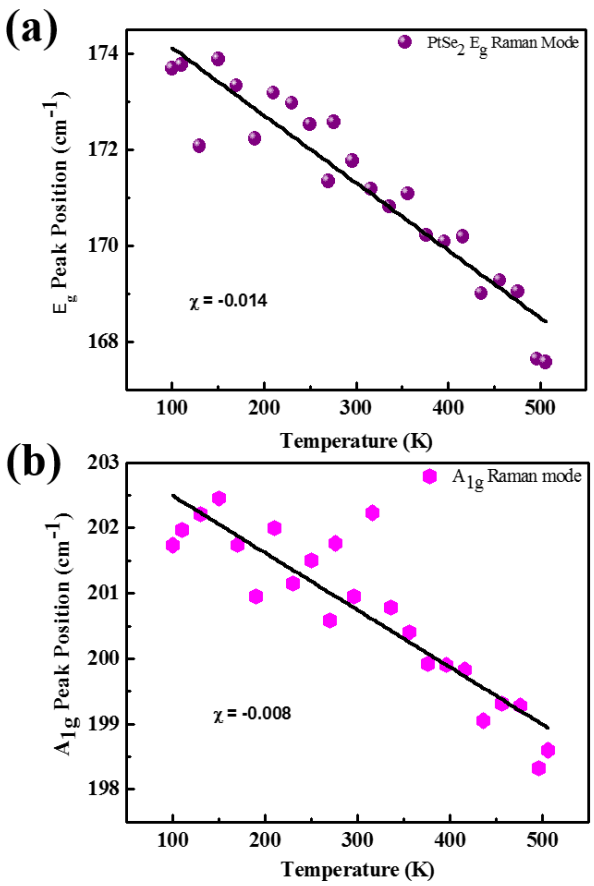

Figure 6: Temperature-dependent Raman spectra analysis for $PtSe_2$ nanosheets for the (a) E_g mode and the (b) A_{1g} mode as a function of temperature.

Table 1: Temperature coefficient values for the A_{1g} and E_g modes in a $PtSe_2$ nanosheet sample.

Material	Raman modes	Temperature coefficient (χ)	Δω (cm^{-1})
$PtSe_2$ nanosheet	E_g	−0.014	6.11
	A_{1g}	−0.008	3.14

double scattering of a created hole pair by phonon, and recombination of an electron–hole pair with emission of phonon. The temperature coefficient for the E_g and A_{1g} modes was found to be −0.014 and −0.008, respectively. The nature of the temperature dependence of the Raman spectra of $PtSe_2$ nanosheets is found to be similar in nature to that of graphene and other 2D materials such as MoS_2, WS_2, $MoSe_2$, WSe_2, BP, TiS_3, multilayer graphene, and $MoTe_2$ [29,31-34]. A comparison of the temperature coefficient values corresponding to various 2D materials are shown in Table 2. The value of Δω for both E_g and A_{1g} modes was found to be 6.11 cm^{-1} and 3.14 cm^{-1}, respectively.

Table 2: Temperature coefficient values for various 2D materials.

TMDCs	Raman modes	Temperature coefficient (χ)	Δω (cm^{-1})	Ref.
$MoSe_2$	A_{1g}	−0.0096	4.75	[29]
WSe_2	A_{1g}	−0.0071	3.81	[29]
MoS_2	E_g	−0.0136	8	[29]
	A_{1g}	−0.0113	6.11	
WS_2	E_g	−0.0098	4.51	[29]
	A_{1g}	−0.014	6.43	
black phosphorous	A_{1g}	−0.008	4.39	[31]
	B_{2g}	−0.013	8.14	
	A_{2g}	−0.014	8.63	
TiS_3	A_{1g}	−0.022, −0.025, −0.024, −0.017	–	[32]
single-layer graphene	G	−0.0162	–	[33]
bilayer graphene	G	−0.0154	–	
$MoTe_2$ (bilayer)	E'_{2g}	−0.0116	–	[34]
	B'_{2g}	−0.0181	–	
$PtSe_2$	E_g	−0.014	6.11	this work
	A_{1g}	−0.008	3.14	

Humidity sensor and photodetector based on few-layer $PtSe_2$ nanosheets

Figure 7a shows the typical resistance of the sensor device vs relative humidity plot. The resistance is significantly decreased from 3.75 GΩ to 0.83 MΩ. The humidity sensing mechanism for the $PtSe_2$ sensor can be explained as follows. When the $PtSe_2$ nanosheet sensor device was exposed to water molecules/vapors, a charge transfer between the water molecules and the $PtSe_2$ nanosheets occurs. This results in the decrease in resistance of the $PtSe_2$ nanosheet sensor device with an increase in the relative humidity. The interactions among the water molecules (electron donor) and the $PtSe_2$ nanosheets results in an enhancement in the conductivity of the sensor device, similar to that observed for other 2D materials such as $SnSe_2$ [35], MoS_2 [36], BP [26], and $MoSe_2$ [37]. Figure 7b shows a typical current–time (*I*–*t*) plot where cycles of 11.3% and 97.3% RH levels were used to calculate the response and recovery time. The response and recovery time for the $PtSe_2$-based humidity sensor device was found to be 118 s and 5 s, respectively. The advantage of the $PtSe_2$-based humidity sensor device is its rapid recovery and its functionality at room temperature. Figure 7c shows a typical *I*–*V* plot in dark conditions and under green light illumination. Figure 7d shows the *I*–*t* plot for the photodetector based on $PtSe_2$ nanosheets with a response time of ≈110 s and a recovery time of ≈129 s.

Conclusion

In conclusion, we report on a wet chemistry method to grow $PtSe_2$ nanosheets. The SEM and TEM analysis confirm the for-

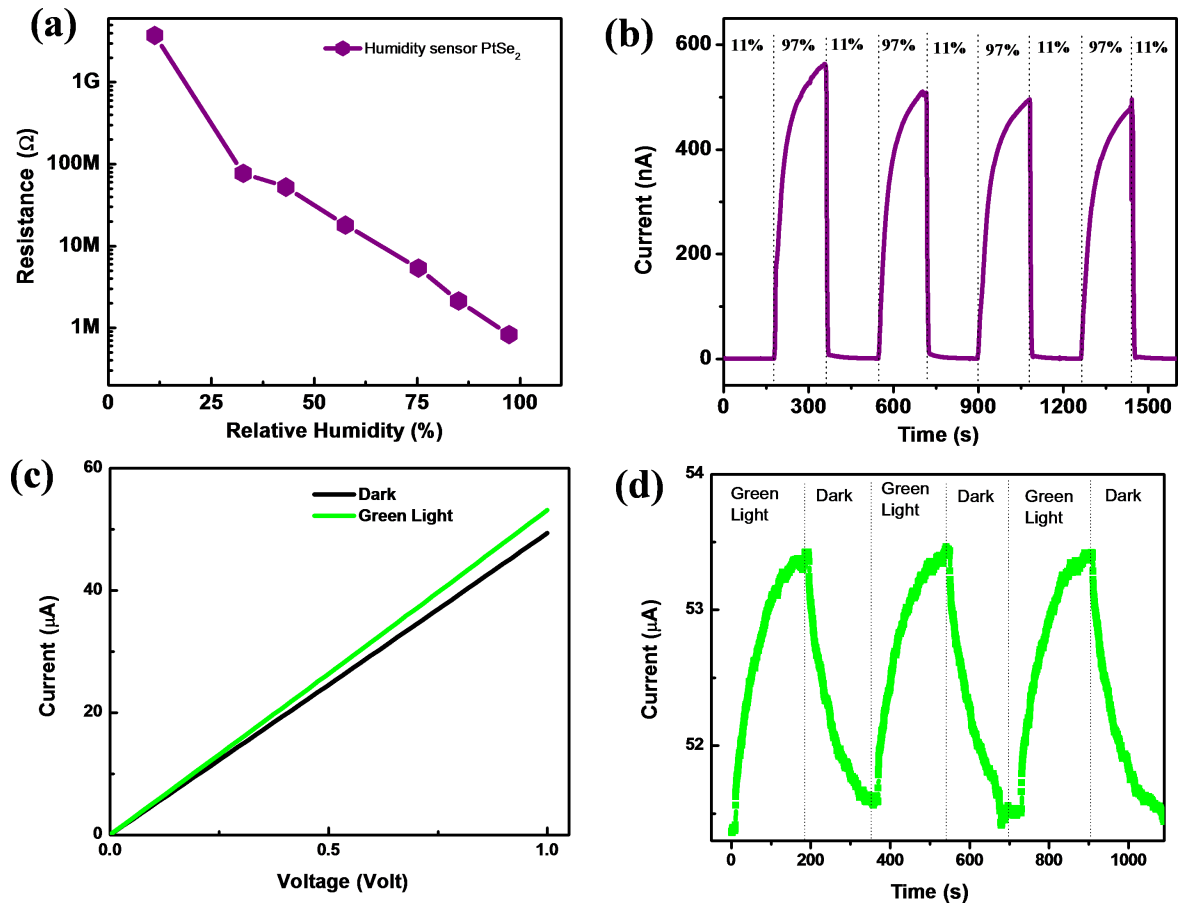

Figure 7: $PtSe_2$ nanosheet based humidity sensor: (a) Typical resistance versus relative humidity plot and (b) current–time (*I*–*t*) plot taken after switching 11% RH and 97% RH. The photodetector application of $PtSe_2$ nanosheets: (c) *I*–*V* in dark conditions and with green LED light and (d) typical *I*–*t* cycle when the LED is on and off, showing a favourable response.

mation of $PtSe_2$ nanosheets. Further, the XRD, Raman and SAED pattern results were used to analyze the crystal structure and to confirm the formation of the $PtSe_2$ phase. Temperature-dependent Raman spectroscopy investigations were carried out on $PtSe_2$ nanosheet films grown on Si substrates between 100–506 K. The temperature coefficient for the E_g and A_{1g} modes was found to be −0.014 and −0.008, respectively. A room temperature humidity sensor based on the $PtSe_2$ nanosheets demonstrated an excellent recovery time of ≈5 s, indicating the great potential of $PtSe_2$-based sensors for future nanoelectronics and sensor devices.

Supporting Information

Supporting Information File 1

Additional figures.
[https://www.beilstein-journals.org/bjnano/content/supplementary/2190-4286-10-46-S1.pdf]

Acknowledgements

This research work was supported by the SERB Government of India under the SERB Research Scientist scheme provided to Dr. D. J. Late.

ORCID® iDs

Mahendra S. Pawar - https://orcid.org/0000-0002-3642-3158
Dattatray J. Late - https://orcid.org/0000-0003-3007-7220

References

1. Geim, A. K.; Novoselov, K. S. *Nat. Mater.* **2007,** *6,* 183–191. doi:10.1038/nmat1849
2. Grigorenko, A. N.; Polini, M.; Novoselov, K. S. *Nat. Photonics* **2012,** *6,* 749–758. doi:10.1038/nphoton.2012.262
3. Stankovich, S.; Dikin, D. A.; Dommett, G. H. B.; Kohlhaas, K. M.; Zimney, E. J.; Stach, E. A.; Piner, R. D.; Nguyen, S. T.; Ruoff, R. S. *Nature* **2006,** *442,* 282–286. doi:10.1038/nature04969
4. Zhao, X.; Zhang, Q.; Chen, D.; Lu, P. *Macromolecules* **2010,** *43,* 2357–2363. doi:10.1021/ma902862u

5. Pawbake, A. S.; Mishra, K. K.; Machuno, L. G. B.; Gelamo, R. V.; Ravindran, T. R.; Rout, C. S.; Late, D. J. *Diamond Relat. Mater.* **2018,** *84,* 146–156. doi:10.1016/j.diamond.2018.03.021
6. Liu, W.; Luo, X.; Bao, Y.; Liu, Y. P.; Ning, G.-H.; Abdelwahab, I.; Li, L.; Nai, C. T.; Hu, Z. G.; Zhao, D.; Liu, B.; Quek, S. Y.; Loh, K. P. *Nat. Chem.* **2017,** *9,* 563–570. doi:10.1038/nchem.2696
7. Wang, Q. H.; Kalantar-Zadeh, K.; Kis, A.; Coleman, J. N.; Strano, M. S. *Nat. Nanotechnol.* **2012,** *7,* 699–712. doi:10.1038/nnano.2012.193
8. Peng, B.; Ang, P. K.; Loh, K. P. *Nano Today* **2015,** *10,* 128–137. doi:10.1016/j.nantod.2015.01.007
9. Li, H.; Shi, Y.; Chiu, M.-H.; Li, L.-J. *Nano Energy* **2015,** *18,* 293–305. doi:10.1016/j.nanoen.2015.10.023
10. Jariwala, D.; Sangwan, V. K.; Lauhon, L. J.; Marks, T. J.; Hersam, M. C. *ACS Nano* **2014,** *8,* 1102–1120. doi:10.1021/nn500064s
11. Shi, J.; Ma, D.; Han, G.-F.; Zhang, Y.; Ji, Q.; Gao, T.; Sun, J.; Song, X.; Li, C.; Zhang, Y.; Lang, X.-Y.; Zhang, Y.; Liu, Z. *ACS Nano* **2014,** *8,* 10196–10204. doi:10.1021/nn503211t
12. Voiry, D.; Salehi, M.; Silva, R.; Fujita, T.; Chen, M.; Asefa, T.; Shenoy, V. B.; Eda, G.; Chhowalla, M. *Nano Lett.* **2013,** *13,* 6222–6227. doi:10.1021/nl403661s
13. Splendiani, A.; Sun, L.; Zhang, Y.; Li, T.; Kim, J.; Chim, C.-Y.; Galli, G.; Wang, F. *Nano Lett.* **2010,** *10,* 1271–1275. doi:10.1021/nl903868w
14. Tongay, S.; Zhou, J.; Ataca, C.; Lo, K.; Matthews, T. S.; Li, J.; Grossman, J. C.; Wu, J. *Nano Lett.* **2012,** *12,* 5576–5580. doi:10.1021/nl302584w
15. Zhang, Y.; Chang, T.-R.; Zhou, B.; Cui, Y.-T.; Yan, H.; Liu, Z.; Schmitt, F.; Lee, J.; Moore, R.; Chen, Y.; Lin, H.; Jeng, H.-T.; Mo, S.-K.; Hussain, Z.; Bansil, A.; Shen, Z.-X. *Nat. Nanotechnol.* **2014,** *9,* 111–115. doi:10.1038/nnano.2013.277
16. Mak, K. F.; Lee, C.; Hone, J.; Shan, J.; Heinz, T. F. *Phys. Rev. Lett.* **2010,** *105,* 136805–136808. doi:10.1103/physrevlett.105.136805
17. Sundaram, R. S.; Engel, M.; Lombardo, A.; Krupke, R.; Ferrari, A. C.; Avouris, P.; Steiner, M. *Nano Lett.* **2013,** *13,* 1416–1421. doi:10.1021/nl400516a
18. Guo, G. Y.; Liang, W. Y. *J. Phys. C: Solid State Phys.* **1986,** *19,* 995–1008. doi:10.1088/0022-3719/19/7/011
19. Wang, Y.; Li, L.; Yao, W.; Song, S.; Sun, J. T.; Pan, J.; Ren, X.; Li, C.; Okunishi, E.; Wang, Y.-Q.; Wang, E.; Shao, Y.; Zhang, Y. Y.; Yang, H.-t.; Schwier, E. F.; Iwasawa, H.; Shimada, K.; Taniguchi, M.; Cheng, Z.; Zhou, S.; Du, S.; Pennycook, S. J.; Pantelides, S. T.; Gao, H.-J. *Nano Lett.* **2015,** *15,* 4013–4018. doi:10.1021/acs.nanolett.5b00964
20. Zhao, Y.; Qiao, J.; Yu, Z.; Yu, P.; Xu, K.; Lau, S. P.; Zhou, W.; Liu, Z.; Wang, X.; Ji, W.; Chai, Y. *Adv. Mater. (Weinheim, Ger.)* **2017,** *29,* 1604230. doi:10.1002/adma.201604230
21. Sattar, S.; Schwingenschlögl, U. *ACS Appl. Mater. Interfaces* **2017,** *9,* 15809–15813. doi:10.1021/acsami.7b00012
22. O'Brien, M.; McEvoy, N.; Motta, C.; Zheng, J.-Y.; Berner, N. C.; Kotakoski, J.; Elibol, K.; Pennycook, T. J.; Meyer, J. C.; Yim, C.; Abid, M.; Hallam, T.; Donegan, J. F.; Sanvito, S.; Duesberg, G. S. *2D Mater.* **2016,** *3,* 021004. doi:10.1088/2053-1583/3/2/021004
23. Grønvold, F.; Haraldsen, H.; Kjekshus, A.; Söderquist, R. *Acta Chem. Scand.* **1960,** *14,* 1879–1893. doi:10.3891/acta.chem.scand.14-1879
24. Yim, C.; Lee, K.; McEvoy, N.; O'Brien, M.; Riazimehr, S.; Berner, N. C.; Cullen, C. P.; Kotakoski, J.; Meyer, J. C.; Lemme, M. C.; Duesberg, G. S. *ACS Nano* **2016,** *10,* 9550–9558. doi:10.1021/acsnano.6b04898
25. Ali Umar, A.; Md Saad, S. K.; Mat Salleh, M. *ACS Omega* **2017,** *2,* 3325–3332. doi:10.1021/acsomega.7b00580
26. Erande, M. B.; Pawar, M. S.; Late, D. J. *ACS Appl. Mater. Interfaces* **2016,** *8,* 11548–11556. doi:10.1021/acsami.5b10247
27. Yu, X.; Yu, P.; Wu, D.; Singh, B.; Zeng, Q.; Lin, H.; Zhou, W.; Lin, J.; Suenaga, K.; Liu, Z.; Wang, Q. J. *Nat. Commun.* **2018,** *9,* 1545. doi:10.1038/s41467-018-03935-0
28. Zhang, K.; Yan, M.; Zhang, H.; Huang, H.; Arita, M.; Sun, Z.; Duan, W.; Wu, Y.; Zhou, S. *Phys. Rev. B* **2017,** *96,* 125102. doi:10.1103/physrevb.96.125102
29. Pawbake, A. S.; Pawar, M. S.; Jadkar, S. R.; Late, D. J. *Nanoscale* **2016,** *8,* 3008–3018. doi:10.1039/c5nr07401k
30. Late, D. J.; Maitra, U.; Panchakarla, L. S.; Waghmare, U. V.; Rao, C. N. R. *J. Phys.: Condens. Matter* **2011,** *23,* 055303. doi:10.1088/0953-8984/23/5/055303
31. Late, D. J. *ACS Appl. Mater. Interfaces* **2015,** *7,* 5857–5862. doi:10.1021/am509056b
32. Pawbake, A. S.; Island, J. O.; Flores, E.; Ares, J. R.; Sanchez, C.; Ferrer, I. J.; Jadkar, S. R.; van der Zant, H. S. J.; Castellanos-Gomez, A.; Late, D. J. *ACS Appl. Mater. Interfaces* **2015,** *7,* 24185–24190. doi:10.1021/acsami.5b07492
33. Calizo, I.; Balandin, A. A.; Bao, W.; Miao, F.; Lau, C. N. *Nano Lett.* **2007,** *7,* 2645–2649. doi:10.1021/nl071033g
34. Late, D. J. *Appl. Mater. Today* **2016,** *5,* 98–102. doi:10.1016/j.apmt.2016.09.013
35. Pawar, M.; Kadam, S.; Late, D. J. *ChemistrySelect* **2017,** *2,* 4068–4075. doi:10.1002/slct.201700261
36. Late, D. J.; Huang, Y.-K.; Liu, B.; Acharya, J.; Shirodkar, S. N.; Luo, J.; Yan, A.; Charles, D.; Waghmare, U. V.; Dravid, V. P.; Rao, C. N. R. *ACS Nano* **2013,** *7,* 4879–4891. doi:10.1021/nn400026u
37. Late, D. J.; Doneux, T.; Bougouma, M. *Appl. Phys. Lett.* **2014,** *105,* 233103. doi:10.1063/1.4903358

License and Terms

BEILSTEIN JOURNAL OF NANOTECHNOLOGY

Wearable, stable, highly sensitive hydrogel–graphene strain sensors

Jian Lv[‡1,2], Chuncai Kong[‡1], Chao Yang[1], Lu Yin[2], Itthipon Jeerapan[2,3], Fangzhao Pu[1], Xiaojing Zhang[1], Sen Yang[*1] and Zhimao Yang[*1,4,5]

Letter

Open Access

Address:
[1]School of Science, MOE Key Laboratory for Non-Equilibrium Synthesis and Modulation of Condensed Matter, Xi'an Jiaotong University, Xi'an 710049, Shaanxi, P. R. China, [2]Department of NanoEngineering, University of California, San Diego, La Jolla, California 92093, USA, [3]Department of Chemistry, Faculty of Science, Prince of Songkla University, Hat Yai, Songkhla 90112, Thailand, [4]Collaborative Innovation Center of Suzhou Nano Science and Technology, Xi'an Jiaotong University Suzhou Academy, Suzhou 21500, P. R. China and [5]Research institute of Xi'an Jiaotong University, Hangzhou, Zhejiang, 311215, P. R. China

Email:
Sen Yang[*] - yangsen@xjtu.edu.cn; Zhimao Yang[*] - zmyang@xjtu.edu.cn

* Corresponding author ‡ Equal contributors

Keywords:
graphene; high sensitivity; hydrogel; strain sensor; wearable sensor

Beilstein J. Nanotechnol. **2019,** *10,* 475–480.
doi:10.3762/bjnano.10.47

Received: 28 October 2018
Accepted: 21 January 2019
Published: 14 February 2019

This article is part of the thematic issue "Low-dimensional materials and systems".

Guest Editor: S. Walia

Abstract

A stable and highly sensitive graphene/hydrogel strain sensor is designed by introducing glycerol as a co-solvent in the formation of a hydrogel substrate and then casting a graphene solution onto the hydrogel in a simple, two-step method. This hydrogel-based strain sensor can effectively retain water in the polymer network due to the formation of strong hydrogen bonding between glycerol and water. The addition of glycerol not only enhances the stability of the hydrogel over a wider temperature range, but also increases the stretchability of the hydrogel from 800% to 2000%. The enhanced sensitivity can be attributed to the graphene film, whereby the graphene flakes redistribute to optimize the contact area under different strains. The careful design enables this sensor to be used in both stretching and bending modes. As a demonstration, the as-prepared strain sensor was applied to sense the movement of finger knuckles. Given the outstanding performance of this wearable sensor, together with the proposed scalable fabrication method, this stable and sensitive hydrogel strain sensor is considered to have great potential in the field of wearable sensors.

Introduction

Wearable, flexible sensors to monitor human body pressure, temperature, strain, and chemicals hold great potential in the field of bioelectronics, artificial intelligence, and soft robotics [1,2]. Among these sensors, strain sensors can translate an external applied tensile force into electrical signal, hence attracting numerous research efforts for health monitoring, biomechanics studies and artificial skin for soft robotics [3,4]. The current, state of the art strategy to fabricate flexible strain

sensors involves the integration of a conductive film on an elastomeric polymer and the embedding of conductive materials into the polymer matrix [5,6]. However, the lack of seamless conformation to curvatures in human skin has impeded further integration as a wearable sensing component [7].

Hydrogels, with mechanical properties like biological tissues and consisting of three-dimensional polymer networks that can retain a large amount of water, can serve as ideal vehicles for wearable devices [8,9]. Several hydrogel-based strain sensors demonstrating high flexibility, self-healing properties and skin-attachable wearability, have been fabricated in the reported literature [2,10,11]. However, their inability to retain water over a long period largely prevents the hydrogel-based strain sensors from being widely used in a realistic environment with extended usage. Lu et al. utilized a water and glycerol binary-solvent system to produce a hydrogel with good thermal tolerance, while maintaining all the properties over a wide temperature range (−20 to 60 °C) [12]. To date, the use of a moisture-retaining hydrogel to fabricate soft, flexible strain sensors is rarely reported. Another issue to be solved is related to increasing the sensitivity of the hydrogel strain sensor as the ionically conductive hydrogel exhibits low resistance changes with applied strain [13].

In this study, a flexible, stable, high-sensitivity, graphene-based, water/glycerol (WG) binary-solvent hydrogel (graphene/WG-hydrogel) strain sensor is designed via a two-step method. Water and glycerol are used as solvents to synthesize the hydrogel substrate with long-lasting moisture-retaining properties [12]. The continuous graphene film is cast onto the hydrogel through drop casting and drying. Although the bare hydrogel already shows resistance changes with respect to strain, the graphene film was used to further increase the sensitivity. The graphene/WG-hydrogel strain sensor can be used to sense human finger movements. This stable, soft, high-sensitivity hydrogel strain sensor shows great promise for the development of applicable, wearable strain sensors.

Experimental

Chemicals: Acrylic acid ($C_3H_4O_2$), ammonium persulfate ($(NH_4)_2S_2O_8$), α-ketoglutarate ($C_5H_6O_5$), glycerol ($C_3H_8O_3$), acrylamide (C_3H_5NO) and methylene-bis-acrylamide ($C_7H_{10}N_2O_2$) were purchased from Aladdin (Shanghai, China). The 2 mg/mL aqueous graphene dispersion was purchased from Tanfeng Graphene (Suzhou, China). Silver epoxy was purchased from Ted Pella (Redding, USA).

Formulation of the hydrogel: Acrylic acid, acrylamide, ammonium persulfate, methylene-bis-acrylamide and α-ketoglutarate were mixed in a beaker containing glycerol/water (1:3 v/v) binary solvent with concentrations of 40 mg/mL, 200 mg/mL, 25 mg/mL, 0.15 mg/mL, and 0.3 mg/mL, respectively, to make the monomer solution. Then the solution was mixed by magnetic stirring for 1 h. After the mixed solution was poured into the mold and irradiated by the UV light for 1 h, the hydrogel substrate was formed. The pure-water hydrogel was formulated in the same way as the binary solvent hydrogel, except that no glycerol was added.

Formulation of the graphene/hydrogel: The graphene film was cast on the hydrogel film using a drop casting and drying process. 5 mL of the 2 mg/mL graphene dispersion was drop casted onto the hydrogel and put in the oven at 35 °C until the graphene was fully dried.

Assembly of the strain sensor: The strain sensor was fabricated by connecting the graphene/hydrogel to a copper foil using the silver epoxy. The size of the graphene/hydrogel sensor is 5 × 30 mm.

Characterization of the hydrogel and graphene/hydrogel: The mechanical properties of the hydrogel were characterized in an electronic universal testing machine (CMT6503, Sans, Shenzhen, China). A field-emission scanning electron microscope (SEM, JSM-7000F, JEOL, Japan) was used for electron microimaging. The resistance changes of the strain sensor under stretching was monitored by a multimeter (Keithley 2400 Source Meter).

Results and Discussion

Figure 1a shows the two-step fabrication process of the graphene/WG-hydrogel composite material. The hydrogel, which is capable of withstanding relatively high temperature, was synthesized by the copolymerization of acrylic acid (AA) and acrylamide (AM) monomer in the water/glycerol solvent system under irradiation with UV light. A common problem of the reported hydrogels is the lack of long term stability, due to the tendency of the material to lose water at high temperature and freeze at low temperature [14]. Glycerol is a commonly used, nontoxic antifreeze additive. Here, hydrogen bonding between glycerol and water competes with hydrogen bonding between the water molecules, and the formation of ice at low temperature is restricted and the evaporation of water at high temperature is prohibited [11].

The graphene layer was formed on the hydrogel by directly drop casting the graphene solution onto the hydrogel and drying in an oven at 35 °C. The drying process removes the extra water in the graphene dispersion without removing the water inside the hydrogel, thus maintaining the mechanical properties of the material. The graphene layer serves to significantly increase the

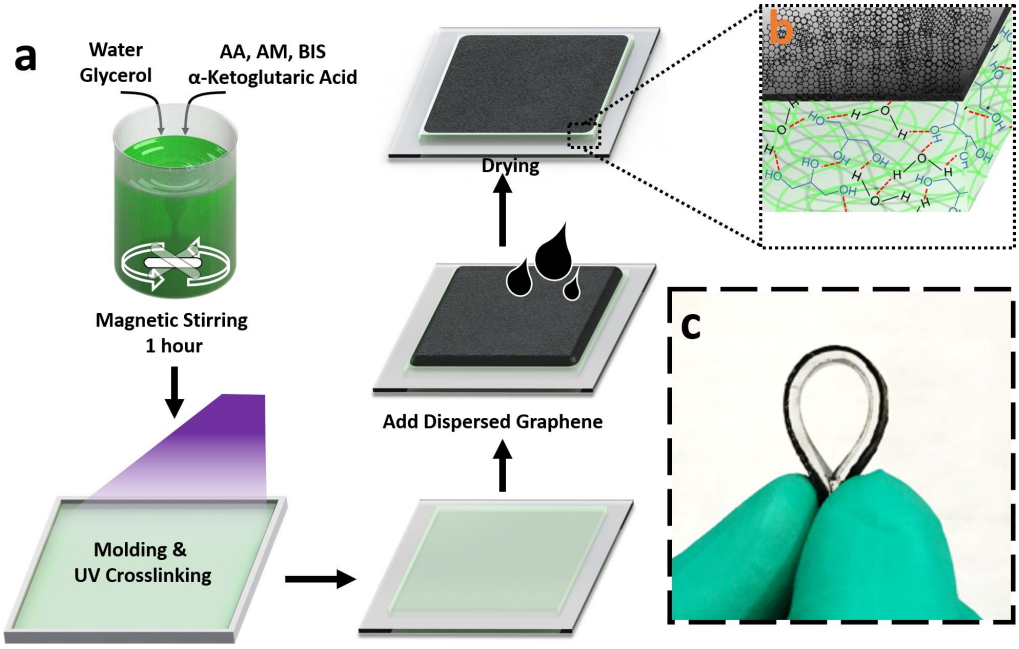

Figure 1: (a) Schematic of the preparation of the graphene/water-glycerol (WG) hydrogel composite material. (b) The double-layer composition of the graphene/WG-hydrogel composite material. (c) Photograph of the as-prepared flexible graphene/WG-hydrogel.

resistance change of the hydrogel under strain because of the spacing variations among graphene flakes. The schematic structure and a photograph of the composite electrode is shown in Figure 1b and Figure 1c, respectively.

Besides serving to retain water in the hydrogel, the presence of glycerol also improves the mechanical performance of the hydrogel, as shown in Figure 2a and 2b. Figure 2a shows the uniaxial tensile strain–stress curves of the hydrogels fabricated with (WG-hydrogel) and without glycerol (W-hydrogel). Under the same strain, the WG-hydrogel shows less stress in the two strain–stress curves, indicating that including the glycerol provides the hydrogel with higher softness, thus making it more adaptable to external force. The complete yield strain–stress curves of the two hydrogels is shown in Supporting Information File 1, Figure S1, in which the fracture strain of the W-hydrogel is around 800% with a stress of 0.03 MPa, while the introduction of glycerol increases the break stress to 0.06 MPa at a strain of 2000%. The difference between the two hydrogels in the compressing strain–stress curve is not much as that in tensile mode, as shown in Figure 2b. An image of the synthesized graphene–hydrogel electrode is shown in Figure 2c. A uniform film is formed on the surface of the hydrogel after the drying process in the oven, which serves to increase the conductivity of the hydrogel. More details of the as-prepared graphene can be seen in the SEM image shown in Figure 2d. The graphene layer shows a randomly interconnected structure which allows the graphene flakes to slide when the layer is stretched, which will enhance the resistance change of the hydrogel under strain. The SEM image of the cross section of the graphene/hydrogel composite is shown in Supporting Information File 1, Figure S2. A great contact between the graphene layer and the hydrogel layer can be seen after the drying of the graphene solution.

The sensing performance of the graphene/WG-hydrogel composite material is shown in Figure 3a. The sensitivity of the graphene/WG-hydrogel composite sensor, represented by the gauge factor (the ratio of the relative electrical resistance change $\Delta R/R$ to the strain), is much higher than that of the WG-hydrogel sensor. At 25% stretching, the gauge factor of the graphene/WG-hydrogel is about 2.4, while that of the hydrogel is only about 0.59. This superior piezoresistive performance comes from two aspects: the intrinsic piezoresistive behavior of the WG-hydrogel and the electron conduction change of the graphene film under different contact conditions [15] (spacing variations and contact area under stretching). The ionic conductivity is responsible for the electrical conductivity of the bare WG-hydrogel. The hysteresis curve for graphene/WG-hydrogel strain sensor is illustrated in Supporting Information File 1, Figure S3. The stretching and releasing curve is almost symmetric, indicating that hysteresis is not obvious. Supporting Information File 1, Figure S4 shows optical images of the graphene/hydrogel composite before and after 10 times 25% stretching. It

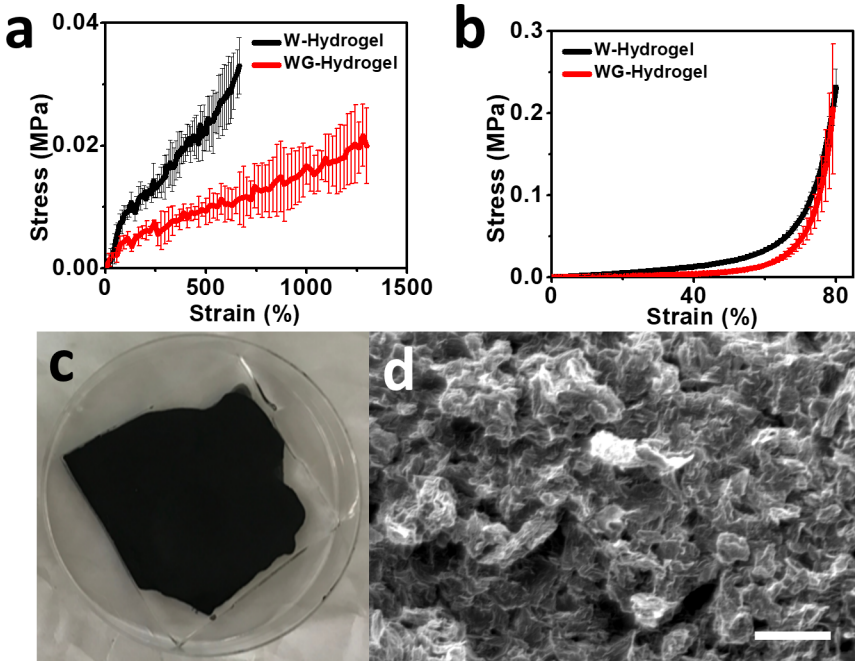

Figure 2: (a) The uniaxial tensile and (b) compressive strain–stress curves of the W-hydrogel and WG-hydrogel, respectively (n = 3). (c) The top view of the graphene/WG-hydrogel composite material. (d) An SEM image of the graphene film. Scale bar: 10 μm.

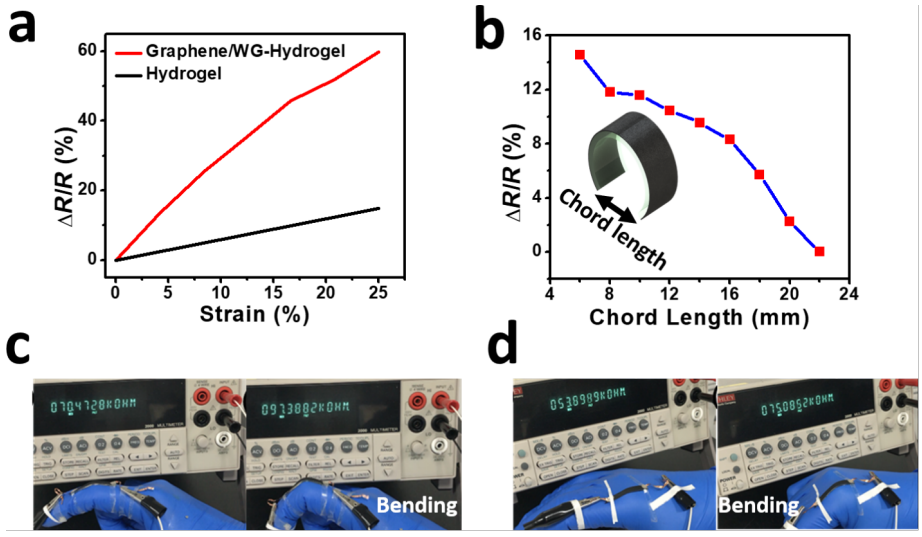

Figure 3: (a) The strain–resistance change curves of the WG-hydrogel and graphene/WG-hydrogel based strain sensors. (b) Resistance change of the graphene–hydrogel strain sensor versus chord length. Photographs showing the real life application of the strain sensor to sense the movement of the proximal interphalangeal joint (c) and the metacarpophalangeal joint (d).

is clear that the bonding between the graphene layer and hydrogel layer is very firm, even after the stretching, suggesting the capability of the composite to endure cyclic stretching.

The graphene/WG-hydrogel strain sensor was also used to sense flexion, another type of human movement, as shown in Figure 3b. The outer curvature of the sensor experiences tensile strain and the inner curvature undergoes a compressive force when the graphene/hydrogel sensor is flexed, as shown in the inset of Figure 3b. The graphene film was set on the outer curvature, so that the graphene flakes are separated under the flexion. When the distance between two ends of the sensor was

decreased from 22 mm to 6 mm, the resistance increased by 14.6%. To show the real workability of the graphene/WG-hydrogel strain sensor, the sensor was mounted on a nitrile glove worn on a human hand to sense the movement of finger knuckles. As shown in Figure 3c, two as-fabricated sensors were put on the proximal interphalangeal (PIP) joint and metacarpophalangeal (MCP) joint, respectively. Before, during and after bending, the graphene/WG-hydrogel sensors showed the expected changes, indicating the potential of our strain sensor to be used in a real working scenario.

Conclusion

We have demonstrated a wearable, stable, and highly sensitive strain sensor, based on a binary solvent, graphene/WG-hydrogel composite material, synthesized using a two-step process. The long-term water-retention properties of the graphene/WG-hydrogel strain sensor can be attributed to the use of glycerol as a co-solvent. The hydrogel bonding between glycerol and water prevents water from being released from the polymer network, hence guaranteeing the long-term stability of the sensor. In addition, a graphene film is cast onto the WG-hydrogel to enhance the sensitivity of the hydrogel strain sensor. The strain sensor is demonstrated to operate in both stretching and flexuous modes, together with the ability to sense the movement of finger knuckles, suggesting the great potential of this soft and stable hydrogel-based strain sensor. In addition, the long-term moisture-retaining property of the WG-hydrogel provides an ideal substrate to cast other kinds of two-dimensional material films, such as MoS_2, through a simple drop casting and drying method [16-18].

Supporting Information

Yield strain stress curve of the hydrogels; Cross-section SEM image of the graphene/hydrogel composite; Hysteresis curve for the graphene/WG-hydrogel strain sensor; Optical cross-section images of the graphene/WG-hydrogel composite before and after stretching.

Supporting Information File 1

Additional figures.
[https://www.beilstein-journals.org/bjnano/content/supplementary/2190-4286-10-47-S1.pdf]

Acknowledgements

This work was supported by the National Natural Science Foundation of China (NSFC No.51501140, 11674263, U1866203), the China Postdoctoral Science Foundation (2016M602808, Natural Science Foundation of Jiangsu Province (BK20161250, BK20171235), the public welfare technology application research project of Zhejiang Province (2017C31099), the Fundamental Research Funds for the Central Universities, the World-Class Universities (Disciplines) and the Characteristic Development Guidance Funds for the Central Universities.

ORCID® iDs

Jian Lv - https://orcid.org/0000-0003-3425-2882
Chao Yang - https://orcid.org/0000-0001-7414-5171
Itthipon Jeerapan - https://orcid.org/0000-0001-8016-6411

References

1. Bandodkar, A. J.; Jeerapan, I.; Wang, J. *ACS Sens.* **2016,** *1,* 464–482. doi:10.1021/acssensors.6b00250
2. Tian, K.; Bae, J.; Bakarich, S. E.; Yang, C.; Gately, R. D.; Spinks, G. M.; in het Panhuis, M.; Suo, Z.; Vlassak, J. J. *Adv. Mater. (Weinheim, Ger.)* **2017,** *29,* 1604827. doi:10.1002/adma.201604827
3. Boland, C. S.; Khan, U.; Backes, C.; O'Neill, A.; McCauley, J.; Duane, S.; Shanker, R.; Liu, Y.; Jurewicz, I.; Dalton, A. B.; Coleman, J. N. *ACS Nano* **2014,** *8,* 8819–8830. doi:10.1021/nn503454h
4. Amjadi, M.; Kyung, K.-U.; Park, I.; Sitti, M. *Adv. Funct. Mater.* **2016,** *26,* 1678–1698. doi:10.1002/adfm.201504755
5. Amjadi, M.; Pichitpajongkit, A.; Lee, S.; Ryu, S.; Park, I. *ACS Nano* **2014,** *8,* 5154–5163. doi:10.1021/nn501204t
6. Wang, T.; Zhang, Y.; Liu, Q.; Cheng, W.; Wang, X.; Pan, L.; Xu, B.; Xu, H. *Adv. Funct. Mater.* **2018,** *28,* 1705551–1705562. doi:10.1002/adfm.201705551
7. Liu, Y.-J.; Cao, W.-T.; Ma, M.-G.; Wan, P. *ACS Appl. Mater. Interfaces* **2017,** *9,* 25559–25570. doi:10.1021/acsami.7b07639
8. Lin, S.; Yuk, H.; Zhang, T.; Parada, G. A.; Koo, H.; Yu, C.; Zhao, X. *Adv. Mater. (Weinheim, Ger.)* **2016,** *28,* 4497–4505. doi:10.1002/adma.201504152
9. Zhang, X.; Sheng, N.; Wang, L.; Tan, Y.; Liu, C.; Xia, Y.; Nie, Z.; Sui, K. *Mater. Horiz.* **2019**. doi:10.1039/c8mh01188e
10. Guo, J.; Liu, X.; Jiang, N.; Yetisen, A. K.; Yuk, H.; Yang, C.; Khademhosseini, A.; Zhao, X.; Yun, S.-H. *Adv. Mater. (Weinheim, Ger.)* **2016,** *28,* 10244–10249. doi:10.1002/adma.201603160
11. Liu, S.; Li, L. *ACS Appl. Mater. Interfaces* **2017,** *9,* 26429–26437. doi:10.1021/acsami.7b07445
12. Han, L.; Liu, K.; Wang, M.; Wang, K.; Fang, L.; Chen, H.; Zhou, J.; Lu, X. *Adv. Funct. Mater.* **2018,** *28,* 1704195. doi:10.1002/adfm.201704195
13. Cai, G.; Wang, J.; Qian, K.; Chen, J.; Li, S.; Lee, P. S. *Adv. Sci.* **2017,** *4,* 1600190. doi:10.1002/advs.201600190
14. Bai, Y.; Chen, B.; Xiang, F.; Zhou, J.; Wang, H.; Suo, Z. *Appl. Phys. Lett.* **2014,** *105,* 151903. doi:10.1063/1.4898189
15. Tian, H.; Shu, Y.; Cui, Y.-L.; Mi, W.-T.; Yang, Y.; Xie, D.; Ren, T.-L. *Nanoscale* **2014,** *6,* 699–705. doi:10.1039/c3nr04521h
16. Wang, Y.; Ou, J. Z.; Balendhran, S.; Chrimes, A. F.; Mortazavi, M.; Yao, D. D.; Field, M. R.; Latham, K.; Bansal, V.; Friend, J. R.; Zhuiykov, S.; Medhekar, N. V.; Strano, M. S.; Kalantar-zadeh, K. *ACS Nano* **2013,** *7,* 10083–10093. doi:10.1021/nn4041987

17. Wang, Y.; Ou, J. Z.; Chrimes, A. F.; Carey, B. J.; Daeneke, T.; Alsaif, M. M. Y. A.; Mortazavi, M.; Zhuiykov, S.; Medhekar, N.; Bhaskaran, M.; Friend, J. R.; Strano, M. S.; Kalantar-Zadeh, K. *Nano Lett.* **2015,** *15,* 883–890. doi:10.1021/nl503563g
18. Liu, X.; Gao, S.; Yang, P.; Wang, B.; Ou, J. Z.; Liu, Z.; Wang, Y. *Appl. Mater. Today* **2018,** *13,* 158–165. doi:10.1016/j.apmt.2018.09.001

License and Terms

BEILSTEIN JOURNAL OF NANOTECHNOLOGY

A porous 3D-RGO@MWCNT hybrid material as Li–S battery cathode

Yongguang Zhang[1], Jun Ren[1], Yan Zhao*[1], Taizhe Tan[2], Fuxing Yin[1] and Yichao Wang*[3]

Full Research Paper

Open Access

Address:
[1]School of Materials Science and Engineering, Hebei University of Technology, Tianjin 300130, China, [2]Synergy Innovation Institute of GDUT, Heyuan, Guangdong Province, China and [3]School of Life and Environmental Sciences, Deakin University, Geelong, Vic 3216, Australia

Email:
Yan Zhao* - yanzhao1984@hebut.edu.cn; Yichao Wang* - yichaowang@gmail.com

* Corresponding author

Keywords:
carbon nanotubes; energy storage and conversion; Li–S batteries; nanocomposites

Beilstein J. Nanotechnol. **2019,** *10,* 514–521.
doi:10.3762/bjnano.10.52

Received: 01 November 2018
Accepted: 11 February 2019
Published: 21 February 2019

This article is part of the thematic issue "Low-dimensional materials and systems".

Guest Editor: S. Walia

Abstract

In this work, a unique three-dimensional (3D) structured carbon-based composite was synthesized. In the composite, multiwalled carbon nanotubes (MWCNT) form a lattice matrix in which porous spherical reduced graphene oxide (RGO) completes the 3D structure. When used in Li–S batteries, the 3D porous lattice matrix not only accommodates a high content of sulfur, but also induces a confinement effect towards polysulfide, and thereby reduces the "shuttle effect". The as-prepared S-3D-RGO@MWCNT composite delivers an initial specific capacity of 1102 mAh·g^{-1}. After 200 charging/discharge cycles, a capacity of 805 mAh·g^{-1} and a coulombic efficiency of 98% were maintained, implying the shuttle effect was greatly suppressed by the composite matrix. In addition, the S-3D-RGO@MWCNT composite also exhibits an excellent rate capability.

Introduction

Li–S batteries are notable for their high theoretical specific capacity (1675 mAh·g^{-1}) and energy density (2600 Wh·kg^{-1}). Sulfur is an abundant element, enabling Li–S batteries to be highly competitive among the various battery technologies. The actual application of Li–S batteries, however, is hindered by several challenges, i.e., i) the poor conductivity of sulfur and ii) the "shuttle effect" of polysulfides (Li_2S_x, $4 < x \leq 8$) [1-4]. To achieve a high specific capacity, a sulfur cathode with high electrical conductivity and high sulfur loading is necessary. The shuttle effect will result in rapid fading of the capacity and coulombic efficiency during the cycling process. Therefore, the development of a sulfur cathode that can "withhold" sulfur and reduce the shuttle effect, together with a high conductivity and sulfur loading is essential for the practical implementation of Li–S batteries [5-7].

To overcome the above-mentioned challenges in Li–S batteries, many strategies have been proposed [8-12]. For example, metal

oxides, such as TiO_2, ZnO, MnO_2, and SiO_2, were reported to provide active sites for strong S–metal bonding that have been reported to suppress the shuttle effect in polysulfides [13-16]. Moreover, designing metal oxides into various unique morphologies, e.g., hollow structures, can also provide a physical (or structural) confinement for sulfur [17]. Metal-oxide materials, however, have a major drawback, i.e., their electronic conductivity is very low [16,18]. To improve the conductivity of the sulfur cathode, it was typically composited with carbon materials [19-23]. Moreover, the high surface area of the carbon substrate was beneficial for a higher sulfur loading [24,25]. Since sulfur is the major active ingredient in the Li–S cathode, adding more non-sulfur components, such as metal oxides, in the cathode will result in a lower specific capacity.

Therefore, the present study will focus on the development of a pure carbon material for the Li–S cathode. It was believed that a carbon-based material network with specific morphology will not only allow for a high sulfur loading but will also provide both the chemical and physical restraints on the polysulfide shuttle effect. In the previous report, we synthesized porous 3D reduced graphene oxide (3D-RGO), showing a reversible capacity of 790 $mAh{\cdot}g^{-1}$ (at 0.2*C*) after 200 cycles [26]. It has been reported that three-dimensional carbon nanotubes/graphene–sulfur (3DCGS) is an excellent cathode template, revealing a final capacity of 975 $mAh{\cdot}g^{-1}$ after 200 cycles [24]. Carbon nanotubes (CNTs) can be used to adjust structure and density of the pores of the composite while improving the electrical conductivity. Following such a strategy, we developed a unique three-dimensional structured carbon-based composite material, referred to as 3D-RGO@MWCNT. Multiwalled carbon nanotubes (MWCNTs) form a lattice network for the composite that is supported by porous spherical reduced graphene oxide (RGO). Furthermore, the functional groups on RGO provide bonding sites for the active sulfur material. The 3D porous carbon structure enabled high sulfur loading and confined the sulfur within the 3D MWCNT network and the porous spherical RGO. Moreover, such a 3D structure can buffer the volume expansion/shrinkage of the sulfur cathode during charge and discharge cycles. Lastly, the electrochemical performance of the resulting S-3D-RGO@MWCNT cathode was evaluated in Li–S batteries.

Results and Discussion

The synthesis of the 3D-RGO@MWCNT composite is illustrated in Figure 1, highlighting the 3D porous RGO structure and the MWCNT lattice matrix. The SEM images confirmed that the precursor composite, RGO@MWCNT@SiO_2, contained 200–300 nm SiO_2 particles that were successfully encased by RGO and MWCNTs (Figure 2a). After HF etching, a 3D-RGO@MWCNT was obtained (Figure 2b,c). The porous spherical indents (ca. 200 nm) remained after the removal of SiO_2 (Figure 3a). Furthermore, after sulfur loading, both SEM (Figure 2d) and TEM (Figure 3b) images revealed that the structure remained in the resulting S-3D-RGO@MWCNT composite. The EDS elemental mapping validated the successful and uniform loading of sulfur into the composite (Figure 2e and Figure 3d). The 3D structure provided: i) higher usable surface area for a higher sulfur loading, ii) empty spaces between the pores and the lattice matrix to reduce the shuttle effect by acting as a lithium polysulfide reservoir, and iii) additional empty spaces to buffer the volume expansion/shrinkage in the charge and discharge processes enhancing the cycling performance of the battery. The electrochemical performance of the S-3D-RGO@MWCNT composite will be discussed later in the electrochemical analysis.

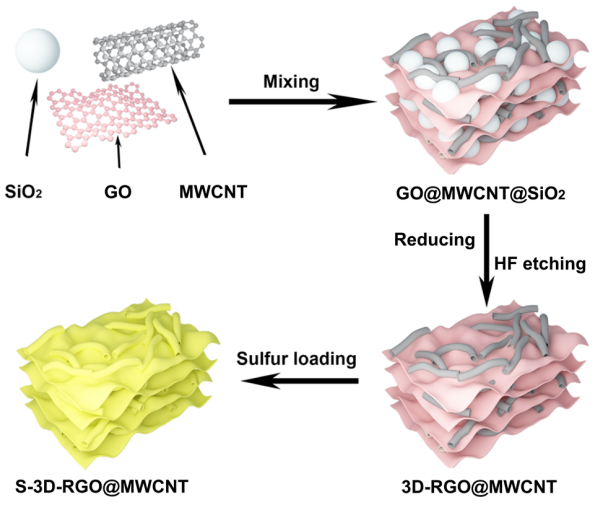

Figure 1: Synthesis of S-3D-RGO@MWCNT.

Figure 4a presents the XRD patterns for pure S, 3D-RGO@MWCNT and the S-3D-RGO@MWCNT composite. The XRD pattern of 3D-RGO@MWCNT exhibits two broad characteristic peaks of RGO at around 22° and 43°. Moreover, a diffraction peak around 26° for 3D-RGO@MWCNT corresponds to the MWCNTs. In the XRD pattern of S-3D-RGO@MWCNT, the major characteristic peaks of crystalline sulfur are observed, which further confirm the preservation of crystalline sulfur in the composite after adding sulfur. The Raman spectra demonstrates that the ratio I_D/I_G decreased from 1.12 in 3D-RGO@MWCNT to 1.04 in S-3D-RGO@MWCNT (Figure 4b), implying that the defects in 3D-RGO@MWCNT were filled or occupied by sulfur [3]. This is also supported by the C 1s XPS pattern of 3D-RGO@MWCNT, in which a C–S bonding state (285.4 eV) is observed (Figure 4d). The O–C=O (288.8 eV), C=O (287.2 eV) and C–O (286.3 eV) peaks in the C 1s pattern confirm the oxide nature of RGO sheets. In addi-

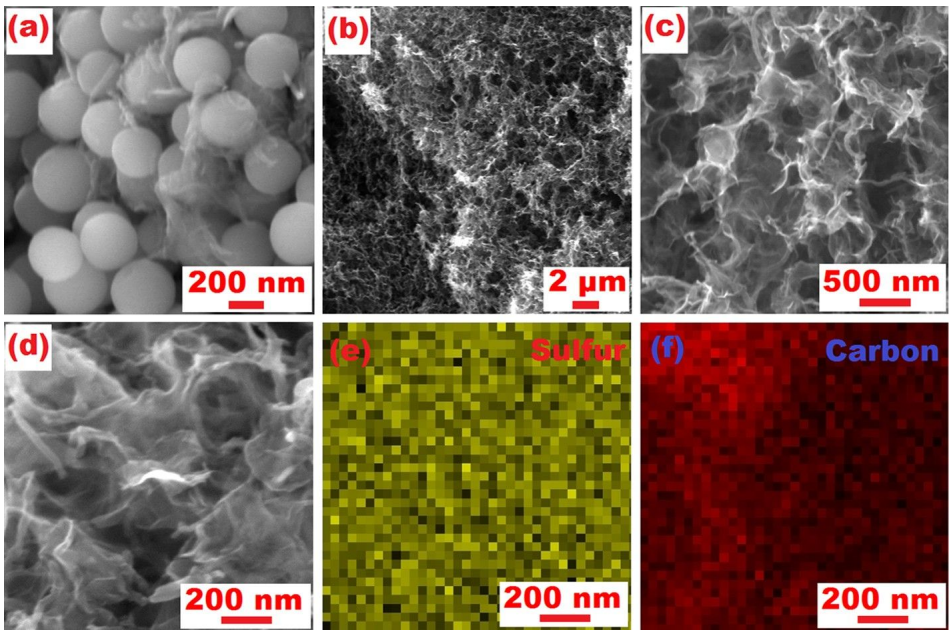

Figure 2: SEM images of (a) RGO@MWCNT@SiO_2, (b, c) 3D-RGO@MWCNT at different magnifications and (d) S-3D-RGO@MWCNT, and corresponding elemental maps of (e) sulfur and (f) carbon.

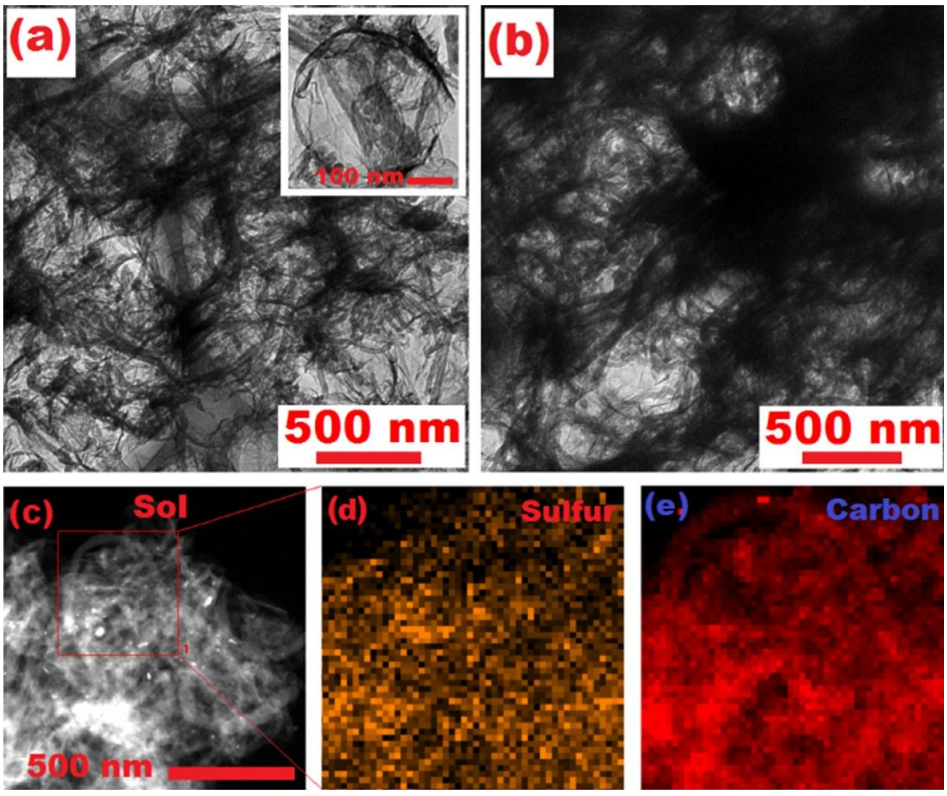

Figure 3: TEM images of (a) 3D-RGO@MWCNT with two different magnifications, (b) S-3D-RGO@MWCNT, (c–e) TEM mapping of (d) sulfur and (e) carbon corresponding to the area outlined by the red square in the TEM image of (c).

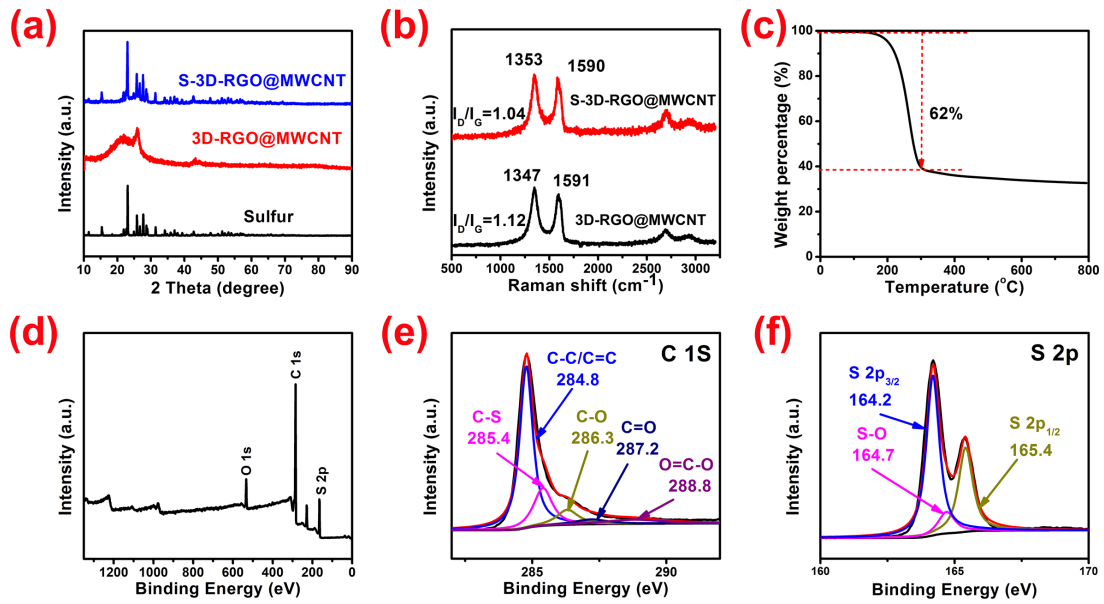

Figure 4: (a) XRD patterns of sulfur, 3D-RGO@MWCNT and S-3D-RGO@MWCNT; (b) Raman spectra of 3D-RGO@MWCNT and S-3D-RGO@MWCNT; (c) TGA of S-3D-RGO@MWCNT; (d) The XPS survey spectrum of S-3D-RGO@MWCNT composite; high-resolution XPS spectra of (e) C 1s, (f) S 2p.

tion to the C–S bonding, O-containing groups also help retain sulfur via S–O bonding, as revealed by the peak located at 164.7 eV in the S 2p spectrum (Figure 4e). The strong chemical bonding of C–S and S–O can immobilize sulfur and polysulfides within S-3D-RGO@MWCNT, reducing the shuttle effect and improving the cycling life of Li–S batteries. The thermogravimetric analysis (TGA) analysis (Figure 4f) shows that the S-3D-RGO@MWCNT composite exhibits a very high weight loss (62 wt %) between 30 and 300 °C, confirming that a great amount of sulfur can be stored in the structure.

Figure 5 displays the first four CV cycles of S-3D-RGO@MWCNT cathode at 0.1 $mV{\cdot}s^{-1}$. During the cathodic cycle, the peaks around 2.30 and 2.05 V correspond to the transformation of elemental sulfur to long-chain polysulfides (Li_2S_n, $n \geq 4$) and the reduction to short-chain polysulfides ($n < 4$), respectively. On the anodic side, the peak located at around 2.40 V corresponds to the oxidation of lithium polysulfides (Li_2S_n, $n < 4$) and Li_2S to Li_2S_8. It can be seen that during the cycling, the anodic peak shifts to a lower voltage, whereas the cathodic peaks remain almost unchanged. These results suggest the superior discharge stability of the S-3D-RGO@MWCNT cathode.

Figure 6a shows the charge and discharge voltage profiles of the S-3D-RGO@MWCNT cathode measured at 1*C*. The plateaus on the discharge (2.30 and 2.05 V) and charge (2.40 V) profiles are consistent with those observed in the CV cycles. The voltage plateaus were preserved after 200 cycles, confirming

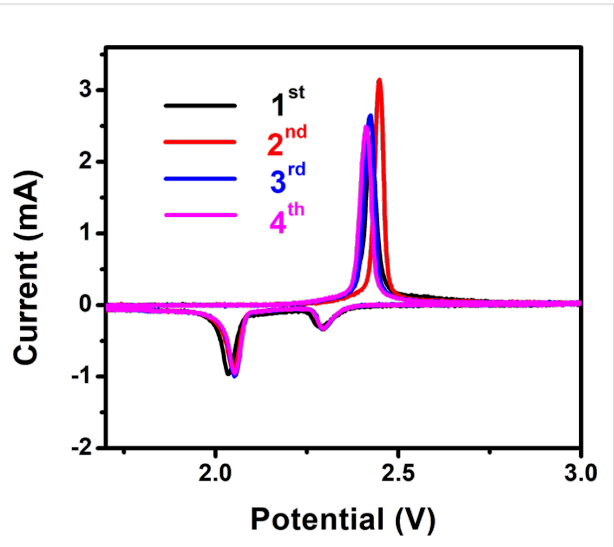

Figure 5: CV curves of the S-3D-RGO@MWCNT cathode at 0.1 $mV{\cdot}s^{-1}$ in the first four cycles.

the excellent electrochemical stability of sulfur in the 3D structure of S-3D-RGO@MWCNT. The S-3D-RGO@MWCNT cathode exhibits an initial specific discharge capacity of 1102 $mAh{\cdot}g^{-1}$ and a retained reversible capacity of 805 $mAh{\cdot}g^{-1}$ after 200 cycles. This result concurs with that observed in the cycling performance of the S-3D-RGO@MWCNT cathode (Figure 6b). The discharge/charge coulombic efficiency was maintained at approximately 98% after 200 cycles. The cycling performance of S-3D-RGO@MWCNT indicates

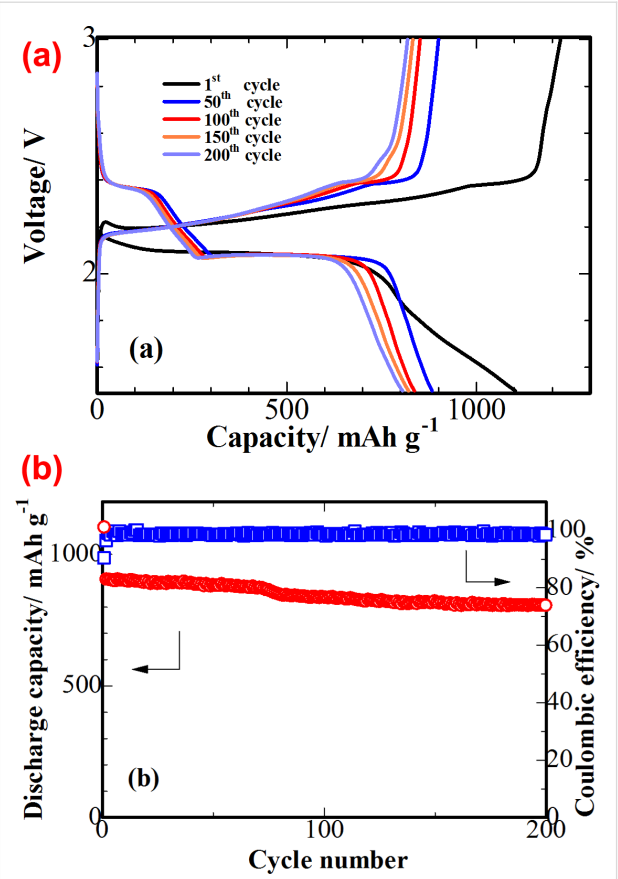

Figure 6: (a) CV measurement of the S-3D-RGO@MWCNT cathode (1st, 50th, 100th, 150th and 200th cycle) at 1*C*; (b) cycling performance of the S-3D-RGO@MWCNT cathode at 1*C* for 200 cycles.

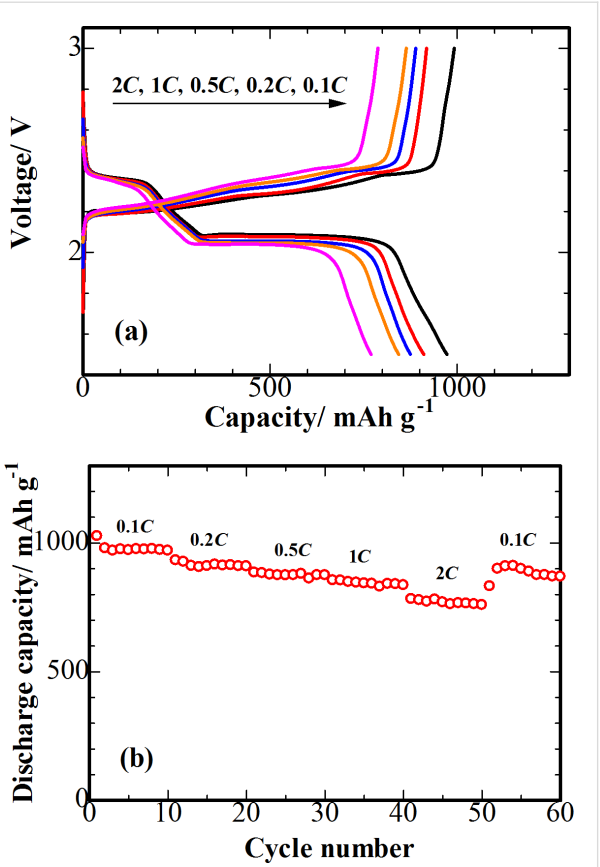

Figure 7: (a, b) Specific capacity and rate performance of S-3D-RGO@MWCNT cathode at different C-rate, ranging from 0.1*C* to 2*C*.

the efficient confinement of sulfur preventing the loss of active material through the shuttle effect.

Figure 7a reveals the charge–discharge voltage profiles of the batteries measured at various rates across the voltage range of 1.5 to 3.0 V. A two-plateau behaviour of the discharge profiles was observed at all current densities, which is consistent with the CV curves peaks (Figure 5). As the current increases from 0.1*C* to 2*C*, the polarization of the plateaus becomes higher, implying a slow decrease in the kinetic efficiency of the reaction process. This may have resulted from a weak influence of the current density on lower discharge plateau [27]. The rate capability of the S-3D-RGO@MWCNT cathode is examined in greater detail in Figure 7b. The impressive rate capability of the S-3D-RGO@MWCNT cathode was verified. Although a decrease of discharge capacity was observed when the current rate increases, a capacity of 770 mAh·g^{-1} was still obtained at 2*C*. When the current returned back to 0.1*C*, a capacity of 889 mAh·g^{-1} was preserved. These observations reveal that the 3D structure upheld the excellent rate performance of the S-3D-RGO@MWCNT cathode.

The changes in the conductivity during cycling a Li–S battery equipped with the S-3D-RGO@MWCNT cathode, were investigated using electrochemical impedance spectroscopy (EIS). Figure 8 presents the Nyquist plots for the Li–S cell assessed before cycling, and after the 1st and the 4th cycle. In the high-

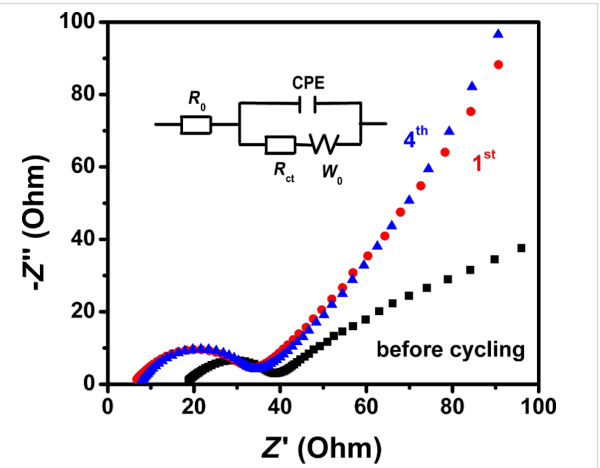

Figure 8: Nyquist plots of S-3D-RGO@MWCNT cathode and the equivalent circuit model (inset).

frequency region the x-intercept is attributed to the contact resistance (R_0), and the semicircle is attributed to the charge-transfer resistance (R_{ct}) at the electrode/electrolyte interface. Finally, the inclined slope in the low-frequency region is associated with the Warburg impedance (W) [28], which correlates to the Li^+ transportation process. Notably, there is a significant shift in the impedance curves before and after cycling. The primary reason for the decrease in the contact resistance after the initial cycle may be the redispersion of sulfur. The significant shift in the Warburg element indicates an improved Li^+ diffusivity [29]. R_{ct} increases slightly, then stabilizes after the initial cycle, which agrees with the cyclability data. The fitted values of R_0 and R_{ct} for the S-3D-RGO@MWCNT cathode are tabulated in Table 1. The impedance curves of the 1st and the 4th cycle are similar and become very stable, indicating the enhanced electrochemical performance of the S-3D-RGO@MWCNT cathode, which can be attributed to its 3D porous lattice matrix structure and the facilitation of rapid Li^+ diffusion.

Table 1: Impedance parameters of the S-3D-RGO@MWCNT cathode.

cycle number	R_0 (Ω)	R_{ct} (Ω)
before cycling	18.08	22.11
1st cycle	6.32	26.4
4th cycle	7.62	26.49

Conclusion

In summary, a unique S-3D-RGO@MWCNT composite, consisting of porous spherical RGO integrated within a MWCNT lattice matrix, was successfully synthesized. The as-prepared S-3D-RGO@MWCNT cathode exhibited a very good electrochemical performance and cycle stability. This can be attributed to i) the conductive network inherently found in the RGO sheets and MWCNTs, which ensured efficient charge transfer within the cathode, ii) the 3D porous spherical RGO possessing a high surface area and pore volume to accommodate a high sulfur content; and iii) the interconnected pores in the spherical RGO and the lattice matrix formed by MWCNTs, which act as polysulfide reservoirs to alleviate the shuttle effect, and thereby improving the cycling stability of the battery. Lastly, the interconnected pores ensured the rapid Li^+ diffusion during the discharge/charge process, and therefore were beneficial for reducing the internal resistance and improving the electrochemical properties.

Experimental

Synthesis of 3D-RGO@MWCNT composite

The synthesis of 3D-RGO@MWCNT composite consists of the following steps: i) the preparation of monodispersed SiO_2 spherical particles using Stober's method [30]; ii) the preparation of graphene oxide (GO) using Hummers method [31]; iii) the incorporation of MWCNTs; iv) the reduction of GO, and v) SiO_2 etching by HF. Firstly, monodispersed SiO_2 spheres with diameters of 200–300 nm were prepared. After washing and drying, the SiO_2 sphere particles was subsequently dispersed in DI water at a concentration of 50 $mg{\cdot}mL^{-1}$ (suspension A). Secondly, the GO from Hummer's method was dispersed into DI water at a concentration of 2 $mg{\cdot}mL^{-1}$, and subsequently mixed with a 2 $mg{\cdot}mL^{-1}$ MWCNT suspension at a mass ratio of 1:1. The as-prepared GO@MWCNT suspension was afterwards mixed with suspension A and volumetric ratio of 3:1 resulting in GO@MWCNT@SiO_2 (suspension B). After sonicated for 30 min, sodium erythorbate was added to suspension B and heated in an oil bath for 2 h. The sodium erythorbate was removed by washing with DI water, while SiO_2 was etched away by subsequent soaking in 10% HF for a week. Lastly, HF was also rinsed out with DI water and ethanol. After drying the compound at 60 °C for 12 h, the 3D-RGO@MWCNT composite was obtained.

Synthesis of S-3D-RGO@MWCNT composite and S-cathode

The as-prepared 3D-RGO@MWCNT was mixed with nano-sulfur at a mass ratio of 1:2. The resulting sample was heated at 155 °C for 12 h in a nitrogen-filled autoclave producing the S-3D-RGO@MWCNT composite. The cathode was fabricated by coating a slurry of S-3D-RGO@MWCNT, polyvinylidene fluoride (PVDF) and carbon black (mass ratio 8:1:1) on a carbon-coated Al foil.

Materials characterization

X-ray diffraction (XRD) patterns of the as-prepared 3D-RGO@MWCNT composite were obtained using XRD (SmartLab, Rigaku Corporation) with Cu Ka radiation. X-ray photoelectron spectroscopy (XPS, Shimadzy Axis Ultra) was applied to investigate the chemical valence states and compositions of the sample. Scanning electron microscopy (SEM, Hitachi S4800) and high-resolution transmission electron microscopy (HRTEM, JEOL JEM-2100F) images were used for investigating surface topology. The content of sulfur in the S-3D-RGO@MWCNT composite was confirmed using thermogravimetric analysis (TGA, SHIMADZU DTG-60) in Ar atmosphere. Raman spectra were recorded on Raman spectrometer (Raman, Renishaw) using 532 nm radiation.

Electrochemical measurements

CR2025 coin batteries were assembled using S-3D-RGO@MWCNT as the cathode, 1 M lithium bistrifluoromethanesulfonimide and 0.1 M $LiNO_3$ in a mixed solution of DME-DOL (1:1 by volume) as electrolyte, a Li foil as anode,

and a Celgard 2300 membrane as separator. The cycling performances of the Li–S battery was investigated using a battery testing station (Neware, Shenzhen) in potential range of 1.5–3.0 V. The electrochemical workstation (Princeton, VersaSTAT 4) was used to evaluate cyclic voltammetry (CV) also in a potential range of 1.5–3.0 V. Electrochemical impedance spectroscopy (EIS) was carried out in the frequency range from 10^{-2} to 10^{5} Hz.

Supporting Information

Supporting Information File 1

Additional experimental data.
[https://www.beilstein-journals.org/bjnano/content/supplementary/2190-4286-10-52-S1.pdf]

Acknowledgements

This work was supported by the Program for the Outstanding Young Talents of Hebei Province; the Science Research Foundation for Selected Overseas Chinese Scholars, Ministry of Human Resources and Social Security of China [grant number CG2015003002]; Cultivation project of National Engineering Technology Center [Grant No. 2017B090903008].

References

1. He, J.; Chen, Y.; Lv, W.; Wen, K.; Li, P.; Wang, Z.; Zhang, W.; Qin, W.; He, W. *ACS Energy Lett.* **2016,** *1,* 16–20. doi:10.1021/acsenergylett.6b00015
2. Mahmood, N.; Hou, Y. *Adv. Sci.* **2014,** *1,* 1400012–1400031. doi:10.1002/advs.201400012
3. Zheng, S.; Wen, Y.; Zhu, Y.; Han, Z.; Wang, J.; Yang, J.; Wang, C. *Adv. Energy Mater.* **2014,** *4,* 1400482–1400490. doi:10.1002/aenm.201400482
4. He, J.; Chen, Y.; Lv, W.; Wen, K.; Li, P.; Qi, F.; Wang, Z.; Zhang, W.; Li, Y.; Qin, W.; He, W. *J. Power Sources* **2016,** *327,* 474–480. doi:10.1016/j.jpowsour.2016.07.088
5. Barchasz, C.; Molton, F.; Duboc, C.; Leprêtre, J.-C.; Patoux, S.; Alloin, F. *Anal. Chem. (Washington, DC, U. S.)* **2012,** *84,* 3973–3980. doi:10.1021/ac2032244
6. Mikhaylik, Y. V.; Akridge, J. R. *J. Electrochem. Soc.* **2003,** *150,* A306–A311. doi:10.1149/1.1545452
7. Manthiram, A.; Fu, Y.; Chung, S.-H.; Zu, C.; Su, Y.-S. *Chem. Rev.* **2014,** *114,* 11751–11787. doi:10.1021/cr500062v
8. Guo, Z.; Nie, H.; Yang, Z.; Hua, W.; Ruan, C.; Chan, D.; Ge, M.; Chen, X.; Huang, S. *Adv. Sci.* **2018,** *5,* 1800026–1800033. doi:10.1002/advs.201800026
9. Rehman, S.; Gu, X.; Khan, K.; Mahmood, N.; Yang, W.; Huang, X.; Guo, S.; Hou, Y. *Adv. Energy Mater.* **2016,** *6,* 1502518–1502525. doi:10.1002/aenm.201502518
10. He, J.; Lv, W.; Chen, Y.; Xiong, J.; Wen, K.; Xu, C.; Zhang, W.; Li, Y.; Qin, W.; He, W. *J. Mater. Chem. A* **2018,** *6,* 10466–10473. doi:10.1039/c8ta02434k
11. Mahmood, N.; Zhang, C.; Yin, H.; Hou, Y. *J. Mater. Chem. A* **2014,** *2,* 15–32. doi:10.1039/c3ta13033a
12. He, J.; Chen, Y.; Manthiram, A. *Energy Environ. Sci.* **2018,** *11,* 2560–2568. doi:10.1039/c8ee00893k
13. Huang, J.-Q.; Wang, Z.; Xu, Z.-L.; Chong, W. G.; Qin, X.; Wang, X.; Kim, J.-K. *ACS Appl. Mater. Interfaces* **2016,** *8,* 28663–28670. doi:10.1021/acsami.6b10032
14. Gu, X.; Tong, C.-j.; Wen, B.; Liu, L.-m.; Lai, C.; Zhang, S. *Electrochim. Acta* **2016,** *196,* 369–376. doi:10.1016/j.electacta.2016.03.018
15. Wang, S.; Yang, Z.; Zhang, H.; Tan, H.; Yu, J.; Wu, J. *Electrochim. Acta* **2013,** *106,* 307–311. doi:10.1016/j.electacta.2013.05.083
16. Qu, Q.; Gao, T.; Zheng, H.; Wang, Y.; Li, X.; Li, X.; Chen, J.; Han, Y.; Shao, J.; Zheng, H. *Adv. Mater. Interfaces* **2015,** *2,* 1500048–1500054. doi:10.1002/admi.201500048
17. Gu, X.; Wang, Y.; Lai, C.; Qiu, J.; Li, S.; Hou, Y.; Martens, W.; Mahmood, N.; Zhang, S. *Nano Res.* **2015,** *8,* 129–139. doi:10.1007/s12274-014-0601-1
18. Li, Z.; Zhang, J.; Lou, X. W. D. *Angew. Chem., Int. Ed.* **2015,** *54,* 12886–12890. doi:10.1002/anie.201506972
19. Gnana kumar, G.; Chung, S.-H.; Raj kumar, T.; Manthiram, A. *ACS Appl. Mater. Interfaces* **2018,** *10,* 20627–20634. doi:10.1021/acsami.8b06054
20. He, J.; Chen, Y.; Lv, W.; Wen, K.; Xu, C.; Zhang, W.; Li, Y.; Qin, W.; He, W. *ACS Nano* **2016,** *10,* 10981–10987. doi:10.1021/acsnano.6b05696
21. He, J.; Chen, Y.; Manthiram, A. *Adv. Mater. (Weinheim, Ger.)* **2017,** *29,* 1702707. doi:10.1002/adma.201702707
22. He, J.; Chen, Y.; Manthiram, A. *iScience* **2018,** *4,* 36–43. doi:10.1016/j.isci.2018.05.005
23. Zhou, W.; Wang, C.; Zhang, Q.; Abruña, H. D.; He, Y.; Wang, J.; Mao, S. X.; Xiao, X. *Adv. Energy Mater.* **2015,** *5,* 1401752–1401759. doi:10.1002/aenm.201401752
24. He, J.; Chen, Y.; Li, P.; Fu, F.; Wang, Z.; Zhang, W. *J. Mater. Chem. A* **2015,** *3,* 18605–18610. doi:10.1039/c5ta04445f
25. He, J.; Chen, Y.; Lv, W.; Wen, K.; Xu, C.; Zhang, W.; Qin, W.; He, W. *ACS Energy Lett.* **2016,** *1,* 820–826. doi:10.1021/acsenergylett.6b00272
26. Zhang, Y.; Sun, L.; Li, H.; Tan, T.; Li, J. *J. Alloys Compd.* **2018,** *739,* 290–297. doi:10.1016/j.jallcom.2017.12.294
27. Qian, W.; Gao, Q.; Zhang, H.; Tian, W.; Li, Z.; Tan, Y. *Electrochim. Acta* **2017,** *235,* 32–41. doi:10.1016/j.electacta.2017.03.063
28. Martha, S. K.; Markovsky, B.; Grinblat, J.; Gofer, Y.; Haik, O.; Zinigrad, E.; Aurbach, D.; Drezen, T.; Wang, D.; Deghenghi, G.; Exnar, I. *J. Electrochem. Soc.* **2009,** *156,* A541–A552. doi:10.1149/1.3125765
29. Zhang, Y.; Zhao, Y.; Bakenov, Z.; Tuiyebayeva, M.; Konarov, A.; Chen, P. *Electrochim. Acta* **2014,** *143,* 49–55. doi:10.1016/j.electacta.2014.07.148
30. Philipse, A. P. *J. Mater. Sci. Lett.* **1989,** *8,* 1371–1373. doi:10.1007/bf00720190
31. Wang, X.; Lu, C.; Peng, H.; Zhang, X.; Wang, Z.; Wang, G. *J. Power Sources* **2016,** *324,* 188–198. doi:10.1016/j.jpowsour.2016.05.085

BEILSTEIN JOURNAL OF NANOTECHNOLOGY

Ultrasonication-assisted synthesis of $CsPbBr_3$ and Cs_4PbBr_6 perovskite nanocrystals and their reversible transformation

Longshi Rao[1,2], Xinrui Ding*[1], Xuewei Du[1], Guanwei Liang[1], Yong Tang[1], Kairui Tang[3] and Jin Z. Zhang[2]

Full Research Paper

Open Access

Address:
[1]Engineering Research Centre of Green Manufacturing for Energy-Saving and New-Energy Technology, School of Mechanical and Automotive Engineering, South China University of Technology, Guangzhou 510640, China, [2]Department of Chemistry and Biochemistry, University of California, Santa Cruz, CA 95064, USA and [3]Mechanical Engineering, Pennsylvania State University, Harrisburg, PA 17057, USA

Email:
Xinrui Ding* - dingxr@scut.edu.cn

* Corresponding author

Keywords:
$CsPbBr_3$ PNCs; Cs_4PbBr_6 PNCs; polar-solvent-free; reversible transformation; ultrasonication

Beilstein J. Nanotechnol. **2019,** *10,* 666–676.
doi:10.3762/bjnano.10.66

Received: 31 October 2018
Accepted: 13 February 2019
Published: 06 March 2019

This article is part of the thematic issue "Low-dimensional materials and systems".

Guest Editor: S. Walia

Abstract

We demonstrate an ultrasonication-assisted synthesis without polar solvent of $CsPbBr_3$ and Cs_4PbBr_6 perovskite nanocrystals (PNCs) and their reversible transformation. The as-prepared $CsPbBr_3$ PNCs and Cs_4PbBr_6 PNCs exhibit different optical properties that depend on their morphology, size, and structure. The photoluminescence (PL) emission and quantum yield (QY) of the $CsPbBr_3$ PNCs can be tuned by changing the ultrasound power, radiation time, and the height of the vibrating spear. The optimized $CsPbBr_3$ PNCs show a good stability and high PL QY of up to 85%. In addition, the phase transformation between $CsPbBr_3$ PNCs and Cs_4PbBr_6 PNCs can be obtained through varying the amount of oleylamine (OAm) and water. The mechanism of this transformation between the $CsPbBr_3$ PNCs and Cs_4PbBr_6 PNCs and their morphology change are studied, involving ions equilibrium, anisotropic growth kinetics, and CsBr-stripping process.

Introduction

Metal halide perovskite nanocrystals (PNCs) are promising candidates for application in the fields of light-emitting diodes (LEDs) [1,2], high-efficiency solar cells [3], low-threshold lasers [4], and photodetectors [5]. Compared to traditional semiconductors, colloidal PNCs demonstrate excellent properites, such as tunable photoluminescence (PL) throughout the visible spectrum, super high PL quantum yield (QY), low trap-state density, and narrow emission linewidth [6-8]. The crystal structure of $CsPbX_3$ ($X = Cl^-$, Br^-, I^-) PNCs consists of a 12-fold coordinated network created by $[PbX_6]^{4-}$ octahedra in which the Cs^+ ions reside in the periphery of this network [9,10]. These PNCs are prone to structural instabilities and phase trans-

formations involving ion migration and interface hydration [11]. However, this phase and structure versatility has become the great advantage of PNCs in their technical applications, especially in optoelectronics. Although the focus has been on the $CsPbX_3$ structure, researchers start to turn their attention on synthesizing new perovskite materials, such as Cs_4PbX_6 PNCs. Under Cs-rich or Pb-poor synthesis conditions, zero-dimensional (0D) structures of Cs_4PbX_6 NCs can be achieved, demonstrating a crystalline structure with well-separated octahedra $[PbBr_6]^{4-}$ isolated by Cs^+ ions [12,13]. This specific structure is expected to result in strong quantum confinement and electron–phonon interactions. This inspires researchers to further explore this structure. The key to this exploration is the development of various approaches to the synthesis of high-quality PNCs.

Since, in 2015, Kovalenko and co-workers synthesized $CsPbX_3$ PNCs by using a hot-injection method, great successes in the controlled synthesis and application of the $CsPbX_3$ PNCs have been achieved in a very short time [14]. To date, the most commonly adopted approach for synthesizing highly efficient PNCs are solution-based procedures, including hot injection, solvothermal synthesis, microreactor synthesis, and room-temperature (RT) ligand-mediated reprecipitation, in which shape and size are tuned through the control of temperature, reaction time, and composition of the precursors [15-17]. Chen et al. demonstrated a facile solvothermal method for preparing $CsPbX_3$ PNCs with adjustable optical properties [18]. Additionally, Li's group reported a poly(lactic acid)-assisted anion-exchange method using a microreactor for tuning the emission spectra of $CsPbX_3$ PNCs from green to near-ultraviolet, which might be applicable for mass production [19]. Besides, great efforts have been made to prepare PNCs through the chemical transformation of pre-synthesized PNCs [20-22]. For example, Wu et al. reported a CsX-stripping method that enabled the transformation of nonluminescent Cs_4PbX_6 PNCs to highly luminescent $CsPbX_3$ PNCs through an interfacial reaction [20]. They focus on investigating the water-triggered transformation process between Cs_4PbX_6 PNCs and $CsPbX_3$ PNCs in a different phase. Similar methods were applied to explore new perovskite materials such as Cs_4PbBr_6. Zhai et al. showed a simple solvothermal approach for synthesizing $CsPbBr_3$ nanoplatelets and their phase transformation to Cs_4PbBr_6 PNCs [23]. Liu and co-workers also demonstrated that $CsPbBr_3$ PNCs were successfully converted to Cs_4PbBr_6 PNCs through a "ligand-mediated transformation" method with the addition of oleylamine (OAm) [24]. Udayabhaskararao's group showed the reversible transformation from $CsPbX_3$ to Cs_4PbX_6 through the ratio of oleic acid (OA) to OAm in a Brønsted acid–base equilibrium [25]. Despite the progress made in obtaining PNCs, in general, inert conditions, high temperature and pre-synthesized precursors are required for hot injection. In addition, RT methods were mostly carried out by mixing a polar solvent with a large amount of nonpolar solvent. Since PNCs are reported to be very sensitive to polar solvents, these methods result in the inevitable degradation of PNCs, especially for iodine-based PNCs [26-28]. Therefore, in order to obtain PNCs with high PL QY and stability, it is crucial to develop synthesis methods free of polar-solvents.

To date, some attempts have been made to synthesize PNCs without the use of polar solvents. Tong's group demonstrated the single-step and polar-solvent-free synthesis of $CsPbX_3$ PNCs with tunable halide ion composition and thickness through the direct ultrasonication of precursors [29]. Whereas this method has been reported for synthesizing PNCs without using polar solvents, it does not allow for a control over dimensionality and phase transformation. We recently reported a fast, low-cost, environmentally friendly, and polar-solvent-free strategy for synthesizing all-inorganic $CsPbBr_3$ NCs with tunable shape and size [30]. During this process, we found that a great excess of OAm results in the formation of a derivative of $CsPbBr_3$ NCs, i.e., Cs_4PbBr_6. However, the underlying transformation mechanism has not been fully understood. Following this, we set out here to expand this study to control the phase transformation. $CsPbBr_3$ PNCs as precursor were obtained by modifying the approach initially presented by Tong, which was recently elaborated by our group [29,30]. We demonstrated in detail how, by tuning the ultrasound power and time, the PL emission of $CsPbBr_3$ PNCs can be precisely controlled. Benefitting from this knowledge, here we attained $CsPbBr_3$ PNCs with a high PL QY (ca. 85%) by optimizing the immersion height of the vibrating spear in the liquid. In addition, the phase transformation of $CsPbBr_3$ PNCs to Cs_4PbBr_6 PNCs was achieved in this study by direct ultrasonication of solid powders or by adding OAm in the solution of pre-synthesized $CsPbBr_3$ PNCs. Finally, inspired by the method proposed by Wu et al. [20], a successful structure conversion from Cs_4PbBr_6 PNCs to $CsPbBr_3$ PNCs was obtained here by simply adding different amounts of water into pre-synthesized Cs_4PbBr_6 PNCs. The mechanism behind phase transformation and morphology change were investigated by using a combination of spectroscopy and microscopy techniques.

Results and Discussion

Characterization of $CsPbBr_3$ PNCs

The typical procedure for synthesizing $CsPbBr_3$ and Cs_4PbBr_6 PNCs and for reversibly transforming them is illustrated in Scheme 1. Cs_2CO_3 and $PbBr_2$ were loaded into the liquid paraffin/OAm/OA solution. Then, the precursors were processed by tip-sonication and purified via centrifuging in the presence of methyl acetate as precipitation agent. Subsequently,

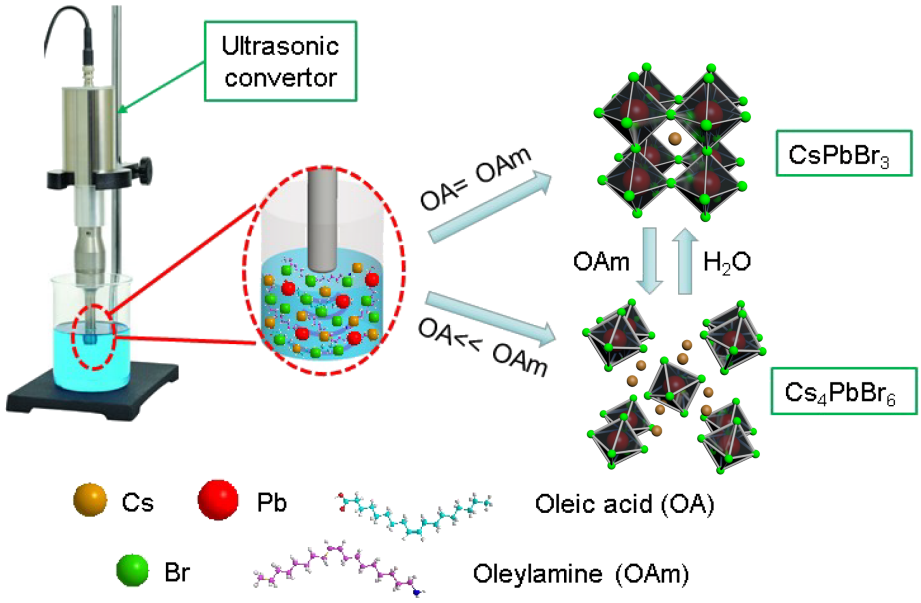

Scheme 1: Illustration of synthesizing $CsPbBr_3$ and Cs_4PbBr_6 PNCs without polar solvent using ultrasonication assistance, and their reversible transformation by adding OAm and water.

the sediment was redispersed in toluene for further characterization. The reversible transformation between Cs_4PbBr_6 PNCs and $CsPbBr_3$ PNCs was achieved by changing the amounts of OAm and water. Detailed synthesis conditions are given in the Experimental section.

The crystal structure and morphology of the as-prepared samples were determined by XRD and TEM. As shown in Figure 1a, the diffraction pattern clearly indicates that orthorhombic $CsPbBr_3$ PNCs (PDF card #18-0364) were formed. No other phases were observed, suggesting the high

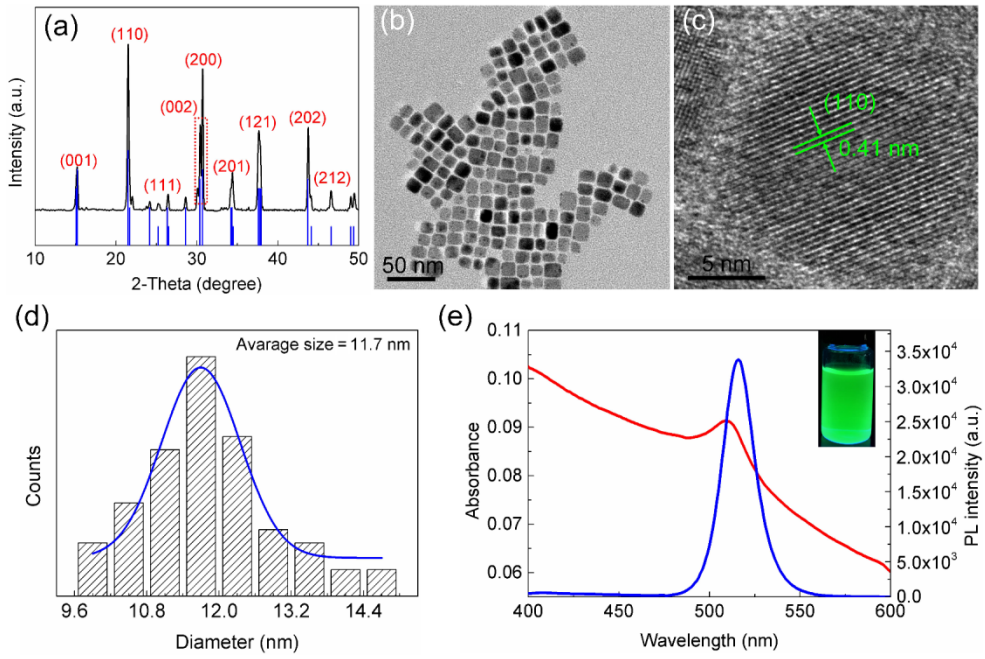

Figure 1: Characterization of the $CsPbBr_3$ PNCs prepared using ultrasonication assistance. (a) XRD patterns. Black line and blue line represent experimental data and standard reference, respectively. (b) TEM image. (c) HRTEM image. (d) Size distribution. (e) UV–vis absorption spectrum (red line) and PL emission spectrum (blue line). Inset is a photograph under 365 nm UV irradiation.

purity of the samples. The TEM image shown in Figure 1b demonstrates that the $CsPbBr_3$ PNCs have a regular square morphology. HRTEM was further carried out to measure the lattice spacing of the product. Figure 1c shows a lattice spacing distance of ca. 0.41 nm for the $CsPbBr_3$ PNCs. The size distribution shown in Figure 1d indicates that the well-dispersed $CsPbBr_3$ PNCs have an average diameter of ca. 11.7 nm. To explore the optical properties of colloidal $CsPbBr_3$ PNCs, UV–vis absorption spectra and PL emission spectra were recorded. As shown in Figure 1e, the first excitonic absorption peak was located at 510 nm and the strong PL emission band centered at 516 nm was observed with a narrow full width at half maximum (FWHM) of 18 nm, indicating a narrow polydispersity of the PNCs obtained by this method. The PL QY of the as-prepared $CsPbBr_3$ PNCs measured to be ca. 85% (Rhodamin 101 as reference, PL QY is 100%) following a previously published report [31]. In addition, Supporting Information File 1, Figure S1 clearly demonstrates the improved photostability and chemical stability of $CsPbBr_3$ PNCs.

Effect of synthesis conditions

Our previous study has shown that ultrasound power and radiation time have a great influence on the optical properties of the $CsPbBr_3$ PNCs [30]. In this study, we found that the immersion height of the vibrating spear in the solvent influences the product properties (the effect will be discussed later). We divided the height of liquid into five equal parts, i.e., from the bottom to the surface of the liquid, 1/5, 2/5, 3/5, 4/5, and 5/5.

We first investigated the effect of ultrasound power on the optical properties of $CsPbBr_3$ PNCs. To avoid breaking the bottle, the immersion height of the vibrating spear and radiation time are 4/5 and 30 min, respectively. Figure 2a shows the change of UV–vis absorption spectra and PL spectra of the $CsPbBr_3$ PNCs that were synthesized at 90, 120, 150, 180, and 210 W of ultrasound power, while keeping other synthesis conditions unchanged. If the ultrasound power is less than 90 W, there is no UV–vis absorption peak and a very weak PL intensity, implying that almost no PNCs formed. However, the first characteristic absorption peak changes to red slowly with an increase of ultrasound power, corresponding to the red-shift of the PL emission peak, which is similar to the findings we recently reported [30]. While higher ultrasound power supports faster dissolution, it has also a strong impact on the homogeneity of the PNCs. For example, when the ultrasound power is 210 W, the UV–vis absorption at long wavelengths is very high, indicating large crystals were formed with strong scattering. Therefore, it is necessary to choose the appropriate ultra-

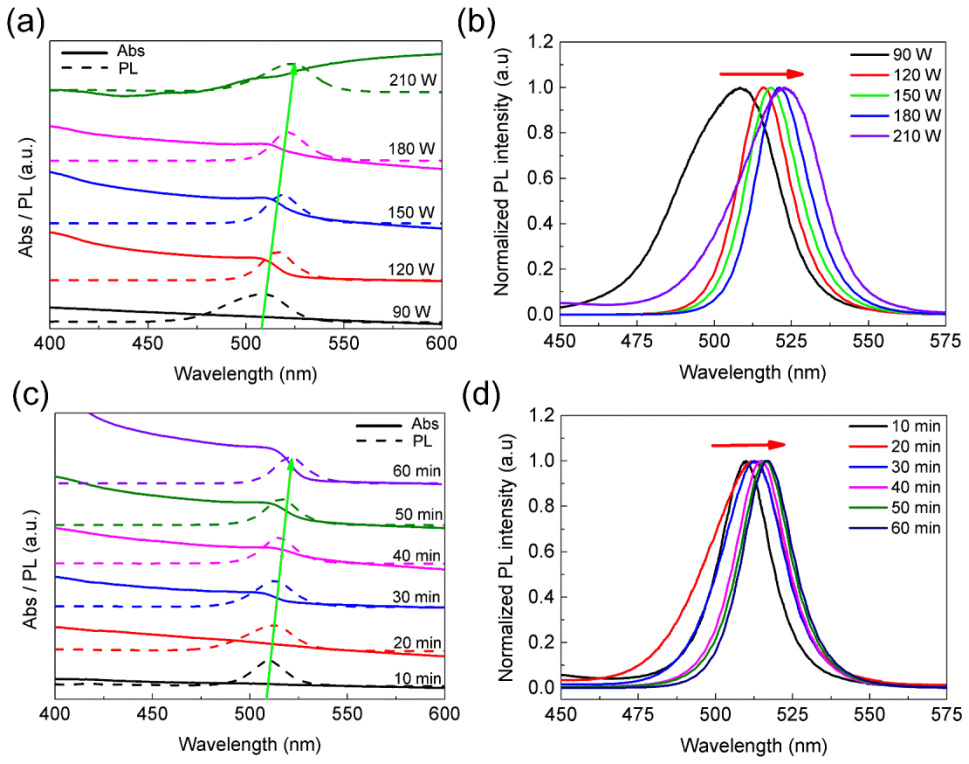

Figure 2: (a) UV–vis absorption spectra and PL emission spectra, and (b) normalized PL emission spectra of the $CsPbBr_3$ PNCs that were synthesized at 90, 120, 150, 180, and 210 W of ultrasound power, respectively. (c) UV–vis absorption spectra and PL spectra, and (d) normalized PL emission spectra of $CsPbBr_3$ PNCs that were synthesized at 10, 20, 30, 40, 50, and 60 min of radiation time.

sound power. The normalized PL emission peaks in Figure 2b shift from 505 to 523 nm, indicating that our approach can precisely modulate PL emission.

Furthermore, we studied the influence of radiation time on the $CsPbBr_3$ PNCs. The immersion height of the vibrating spear and ultrasound power are 4/5 and 120 W, respectively. As shown in Figure 2c and Figure 2d, when the radiation time is increased, both the UV–vis absorption and PL spectra are redshifted, we suggest that it is the size effect that is dominant over ionic bond strength in causing the spectral shift, which is different from the effects of radiation time that we observed recently [30]. This phenomenon indicates that the immersion height of the vibrating spear would affect PNCs properties.

The effects of the immersion height of the vibrating spear in the liquid were also investigated. The total liquid height was divided into five equal parts as shown in the inset of Figure 3a. Figure 3a shows the PL intensity (UV–vis absorbance at 400 nm) of four samples that were synthesized by setting the immersion height of the vibrating spear to 1/5, 2/5, 3/5, and 4/5 of the total liquid height. As the immersion height increases, the corresponding PL intensity obviously decreases. In addition, the PL QY in Figure 3b further confirmed that the $CsPbBr_3$ PNCs exhibit the best performance when the immersion height of the vibrating spear is set at 1/5 of the total liquid height. Ultrasonication results in a combination of thermal, vibrational, and acoustic cavitation, i.e., the formation, growth, and implosive collapse of bubbles in liquids [32-34]. In the center of these bubbles, extremely high temperatures of about 5000 K and high pressures of about 20 MPa were achieved by high-intensity ultrasound [32], enabling a quick decomposition of the particles. The lower the immersion height of vibrating spear, the higher temperature and pressure is achieved, which, as a result, benefits the formation of PNCs.

Characterization of Cs_4PbBr_6 PNCs

The current approach can be further used for controlling phase and structure transformations in the PNCs. The method introduced in this work enables the successful synthesis of rhombohedral Cs_4PbBr_6 PNCs via changing the amount of OAm. The amount of OAm was increased to 3.0 mL, while all other conditions were kept the same. The phase of the obtained product was characterized by XRD, as shown in Figure 4a. The XRD pattern with peaks at 2θ = 12.9, 20.1, 22.4, 25.6, 28.6 30.3, 30.9, 34.1, 39.3, and 45.7° correspond to diffractions from (110), (113), (300), (024), (214), (223), (006), (134), (330), and (600) crystal planes of rhombohedral Cs_4PbBr_6 (PDF card #73-2478) [13]. Meanwhile, weak peaks of $CsPbBr_3$ were observed, indicating both $CsPbBr_3$ and Cs_4PbBr_6 PNCs were formed during the process.

TEM was further performed to characterize the morphology of as-prepared PNCs. Figure 4b shows the formation of Cs_4PbBr_6 PNCs with hexagonal crystal structure and confirms the existence of square-shaped $CsPbBr_3$ PNCs. Additionally, Figure 4c shows that the small black spots (green arrows) existing on the surface of the Cs_4PbBr_6 PNCs are metallic lead nanoparticles that have been reported before [23,35,36]. The HRTEM image shown in Figure 4d demonstrates an interplanar spacing of 0.39 nm, corresponding to the (300) crystal plane of bulk Cs_4PbBr_6, which is also consistent with the PDF card #73-2478. The size of the Cs_4PbBr_6 PNCs is defined here as the longest distance between hexagonal corners, which is ca. 65 nm for the example shown. Besides, the SEM image illustrates that Cs_4PbBr_6 particles are hexagonal prisms with a thickness of ca. 15 nm, as presented in Figure 4d inset and Supporting Information File 1, Figure S2.

The absorption spectrum of the Cs_4PbBr_6 PNCs is very different from that of the $CsPbBr_3$ PNCs, as shown in Figure 4e. The

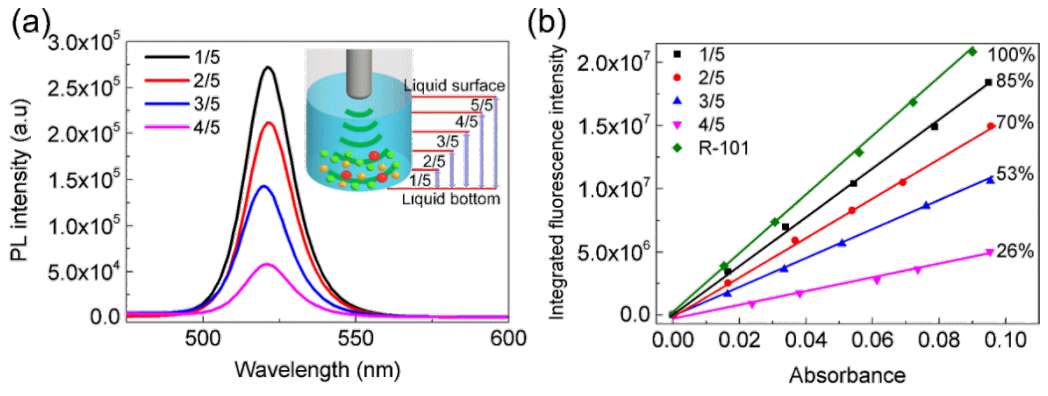

Figure 3: (a) PL emission spectra and (b) PL QY of the $CsPbBr_3$ PNCs that were synthesized at 1/5, 2/5, 3/5, and 4/5 of total liquid height, respectively. 1/5, 2/5, 3/5, 4/5, and 5/5 in (a) inset is one of the five equal parts from liquid bottom to liquid surface. R-101 in (b) is rhodamine 101 (PL QY, 100%) as the standard sample to test PL QY of PNCs.

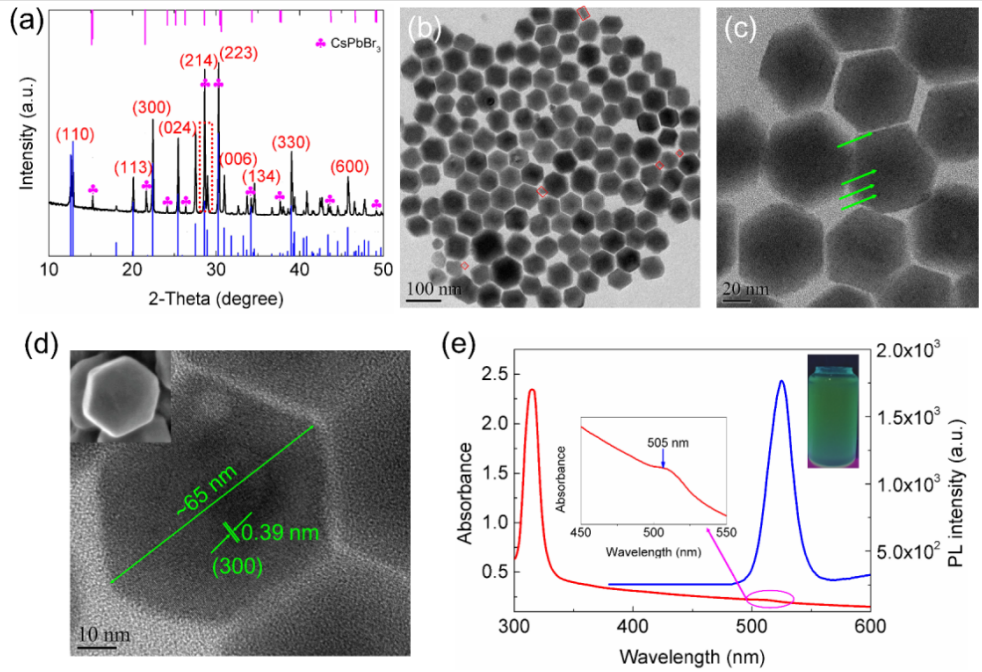

Figure 4: Characterization of the Cs_4PbBr_6 PNCs synthesized using ultrasonication. (a) XRD patterns. Black line represents experimental data; blue line (below) and pink line (upper) represent standard reference bulk $CsPbBr_3$ and Cs_4PbBr_6, respectively. (b) TEM image, red squares represent $CsPbBr_3$ PNCs. (c),(d) HRTEM images, green arrows in (c) represent metallic lead nanoparticles and inset in (d) is SEM image of Cs_4PbBr_6 PNCs, respectively. (e) UV–vis absorption spectra (red line) and PL emission spectra (blue line). Insets are high resolution absorption spectrum and representative digital photograph.

first excitonic absorption has been shifted from 510 nm for $CsPbBr_3$ PNCs to 315 nm for Cs_4PbBr_6 PNCs. This absorption feature is consistent with that of bulk Cs_4PbBr_6, which was proven to be the localized $6s_{1/2}$–$6p_{1/2}$ transition within the isolated $[PbBr_6]^{4-}$ octahedra separated by Cs^+ ions [24]. A weak characteristic UV–vis absorption and a PL emission peak for $CsPbBr_3$ PNCs at 505 nm and 520 nm, respectively, further confirmed the existence $CsPbBr_3$ PNCs.

In Cs_4PbBr_6 PNCs, typically a green emission arises either from defects or from impurities or from a combination of both [37,38]. Herein, the purified Cs_4PbBr_6 PNCs did not demonstrate PL emission over the whole visible spectrum due to their wide bandgap ($E_g(Cs_4PbBr_6)$ = 3.94 eV), while the observed weak PL emission results from a small portion of $CsPbBr_3$ impurities in the Cs_4PbBr_6 PNCs (see Figure 3a–e). Since $CsPbBr_3$ PNCs exhibit a high PL QY, the green PL emission is ascribed to minor $CsPbBr_3$ impurities in the samples. This result coincides with previous works on Cs_4PbBr_6 PNCs that show a strong green emission at about 500 nm and confirmed that these green PL emissions originate from $CsPbBr_3$ PNC impurities [10,39,40].

Furthermore, the effect of the amount of OAm on the phase transformation was investigated. As shown in Figure 5a, when the amount of OAm ranged from 0.5 to 3.0 mL, the first characteristic absorption peak (ca. 510 nm) and the PL emission intensity of $CsPbBr_3$ PNCs slowly decrease, while new strong absorption features in the UV region (ca. 315 nm) emerge, which have been confirmed to result from the formation of Cs_4PbBr_6 PNCs [25]. When adding equal amounts of OAm and OA, there are no other peaks in the UV–vis absorption spectra except for that at ca. 510 nm. With increasing amount of OAm, the absorption intensity at ca. 510 nm decreases. Simultaneously, the absorption intensity at ca. 315 nm increases, while the PL intensity decreases (Figure 5b), and is blue-shifted followed by an increase in the FWHM of the PL peak. All these effects suggest the decomposition of the $CsPbBr_3$ PNCs. Based on this process it can be concluded that the excess amount of OAm triggers the transformation between $CsPbBr_3$ PNCs and Cs_4PbBr_6 PNCs.

The morphology change from $CsPbBr_3$ PNCs to Cs_4PbBr_6 PNCs was further confirmed by using TEM. When the amount of OAm is between 0.5 and 1.5 mL, the morphology of PNCs gradually becomes irregular and some hexagonal shapes emerge (Figure 5c–e). As the amount of OAm increase to 3.0 mL, Cs_4PbBr_6 PNCs with homogeneous hexagonal shape can be achieved (Figure 5h). These results suggest that the growth kinetics of this process can be controlled by adding OAm, and the PNCs are prone to crystallize in the Cs-rich Cs_4PbBr_6 phase when OAm is present in excess. The transformation from

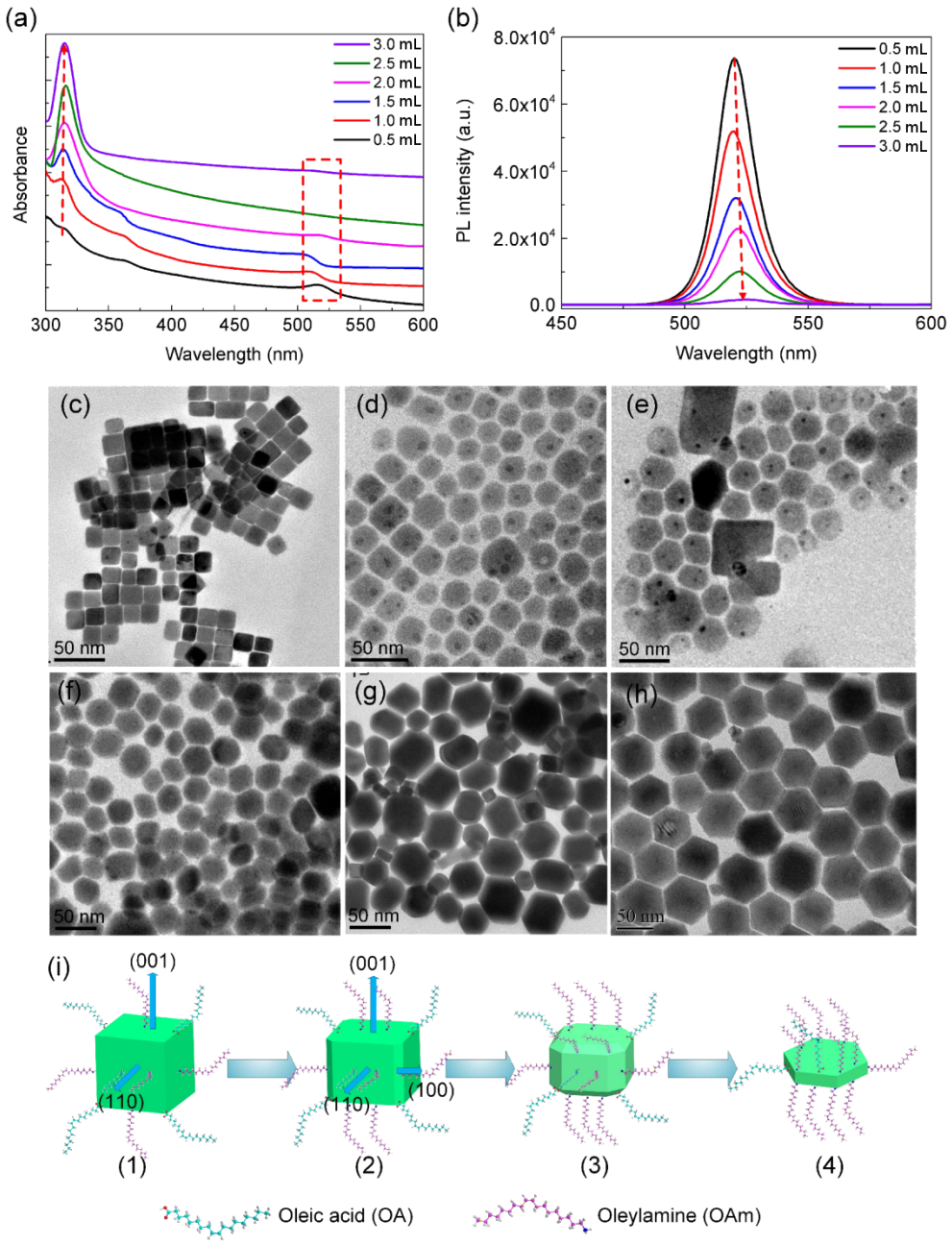

Figure 5: The change of (a) UV–vis absorption spectra, (b) PL spectra, and (c)–(h) TEM images of $CsPbBr_3$ PNCs synthesized at 0.5, 1.0, 1.5, 2.0, 2.5, and 3.0 mL of OAm, respectively, while keeping OA unchanged. (i) Schematic illustration of the morphology change from $CsPbBr_3$ PNCs to Cs_4PbBr_6 PNCs.

$CsPbBr_3$ to Cs_4PbBr_6 leads to a remarkable change in crystal structure and atomic composition. Udayabhaskararao et al. demonstrated that this transformation is driven by recrystallization induced by micelle formation or soft-ligand templating [25]. This mechanism, however, cannot explain the phase transformation from $CsPbBr_3$ to Cs_4PbBr_6 in this work because there are no intermediate stages observed by TEM. Therefore, we suppose the transformation between the two phases involves ion equilibria. A large amount of OAm can form oleylammonium and dissolve $PbBr_2$, resulting in the formation of lead oleate and oleylammonium bromide, thus driving the transformation [41]. An even larger amount of OAm can also dissolve $CsPbBr_3$ PNCs and accelerate the transformation into Cs_4PbBr_6 PNCs. This process is related to Ostwald ripening that was found during the nucleation and growth of PNCs [42]. Therefore, the formation of Cs_4PbBr_6 PNCs is promoted by the capacity of the organic ligands to dissolve $PbBr_2$ and by the dissociation of $CsPbBr_3$ PNCs.

A series of TEM images (Figure 4c–h) clearly confirm that the morphology of these PNCs can be tuned easily by changing the amount of OAm in the precursor solution, while keeping the amount of OA unchanged. We attribute this morphology change to the crystal anisotropy induced by the growth kinetics. The capping ligands are preferentially attached to the PNCs facets, resulting in different growth rates on different crystal facets [43]. A schematic illustration of the morphology change between $CsPbBr_3$ PNCs and Cs_4PbBr_6 PNCs is shown in Figure 5i. When equal amounts of OA and OAm are added, the reaction favors isotropic growth, since OA and OAm play a cooperative role (Figure 5i(1)). When more OAm is added, the long-chain OAm are more easily bound to the surface of the PNCs and restrict the perpendicular growth (001) [44]. Additionally, the growth rates for the side planes are different due to excess amount of OAm easily aggregated at the boundary of two adjacent planes [45], which possibly leads to the formation of (100) planes and the appearance of diamond-like product, as demonstrated in Figure 5i(2,3). This inhibiting effect is distinct when OAm is added in large excess, yielding a hexagonal structure with sharp edges, as shown in Figure 5i(4).

Reversible transformation between Cs_4PbBr_6 PNCs and $CsPbBr_3$ PNCs

After a few weeks, the prepared Cs_4PbBr_6 PNCs solution became milky white, indicating that untransformed $CsPbBr_3$ PNCs decomposed completely. We further explored a possible reversible transformation by introducing different amounts of water. When little water was added, the color of Cs_4PbBr_6 solution changed from colorless to light-green rapidly (Supporting Information File 2), implying a possible structural transformation. In order to monitor the transformation process, different amounts of water were gradually dropped into a Cs_4PbBr_6 PNCs solution (Figure 6a). When more water was added, the solution became green-yellow.

Furthermore, the transformation process was studied by using UV–vis absorption and PL emission spectroscopy. As shown in Figure 6b, the colorless Cs_4PbBr_6 PNCs solution exhibits a strong first excitonic absorption peak at 315 nm. When a small amount of water was slowly added, the intensity of the first excitonic absorption peak declined gradually, indicating the decomposition of Cs_4PbBr_6 PNCs. Correspondingly, a weak absorption peak at 510 nm emerged. Moreover, as the amount of water was increased, the intensity of the absorption peak at about 510 nm increased steadily (inset in Figure 6b). Compared with the excitonic absorption peak of Cs_4PbBr_6 PNCs, the product displayed only weak absorbance. Figure 6c demonstrates the PL emission spectra of the samples during the transformation process. After the addition of small amounts of water, a PL emission peak at 518 nm appeared and gradually increased in intensity, suggesting a luminescent product was formed. XRD measurements were carried out to determine the phase of the obtained product. As shown in Figure 6d, the XRD diffraction pattern of final product is consistent with bulk orthorhombic $CsPbBr_3$ (PDF card #18-0364), suggesting the formation of $CsPbBr_3$ PNCs. Moreover, the PL QY of as-prepared $CsPbBr_3$ PNCs was calculated to be ca. 70%. Interestingly, the $CsPbBr_3$ PNCs show a high stability in ambient environment, as shown in Figure 6e. Upon the addition of a large amount of OAm and upon ultrasonication, the conversion from $CsPbBr_3$ PNCs to Cs_4PbBr_6 PNCs was achieved (Supporting Information File 1, Figure S3) and can be repeated more than two times, similar to previous reports [25].

The addition of led to the decomposition of Cs_4PbBr_6 and the formation of $CsPbBr_3$ PNCs, triggered by the stripping of water-soluble CsBr. During this process, the rhombohedral Cs_4PbBr_6 PNCs are slowly converted to orthorhombic $CsPbBr_3$ PNCs (Figure 6d) and the rate of this conversion depends on the amount of water. The CsBr-stripping can be proven by the reduction of crystal size from 65 to 11.7 nm (Figure 1 and Figure 4). This is consistent with the findings reported by Wu and co-workers [20]. As the solubility of liquid paraffin or capping ligands in water is very low, further dissolution of $CsPbBr_3$ PNCs is inhibited, which is similar to the effect demonstrated by Wu's group who took advantage of the very low (only 9.5 mg/L) solubility of hexane in water [20]. The above result indicates that the $CsPbBr_3$ PNCs have a higher stability than Cs_4PbBr_6 PNCs against water.

Conclusion

In summary, we demonstrate the effect of small changes in the environment of capping ligands and water on the crystal structure and stoichiometry of PNCs. This study expanded our recent work of synthesizing differently shaped $CsPbBr_3$ PNCs [30]. Similarly as demonstrated in our recent study, by changing the ultrasound power and radiation time, the PL emission of $CsPbBr_3$ PNCs could be easily tuned. More importantly, with lower the immersion heights of the vibrating spear higher PL QY of $CsPbBr_3$ PNCs were achieved. The as-prepared $CsPbBr_3$ PNCs show a high PL QY of up to 85% and a considerable photostability and chemical stability. The Cs_4PbBr_6 PNCs are obtained via direct ultrasonication of precursors or after adding OAm in the pre-synthesized $CsPbBr_3$ PNCs solution. The phase transformation of orthorhombic $CsPbBr_3$ NCs to rhombohedral Cs_4PbBr_6 NCs is promoted by the capacity of organic ligands to dissolve $PbBr_2$, and by the formation of lead oleate and the dissociation of $CsPbBr_3$ PNCs. Morphology changes are mainly ascribed to the anisotropic growth of the crystals. In addition, a reverse transformation from Cs_4PbBr_6 PNCs to $CsPbBr_3$ PNCs can be achieved by adding water to pre-synthesized Cs_4PbBr_6

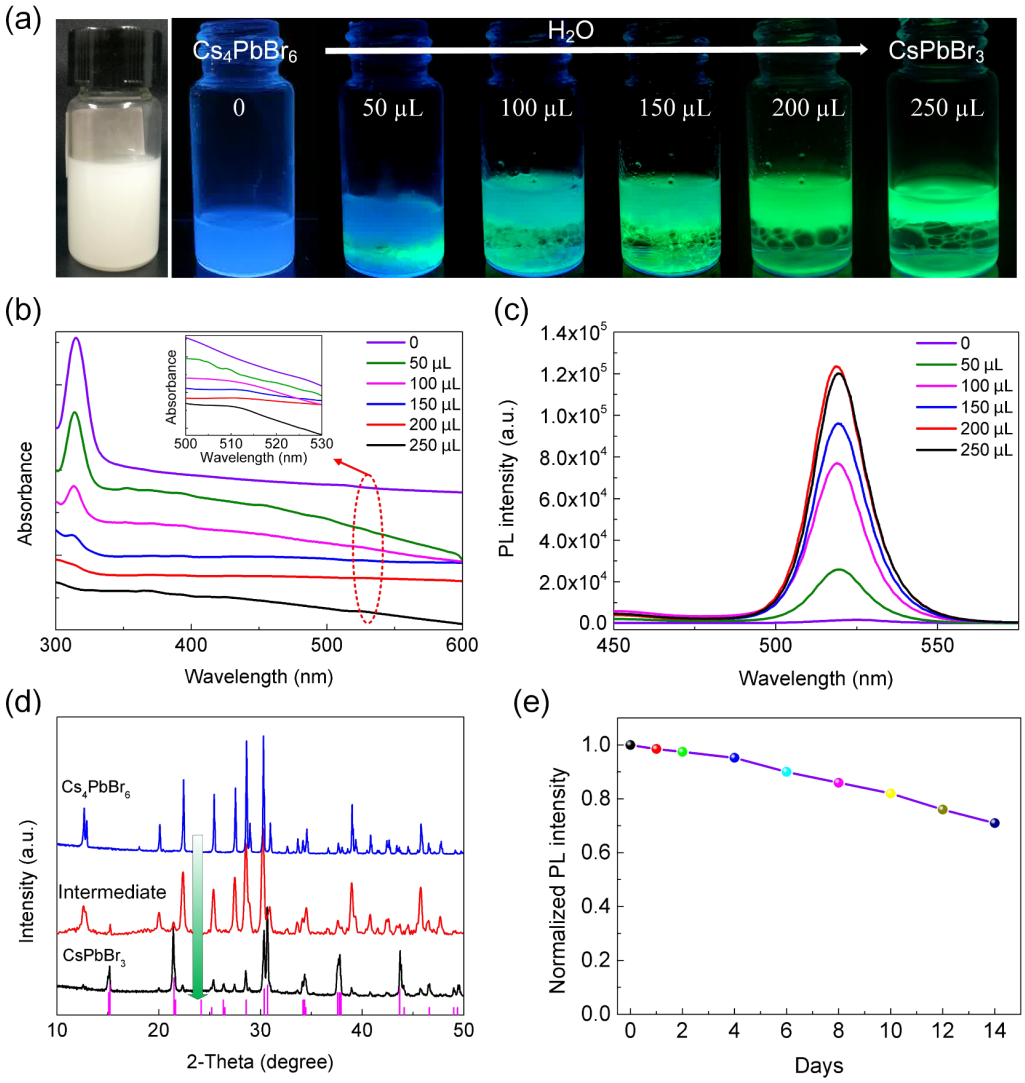

Figure 6: (a) The transformation process from Cs_4PbBr_6 PNCs to $CsPbBr_3$ PNCs. The products were illuminated under a 365 nm UV light. Both (b) UV–vis absorption spectra and (c) PL spectra of products were recorded during the transformation process. (d) XRD diffraction patterns of typical products prepared by changing the amount of added water, demonstrating the transformation from rhombohedral Cs_4PbBr_6 PNCs to orthorhombic $CsPbBr_3$ PNCs. (e) Stability of as-prepared $CsPbBr_3$ PNCs in ambient environment.

PNCs. The developed ultrasonication assistance results in the successful control over the phase transformation of PNCs, which can find widespread application in photoelectronic devices. We anticipate that this work can be extended to prepare other halide perovskites.

Experimental

Chemicals

Cesium carbonate (Cs_2CO_3, 99%), lead bromide ($PbBr_2$, 98%), liquid paraffin (90%), oleic acid (OA, 90%), oleylamine (OAm, 70%), and anhydrous toluene (99.8%) were purchased from Shanghai Aladdin Biochemical Technology Co. The chemicals used in the present work were of analytical grade and used without further purifications.

Synthesis of $CsPbBr_3$ PNCs and Cs_4PbBr_6 PNCs

$CsPbBr_3$ PNCs: The PNCs were prepared via modifying the procedures reported by Tong and Rao and co-workers [29,30]. In a typical process, Cs_2CO_3 (0.15 mmol) and $PbBr_2$ (0.30 mmol) powders were added to a mixture of 10 mL liquid paraffin (LP), 0.50 mL OA and 0.50 mL OAm. Then the reaction medium was processed by tip-sonication at a power of 120 W for 40 min. During the sonication, the colorless reaction medium gradually transformed into a yellow and then an orange-yellow solution, which suggests the formation of PNCs and demonstrates strong fluorescence emission under 365 nm UV light excitation. After completion of the reaction, unreacted precursors and excess ligands were removed by centrifugation

at a speed of 3000 rpm for 10 min and then the precipitate was redispersed in 5.0 mL of toluene. Then, the colloidal solution was centrifuged at a speed of 12000 rpm for 5 min and the sediment was redispersed in toluene for further characterization.

Cs_4PbBr_6 PNCs: Cs_2CO_3 (0.15 mmol) and $PbBr_2$ (0.30 mmol) powders were added to a mixture of 10 mL liquid paraffin, 0.50 mL OA and 3.0 mL OAm, while keeping other synthesis conditions as the same as that of $CsPbBr_3$ PNCs.

Reversible transformation from Cs_4PbBr_6 PNCs to $CsPbBr_3$ PNCs

50–250 μL of water was added to 5.0 mL of the pre-synthesized Cs_4PbBr_6 PNCs solution and shaken slightly, which is a modification of the work reported by Wu and co-workers [20].

Characterizations

The crystal surface morphology of the PNCs was characterized by transmission electron microscopy (TEM, JEM-2100F, JEOL, Japan) with an accelerating voltage of 100 kV. High-resolution TEM (HRTEM) was carried out on a JEOL JEM-2100F instrument operating at 200 kV. The crystal phases of the products were measured using an X-ray diffractometer (XRD, D8-Advance, Bruker, Germany) with a Cu Kα radiation source (λ = 0.15418 nm) at a counting rate of 2° per minute in the scanning angle (2θ) range from 5° to 50°. The surface morphology of Cs_4PbBr_6 PNCs was characterized by using a field-emission scanning electron microscope (SEM, Merlin). The UV–vis absorption spectra of the samples were measured using a UV–vis spectrometer (Shimadzu, Japan) over the wavelength range from 300 to 700 nm, at 1 nm intervals. The PL spectra of the PNCs were recorded using a fluorescence spectrophotometer (RF-6000, Shimadzu, Japan) using a Xe lamp as an excitation source.

Supporting Information

Supporting Information File 1

Additional PL spectra, SEM image, and UV–vis absorption spectra.
[https://www.beilstein-journals.org/bjnano/content/supplementary/2190-4286-10-66-S1.pdf]

Supporting Information File 2

Video showing the transformation from Cs_4PbBr_6 to $CsPbBr_3$ PNCs after addition of water.
[https://www.beilstein-journals.org/bjnano/content/supplementary/2190-4286-10-66-S2.mp4]

Acknowledgements

This work is financially supported by National Natural Science Foundation of China (51735004, 51805173, and 51775199), Natural Science Foundation of Guangdong Province (2014A030312017), Science & Technology Program of Guangdong Province (2017B010115001), and the SCUT Fundamental Research Funds for the Central Universities.

ORCID® iDs

Jin Z. Zhang - https://orcid.org/0000-0003-3437-912X

References

1. Pan, J.; Quan, L. N.; Zhao, Y.; Peng, W.; Murali, B.; Sarmah, S. P.; Yuan, M.; Sinatra, L.; Alyami, N. M.; Liu, J.; Yassitepe, E.; Yang, Z.; Voznyy, O.; Comin, R.; Hedhili, M. N.; Mohammed, O. F.; Lu, Z. H.; Kim, D. H.; Sargent, E. H.; Bakr, O. M. *Adv. Mater. (Weinheim, Ger.)* **2016,** *28,* 8718–8725. doi:10.1002/adma.201600784
2. Li, J.; Xu, L.; Wang, T.; Song, J.; Chen, J.; Xue, J.; Dong, Y.; Cai, B.; Shan, Q.; Han, B.; Zeng, H. *Adv. Mater. (Weinheim, Ger.)* **2017,** *29,* 1603885. doi:10.1002/adma.201603885
3. Jeon, N. J.; Na, H.; Jung, E. H.; Yang, T.-Y.; Lee, Y. G.; Kim, G.; Shin, H.-W.; Il Seok, S.; Lee, J.; Seo, J. *Nat. Energy* **2018,** *3,* 682–689. doi:10.1038/s41560-018-0200-6
4. Wang, X.; Shoaib, M.; Wang, X.; Zhang, X.; He, M.; Luo, Z.; Zheng, W.; Li, H.; Yang, T.; Zhu, X.; Ma, L.; Pan, A. *ACS Nano* **2018,** *12,* 6170–6178. doi:10.1021/acsnano.8b02793
5. Yang, T.; Zheng, Y.; Du, Z.; Liu, W.; Yang, Z.; Gao, F.; Wang, L.; Chou, K.-C.; Hou, X.; Yang, W. *ACS Nano* **2018,** *12,* 1611–1617. doi:10.1021/acsnano.7b08201
6. Vickers, E. T.; Graham, T. A.; Chowdhury, A. H.; Bahrami, B.; Dreskin, B. W.; Lindley, S.; Bonabi Naghadeh, S.; Qiao, Q.; Zhang, J. Z. *ACS Energy Lett.* **2018,** *3,* 2931–2939. doi:10.1021/acsenergylett.8b01754
7. Koscher, B. A.; Swabeck, J. K.; Bronstein, N. D.; Alivisatos, A. P. *J. Am. Chem. Soc.* **2017,** *139,* 6566–6569. doi:10.1021/jacs.7b02817
8. Wu, K.; Liang, G.; Shang, Q.; Ren, Y.; Kong, D.; Lian, T. *J. Am. Chem. Soc.* **2015,** *137,* 12792–12795. doi:10.1021/jacs.5b08520
9. Akkerman, Q. A.; Park, S.; Radicchi, E.; Nunzi, F.; Mosconi, E.; De Angelis, F.; Brescia, R.; Rastogi, P.; Prato, M.; Manna, L. *Nano Lett.* **2017,** *17,* 1924–1930. doi:10.1021/acs.nanolett.6b05262
10. Yin, J.; Zhang, Y.; Bruno, A.; Soci, C.; Bakr, O. M.; Brédas, J.-L.; Mohammed, O. F. *ACS Energy Lett.* **2017,** *2,* 2805–2811. doi:10.1021/acsenergylett.7b01026
11. Yin, J.; Maity, P.; De Bastiani, M.; Dursun, I.; Bakr, O. M.; Brédas, J.-L.; Mohammed, O. F. *Sci. Adv.* **2017,** *3,* e1701793. doi:10.1126/sciadv.1701793
12. Saidaminov, M. I.; Almutlaq, J.; Sarmah, S.; Dursun, I.; Zhumekenov, A. A.; Begum, R.; Pan, J.; Cho, N.; Mohammed, O. F.; Bakr, O. M. *ACS Energy Lett.* **2016,** *1,* 840–845. doi:10.1021/acsenergylett.6b00396
13. Seth, S.; Samanta, A. *J. Phys. Chem. Lett.* **2017,** *8,* 4461–4467. doi:10.1021/acs.jpclett.7b02100
14. Protesescu, L.; Yakunin, S.; Bodnarchuk, M. I.; Krieg, F.; Caputo, R.; Hendon, C. H.; Yang, R. X.; Walsh, A.; Kovalenko, M. V. *Nano Lett.* **2015,** *15,* 3692–3696. doi:10.1021/nl5048779
15. Pan, A.; He, B.; Fan, X.; Liu, Z.; Urban, J. J.; Alivisatos, A. P.; He, L.; Liu, Y. *ACS Nano* **2016,** *10,* 7943–7954. doi:10.1021/acsnano.6b03863

16. He, X.; Qiu, Y.; Yang, S. *Adv. Mater. (Weinheim, Ger.)* **2017,** *29,* 1700775. doi:10.1002/adma.201700775
17. Bekenstein, Y.; Koscher, B. A.; Eaton, S. W.; Yang, P.; Alivisatos, A. P. *J. Am. Chem. Soc.* **2015,** *137,* 16008–16011. doi:10.1021/jacs.5b11199
18. Chen, M.; Zou, Y.; Wu, L.; Pan, Q.; Yang, D.; Hu, H.; Tan, Y.; Zhong, Q.; Xu, Y.; Liu, H.; Sun, B.; Zhang, Q. *Adv. Funct. Mater.* **2017,** *27,* 1701121. doi:10.1002/adfm.201701121
19. Rao, L.; Tang, Y.; Yan, C.; Li, J.; Zhong, G.; Tang, K.; Yu, B.; Li, Z.; Zhang, J. Z. *J. Mater. Chem. C* **2018,** *6,* 5375–5383. doi:10.1039/c8tc00582f
20. Wu, L.; Hu, H.; Xu, Y.; Jiang, S.; Chen, M.; Zhong, Q.; Yang, D.; Liu, Q.; Zhao, Y.; Sun, B.; Zhang, Q.; Yin, Y. *Nano Lett.* **2017,** *17,* 5799–5804. doi:10.1021/acs.nanolett.7b02896
21. Palazon, F.; Urso, C.; De Trizio, L.; Akkerman, Q.; Marras, S.; Locardi, F.; Nelli, I.; Ferretti, M.; Prato, M.; Manna, L. *ACS Energy Lett.* **2017,** *2,* 2445–2448. doi:10.1021/acsenergylett.7b00842
22. Palazon, F.; Almeida, G.; Akkerman, Q. A.; De Trizio, L.; Dang, Z.; Prato, M.; Manna, L. *Chem. Mater.* **2017,** *29,* 4167–4171. doi:10.1021/acs.chemmater.7b00895
23. Zhai, W.; Lin, J.; Li, Q.; Zheng, K.; Huang, Y.; Yao, Y.; He, X.; Li, L.; Yu, C.; Liu, C.; Fang, Y.; Liu, Z.; Tang, C. *Chem. Mater.* **2018,** *30,* 3714–3721. doi:10.1021/acs.chemmater.8b00612
24. Liu, Z.; Bekenstein, Y.; Ye, X.; Nguyen, S. C.; Swabeck, J.; Zhang, D.; Lee, S.-T.; Yang, P.; Ma, W.; Alivisatos, A. P. *J. Am. Chem. Soc.* **2017,** *139,* 5309–5312. doi:10.1021/jacs.7b01409
25. Udayabhaskararao, T.; Houben, L.; Cohen, H.; Menahem, M.; Pinkas, I.; Avram, L.; Wolf, T.; Teitelboim, A.; Leskes, M.; Yaffe, O.; Oron, D.; Kazes, M. *Chem. Mater.* **2018,** *30,* 84–93. doi:10.1021/acs.chemmater.7b02425
26. Huang, H.; Xue, Q.; Chen, B.; Xiong, Y.; Schneider, J.; Zhi, C.; Zhong, H.; Rogach, A. L. *Angew. Chem.* **2017,** *129,* 9699–9704. doi:10.1002/ange.201705595
27. Fang, F.; Chen, W.; Li, Y.; Liu, H.; Mei, M.; Zhang, R.; Hao, J.; Mikita, M.; Cao, W.; Pan, R.; Wang, K.; Sun, X. W. *Adv. Funct. Mater.* **2018,** *28,* 1706000. doi:10.1002/adfm.201706000
28. Li, X.; Yu, D.; Cao, F.; Gu, Y.; Wei, Y.; Wu, Y.; Song, J.; Zeng, H. *Adv. Funct. Mater.* **2016,** *26,* 5903–5912. doi:10.1002/adfm.201601571
29. Tong, Y.; Bladt, E.; Aygüler, M. F.; Manzi, A.; Milowska, K. Z.; Hintermayr, V. A.; Docampo, P.; Bals, S.; Urban, A. S.; Polavarapu, L.; Feldmann, J. *Angew. Chem., Int. Ed.* **2016,** *55,* 13887–13892. doi:10.1002/anie.201605909
30. Rao, L.; Tang, Y.; Song, C.; Xu, K.; Vickers, E. T.; Bonabi Naghadeh, S.; Ding, X.; Li, Z.; Zhang, J. Z. *Chem. Mater.* **2019,** *31,* 365–375. doi:10.1021/acs.chemmater.8b03298
31. Brouwer, A. M. *Pure Appl. Chem.* **2011,** *83,* 2213–2228. doi:10.1351/pac-rep-10-09-31
32. Qi, X.; Zhou, T.; Deng, S.; Zong, G.; Yao, X.; Fu, Q. *J. Mater. Sci.* **2014,** *49,* 1785–1793. doi:10.1007/s10853-013-7866-8
33. Mphuthi, N. G.; Adekunle, A. S.; Fayemi, O. E.; Olasunkanmi, L. O.; Ebenso, E. E. *Sci. Rep.* **2017,** *7,* 43181. doi:10.1038/srep43181
34. Yuwen, L.; Yu, H.; Yang, X.; Zhou, J.; Zhang, Q.; Zhang, Y.; Luo, Z.; Su, S.; Wang, L. *Chem. Commun.* **2016,** *52,* 529–532. doi:10.1039/c5cc07301d
35. Akkerman, Q. A.; Motti, S. G.; Srimath Kandada, A. R.; Mosconi, E.; D'Innocenzo, V.; Bertoni, G.; Marras, S.; Kamino, B. A.; Miranda, L.; De Angelis, F.; Petrozza, A.; Prato, M.; Manna, L. *J. Am. Chem. Soc.* **2016,** *138,* 1010–1016. doi:10.1021/jacs.5b12124
36. Dang, Z.; Shamsi, J.; Palazon, F.; Imran, M.; Akkerman, Q. A.; Park, S.; Bertoni, G.; Prato, M.; Brescia, R.; Manna, L. *ACS Nano* **2017,** *11,* 2124–2132. doi:10.1021/acsnano.6b08324
37. Seth, S.; Samanta, A. *J. Phys. Chem. Lett.* **2018,** *9,* 176–183. doi:10.1021/acs.jpclett.7b02931
38. Akkerman, Q. A.; Abdelhady, A. L.; Manna, L. *J. Phys. Chem. Lett.* **2018,** *9,* 2326–2337. doi:10.1021/acs.jpclett.8b00572
39. Zhang, Y.; Saidaminov, M. I.; Dursun, I.; Yang, H.; Murali, B.; Alarousu, E.; Yengel, E.; Alshankiti, B. A.; Bakr, O. M.; Mohammed, O. F. *J. Phys. Chem. Lett.* **2017,** *8,* 961–965. doi:10.1021/acs.jpclett.7b00105
40. Chen, D.; Wan, Z.; Chen, X.; Yuan, Y.; Zhong, J. *J. Mater. Chem. C* **2016,** *4,* 10646–10653. doi:10.1039/c6tc04036e
41. Almeida, G.; Goldoni, L.; Akkerman, Q.; Dang, Z.; Khan, A. H.; Marras, S.; Moreels, I.; Manna, L. *ACS Nano* **2018,** *12,* 1704–1711. doi:10.1021/acsnano.7b08357
42. Koolyk, M.; Amgar, D.; Aharon, S.; Etgar, L. *Nanoscale* **2016,** *8,* 6403–6409. doi:10.1039/c5nr09127f
43. Liang, Z.; Zhao, S.; Xu, Z.; Qiao, B.; Song, P.; Gao, D.; Xu, X. *ACS Appl. Mater. Interfaces* **2016,** *8,* 28824–28830. doi:10.1021/acsami.6b08528
44. Liu, W.; Zheng, J.; Cao, S.; Wang, L.; Gao, F.; Chou, K.-C.; Hou, X.; Yang, W. *Inorg. Chem.* **2018,** *57,* 1598–1603. doi:10.1021/acs.inorgchem.7b02941
45. Li, G.; Wang, H.; Zhu, Z.; Chang, Y.; Zhang, T.; Song, Z.; Jiang, Y. *Chem. Commun.* **2016,** *52,* 11296–11299. doi:10.1039/c6cc05877a

License and Terms

BEILSTEIN JOURNAL OF NANOTECHNOLOGY

An iridescent film of porous anodic aluminum oxide with alternatingly electrodeposited Cu and SiO_2 nanoparticles

Menglei Chang[1], Huawen Hu*[1], Haiyan Quan[1], Hongyang Wei[1], Zhangyi Xiong[1], Jiacong Lu[1], Pin Luo[1], Yaoheng Liang[1], Jianzhen Ou*[2] and Dongchu Chen*[1]

Full Research Paper

Open Access

Address:
[1]College of Materials Science and Energy Engineering, Foshan University, Jiangwan First Road, Chancheng, Foshan, Guangdong, China and [2]School of Engineering, RMIT University, Melbourne, VIC, Australia

Email:
Huawen Hu* - huawenhu@126.com; Jianzhen Ou* - Jianzhen.ou@rmit.edu.au; Dongchu Chen* - cdcever@163.com

* Corresponding author

Keywords:
aluminum alloys; anodic aluminum oxidation; interference-enabled color production; rainbow effect; structural color

Beilstein J. Nanotechnol. **2019,** *10,* 735–745.
doi:10.3762/bjnano.10.73

Received: 04 November 2018
Accepted: 22 February 2019
Published: 19 March 2019

This article is part of the thematic issue "Low-dimensional materials and systems".

Associate Editor: E. Meyer

Abstract

The structurally colored surface of anodic aluminum oxide (AAO) is highly useful for decoration and anti-counterfeiting applications, which are of significance for both scientific and industrial communities. This study presents the first demonstration of the fabrication of an iridescent film of porous AAO on an industrial aluminum alloy substrate, with alternatingly electrodeposited Cu and SiO_2 nanoparticles (NPs). A rainbow effect was effectively obtained for the optimized sample with appropriate alternating electrodeposition times. The structure and optical properties of a series of the electrodeposited AAO-based thin film were investigated. The Cu and SiO_2 NPs were found to be uniformly deposited into the porous structure of the AAO film, and the alternating electrodeposition repeating twice led to the formation of the optimal AAO-based thin film that exhibited a rainbow effect and superior anti-corrosion performance.

Introduction

Due to the low cost, high mechanical strength and ductility, and well-developed production procedures, aluminum alloys have been extensively used as nonferrous structural materials [1-12]. Aluminum alloys are generally prepared by doping aluminum with other elements at a low content [13]. Anodic aluminum oxidation processing and electrodeposition treatment can allow the aluminum alloy to bear different structural colors, providing exciting opportunities for bringing such materials to the fields of decorative materials [14-17]. However, only a limited number of colors has been produced by the traditional coloration techniques [14,16,18,19]. To widen the spectrum of colors, many researchers turn to mimic the structural color from nature, which is expected as the origin for the artificial creation of multiple and stable colors existing on the surface of aluminum

alloys [15,20]. Furthermore, their own characteristics of the structural colors are also expected to enrich the aluminum alloys with vivid optical properties [21].

Structural colors are generated by light diffraction, interference and scattering [20], completely different from pigment colors involving the selective absorption of a certain light waves and the reflection of the complementary light waves. Structural colors do not absorb light, implying that the light intensity will not decrease, and significantly, a local iridescent phenomenon appears as a result of light diffraction and reflection. This rainbow effect of structural colors refers to that different colors are displayed with a change of the viewing angle [16,22]. By contrast, no rainbow effect occurs in the pigment colors. The artificial structural color is inspired from nature, e.g., the bright tail of the peacock feathers, the mixed cyan and green shell of the Coleoptera beetles, and the wings of butterflies [15]. In comparison with pigment colors, structural colors are much more stable, as a color change can only take place when the physical structure is varied [23].

Two types of strategies have been employed to produce structural colors, one is based on self-assembly methods [24], and the other is based on electrodeposition [18]. The former involves the simultaneous assembly of the basic structural units such as molecules, nanomaterials, and the materials on the microscale or even larger scales to form an ordered structure. During the self-assembly process, the basic structural units organize or aggregate, in a simultaneous way, into a stable structure possessing a regular geometric appearance. In contrast, electrodeposition involves the nucleation at an electrode surface under the action of an electric field [25]. For example, a high-purity aluminum foil was directly used as a template, on which anodic aluminum oxide (AAO) films with different thicknesses were generated by anodization for different durations. Subsequently, the electrodeposition of Co and Cu were performed. Under irradiation of natural light perpendicular to the surface, different colors (including purple, blue, blue-green, green, and yellow) appeared in the Co/AAO films depending on the anodization duration, and another set of colors (including purple, indigo, blue, blue-green, and green) also appeared in the Cu/AAO films depending on the oxidation time. This colorful AAO composite film with the electrodeposited metal was a result of an increase in the effective refractive index and hence reduction of the reflection of the aluminum substrate [25]. The saturation of the structural colors of the metal-deposited AAO composite film was largely enhanced [25-27]. An electrostatic self-assembly technique was also employed to produce large-area, ordered interference-enabled colored films with uniform structural colors on the surface of inorganic nanoparticles (NPs) that had been prepared to bear surface charges [28]. On the substrates of quartz glass, PET and PP, twenty cycles of the assembly of a SiO_2 film led to the formation of dark red, orange-yellow, and lake-green films, respectively. With a change in the particle size of SiO_2, the PET substrate after being exposed to twenty cycles of SiO_2 film deposition exhibited a color variation from blue over magenta to green. Varying the cycles of the deposition of 50 nm SiO_2 film, color changes were demonstrated with the incident light angle, e.g., from cyan to blue, from orange-red to yellow, from blue-green to blue-purple, and from magenta to dark green. The SiO_2/PET film was also applied to the surface of textile fibers, yielding structural colors [29-31]. Using a one-step oxidation method in phosphoric acid solution, AAO/Al was firstly prepared, onto which a non-magnetic Ag@AAO composite film was further fabricated by an alternating electrodeposition technique. It was found that under incident light at 0°, the color of the Ag/AAO film changed with the electrodeposition time, including purple, blue, green, yellow, pink, and red. Varying the incident light angle, different colors were exhibited including dark yellow, dark green, dark blue, and light purple. A picture was also created on an organic coating that was previously applied onto the Ag/AAO film, and different patterns could be generated with the variation of the incident light angle, satisfying the requirements for optical anti-counterfeiting applications [32]. A self-made electrophoresis-based deposition device was also adopted to deposit negatively charged PS spheres onto the surface of a carbon fiber using a stainless steel tube and a carbon fiber as the anode and cathode under the action of a circular electric field, respectively, resulting in a cylindrical fibrous structure. The control over the electrodeposition voltage and time allowed for the fabrication of fibers with different thicknesses, and the resulting fibers exhibited structural colors of blue, green, and red when the PS spheres with a diameter of 185, 230 and 290 nm, respectively, were employed [33-35]. A natural sedimentation method was also used to prepare a structurally colored SiO_2 photonic crystal film. Changing the incident light angles led to a variation of the structural color from red to blue-purple, and the SiO_2 particle size was also found to have an influence on the film color [14]. Furthermore, an AAO template was firstly prepared in an electrolyte with an alkaline silica gel and phosphate, onto which a layer of an Au film was deposited via sputtering, yielding a colorful filter material. Different structural colors could be obtained via changing the anodization time [17].

In this context, instead of using high-purity aluminum foils and titanium foils as the substrate for the anodization treatment, which have been widely explored [25,32,36,37], we employed an industrial aluminum alloy as substrate to first generate porous AAO films and subsequently investigated the structural color exhibited in the AAO films after alternating electrodeposi-

tion of Cu NPs and SiO_2 NPs with high and low refractive indexes, respectively. The NPs grew in the porous AAO film in a confined manner. The large difference between the refractive indexes of the Cu NPs and the SiO_2 NPs could result in the generation of vivid colors. This study presents the first demonstration of tailoring the structural coloring of AAO film-decorated industrial aluminum alloy plates by controlling the times of the alternating electrodeposition of Cu and SiO_2 NPs. Interference-related colors were achieved and the rainbow effect of the structural color was also observed. The study presented here will stimulate the advancements of the utilization of structural colors with high stabilities for a wide range of applications such as colorful case shells of electronic devices, automobile bodies, and anti-counterfeiting labels.

Experimental

Materials

The 6063 aluminum alloy was adopted as substrate. Tetraethoxysilane and sodium dodecyl sulfate (SDS, used as a surfactant) were of analytical reagent (AR) grade and obtained from Fuchen Chemical Reagent Factory. Potassium nitrate (AR) was supplied by Guangzhou Chemical Reagent Factory, and all the other reagents were AR grade and purchased from Guangdong Guanghua Sci-Tech Co., Ltd.

Anodization and electrodeposition-based structural coloring of the aluminum alloy

Pretreatment

For removing oily contaminants and dirt, the 6063 aluminum alloy sample was first washed in an alkaline solution for 3–4 min, and then washed with deionized (DI). Afterward, it was put into an acidic eluent for the acid-based washing for 2–3 min and then thoroughly washed with DI water. Before stored for later use, the sample was blow-dried. The alkaline solution was composed of NaOH (40.0 g), SDS (1.0 g) and DI water (1.0 L), while the acidic solution consisted of sulfuric acid solution (40%) and nitric acid solution (10%).

Anodization

The pretreated sample was placed in a sulfuric acid solution (117 g/L), and the DC electrical power supply (KXN-305D) was switched on. The anodization was conducted for 30 min at 0–6 °C and an oxidation current of 1.2 A. During the oxidation, the sample was kept parallel to the two cathodes, with equal distances between sample and each cathode.

Pore-enlarging treatment with phosphoric acid

After anodization, the sample was put into a phosphoric acid solution (5%) and allowed to stand for 12 min, and then DI water was employed to remove the excess phosphoric acid solution, followed by blow-drying.

Galvanic deposition of Cu NPs

In a $CuSO_2$ solution (60 g/L), the anodically oxidized sample was colorized using an electrical supply (EOECD-30A) with a constant voltage of 15 V for a deposition time of 35 s. During the electrodeposition process, the sample was kept parallel to the electrodes and at equal distances between them. The sample was taken out of the electrolyte and then blow-dried before storage for later use.

Galvanic deposition of SiO_2 NPs

The sample with the electrodeposited Cu was put into a SiO_2 deposition liquid, and the power supply (EOECD-30A) started with a constant voltage of 3 V for 35 s deposition. The sample was kept parallel to the electrode, and the distance between the sample and electrodes was kept equal during the deposition process. After the deposition, the sample was removed, washed with DI water to get rid of the SiO_2 deposition liquid, blow-dried with a hair dryer, and finally put into a sealed pocket for later use. The SiO_2 deposition liquid was prepared by mechanically mixing potassium nitrate (10.11 g), DI water (500 mL), absolute ethyl alcohol (500 mL), adding tetraethoxysilane (50 mL) after the pH value was adjusted to 3. The flow chart for the stepwise galvanic deposition is presented in Table 1.

Table 1: Alternating electrodeposition of Cu and SiO_2 for the preparation of different samples.

sample	deposition order
S1	Cu
S2	Cu→SiO_2
S3	Cu→SiO_2→Cu→SiO_2
S4	Cu→SiO_2→Cu→SiO_2→Cu→SiO_2

Hole sealing by hot water

After the alternating electrodeposition, the sample was immediately put into pre-boiled distilled water, and allowed to stand for 40 min. It was subsequently removed and blow-dried before placed into a sealed pocket for later use. The purpose of sealing the pores with hot water was to close the pores in the anodic oxide film and hence to avoid impurities entering the film.

Electrochemical properties

Electrochemical impedance testing was carried out by applying a small-amplitude AC voltage to the system and measuring the ratio of the signal voltage to the current (this ratio was defined as the system impedance) with the change of the sinusoidal-wave frequency, or the variation of the phase angle of the impedance with the change in frequency. Nyquist and Bode diagrams can be obtained by the electrochemical impedance measurements. The interfacial impedance of the sample was

estimated on the basis of the analysis described above, and the corrosion resistance performance was evaluated in more detail. Furthermore, the electrical polarization process of the sample in the test solution was studied by analyzing the Nyquist and Bode diagrams.

The test sample was immobilized onto a PVC tube with epoxy resin, and then naturally dried for 12 h. After that, a NaCl solution (3.5%) was poured into the PVC tube, and the level of the NaCl solution was in the range of a half to two-thirds of the tube volume. The exposed area of the PVC tube was approximately 5.7 cm^2. After being allowed to stand for 24 h, the sample was exposed to the electrochemical impedance measurements. A three-electrode system was adopted for the measurements, and a Pt wire and a saturated calomel electrode (SCE) were employed as the auxiliary electrode and reference electrode, respectively. Because such an electrochemical impedance measurement is sensitive to the outside interferences, the workstation was not permitted to be disrupted during the measurement, and electronic devices such as mobile phones were placed far away from the experiment.

The polarization test was divided into constant-potential scanning and constant-current scanning, while the former was divided into electrostatic potential scanning and dynamic potential scanning. The dynamic potential scanning was mainly implemented because of its advantages of automatic mapping and controllable scanning speed. The potentiodynamic sweep was performed by controlling the electrode potential in a manner of continuously changing (scanning) at a slower speed, and the instantaneous current value at the corresponding potential was measured. The instantaneous current was plotted as a function of the corresponding electrode potential to obtain the entire polarization curve. Since the potential of the electrode applied by the potentiostatic potential was sufficient to destroy the barrier layer of the sample to be tested, the potentiodynamic scanning must be performed after the electrical impedance test had been completed. The potentiodynamic sweep proceeded from −1.5 V to 1.5 V; the scanning speed, sampling interval, and frequency were set as 1.5 mV/s, 0.5 s, and 2 Hz, respectively.

Characterizations

A DC power supply (KXN-305D) was employed to conduct the alternating electrodeposition for achieving the structural coloring. The power supply (EOECD-30A) was adopted for the anodization processing of 6063 aluminum alloy samples. During the anodization, a conversion-based refrigerator (BC/BD-143), a non-contact infrared thermometer (AR842A+), and an electrically heated thermostatic water bath were used to strictly control the temperature. The electrochemical measurements were carried out using an electrochemical workstation (CS-310) in a three-electrode system, where the platinum electrode and saturated calomel electrode (SCE) worked as the counter and reference electrodes, respectively. The scanning range of the potentiodynamic polarization curve was set from −1.0 to +0.5 V, with a scanning rate and a sampling interval of 1 mV/s and 1 s, respectively. The range of the AC impedance test rate and the AC amplitude of the sinusoidal wave were set from 10^{-2} to 10^5 Hz and to 10 mV, respectively. The wide-band responses at the frequencies above 10 Hz and below 10 Hz were 470 pF and 2.2 nF, respectively. The parameters related to filter and earthing modes were set as 470 nF and field, respectively. The prepared samples were observed using a TM3030 scanning electron microscope (SEM, Hitachi). The absorbance and emissivity properties were measured using an ultraviolet–visible–near infrared (UV–vis–NIR) spectrophotometer (UV-4100, Hitachi, Japan). Microstructure observation and phase-composition analyses were performed using a TD-3500 X-ray diffraction (XRD) instrument. For measuring the thickness of the thin films formed on the sample, the work probe of a cladding thickness gauge (MINITEST 600) was placed on the specimen surface after the anodization, and the thickness could be directly read on the gauge. We arbitrarily selected 7–8 positions that were distributed all over the film surface in order to measure the average thickness of the film.

To scientifically describe the color of the sample, CIERGB, CIEXYZ and CIELAB models were successively established by International Lighting Commission, and CIELAB is considered as the most complete color model to describe the color observable by the naked eye. CIELAB (CIE1976*) consists of three channels, i.e., the L, a and b channels that represent brightness, red and green, and yellow and blue, respectively (where the larger the a value, the closer to red is the color, and the inverse leads to green color; the larger the b value, the closer to yellow is the color, and inverse results in blue color. The color difference between two samples can be evaluated according to the established color difference formula.

The change of the incident light angle led us to observe the rainbow effect of the structurally colored film. In this study, the most obvious rainbow effect of the structure was regarded as the best sample, that is, the sample bearing the maximum color difference under varying angles of incident light. According to the spectral photometric method in the standard GB/T 3979-2008, the object colors of the sample under 2° incident light and 10° incident light were measured. The chromatic aberration of each sample at two different angles of incident light was calculated, and the optimal group had the most chromatic aberration. The chromatic difference formula (E^*) is given below:

$$E^* = \left[\left(L_1^* - L_2^* \right)^2 + \left(a_1^* - a_2^* \right)^2 + \left(b_1^* - b_2^* \right)^2 \right]^{1/2} . \quad (1)$$

Results and Discussion

The oxidation was performed for 30 min in the oxidizing solution at 0–6 °C with an oxidation current of 1.2 A. The thickness of the resulting anodized film was maintained at 16–18 μm. Film thickness tests were performed on the samples deposited with Cu and SiO_2 NPs, and no thickness growth could be detected after the alternating electrodeposition. This is most likely due to that both Cu and SiO_2 were deposited into the pores of the porous AAO film, and thus the film thickness was consistent with the initial one. Figure 1a shows the microscopic morphology of the bare aluminum alloy before anodization, and a smooth surface of the aluminum alloy, without any big cracks, can be seen. In contrast, after anodization, the aluminum alloy becomes more porous, with a large number of holes on the AAO film (Figure 1b), revealing that the anodization treatment leads to the generation of a porous aluminum oxide film on the surface of the aluminum alloy substrate. Considering the limited size of the pores in the AAO film, the pore-enlarging treatment is needed to facilitate the electrodeposition process.

From Figure 2a, pores in the AAO film can be clearly observed for the sample S1, which also indicates that only one step of electrodeposition of Cu NPs into the holes does not significantly alter the structure and morphology of the AAO film. After deposition of SiO_2, the morphology is greatly changed for sample S2, and it is more difficult to notice the distribution of the AAO film in Figure 2b. In addition to the Cu NPs deposited in the pores of the AAO film, SiO_2 NPs can also be observed within the pores. The electrodeposition of an additional Cu layer resulted in the sample S3 with reduced visibility of the AAO film pores (Figure 2c). Most of the pores are filled after the repeated electrodeposition, and the entire surface appears even, without observable cracks. The SEM image of sample S4 is presented in Figure 2d, and the porous AAO film becomes more densely packed with electrodeposition layers that are homogeneously distributed over the entire surface in a crack-free way. It can be noted from Figure 2 that the electrodeposited layers of Cu and SiO_2 NPs were arranged in an ordered manner, which might be the cause of the iridescence.

The colors of the various prepared samples are presented in Figure 3, with the incident light perpendicular to the sample surface. At the same angle of the incident light, the electrodeposited films exhibit colors progressing from purple-red, light brown, brown, purple, red and to brown-green with increasing numbers of electrodeposition cycles. Upon the change of the angle of the incident light from 0° to 30°, the rainbow effect appears only for the sample S3, as shown in Supporting Information File 1, Figure S1. The structural color changes from light purple to dark purple with the variation of the incident light angle from 0 to 30°.

From the elemental mapping images of the S1 sample shown in Figure 4a, the sample includes the elements of Al, O, Cu and Au. The appearance of Au is due to the sputtering of the surface with Au (to enhance the electrical conductivity of the sample) before scanning. Cu can be seen as numerous particles at the nanoscale homogeneously distributed over the entire surface. In sample S2 (Figure 4b), Si can be observed all over the sample surface, revealing the uniform deposition of SiO_2. The electrodeposited Cu and SiO_2 are believed to be confined to the pores of the AAO film. Similarly, the S3 and S4 samples also exhibit a uniform distribution of Cu and SiO_2 NPs.

In the UV–vis spectra (Figure 5), all samples exhibit a strong absorption at 578 nm and a relatively weak absorption at

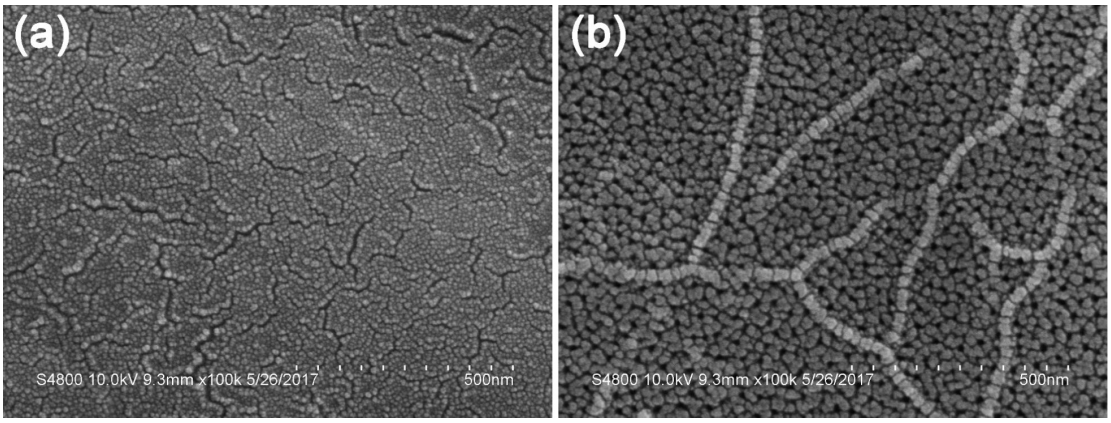

Figure 1: a,b) SEM images of the surface of the aluminum alloy before (a) and after (b) anodization.

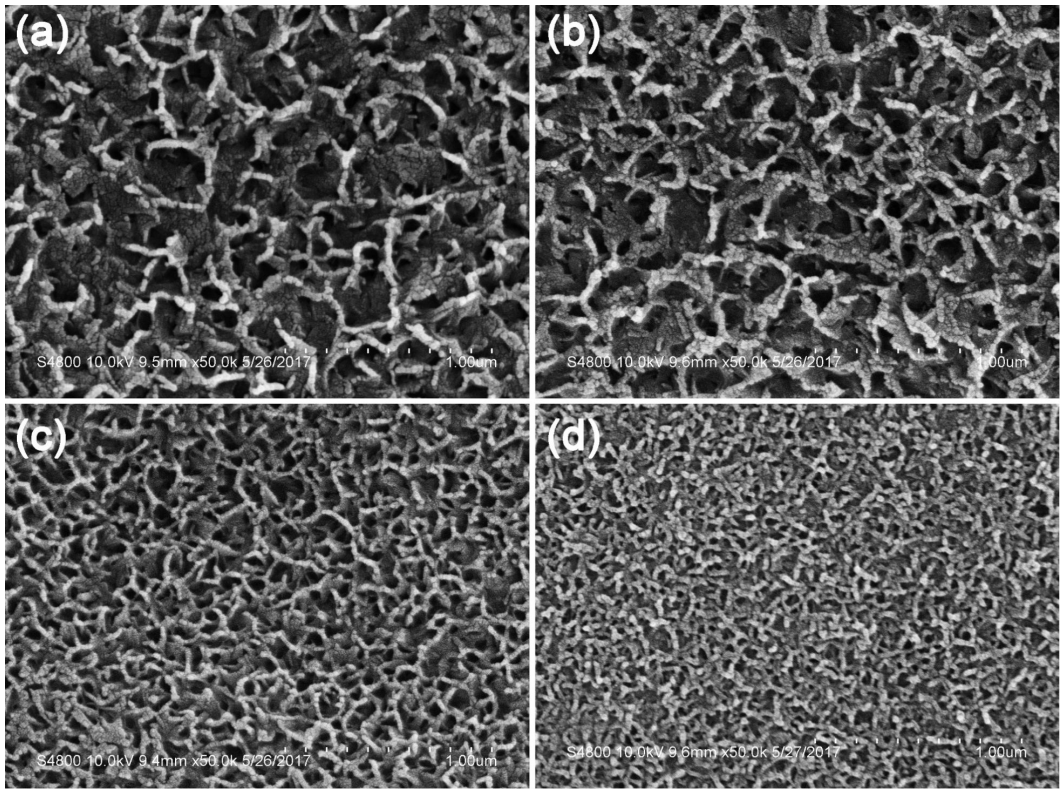

Figure 2: a–d) SEM images of the prepared samples: S1 (a), S2 (b), S3 (c), and S4 (d).

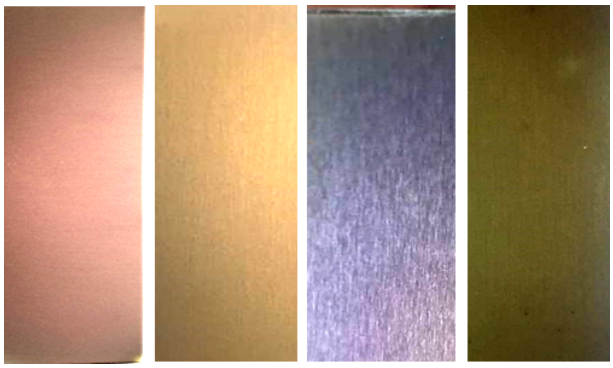

Figure 3: Digital images showing the colors of the prepared samples (from left to right: S1, S2, S3, and S4); the sample surface is perpendicular to the incident light.

350 nm, which indicates the existence of the Cu NPs. The UV–vis absorption of SiO_2 is mainly in the ultraviolet and far ultraviolet. The absorption at 350 nm is a result of plasmonic resonance absorption from Cu, while the peak at 578 nm can be assigned to Cu NPs. The absorption intensities at 350 and 578 nm gradually increase with the increase of the electrodeposition times corresponding to the samples S1 to S3, but decrease again for sample S4.

To further validate the color difference of the samples, the chromatic difference was analyzed according to the spectrophotometric colorimetry in the standard GB/T3979-2008, and the values of L^*, a^*, and b^* were estimated under incident light at angles of 2° and 10°. The rainbow effect is useful for anti-counterfeiting applications. The sample with the most obvious rainbow effect, that is the largest chromatic difference, can be regarded as optimal one. The values of L^*, a^*, b^* and color difference (E^*) are presented in Table 2 and Table 3. Among the prepared samples, sample S3 exhibits the largest value of E^* (1.9038). As also proven in Supporting Information File 1, Figure S1, the change of the incident light angle from 0° to 30° results in a noticeable color variation of sample S3. By contrast, the color of the other sample samples is independent of the incident light angles.

The color results from interference in the film, and the thickness of the film must not be too large if to produce a color effect. This is because two waves of reflected light will be generated at the top and the bottom surface of the irradiated film. The occurrence of interference requires that the frequencies of the two reflected light waves keep the same, with the same vibrational direction. As a result, the film thickness should be sufficiently low to ensure that the two reflected waves have

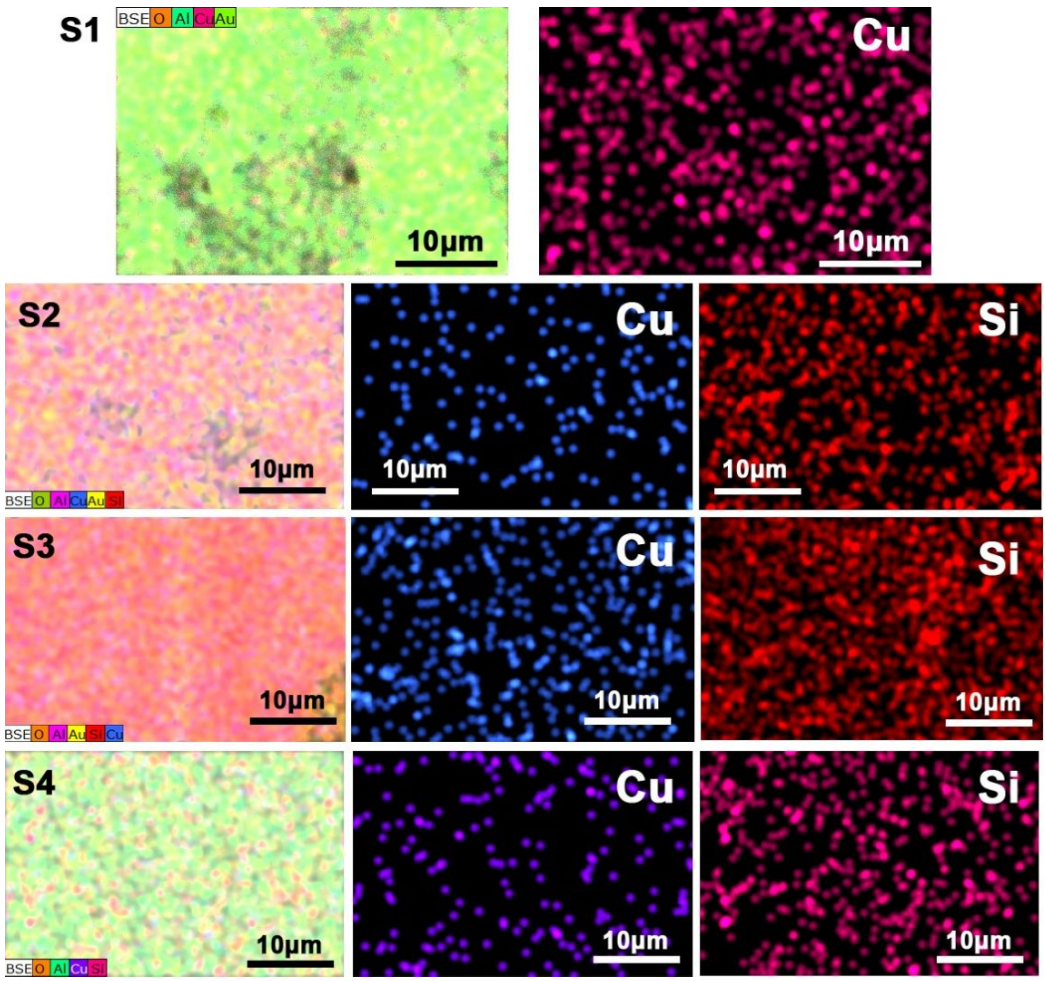

Figure 4: Elemental mapping images of the prepared S1, S2, S3, and S4 samples (progressing from top to bottom); the leftmost images correspond to the mapping images of full elements.

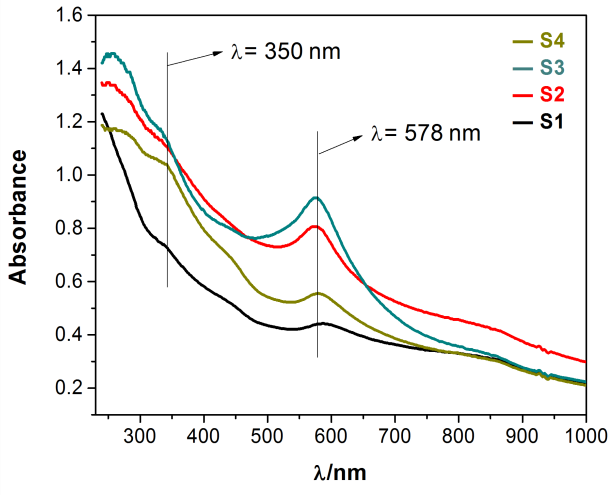

Figure 5: UV–vis–NIR absorption spectra of the various prepared samples.

the same frequency and vibrational direction. When the thickness of the film is too large, there is a big difference in the optical path length, which is detrimental to the consistency of the frequency and vibrational direction. This explains why sample S4 exhibits less interference than sample S3.

The relationship among the interference wavelength of the multilayer film, and the refractive index, thickness and refraction angle of the double-layer film can be expressed by Equation 2, and the schematic diagram is presented in Supporting Information File 1, Figure S2.

$$m\lambda = 2\left(n_1 d_1 \cos\theta_1 + n_2 d_2 \cos\theta_2\right), \quad (2)$$

where n_1 and n_2 represent the refractive indexes of the film, θ_1 and θ_2 are the refraction angles, and d_1 and d_2 are the film thicknesses [29-31].

Table 2: L^*, a^*, and b^* values under different incident light angles.[a]

sample code	incident light at 2°			incident light at 10°		
	L^*_1	a^*_1	b^*_1	L^*_2	a^*_2	b^*_2
S1	57.2714	−2.4112	4.2059	57.2272	−2.6253	4.5684
S2	49.1042	2.2042	4.5211	49.0606	1.3158	4.8799
S3	47.0084	5.2818	−0.4565	47.1218	3.4356	−0.0056
S4	59.5853	−2.4937	11.2013	59.3624	−2.2635	11.5646

[a]All calculations were conducted in triplicate, with the uncertainties (u) of the above parameters calculated as the standard deviation, and the u values of all of the above parameters were found to be within 6×10^{-4}.

Table 3: Color difference (E^*).

sample	S1	S2	S3	S4
E^*	0.4253	0.9591	1.9038	0.4844

At a given thickness, the larger the number of the layers is, the larger is the difference in the refractive index, leading to stronger interference. Theoretically, the highest interference can be obtained when n_1d_1, n_2d_2, and $\lambda/4$ are equal to each other.

Progressing from S1 to S4, the color difference increases first and then decreases again; the former is attributed to the multilayer interference that makes the rainbow effect increasingly more obvious. In sample S4, the film thickness becomes too large reducing any interference effects.

XRD patterns of the prepared samples are presented in Figure 6, and all of the samples exhibit similar diffraction patterns with peaks at 38.46°, 44.76°, 65.24°, and 68.31°, assigned to the diffraction planes of Al(111), Al(200), Al(220), Al(311), respectively. There is no diffraction that can be indexed to SiO_2, which might because it is present in the film as an amorphous state. Also, no signal can be noted for Cu species, which is most likely due to the low content of Cu that is below the detection limit of the XRD equipment.

In the electrical polarization measurements, the self-corrosion current, I_{corr}, and self-corrosion potential, E_{corr}, are critical parameters to evaluate the corrosion resistance of materials, especially aluminum profiles (Figure 7 and Table 4). Generally, the smaller the value of I_{corr} is, the higher is the hole-sealing quality. Larger values of E_{corr} can be an indication of higher corrosion resistance. From the values of I_{corr}, the best hole-sealing quality can be found in the sample S3, while the sample S2 can be regarded as the optimal one as far as E_{corr} is concerned. Nevertheless, the quality evaluation based on the values of I_{corr} is more widely employed, and therefore the results obtained via electric polarization measurements demonstrate that the sample S3 possesses the best quality in hole sealing.

The sealed AAO film is mainly composed of porous and resistant layers. A porous layer, an impedance layer, and an alumi-

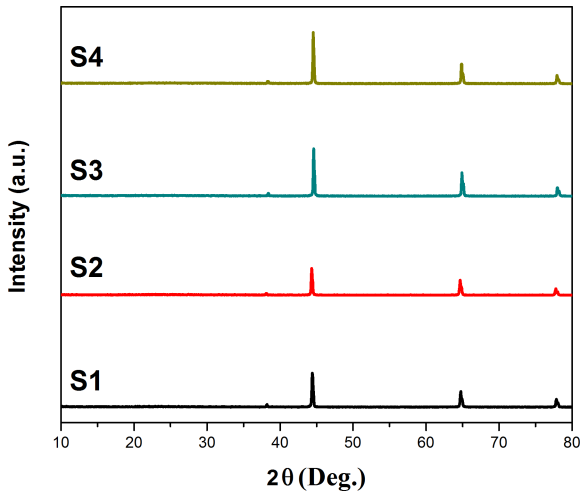

Figure 6: XRD patterns of the various prepared samples.

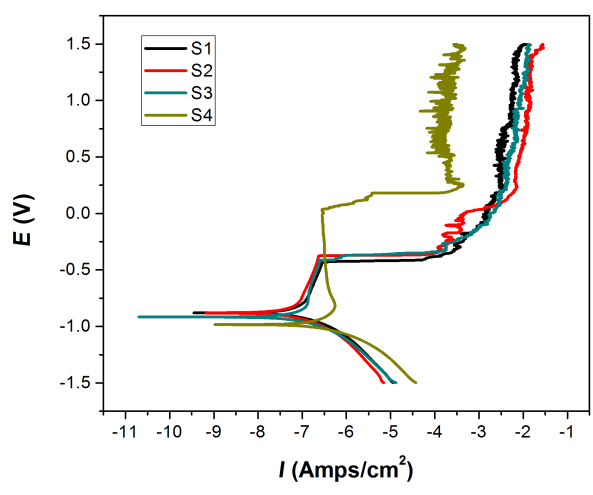

Figure 7: Electric polarization curve for the various prepared samples.

Table 4: Polarization parameters of the prepared samples.[a]

sample code	polarization parameter				
	Ba (mV)	*Bc* (mV)	I_{corr} (A/cm^2)	E_{corr} (V)	R_{corr} (Ω cm^2)
S1	385.95	142.84	8.5422×10^{-8}	−0.88067	0.0010047
S2	556.19	164.64	8.0341×10^{-8}	−0.88038	0.00094498
S3	214.47	110.87	5.4434×10^{-8}	−0.92124	0.00064026
S4	545.35	153.87	3.6714×10^{-7}	−0.9837	0.0043183

[a]The polarization parameters were calculated based on the Tafel fitting of the curves presented in Figure 7, with the u(*Ba*) < 0.05, u(*Bc*) < 0.04, u(I_{corr}) < 8×10^{-12}, u(E_{corr}) < 2×10^{-4}, and u(R_{corr}) < 3×10^{-7}.

num alloy substrate are present from top to bottom. While the electrical impedance test was performed to evaluate the performance of the porous layer of the AAO film, the low-frequency region corresponds to the performance of the impedance layer of the AAO film. During the electrical impedance measurements, the scanning begins in the high-frequency region and ends in the low-frequency region. From the Nyquist diagrams (Figure 8 and Figure 9), it can be noted that the data points remain roughly constant in the low-frequency region for all the prepared samples, but the capacitive loop varies from sample to sample. This reflects in an indirect way the different extents of corrosion in the porous layers. The capacitive loops as generated by the impedance layer exhibit the same trend. This demonstrates that the samples do not suffer from corrosion or corrode only to a very little extent. The Nyquist and Bode diagrams were fitted using the ZView software, and after a careful adjustment, equivalent circuit diagrams were obtained with the lowest fitting error (Supporting Information File 1, Figure S3).

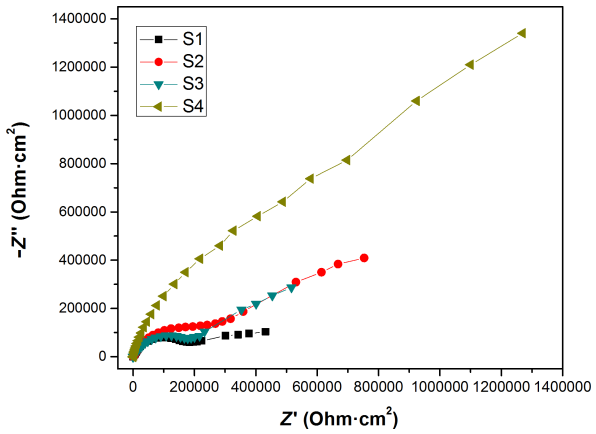

Figure 8: Nyquist diagram of the prepared samples.

As presented in Supporting Information File 1, Figure S3, the symbol *C* represents the capacitance, and CPE is the constant phase angle element that is used to refer to the electrical double-layer capacitance deviating from an ideal capacitance. The element with the capacitance *C* parallel to *R*1 designates the porous layer of the AAO film, while the other element with constant phase angle element parallel to *R*2 refers to the impedance layer in the AAO film. *R*2 represents the interfacial resistance of each blocking layer. The *R*2 values are presented for all the prepared samples in Table 5.

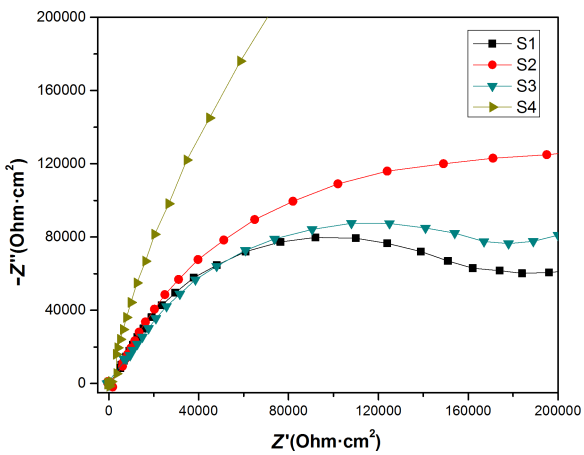

Figure 9: The zoomed portion of the high-frequency region of the Nyquist diagram for the various prepared samples.

The larger the value of CPE-P in the CPE is, the larger is the deviation of the artificial circuit capacitance from the theoretical capacitance, and the blocking layer of the sample S4 is closest to the theoretical capacitance among all the prepared samples. According to the results obtained via the electrical polarization and electrochemical measurements, the sample S3 possesses the best anti-corrosion performance.

Conclusion

This paper has presented the preparation of a series of Cu–SiO_2 NPs on a porous AAO film matrix by means of an alternating electrodeposition. As evidenced by SEM, XRD, EDS mapping, colorimetry, and electrochemical tests, both Cu and SiO_2 NPs are uniformly dispersed in the porous AAO film matrices, albeit

Table 5: Parameters obtained for each artificial circuit.

Sample[a]	Electrical impedance parameters				
	*C*1	*R*1 (Ω cm^2)	*CPE*1-*T*	*CPE*1-*P*	*R*2 (Ω cm^2)
S1	1.8593×10^{-4}	86302	2.3295×10^{-9}	3.0000	0.8407×10^{5}
S2	4.4100×10^{-3}	1.34700×10^{-3}	2.2645×10^{-12}	3.1870	1.1798×10^{5}
S3	7.1404×10^{-14}	22.15	1.4296×10^{-5}	0.6978	3.5171×10^{5}
S4	8.2153×10^{-7}	54.38	4.8482×10^{-6}	1.1470	5.1120×10^{5}

[a]Sample S1: u(*C*1) = 3×10^{-8}, u(*R*1) = 4, u(*CPE*1-*T*) = 2×10^{-13}, u(*CPE*1-*P*) = 5×10^{-4}, u(*R*2) = 60; Sample S2: u(*C*1) = 2×10^{-7}, u(*R*1) = 9×10^{-8}, u(*CPE*1-*T*) = 4×10^{-16}, u(*CPE*1-*P*) = 3×10^{-4}, u(*R*2) = 50; Sample S3: u(*C*1) = 5×10^{-18}, u(*R*1) = 0.02, u(*CPE*1-*T*) = 7×10^{-9}, u(*CPE*1-*P*) = 6×10^{-4}, u(*R*2) = 50; Sample S4: u(*C*1) = 3×10^{-11}, u(*R*1) = 0.04, u(*CPE*1-*T*) = 5×10^{-10}, u(*CPE*1-*P*) = 2×10^{-4}, u(*R*2) = 70.

with a low content. There is strong XRD peak indexed to Al, but characteristic diffraction peaks assigned to Cu cannot be observed in the XRD patterns of all the prepared samples, revealing the low concentration of Cu NPs within the AAO film matrix beyond the detection limit of the XRD equipment. Only the sample S3 shows an obvious color change under different angles of incident light, i.e., the dark purple color changes to light purple when the incident light angle is changed from 0° to 30°. The electrochemical impedance and polarization test results reveal that the sample S3 exhibits the best anti-corrosion performance due to the optimal electrodeposition processing, yielding the highest quality of hole sealing in the porous AAO film.

Supporting Information

Supporting Information File 1

Additional figures.
[https://www.beilstein-journals.org/bjnano/content/supplementary/2190-4286-10-73-S1.pdf]

Acknowledgements

The authors greatly appreciate National Natural Science Foundation of China (21671038, 51702050), the key Project of the Department of Education of Guangdong Province (2016GCZX008), the Featured Innovation Project of the Department of Education of Guangdong Province (2017KTSCX188), and the Open Research Foundation of Guangdong Provincial Key Laboratory of New and Renewable Energy Research and Development (Y807s31001).

References

1. Boinovich, L. B.; Modin, E. B.; Sayfutdinova, A. R.; Emelyanenko, K. A.; Vasiliev, A. L.; Emelyanenko, A. M. *ACS Nano* **2017,** *11,* 10113–10123. doi:10.1021/acsnano.7b04634
2. Wei, H. L.; Elmer, J. W.; DebRoy, T. *Acta Mater.* **2017,** *126,* 413–425. doi:10.1016/j.actamat.2016.12.073
3. Chen, K.; Scales, M.; Kyriakides, S. *Int. J. Mech. Sci.* **2018,** *138–139,* 476–488. doi:10.1016/j.ijmecsci.2018.02.002
4. Chang, M.; Wei, H.; Chen, D.; Hu, H.; Zhang, Y.; Ye, X.; Zeng, K.; Li, D. *Nano Res. Appl.* **2017,** *3,* 2. doi:10.21767/2471-9838.100024
5. Wei, H.; Hu, H.; Chang, M.; Zhang, Y.; Chen, D.; Wang, M. *Ceram. Int.* **2017,** *43,* 12472–12479. doi:10.1016/j.ceramint.2017.06.117
6. Oddone, V.; Boerner, B.; Reich, S. *Sci. Technol. Adv. Mater.* **2017,** *18,* 180–186. doi:10.1080/14686996.2017.1286222
7. Mrad, M.; Ben Amor, Y.; Dhouibi, L.; Montemor, M. F. *Surf. Coat. Technol.* **2018,** *337,* 1–11. doi:10.1016/j.surfcoat.2017.12.053
8. Mugada, K. K.; Adepu, K. *J. Manuf. Processes* **2018,** *32,* 625–634. doi:10.1016/j.jmapro.2018.03.034
9. Edalati, K.; Horita, Z.; Valiev, R. Z. *Sci. Rep.* **2018,** *8,* 6740. doi:10.1038/s41598-018-25140-1
10. Fu, J.; Wang, S.; Wang, K. *J. Mater. Sci.* **2018,** *53,* 9790–9805. doi:10.1007/s10853-018-2246-z
11. Martinez, N.; Kumar, N.; Mishra, R. S.; Doherty, K. J. *J. Mater. Sci.* **2018,** *53,* 9273–9286. doi:10.1007/s10853-018-2201-z
12. Mrad, M.; Dhouibi, L.; Montemor, M. F. *Prog. Org. Coat.* **2018,** *121,* 1–12. doi:10.1016/j.porgcoat.2018.04.005
13. Seki, Y.; Ebihara, K. Surface-treated aluminum material and zinc-supplemented aluminum alloy. U.S. Patent US20170137956A1, May 18, 2017.
14. Gao, W.; Rigout, M.; Owens, H. *Appl. Surf. Sci.* **2016,** *380,* 12–15. doi:10.1016/j.apsusc.2016.02.106
15. Zhao, X.; Meng, G.; Xu, Q.; Han, F.; Huang, Q. *Adv. Mater. (Weinheim, Ger.)* **2010,** *22,* 2637–2641. doi:10.1002/adma.200904370
16. Zhang, S.-Y.; Xu, Q.; Wang, Z.-J.; Hao, S.-Z.; Sun, C.-X.; Ma, W.-J. *Surf. Coat. Technol.* **2018,** *346,* 48–52. doi:10.1016/j.surfcoat.2018.04.052
17. Liang, C.-J.; Huang, K.-Y.; Hung, L.-T.; Su, C.-Y. *Surf. Coat. Technol.* **2017,** *319,* 170–181. doi:10.1016/j.surfcoat.2017.04.011
18. Wei, H.; Chen, D.; Hu, H.; Chang, M.; Ye, X.; Wang, M. *RSC Adv.* **2017,** *7,* 55653–55667. doi:10.1039/c7ra10633e
19. Tong, L.; Qi, W.; Wang, M.; Huang, R.; Su, R.; He, Z. *Small* **2016,** *12,* 3433–3443. doi:10.1002/smll.201600148
20. Kinoshita, S.; Yoshioka, S.; Miyazaki, J. *Rep. Prog. Phys.* **2008,** *71,* 076401. doi:10.1088/0034-4885/71/7/076401
21. Liu, Y.; Chang, Y.; Ling, Z.; Hu, X.; Li, Y. *Electrochem. Commun.* **2011,** *13,* 1336–1339. doi:10.1016/j.elecom.2011.08.008
22. Shi, P.; Wang, F.; Zhu, J.; Zhang, B.; Zhao, T.; Wang, Y.; Qin, Y. *Ceram. Int.* **2017,** *43,* 2943–2949. doi:10.1016/j.ceramint.2016.11.019

23. Yang, S. M.; Gu, J. J.; Qi, Y. K. The study on structural color of porous anodic alumina thin film fabricated in phosphoric electrolyte. In *Electronics, Electrical Engineering and Information Science;* Wang, J.; Li, X., Eds.; World Scientific Publishing Co Pte Ltd: Singapore, 2016; pp 975–982. doi:10.1142/9789814740135_0100
24. Gao, W.; Rigout, M.; Owens, H. *J. Nanopart. Res.* **2017,** *19,* 303. doi:10.1007/s11051-017-3991-7
25. Xu, Q.; Sun, H.-Y.; Yang, Y.-H.; Liu, L.-H.; Li, Z.-Y. *Appl. Surf. Sci.* **2011,** *258,* 1826–1830. doi:10.1016/j.apsusc.2011.10.054
26. Xu, Q.; Yang, Y.-H.; Liu, L.-H.; Gu, J.-J.; Liu, J.-J.; Li, Z.-Y.; Sun, H.-Y. *J. Electrochem. Soc.* **2011,** *159,* C25–C28. doi:10.1149/2.016201jes
27. Xu, Q.; Yang, Y.; Gu, J.; Li, Z.; Sun, H. *Mater. Lett.* **2012,** *74,* 137–139. doi:10.1016/j.matlet.2012.01.076
28. Yavuz, G.; Zille, A.; Seventekin, N.; Souto, A. P. *Carbohydr. Polym.* **2018,** *193,* 343–352. doi:10.1016/j.carbpol.2018.03.084
29. Jia, Y.; Zhang, Y.; Zhou, Q.; Fan, Q.; Shao, J. *Thin Solid Films* **2014,** *569,* 10–16. doi:10.1016/j.tsf.2014.08.022
30. Jia, Y.; Zhang, Y.; Liu, G.; Zhuang, G.; Fan, Q.; Shao, J. *J. Coat. Technol. Res.* **2015,** *12,* 1031–1039. doi:10.1007/s11998-015-9708-x
31. Jia, Y. R.; Shao, J. Z.; Fan, Q. G. *Adv. Mater. Res.* **2012,** *441,* 699–702. doi:10.4028/www.scientific.net/amr.441.699
32. Zhang, Z.; Zhang, J.; Hou, X.; Wu, T.; Sun, H. *Thin Solid Films* **2014,** *558,* 344–348. doi:10.1016/j.tsf.2014.03.044
33. Yuan, W.; Zhou, N.; Shi, L.; Zhang, K.-Q. *ACS Appl. Mater. Interfaces* **2015,** *7,* 14064–14071. doi:10.1021/acsami.5b03289
34. Li, Q.; Zeng, Q.; Shi, L.; Zhang, X.; Zhang, K.-Q. *J. Mater. Chem. C* **2016,** *4,* 1752–1763. doi:10.1039/c5tc04029a
35. Zeng, Q.; Ding, C.; Li, Q.; Yuan, W.; Peng, Y.; Hu, J.; Zhang, K.-Q. *RSC Adv.* **2017,** *7,* 8443–8452. doi:10.1039/c6ra26526j
36. Wang, Y.; Han, R.; Qi, L.; Liu, L.; Sun, H. *Appl. Opt.* **2016,** *55,* 10002. doi:10.1364/ao.55.010002
37. Liu, H.; Sun, H.; Liu, L.; Hou, X.; Jia, X. *Opt. Mater.* **2015,** *44,* 9–12. doi:10.1016/j.optmat.2015.02.017

License and Terms

BEILSTEIN JOURNAL OF NANOTECHNOLOGY

Synthesis of MnO_2–CuO–Fe_2O_3/CNTs catalysts: low-temperature SCR activity and formation mechanism

Yanbing Zhang*[1,2], Lihua Liu[1,2], Yingzan Chen[1,2], Xianglong Cheng[1,2], Chengjian Song[1,2], Mingjie Ding[1,2] and Haipeng Zhao*[1,2]

Full Research Paper

Open Access

Address:
[1]College of Materials and Chemical Engineering, Henan University of Urban Construction, Pingdingshan 467000, People's Republic of China and [2]Engineering Laboratory of Henan Province for Efficient Utilization of Coal Salt Resources, Pingdingshan 467000, People's Republic of China

Email:
Yanbing Zhang* - zyb481428@hncj.edu.cn; Haipeng Zhao* - zhaohaipeng@hncj.edu.cn

* Corresponding author

Keywords:
amorphous materials; carbon nanotubes; low-dimensional materials; low-temperature catalysis; SCR activity

Beilstein J. Nanotechnol. **2019,** *10,* 848–855.
doi:10.3762/bjnano.10.85

Received: 10 January 2019
Accepted: 29 March 2019
Published: 11 April 2019

This article is part of the thematic issue "Low-dimensional materials and systems".

Guest Editor: S. Walia

Abstract

MnO_2–CuO–Fe_2O_3/CNTs catalysts, as a low-dimensional material, were fabricated by a mild redox strategy and used in denitration reactions. A formation mechanism of the catalysts was proposed. NO conversions of 4% MnO_2–CuO–Fe_2O_3/CNTs catalyst of 43.1–87.9% at 80–180 °C were achieved, which was ascribed to the generation of amorphous MnO_2, CuO and Fe_2O_3, and a high surface-oxygen (O_s) content.

Introduction

Nitrogen oxides, NO_x (x = 1, 2), contribute to acid rain, photochemical smog, greenhouse effect and ozone depletion [1-3]. The selective catalytic reduction of NO with NH_3 (SCR), as a commercialized NO_x abatement technology, has received a great deal of attention [4,5]. However, the catalyst of the SCR reaction, V_2O_5+WO_3(MoO_3)/TiO_2, has some drawbacks, such as the toxic V-based material and the high operating temperature window (300–400 °C) [6-8]. Additionally, this kind of catalyst is easily influenced by ash and SO_2, which makes it necessary to be installed downstream of electrostatic precipitator and desulfurizer, where the flue gas temperature is normally below 200 °C [9]. Therefore, it is of importance to develop a SCR catalyst with high catalytic activity below 200 °C.

Carbon nanotubes (CNTs), a low-dimensional material, exhibit a one-dimensional tubular structure and outstanding chemical and physical properties. Hence, they are extensively studied for the application in SCR, e.g., in MnO_x/CNTs [10], Mn–CeO_x/CNTs [11] and CuO_x/carbonaceous-materials catalysts [12]. However, the working temperature window of these SCR catalysts is still between 200 and 300 °C.

A series of Cu-based [12,13] and (Mn + Fe)-based [14,15] catalysts have been applied in the SCR reaction and presented good catalytic activity. Nevertheless, the preparation procedures of the catalysts always need high-temperature calcination or high-pressure hydrothermal reactions, which are uneconomic and unsafe. Our previous studies, including MnO_2–Fe_2O_3–CeO_2–Ce_2O_3/CNTs [16] and Ce_2O_3–CeO_2–CuO–MnO_2/CNTs [17] catalysts, have reported a simple and mild redox method for the preparation of ternary and quaternary catalysts, and the resultant catalysts show outstanding denitration activity at 80–180 °C. The mechanisms of above preparation method are redox reactions between MnO_4^- (from $KMnO_4$) and Cl^- (from $FeCl_3$ and $CeCl_3$), or Mn^{7+} and O^{2-} (from $KMnO_4$) as well as MnO_4^- (from the $KMnO_4$) and Cl^- (from $CeCl_3$). The generation of Cl^- anions in the preparation process can result in corrosion of the equipment. On the basis of the above issues, a redox method with the formation of HNO_3 between Mn^{7+} and O^{2-} (only from $KMnO_4$) was developed, and the passivation through HNO_3 can protect the metal equipment. This redox method yielded MnO_2–CuO–Fe_2O_3/CNTs catalysts, and the as-synthesized catalysts were applied in the SCR reaction at 80–180 °C.

Results and Discussion

Catalytic activity

Figure 1 shows the NO conversion as a function of temperature for the CNT-based catalysts. As shown in Figure 1, the NO conversion of MnO_2–CuO–Fe_2O_3/CNTs prepared by the mild method was better than that of Mn–Cu–FeO_x/CNTs-IWIM fabricated through incipient wetness impregnation, except for the 1% MnO_2–CuO–Fe_2O_3/CNTs, and reached 69.9–87.9% between 140 to 180 °C. The SCR activity over 4% MnO_2–CuO–Fe_2O_3/CNTs reached maximum values of 43.1–87.9% at 80–180 °C at a weight hourly space velocity of 280 $L \cdot g_{cat}^{-1} \cdot h^{-1}$.

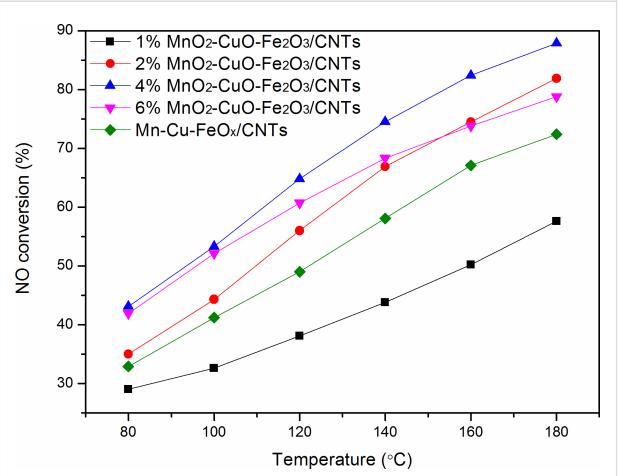

Figure 1: NO conversion as a function of the temperature over CNT-based catalysts. Reaction conditions: [NO] = [NH_3] = 400 ppm, [O_2] = 5%, N_2 as balance gas, WHSV=280 $L \cdot g_{cat}^{-1} \cdot h^{-1}$, 0.15 g catalyst.

X-ray diffraction measurements

Figure 2 shows the XRD patterns of the acid-treated CNTs and the as-synthesized catalysts. All samples present the characteristic diffraction peaks at 26.3°, 42.6° and 53.7°, corresponding to the (002), (100), and (004) planes of graphite, respectively [18]. For MnO_2–CuO–Fe_2O_3/CNTs, only a weak peak of MnO_2 (PDF#53-0633) can be observed when the loading was greater than or equal to 4%, whereas no diffraction peaks of metal oxides could be found, suggesting the formation of amorphous metal oxide phases. Amorphous catalytic materials are conducive to SCR activity [19], which is also shown in the results of NO conversion (Figure 1) and our previous studies [6,16,17]. In the case of Mn–Cu–FeO_x/CNTs-IWIM, a series of peaks corresponding to Mn_3O_4 (PDF#18-0803) can be seen. Metal oxide catalysts with higher crystallinity show a smaller catalytic activity [20]. This is corroborated by the results of NO conversion. Besides, the intensities of the graphite peaks declines with increased loading, which is due to the interaction between the metal oxide catalysts and CNTs [21-25].

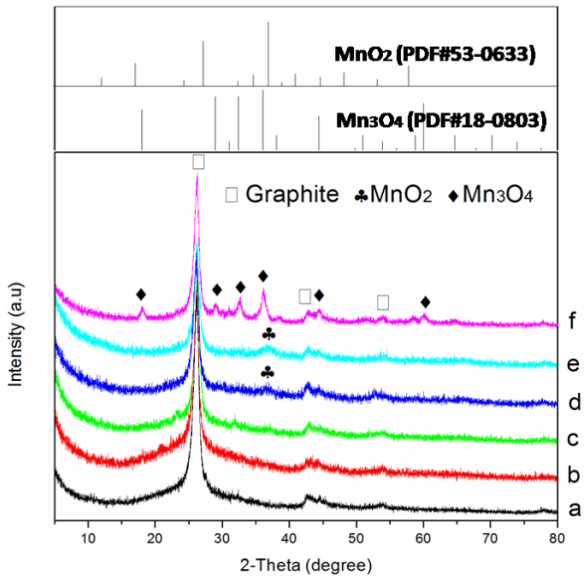

Figure 2: XRD patterns of the acid-treated CNTs and the as-synthesized catalysts: (a) acid-treated CNTs, (b) 1% MnO_2–CuO–Fe_2O_3/CNTs, (c) 2% MnO_2–CuO–Fe_2O_3/CNTs, (d) 4% MnO_2–CuO–Fe_2O_3/CNTs, (e) 6% MnO_2–CuO–Fe_2O_3/CNTs, and (f) Mn–Cu–FeO_x/CNTs-IWIM.

Transmission electron microscopy and energy dispersive X-ray spectrometry

The morphologies of the acid-treated CNTs and the catalysts were investigated by TEM and HRTEM (Figure 3). The acid-

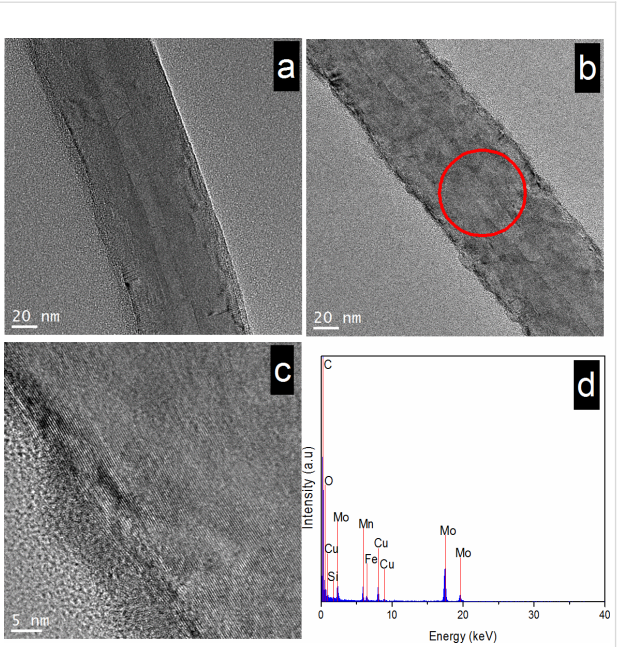

Figure 3: TEM and HRTEM images, as well as EDX spectrum of CNT-based samples: (a) CNTs, (b–d) 4% MnO_2–CuO–Fe_2O_3/CNTs.

treated CNTs have a smooth external surface (Figure 3a) that becomes coarse after being loaded with active metal oxide (Figure 3b). Additionally, the HRTEM images show the presence of catalysts nanoflakes, also verifying the generation of metal oxide catalysts on the CNT surface. The EDX spectrum (Figure 3d) shows signals of Mn, Cu, Fe, O and C. Clear lattice fringes of the metal oxides cannot be observed in the HRTEM images, indicating the generation of amorphous materials, which is consistent with the results of XRD (Figure 2).

X-ray photoelectron spectroscopy

The XPS spectra of the as-prepared catalysts are given in Figure 4. The elements Mn, Cu, Fe, C, and O were detected in the XPS full-scan spectrum of Figure 4A. For the Mn 2p spectrum of 4% MnO_2–CuO–Fe_2O_3/CNTs (Figure 4B), the binding energies at 654.2 and 642.4 eV, attributed to Mn $2p_{1/2}$ and Mn $2p_{3/2}$, respectively, can be observed. These values together with the energy separation of 11.8 eV demonstrate the formation of MnO_2 [26]. The high oxidation state of MnO_2 is advantageous to the SCR reaction [27], which is in accordance with the results of XRD and NO conversion measurements. The binding energies of Cu $2p_{1/2}$ and Cu $2p_{3/2}$ of the 4% MnO_2–CuO–Fe_2O_3/CNTs catalyst (Figure 4C) are located at 954.3 and 934.4 eV, respectively, along with satellites at higher energies, indicating the formation of CuO [28]. The energy separation between Cu $2p_{1/2}$ and Cu $2p_{3/2}$ is 19.9 eV, also demonstrating the generation of CuO [29]. The Auger spectrum of Cu (Figure 4D) presents a peak at 917.2 eV, typical for CuO [30,31].

In the Fe 2p spectra of 4% MnO_2–CuO–Fe_2O_3/CNTs and Mn–Cu–FeO_x/CNTs-IWIM (Figure 4E, spectrum a), the Fe $2p_{1/2}$ and Fe $2p_{3/2}$ peaks at 724.7 and 711.2 eV, respectively, can be attributed to Fe_2O_3 [32]. The energy separation of 13.5 eV is typical for Fe_2O_3 [33]. The two satellites at 732.7 and 718.4 eV also verify the formation of Fe_2O_3 [34]. In spectrum b of Figure 4E, the binding energies of Fe $2p_{1/2}$ and Fe $2p_{3/2}$ (724.4 and 711.0 eV) of the Mn–Cu–FeO_x/CNTs-IWIM catalyst appear at lower energies than those of 4% MnO_2–CuO–Fe_2O_3/CNTs catalyst, revealing the formation of Fe_3O_4 [35]. Moreover, the absence of any satellites further proved the presence of Fe_3O_4. It is noteworthy that Fe_2O_3 exhibits a better low-temperature SCR activity than Fe_3O_4 [36], which is corroborated by the NO conversion measurements.

The O 1s peak can be divided into three peaks (Figure 4F). The peak at 529.9 eV is attributed to lattice oxygen (designated as O_L), while the binding energies at 530.5–534.0 eV are ascribed to surface oxygen (labeled as O_S). The O_S content (Table S2, Supporting Information File 1) of the 4% MnO_2–CuO–Fe_2O_3/CNTs catalyst is 66.7%, whereas it is 36.8% in Mn–Cu–FeO_x/CNTs-IWIM catalyst. O_S has a higher mobility than O_L, which is in favor of the oxidation of NO to NO_2, accelerating the SCR reaction [37]. This was also confirmed by the results of NO conversion and of previous studies [6,16,17].

Scanning transmission electron microscopy

STEM and element mapping were adopted to further investigate the morphology of the catalyst. As shown in Figure 5a, bright dots associated to the metal elements can be found, indicating the formation of metal oxide catalysts on CNTs. The STEM-EDX mappings (Figure 5b–g) exhibit a series of columnar element-distribution images, further proving that the metal oxide catalysts have been successfully loaded on the CNTs.

Hydrogen temperature-programmed reduction analysis

In SCR reaction, the redox performance of the catalyst plays a significant role in the catalytic cycle. Therefore, the reducibility of the as-obtained catalysts was evaluated by using hydrogen temperature-programmed reduction (H_2-TPR). The results are listed in Figure 6. The catalysts exhibits three reduction peaks. For 4% MnO_2–CuO–Fe_2O_3/CNTs catalyst (Figure 6a), the peaks at 150–300 °C (centered at 249 °C) are overlapping reduction peaks of MnO → Mn_2O_3 [26] and CuO → Cu_2O [12,38,39]. The reduction peaks between 300–380 °C are overlapping peaks of Mn_2O_3 → Mn_3O_4 → MnO [26] and Cu_2O → Cu [12]. Moreover, a reduction peak could be found at 580 °C, which is attributed to the oxygen groups on the CNT surface. For the Mn–Cu–FeO_x/CNTs-IWIM catalyst

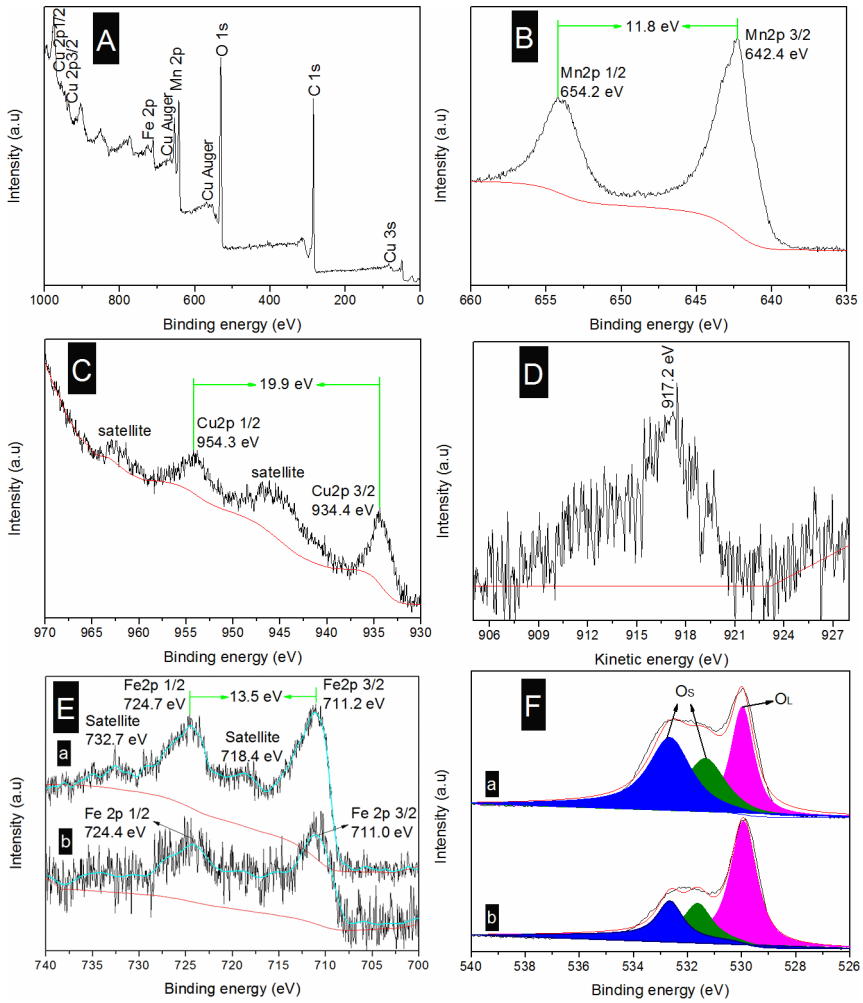

Figure 4: XPS results of the as-prepared catalysts: (A) XPS full-scan spectrum, (B) Mn 2p, (C) Cu 2p, and (D) Cu Auger spectra of 4% MnO_2–CuO–Fe_2O_3/CNTs; (E) Fe 2p and (F) O 1s spectra for (a) 4% MnO_2–CuO–Fe_2O_3/CNTs and (b) Mn–Cu–FeO_x/CNTs-IWIM.

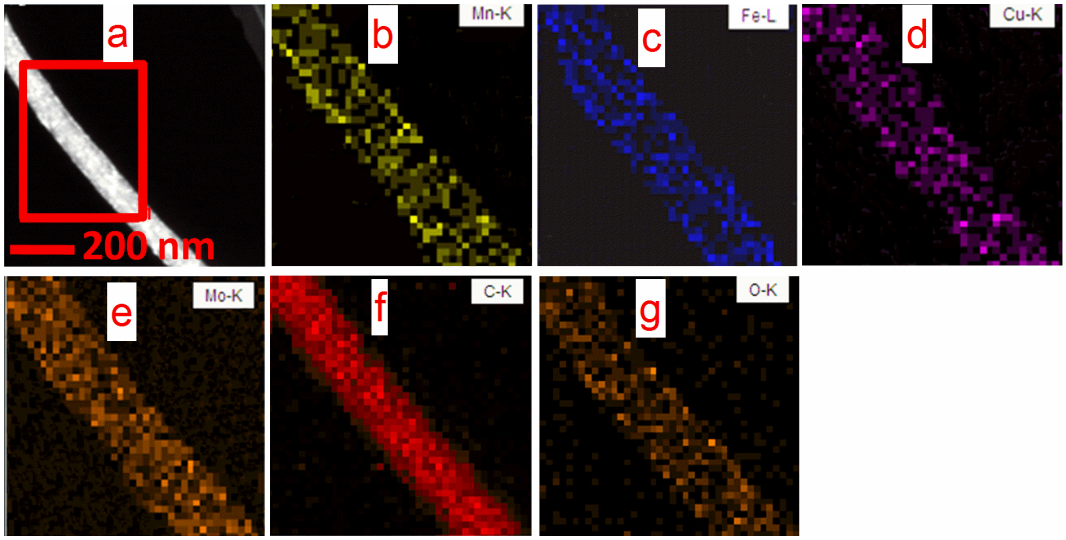

Figure 5: (a) STEM images and (b–g) element mappings of 4% MnO_2–CuO–Fe_2O_3/CNTs.

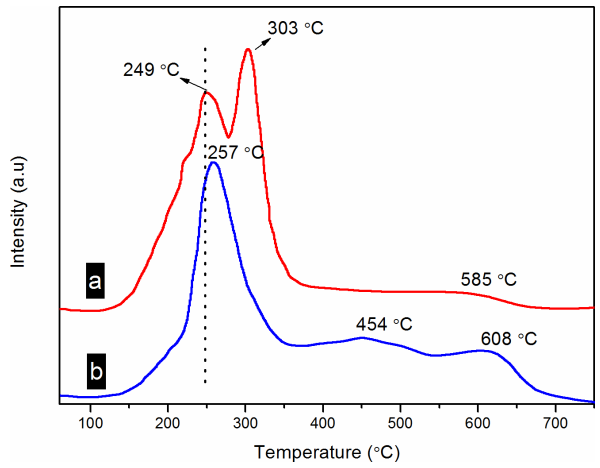

Figure 6: H_2-TPR curves of two catalysts: (a) 4% MnO_2–CuO–Fe_2O_3 / CNTs and (b) Mn–Cu–FeO_x/CNTs-IWIM.

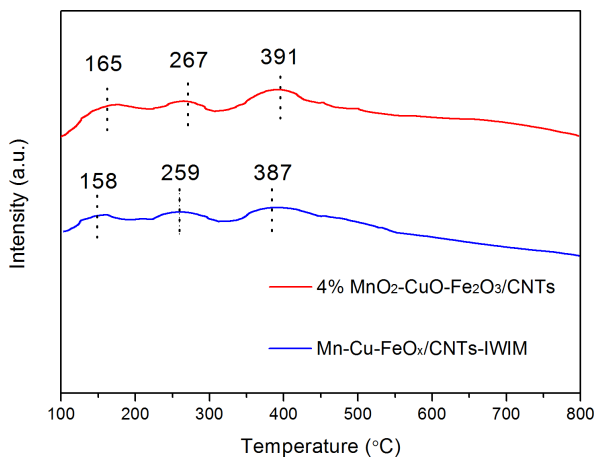

Figure 7: NH_3-TPD curves of 4% MnO_2–CuO–Fe_2O_3/CNTs and Mn–Cu–FeO_x/CNTs-IWIM catalysts.

(Figure 6b), the centers of the first and second reduction peaks (257 and 454 °C) were all at higher temperatures than those of 4% MnO_2–CuO–Fe_2O_3/CNTs catalyst. This means that the reducibility is lower compared with that of 4% MnO_2–CuO–Fe_2O_3/CNTs.

Ammonia temperature-programmed desorption analysis

The chemisorption and activation of NH_3 on the surface acid sites of a catalyst are generally viewed as the primary processes in the SCR of NO. Therefore, ammonia temperature-programmed desorption (NH_3-TPD) measurements were carried out and the results are shown in Figure 7. The two catalysts presents three desorption peaks of NH_3 corresponding to weak, intermediate and strong acid sites. For 4% MnO_2–CuO–Fe_2O_3/CNTs catalyst, the centers of the three desorption peaks of NH_3 are located at 165, 267 and 391 °C. These values are higher than those of Mn–Cu–FeO_x/CNTs-IWIM catalyst (158, 259 and 387 °C), which means that the acid sites are stronger in 4% MnO_2–CuO–Fe_2O_3/CNTs catalyst [11]. In addition, the number of Brønsted acid sites and Lewis acid sites at low and high temperature of the 4% MnO_2–CuO–Fe_2O_3/CNTs catalyst is higher than that of the MnO_2–CuO–Fe_2O_3/CNTs catalyst [40]. In general, stronger acid sites and a higher number of acid sites are advantageous to the SCR reaction [41], which is corroborated by the results of the NO conversion.

Cyclic and long-term stability of catalysts

In practical applications, the cyclic and long-term stability of a catalyst are crucial factors. The cyclic and long-term stability of the optimal 4% MnO_2–CuO–Fe_2O_3/CNTs catalyst are listed in Figure 8. Figure 8A shows that the catalytic activity of 4% MnO_2–CuO–Fe_2O_3/CNTs in run 2 and run 3 reaches 44.5–88.4% at 80–180 °C, which is similar with to the catalytic

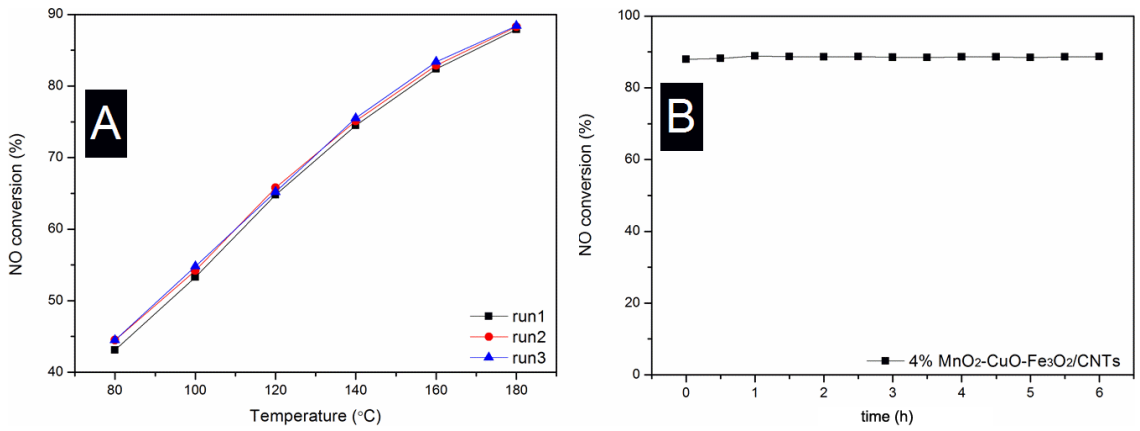

Figure 8: Cyclic and long-term stabilities of 4% MnO_2–CuO–Fe_2O_3/CNTs catalyst.

activity of 4% MnO_2–CuO–Fe_2O_3/CNTs in run 1 (43.1–87.9%), suggesting an excellent cyclic stability of the catalyst. Figure 8B shows that the catalytic activity of 4% MnO_2–CuO–Fe_2O_3/CNTs exhibits no obvious changes and reaches up to 87.9% at 180 °C during a test of 6 h, revealing the outstanding long-term stability. In view of the above favorable properties, the 4% MnO_2–CuO–Fe_2O_3/CNTs catalyst will be potentially applicable in the low-temperature NO reduction with NH_3.

Comparison of the catalytic performance of three catalysts

Table 1 shows three catalysts with excellent performance in the low-temperature NO reduction with NH_3, but the chemical reactions during preparation are different. The 6% Ce_2O_3–CeO_2–CuO–MnO_2/CNTs and 4% MnO_2–Fe_2O_3–CeO_2–Ce_2O_3/CNT catalysts present outstanding denitration efficiency values over the test temperature range, but Cl^- anions are formed in the preparation process, which might lead to a corrosion of metal equipment. The 4% MnO_2–CuO–Fe_2O_3/CNTs catalyst reaches NO conversions of 43.1–87.9% at 80–180 °C, which is similar to two catalysts in our previous papers. Moreover, HNO_3 is formed in the preparation process, which leads to an inactivation of the metal equipment.

The generation mechanism for the MnO_2–CuO–Fe_2O_3/CNTs catalyst

A reaction mechanism of the synthesis of the MnO_2–CuO–Fe_2O_3/CNTs catalystis proposed. Based on the results of XRD and XPS, active components of MnO_2, CuO, and Fe_2O_3 are formed. The following formation mechanism was inferred: Cu^{2+} and Fe^{3+} ions are first adsorbed on the surface of acid-treated CNTs via electrostatic interaction. Then the $Cu(NO_3)_2$ and $Fe(NO_3)_3$ are partly hydrolyzed in situ into $Cu(OH)_2$, $Fe(OH)_3$, and HNO_3 on the CNTs. Afterwards, MnO_2 is formed through the reaction between $KMnO_4$ and HNO_3, and the hydrolysis process is accelerated. MnO_2–$Cu(OH)_2$–$Fe(OH)_3$/CNTs samples are obtained, and the MnO_2–CuO_2–Fe_2O_3/CNTs catalysts are prepared through thermal dehydration of the MnO_2–$Cu(OH)_2$–$Fe(OH)_3$/CNTs samples [42,43]. The detailed reaction equations are:

$$Cu(NO_3)_2 + 2H_2O \rightleftharpoons Cu(OH)_2\downarrow + 2HNO_3$$
$$4HNO_3 + 4KMnO_4 \longrightarrow 4MnO_2\downarrow + 4KNO_3 + 2H_2O + 3O_2\uparrow$$
sum: (1)
$$2Cu(NO_3)_2 + 4KMnO_4 + 2H_2O \longrightarrow 2Cu(OH)_2\downarrow + 4MnO_2\downarrow + 3O_2\uparrow + 4KNO_3$$

$$Fe(NO_3)_3 + 3H_2O \rightleftharpoons Fe(OH)_3\downarrow + 3HNO_3$$
$$4HNO_3 + 4KMnO_4 \longrightarrow 4MnO_2\downarrow + 4KNO_3 + 2H_2O + 3O_2\uparrow$$
sum: (2)
$$4Fe(NO_3)_3 + 12KMnO_4 + 6H_2O \longrightarrow 4Fe(OH)_3\downarrow + 12MnO_2\downarrow + 9O_2\uparrow + 12KNO_3$$

$(1)+(2)$ total reaction:
$$2Cu(NO_3)_2 + 4Fe(NO_3)_3 + 16KMnO_4 + 8H_2O \longrightarrow 2Cu(OH)_2\downarrow + 4Fe(OH)_3\downarrow + 16MnO_2\downarrow + 12O_2\uparrow + 16KNO_3$$ (3)
thermal dehydration:
$$2Cu(OH)_2 + 4Fe(OH)_3 + 16MnO_2 \xrightarrow{\Delta} 2CuO + 2Fe_2O_3 + 16MnO_2 + 8H_2O\uparrow$$

Conclusion

MnO_2–CuO–Fe_2O_3/CNTs catalysts were synthesized via a mild preparation method. The 4% MnO_2–CuO–Fe_2O_3/CNTs catalyst showed the optimum low-temperature catalytic activity at 80–180 °C with a weight hourly space velocity of 280 $L{\cdot}g_{cat}^{-1}{\cdot}h^{-1}$, benefitting from its amorphous metal oxide catalysts as well as high surface-oxygen content. The mild preparation conditions of the MnO_2–CuO–Fe_2O_3/CNTs catalyst, can also provide a promising application in other catalytic fields.

Experimental

Materials

The raw CNTs (multi-wall) of 60–100 nm in diameter were purchased from Shenzhen Nanoport Company (China). $KMnO_4$ (AR), $Cu(NO_3)_2{\cdot}3H_2O$ (AR), $Fe(NO_3){\cdot}9H_2O$ (AR) and ethanol (AR) were purchased from Shanghai Chemical Reagent Ltd. All chemical were used without further purification. Deionized water with a resistivity above 18.0 MΩ·cm was obtained from a JL-RO100 Millipore-Q Plus.

Table 1: Catalytic performance of three catalysts.

catalyst	NO conversion at 80–180 °C and 180 °C (%)		weight hourly space velocity ($L{\cdot}g_{cat}^{-1}{\cdot}h^{-1}$)
4% MnO_2–CuO–Fe_2O_3/CNTs	43.1–87.9	87.9	280
6% Ce_2O_3–CeO_2–CuO–MnO_2/CNTs [17]	66.0–85.0	85.0	280
4% MnO_2–Fe_2O_3–CeO_2–Ce_2O_3/CNT [16]	52.8–99.4	99.4	210

Modification of CNTs and the synthesis of MnO_2–CuO–Fe_2O_3/CNTs catalysts

The raw CNTs were first treated with HNO_3 (65–68%) for 4 h at 140 °C, and then washed with deionized water and ethanol until pH 7. Finally, the solid product was dried at 70 °C for 12 h and grinded in an agate mortar.

First, acid-treated CNTs, $Cu(NO_3)_2{\cdot}3H_2O$, and $Fe(NO_3){\cdot}9H_2O$ were dispersed in 40 mL deionized water under stirring for 12 h. Afterward, 40 mL of $KMnO_4$ solution was added under continuous stirring at room temperature for another 12 h. Subsequently, the solid product was obtained by filtration, and washed with deionized water and ethanol until pH 7. Finally, the product was dried at 105 °C in air for 10 h. The as-prepared catalyst is denoted as *y* MnO_2–CuO–Fe_2O_3/CNTs, where *y* represents the molar ratio of [$KMnO_4$ + $Cu(NO_3)_2$ + $Fe(NO_3)_3$]/CNTs. For further details see [17]. The detailed molar ratios of precursors of 4% MnO_2–CuO–Fe_2O_3/CNTs catalyst were obtained as follows: A molar ratio of 16 $KMnO_4$:4$Fe(NO_3)_3$:2$Cu(NO_3)_2$ is obtained from Equations 1–3, and the molar ratio of [$KMnO_4$ + $Cu(NO_3)_2$ + $Fe(NO_3)_3$]/CNTs = 4%. The mass of CNTs is 0.3 g (0.025 mol). The total amount of substance is then [$KMnO_4$ + $Cu(NO_3)_2$ + $Fe(NO_3)_3$] = 4% × 0.025 mol = 0.001 mol. The amount of substance of $KMnO_4$, $Cu(NO_3)_2$, and $Fe(NO_3)_3$ is 0.0007273 mol $KMnO_4$, 0.0000909 mol $Cu(NO_3)_2$, and 0.0001818 mol $Fe(NO_3)_3$. For a comparative experiment, incipient wetness impregnation [44,45], as a common preparation method of catalysts, was applied to fabricate the Mn–Cu–FeO_x/CNTs-IWIM catalyst with an optimal load of 4%.

Characterization techniques

X-ray diffraction (XRD) was measured with an X'Pert Pro MPD X-ray diffractometer using Cu Kα radiation (λ = 0.15406 nm) with a 2θ range from 5° to 80°. Transmission electron microscopy (TEM) was performed on a JEOL model JEM 2010 EX instrument. Temperature-programmed reduction by H_2 (H_2-TPR) was assessed by using a custom-built TCD apparatus. Before the H_2-TPR test, 50 mg catalyst was firstly purged in N_2 at 200 °C for 1.5 h. The test was carried out in N_2 (containing 6% H_2) with a heating rate of 10 °C/min. X-ray photoelectron spectroscopy (XPS) was carried on a Thermo Scientific ESCALAB 250 spectrometer equipped with a dual Al/Mg anode (0.6 eV resolution).

Catalytic activity

The SCR activity tests were carried out in a fixed-bed quartz reactor using 0.15 g catalyst in each test. The reaction gas consisted of [O_2] = 5%, [NO] = [NH_3] = 400 ppm, balanced by N_2 gas. The total flow rate was 700 mL/min equivalent to a weight hourly space velocity (WHSV) of 280 $L{\cdot}g_{cat}^{-1}{\cdot}h^{-1}$. A flue-gas analyzer (Kane International Limited, KM950) equipped with the NO, NO_2, SO_2, and O_2 sensors was used to monitor the gas concentration. All data were recorded after 30 min till the catalytic reaction reached a steady state.

Supporting Information

Supporting Information File 1

Additional experimental data.
[https://www.beilstein-journals.org/bjnano/content/supplementary/2190-4286-10-85-S1.pdf]

Acknowledgements

This work was funded by Scientific and Technological Program-Funded Project of Fuzhou City (Grant No. 2015H0016), as well as Engineering Laboratory of Henan Province for Efficient Utilization of Coal Salt Resources.

ORCID® iDs

Yingzan Chen - https://orcid.org/0000-0002-2100-1681

References

1. Jiang, H.; Zhou, J.; Wang, C.; Li, Y.; Chen, Y.; Zhang, M. *Ind. Eng. Chem. Res.* **2017,** *56,* 3542–3550. doi:10.1021/acs.iecr.6b03568
2. Liu, Z.; Feng, X.; Zhou, Z.; Feng, Y.; Li, J. *Appl. Surf. Sci.* **2018,** *428,* 526–533. doi:10.1016/j.apsusc.2017.09.175
3. Zha, K.; Kang, L.; Feng, C.; Han, L.; Li, H.; Yan, T.; Maitarad, P.; Shi, L.; Zhang, D. *Environ. Sci.: Nano* **2018,** *5,* 1408–1419. doi:10.1039/c8en00226f
4. Andreoli, S.; Deorsola, F. A.; Pirone, R. *Catal. Today* **2015,** *253,* 199–206. doi:10.1016/j.cattod.2015.03.036
5. Kang, L.; Han, L.; He, J.; Li, H.; Yan, T.; Chen, G.; Zhang, J.; Shi, L.; Zhang, D. *Environ. Sci. Technol.* **2019,** *53,* 938–945. doi:10.1021/acs.est.8b05637
6. Zhang, Y.; Ding, M.; Song, C.; Lv, Y.; Zhao, H. *New J. Chem.* **2018,** *42,* 11273–11275. doi:10.1039/c8nj02269k
7. Zha, K.; Cai, S.; Hu, H.; Li, H.; Yan, T.; Shi, L.; Zhang, D. *J. Phys. Chem. C* **2017,** *121,* 25243–25254. doi:10.1021/acs.jpcc.7b08600
8. Yan, L.; Liu, Y.; Zha, K.; Li, H.; Shi, L.; Zhang, D. *ACS Appl. Mater. Interfaces* **2017,** *9,* 2581–2593. doi:10.1021/acsami.6b15527
9. Lu, X.; Song, C.; Chang, C.-C.; Teng, Y.; Tong, Z.; Tang, X. *Ind. Eng. Chem. Res.* **2014,** *53,* 11601–11610. doi:10.1021/ie5016969
10. Su, Y.; Fan, B.; Wang, L.; Liu, Y.; Huang, B.; Fu, M.; Chen, L.; Ye, D. *Catal. Today* **2013,** *201,* 115–121. doi:10.1016/j.cattod.2012.04.063
11. Zhang, L.; Zhang, D.; Zhang, J.; Cai, S.; Fang, C.; Huang, L.; Li, H.; Gao, R.; Shi, L. *Nanoscale* **2013,** *5,* 9821–9829. doi:10.1039/c3nr03150k
12. Li, Q.; Yang, H.; Ma, Z.; Zhang, X. *Catal. Commun.* **2012,** *17,* 8–12. doi:10.1016/j.catcom.2011.10.008
13. Zhu, Z.; Liu, Z.; Liu, S.; Niu, H.; Hu, T.; Liu, T.; Xie, Y. *Appl. Catal., B* **2000,** *26,* 25–35. doi:10.1016/s0926-3373(99)00144-7

14. Schill, L.; Putluru, S. S. R.; Fehrmann, R.; Jensen, A. D. *Catal. Lett.* **2014,** *144,* 395–402. doi:10.1007/s10562-013-1176-2
15. Li, H.; Zhang, D.; Maitarad, P.; Shi, L.; Gao, R.; Zhang, J.; Cao, W. *Chem. Commun.* **2012,** *48,* 10645–10647. doi:10.1039/c2cc34758j
16. Zhang, Y.; Zheng, Y.; Zou, H.; Zhang, X. *Catal. Commun.* **2015,** *71,* 46–50. doi:10.1016/j.catcom.2015.08.011
17. Zhang, Y.; Zheng, Y.; Chen, X.; Fu, B. *RSC Adv.* **2016,** *6,* 65392–65396. doi:10.1039/c6ra10482g
18. Xia, H.; Wang, Y.; Lin, J.; Lu, L. *Nanoscale Res. Lett.* **2012,** *7,* 33. doi:10.1186/1556-276x-7-33
19. Jiang, B.; Liu, Y.; Wu, Z. *J. Hazard. Mater.* **2009,** *162,* 1249–1254. doi:10.1016/j.jhazmat.2008.06.013
20. Wang, L.; Huang, B.; Su, Y.; Zhou, G.; Wang, K.; Luo, H.; Ye, D. *Chem. Eng. J.* **2012,** *192,* 232–241. doi:10.1016/j.cej.2012.04.012
21. Zhang, Y.; Xu, Z.; Wang, X.; Lu, X.; Zheng, Y. *Nano* **2015,** *10,* 1550050. doi:10.1142/s1793292015500502
22. Yang, G.; Zhao, H.; Luo, X.; Shi, K.; Zhao, H.; Wang, W.; Chen, Q.; Fan, H.; Wu, T. *Appl. Catal., B* **2019,** *245,* 743–752. doi:10.1016/j.apcatb.2018.12.080
23. Wang, T.; Wan, Z.; Yang, X.; Zhang, X.; Niu, X.; Sun, B. *Fuel Process. Technol.* **2018,** *169,* 112–121. doi:10.1016/j.fuproc.2017.09.029
24. Zhang, D.; Zhang, L.; Shi, L.; Fang, C.; Li, H.; Gao, R.; Huang, L.; Zhang, J. *Nanoscale* **2013,** *5,* 1127–1136. doi:10.1039/c2nr33006g
25. Wang, X.; Zheng, Y.; Xu, Z.; Liu, Y.; Wang, X. *Catal. Sci. Technol.* **2014,** *4,* 1738–1741. doi:10.1039/c4cy00026a
26. Wang, X.; Zheng, Y.; Xu, Z.; Wang, X.; Chen, X. *RSC Adv.* **2013,** *3,* 11539–11542. doi:10.1039/c3ra41512k
27. Kapteijn, F.; Singoredjo, L.; Andreini, A.; Moulijn, J. *Appl. Catal., B* **1994,** *3,* 173–189. doi:10.1016/0926-3373(93)e0034-9
28. Seo, C.-K.; Choi, B.; Kim, H.; Lee, C.-H.; Lee, C.-B. *Chem. Eng. J.* **2012,** *191,* 331–340. doi:10.1016/j.cej.2012.03.027
29. Li, F.; Liu, X.; Zhang, Q.; Kong, T.; Jin, H. *Cryst. Res. Technol.* **2012,** *47,* 1140–1147. doi:10.1002/crat.201200143
30. Ghijsen, J.; Tjeng, L. H.; van Elp, J.; Eskes, H.; Westerink, J.; Sawatzky, G. A.; Czyzyk, M. T. *Phys. Rev. B* **1988,** *38,* 11322–11330. doi:10.1103/physrevb.38.11322
31. Long, J.; Dong, J.; Wang, X.; Ding, Z.; Zhang, Z.; Wu, L.; Li, Z.; Fu, X. *J. Colloid Interface Sci.* **2009,** *333,* 791–799. doi:10.1016/j.jcis.2009.02.036
32. Yamashita, T.; Hayes, P. *Appl. Surf. Sci.* **2008,** *254,* 2441–2449. doi:10.1016/j.apsusc.2007.09.063
33. Qu, Z.; Miao, L.; Wang, H.; Fu, Q. *Chem. Commun.* **2015,** *51,* 956–958. doi:10.1039/c4cc06941b
34. Nasibulin, A. G.; Rackauskas, S.; Jiang, H.; Tian, Y.; Mudimela, P. R.; Shandakov, S. D.; Nasibulina, L. I.; Jani, S.; Kauppinen, E. I. *Nano Res.* **2009,** *2,* 373–379. doi:10.1007/s12274-009-9036-5
35. Seki, M.; Takahashi, M.; Adachi, M.; Yamahara, H.; Tabata, H. *Appl. Phys. Lett.* **2014,** *105,* 112105. doi:10.1063/1.4896316
36. Yao, G.-H.; Gui, K.-T.; Wang, F. *Chem. Eng. Technol.* **2010,** *33,* 1093–1098. doi:10.1002/ceat.201000015
37. Liu, F.; He, H.; Ding, Y.; Zhang, C. *Appl. Catal., B* **2009,** *93,* 194–204. doi:10.1016/j.apcatb.2009.09.029
38. Wan, Y.; Ma, J.; Wang, Z.; Zhou, W.; Kaliaguine, S. *Appl. Catal., B* **2005,** *59,* 235–242. doi:10.1016/j.apcatb.2004.12.014
39. Shi, L.; Chu, W.; Deng, S. *J. Nat. Gas Chem.* **2011,** *20,* 48–52. doi:10.1016/s1003-9953(10)60145-4
40. Jin, R.; Liu, Y.; Wu, Z.; Wang, H.; Gu, T. *Chemosphere* **2010,** *78,* 1160–1166. doi:10.1016/j.chemosphere.2009.11.049
41. Cai, S.; Hu, H.; Li, H.; Shi, L.; Zhang, D. *Nanoscale* **2016,** *8,* 3588–3598. doi:10.1039/c5nr08701e
42. Lu, C.; Qi, L.; Yang, J.; Zhang, D.; Wu, N.; Ma, J. *J. Phys. Chem. B* **2004,** *108,* 17825–17831. doi:10.1021/jp046772p
43. Au-Yeung, S. C. F.; Denes, G.; Greedan, J. E.; Eaton, D. R.; Birchall, T. *Inorg. Chem.* **1984,** *23,* 1513–1517. doi:10.1021/ic00179a009
44. Wang, X.; Zheng, Y.; Xu, Z.; Liu, X.; Zhang, Y. *Catal. Commun.* **2014,** *50,* 34–37. doi:10.1016/j.catcom.2014.02.016
45. Wang, X.; Zheng, Y.; Lin, J. *Catal. Commun.* **2013,** *37,* 96–99. doi:10.1016/j.catcom.2013.03.035

License and Terms

BEILSTEIN JOURNAL OF NANOTECHNOLOGY

Materials nanoarchitectonics at two-dimensional liquid interfaces

Katsuhiko Ariga*[1,2], Michio Matsumoto[1], Taizo Mori[1,2] and Lok Kumar Shrestha[1]

Review

Open Access

Address:
[1]WPI Research Center for Materials Nanoarchitectonics (MANA), National Institute for Materials Science (NIMS), 1-1 Namiki, Tsukuba, Ibaraki 305-0044, Japan and [2]Graduate School of Frontier Sciences, The University of Tokyo, 5-1-5 Kashiwanoha, Kashiwa, Chiba 277-8561, Japan

Email:
Katsuhiko Ariga* - ariga.katsuhiko@nims.go.jp

* Corresponding author

Keywords:
film; interface; low-dimensional material; nanoarchitectonics; self-assembly

Beilstein J. Nanotechnol. **2019,** *10,* 1559–1587.
doi:10.3762/bjnano.10.153

Received: 23 February 2019
Accepted: 16 July 2019
Published: 30 July 2019

This article is part of the thematic issue "Low-dimensional materials and systems".

Guest Editor: S. Walia

Abstract

Much attention has been paid to the synthesis of low-dimensional materials from small units such as functional molecules. Bottom-up approaches to create new low-dimensional materials with various functional units can be realized with the emerging concept of nanoarchitectonics. In this review article, we overview recent research progresses on materials nanoarchitectonics at two-dimensional liquid interfaces, which are dimensionally restricted media with some freedoms of molecular motion. Specific characteristics of molecular interactions and functions at liquid interfaces are briefly explained in the first parts. The following sections overview several topics on materials nanoarchitectonics at liquid interfaces, such as the preparation of two-dimensional metal-organic frameworks and covalent organic frameworks, and the fabrication of low-dimensional and specifically structured nanocarbons and their assemblies at liquid–liquid interfaces. Finally, interfacial nanoarchitectonics of biomaterials including the regulation of orientation and differentiation of living cells are explained. In the recent examples described in this review, various materials such as molecular machines, molecular receptors, block-copolymer, DNA origami, nanocarbon, phages, and stem cells were assembled at liquid interfaces by using various useful techniques. This review overviews techniques such as conventional Langmuir–Blodgett method, vortex Langmuir–Blodgett method, liquid–liquid interfacial precipitation, instructed assembly, and layer-by-layer assembly to give low-dimensional materials including nanowires, nanowhiskers, nanosheets, cubic objects, molecular patterns, supramolecular polymers, metal-organic frameworks and covalent organic frameworks. The nanoarchitecture materials can be used for various applications such as molecular recognition, sensors, photodetectors, supercapacitors, supramolecular differentiation, enzyme reactors, cell differentiation control, and hemodialysis.

Review

1 Introduction: nanoarchitectonics for low-dimensional materials

To realize a sustainable society, there are many challenges to overcome in the next 30 years: fulfilling the needs regarding energy consumption, reducing unnecessary emissions, protecting the environment, and maximizing the efficiency of processes [1]. Various molecular technologies including chemical syntheses [2-6], ultrafine fabrications [7-11], physical analyses [12-16], materials productions [17-24], energy and environmental improvements [25-31], and biotechnological and biomedical developments [32-37] have been explored to achieve these objectives. One of the common key concepts for all these developments is regulating functional molecular systems with high spatial precision, which can often induce the efficient production, transmission, and conversion of materials, energies, and information [38]. In those examples, anisotropies in spatially defined materials or systems trigger directional and efficient flows of signals and energies. Despite many reported examples to create highly sophisticated molecular systems, there is still only a limited number of examples in which functional molecular systems are oriented or spatially confined in the bulk [39]. From these viewpoints, functional materials with low-dimensionality become a relevant part of these technologies.

Low-dimensional materials have been extensively explored because they often exhibit unique and superior properties due to quantum effects and anisotropic effects [40-44] (Figure 1). Synthetic methodologies to yield nanoparticles and zero-dimensional materials have been developed using conventional chemical methods and/or physical perturbations such as microwave and plasma irradiation [45-51]. Carbon nanotubes, representative one-dimensional objects, were produced using catalysts as well [52-55]. Recently, two-dimensional materials such as graphene and MoS_2 nanosheets attracted the interests of researchers because of their superior electric/electrochemical properties that make them suitable for energy and electrochemical applications [56-60]. The works include the use of two-dimensional metal oxide nanosheets for artificial photosynthesis systems, i.e., photocatalytic water splitting and fixation of carbon dioxide, which were recently reviewed by Maeda and Mallouk [61].

Despite these many intriguing demonstrations of two-dimensional materials, most of the examples reported so far utilize two-dimensional sheet materials synthesized in a top-down manner, and there is only a limited number of examples using bottom-up approaches [62]. In bottom-up approaches low-dimensional materials are constructed from small precursors such as functional molecules in order to obtain novel low-dimensional materials with various functional units [63-68]. The essential processes within these bottom-up approaches are self-assembly and self-organization based on supramolecular chemistry [69]. These supramolecular mechanisms can be widely observed in various species including small molecules, nanomaterials, and biomolecules [70-75]. Despite this generality, there are still many nontrivial fundamental challenges, which are actively studied using the quantitative analysis of self-assembly processes proposed by Hiraoka [76] and the temporal control of supramolecular polymerization by Dhiman

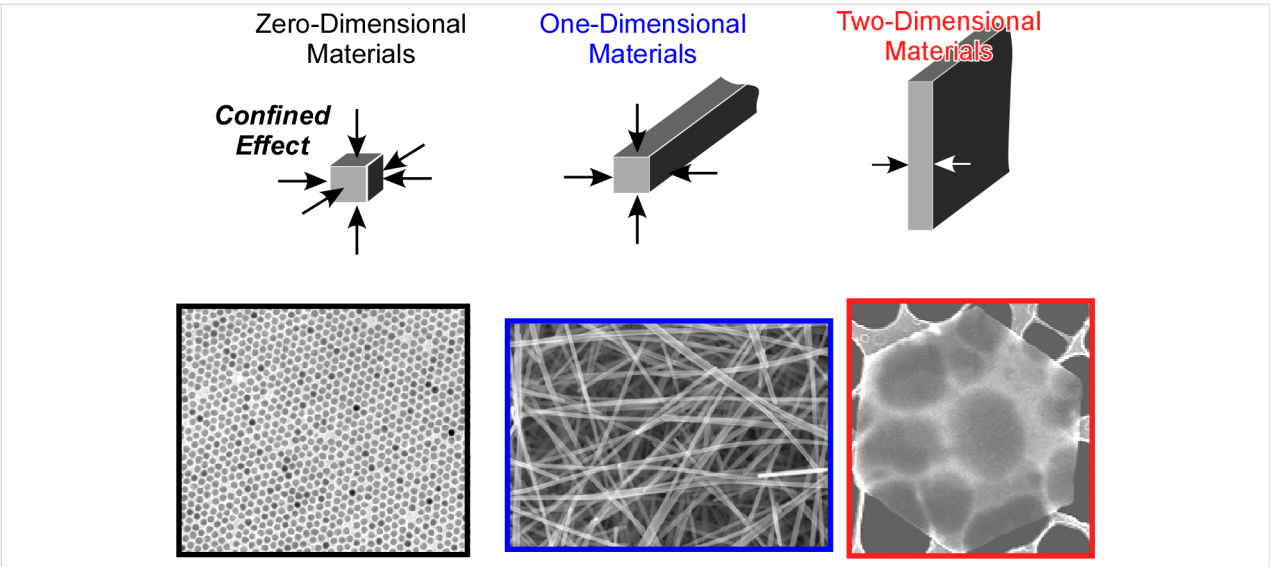

Figure 1: Various low-dimensional materials (zero-dimensional, one-dimensional, and two-dimensional materials) with morphology examples.

and George [77]. Shimizu summarized various parameters regulating the self-assembly of lipid molecules for producing structurally well-regulated one-dimensional nanotubes [78]. Self-assembled and polymerized materials are often used in sensing devices utilizing molecular imprinting mechanisms [79]. Two-dimensional films made of assemblies of ion-recognizing macrocyclic host molecules, ion-exchangers, and indicative dyes were incorporated in an optode system detecting caesium ions in tap water and seawater [80]. Photo-controllable molecular devices were successfully fabricated using two-dimensional self-assembled monolayer technology as recently reviewed by Suda [81].

Hierarchic functional systems fabricated with low-dimensional materials are actively investigated. For example, Lvov and co-workers reported the immobilization of small functional materials such as metal clusters and metal catalysts within one-dimensional halloysite clay nanotubes to make them work under appropriate protection from external disturbances [82-84]. Zhong and Xu summarized, in their recent review, the preparation of metal nanoparticles for hydrogen generation from liquid chemical hydrides [85]. In their review, the usage of effective catalysts within low-dimensional cages of metal-organic frameworks was reported. Jayavel, Shrestha, and co-workers demonstrated the enhanced performance of electrochemical supercapacitors using composites of cobalt oxide nanoparticles and reduced graphene oxide, which are zero-dimensional and two-dimensional nanomaterials, respectively [86]. Leong and co-workers reported a sophisticated strategy to realize chemotherapy targeting at cancer cells using the controlled assembly and disassembly of layer-by-layer hybrid structures made of two dimensional MoS_2 nanosheets with DNA [87].

The preparation of functional low-dimensional materials requires preservation of nanoscale features in their construction processes. This characteristic is also important in the emerging concept of nanoarchitectonics, which was initiated by Masakazu Aono in 2000 [88-91]. This concept is even regarded as the next step of nanotechnology combining various research disciplines such as organic synthesis, physical materials control, supramolecular chemistry, and biology [92-94]. In this concept, materials and systems can be engineered through the manipulation of atoms and molecules, self-assembly and self-organization, and field-controlled organization (Figure 2). Unlike the well-established microfabrication and other techniques at microscopic and macroscopic levels, the nanoarchitectonics procedures have to take into account several uncertainties such as thermal fluctuations, quantum effects, and uncontrolled mutual interactions at the nanoscale [95,96].

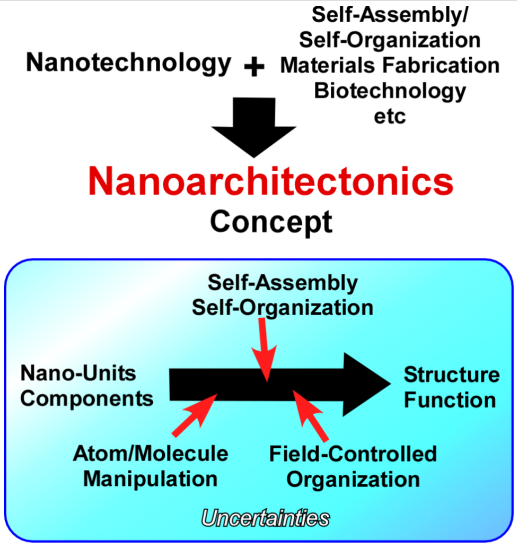

Figure 2: Outline of nanoarchitectonics strategies to obtain structures and functions through the manipulation of atoms and molecules, self-assembly and self-organization, and field-controlled organization.

Because of its general applicability, research approaches with the nanoarchitectonics concept are now seen in many recent publications in various fields including materials production [97,98], structural fabrication [99-108], sensing [109-112], energy applications [113-117], environmental protection [118,119], catalysts [120,121], biology [122-124], and biomedical applications [125,126]. For example, the following recent research works on low-dimensional materials have been carried out using the nanoarchitectonics concept: Hasegawa and co-workers used atom-manipulation nanoarchitectonics (controlled single atom/ion transfer) to regulate the number of dopant atoms in one-dimensional solid electrolyte nanodots (α-$Ag_{2+\delta}S$) [127]. The nanoarchitectonic construction of one-dimensional nanowires from II–VI semiconductors was demonstrated for the use as wavelength division multiplexer as reported by Yan, Zhao and co-workers [128]. Other one-dimensional functional structures such as porphyrin-functionalized DNA (by Stulz [129]), DNA-based complex structures for ultrasensitive mercury detection (by Govindaraju and co-workers [130]), self-assembled chiral twisted and helical nanofibers (by Liu and co-workers [131]), and supramolecular assemblies with short peptides and their bio-functions (by Yan and co-workers [132]) have been investigated. As examples of research efforts regarding two-dimensional nanoarchitectures, the enhanced reduction of nitrogen oxides by facet-engineered two-dimensional CuO petal assemblies (by Abe and co-workers [133]), perovskite nanosheets and their layer-by-layer assemblies as high-*k* dielectric/ferroelectric materials (by Osada and Sasaki [134]), the manipulation of transition-metal dichalcogenides nanosheets for the usage in energy storage/conversion applications (by Xu, Lee, and co-workers [135]) and substrate chan-

nelling between enzymes with graphene oxide nanosheets (by Yang and co-workers [136]) can be mentioned.

The nanoarchitectonics bottom-up approaches preserving the nanostructural properties are highly useful for the fabrication of low-dimensional materials and the subsequent construction of functional structures from low-dimensional materials. Especially, nanoarchitectonics fabrication in motional restricted and dimensionally confined media would be beneficial for the production of low-dimensional materials. Therefore, in this review article, we overview recent research progresses on materials nanoarchitectonics at two-dimensional liquid interfaces, which are dimensionally restricted media with certain degrees of motional freedom [137,138]. In the next section, specific features of molecular interactions and functions at liquid interfaces, as well as two-dimensional molecular patterning, are briefly explained. In the following sections, several topics of materials nanoarchitectonics at liquid interfaces such as the preparation of two-dimensional metal-organic frameworks (MOFs) and covalent organic frameworks (COFs), the fabrication of multi-dimensionally structured nanocarbons and their assemblies, and the interfacial nanoarchitectonics of biomaterials are exemplified.

2 Unique features of liquid interfaces and formation of two-dimensional patterns

2.1 Unique features of liquid interfaces

Gas–liquid interfaces and liquid–liquid interfaces are categorized as interfacial environments with certain degrees of freedom of molecular mobility (dynamism). These interfaces with liquids have several intrinsic features: (i) They are environments of two different phases; (ii) they exhibit a discontinuous change of the dielectric constant; (iii) they are highly directional environments restricting molecular motion only in the vertical direction. These features create several unique features that are described in the following.

Interfaces are generally formed by two immiscible phases. In many research examples utilizing liquid–liquid interfaces, the immiscible liquids dissolve different species that can only come into contact at the interface. At gas–liquid interfaces, insoluble components remain only at the interface and interact with other molecules (or materials) diffused from the underneath liquid phase. These circumstances can induce the generation of low-dimensional materials. In addition, physics and chemistry of molecular interactions at liquid interfaces are significantly different from those observed in homogeneous solutions [139-141].

Unique features of molecular interactions can be clearly observed at the air–water interface [142-144]. Although molecular recognition via hydrogen bonding are quite difficult in a highly polar aqueous media, the molecular recognition of sugars [145,146], peptides [147-149], amino acids [150], nucleic acid bases [151,152], and nucleotides [153,154] is accomplishable at the air–water interface even though this recognition relies on hydrogen bonding. Systematic studies on binding constants of a fixed recognition pair, phosphate and guanidinium ions, revealed a significant influence of the interfacial environment on the interactions between the molecules embedded at various interfaces (Figure 3) [155]. The binding constant between phosphate and guanidinium ions dispersed in water was reported as 1.4 M^{-1} [156]. Altering the recognition media to rather disorganized mesoscopic interfaces drastically increases the binding constants. The binding constants of phosphate derivatives to the surfaces of guanidinium-functionalized aqueous micelles and lipid bilayers reaches values of 10^2 to 10^4 M^{-1}. Surprisingly, the binding constant of the same recognition pair further increases to 10^6 to 10^7 M^{-1} when a macroscopic less dynamic interface, the air–water interface, is used as the recognition medium [157,158]. Similarly, strongly enhanced binding constants were commonly observed at the air–water interface for various recognition pairs.

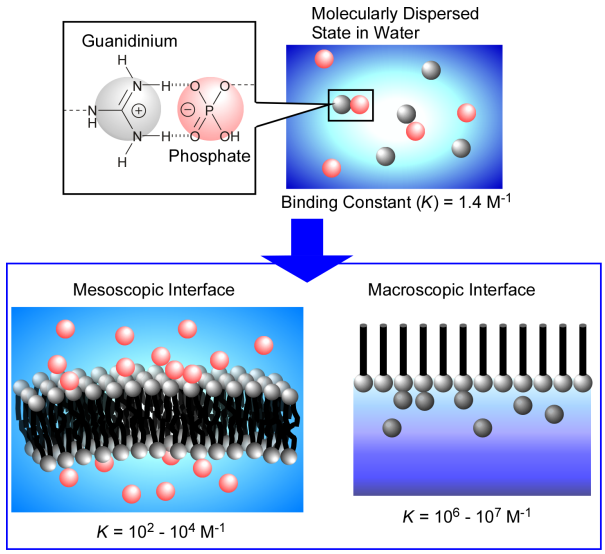

Figure 3: Systematic studies on binding constants for phosphate and guanidinium in different aqueous environments: 1.4 M^{-1} dispersed in water; 10^2 to 10^4 M^{-1} at disorganized mesoscopic interfaces; 10^6 to 10^7 M^{-1} at the macroscopic air–water interface. Adapted with permission from [144], copyright 2019 American Chemical Society.

Mechanisms enhancing the molecular interaction at the air–water interface were investigated through quantum chemical approaches [159-161]. As simply illustrated in Figure 4, simplified recognition-pair structures of phosphate and guanidinium were placed at a model interface of two phases with different dielectric constants of 2 (lipid phase) and 80 (water

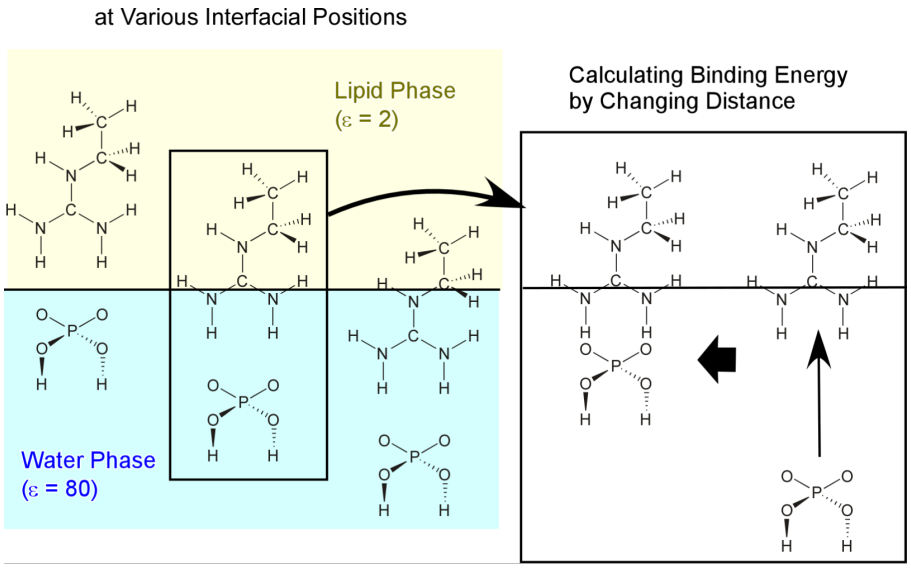

Figure 4: A model for calculations of the binding constant between guanidinium and phosphate at the air–water interface where the pair structures of phosphate and guanidinium are placed in a model of two phases with different dielectric constants of 2 (lipid phase) and 80 (water phase). The binding energy and binding constant was calculated while changing distance between guanidinium and phosphate.

phase). By fixing the position of the guanidinium moiety at the interface and changing the relative location of the phosphate functional group, the recognition energy was monitored as a function of the relative location. The most stable relative distance was estimated from the energy minimum in the energy diagram, and the binding energies and binding constants were calculated at those interfacial positions. A series of calculations revealed that large binding constants can be obtained when the binding site locates in the phase of the lower dielectric constant. In contrast, when the binding site was located to be deep in the phase of the higher dielectric constant, the binding constants were calculated to decrease significantly. Interestingly, sufficiently high binding constants were confirmed even when the hydrogen bonding sites were exposed to the high-dielectric medium at the very vicinity of the low-dielectric medium. These simulations hint at the mechanism of enhanced molecular recognition at these interfaces. The non-polar phase greatly contributes to enhance molecular recognition.

These facts may answer the question of biological molecular recognition in aqueous media, in which hydrogen bonding plays an essential role in realizing those highly sophisticated systems [162]. Molecular recognitions in biological systems occur mostly at interfaces including cell membrane surfaces, inner surfaces of receptor pockets in enzymes, and macromolecular interfaces of DNA. We expect materials nanoarchitectonics with features of enhanced molecular interactions to create low-dimensional materials at interfaces of two phases with different dielectric natures.

Another distinctive characteristic of liquid interfaces is the anisotropic environment regarding molecular motion. Certain degrees of motional freedom exist along the interfacial plane, which can be deformed at the macroscopic level (compression, expansion, and bending). In contrast, molecular motion is virtually inhibited in the vertical direction. Therefore, two significantly different scales of motion, macroscopic lateral motion and nanoscopic vertical motion, are connected at liquid interfaces [163-166]. For example, motion and function of molecular machines and molecular receptors in monolayers at the air–water interface can be controlled by macroscopic lateral motion such as mechanical compression and expansion of the monolayers. Macroscopic mechanical deformation of the interfacial media at the scale of centimetres or metres can regulate nanometre-scale conformational changes of the molecular machines, for instance, to capture and release guest molecules [167,168], to rotate of molecular rotors [169,170], to open and close molecular pliers [171,172], or in indicator displacement assays of glucose based on fluorescence resonance energy transfer [173]. Subtle conformational changes of molecular receptors at the air–water interface results in a change of the chiral selectivity towards aqueous amino acids [174,175], or of the optimum guest structure from thymine to uracil derivatives [176,177]. Regulation of molecular interaction at liquid interfaces yields a novel concept for the molecular tuning of functions [178-180]. This is a new concept beyond the following well-known important concepts: the 1st generation of molecular recognition at the most stable state (basics for supramolecular chemistry, Nobel prize in 1987 [181-183]); the 2nd genera-

tion molecular controls based on external stimuli switching [184-188] (basics for molecular machines, Nobel prize in 2016 [189-191]). The anisotropic dynamics at liquid interfaces described above are expected to play a crucial role in the production of low-dimensional materials and systems.

2.2 Two-dimensional molecular patterning and production of low-dimensional materials

Enhanced molecular interaction and two-dimensionally confined motion at liquid interfaces are advantageous for the fabrication of two-dimensional patterned structures with high structural precision [192,193]. In the case exemplified in Figure 5, flavin adenine dinucleotide (FAD) was dissolved in an aqueous subphase [194,195]. FAD can bind specifically to two monolayer components, a guanidinium lipid or an orotate lipid. These molecules bind site-specifically to the phosphate moieties or the adenosine part, respectively. Lateral compression of the complexed monolayer finally results in two-dimensional regular molecular patterns. The difference between the molecular lengths of the guanidinium/phosphate and orotate/adenosine pairs yields regular dip patterns with sub-nanometre precision. Similar methodologies, i.e., crystallinity controlled two-dimensional patterns based on guanidinium/carboxylate molecular recognition [196] and the two-dimensional assembly of one-dimensional supramolecular polymers formed between alkylated melamine and aqueous barbiturate [197] have been also accomplished.

Oishi and co-workers utilized the balance between two competitive interactions, the phase separation of fluorocarbons and hydrocarbons and the attractive interaction between guanidiuium and carboxylate, to fabricate nanoscopic domains within a two-dimensional mixture of hydrocarbon guanidinium and fluorocarbon carboxylic acid [198]. The domain sizes can be tuned by altering the mixing ratio of the two components. In a recent review article by Krafft and co-workers [199], the formation of surface nanodomains and their hierarchical organization with higher complexity with semi-fluorinated alkanes and

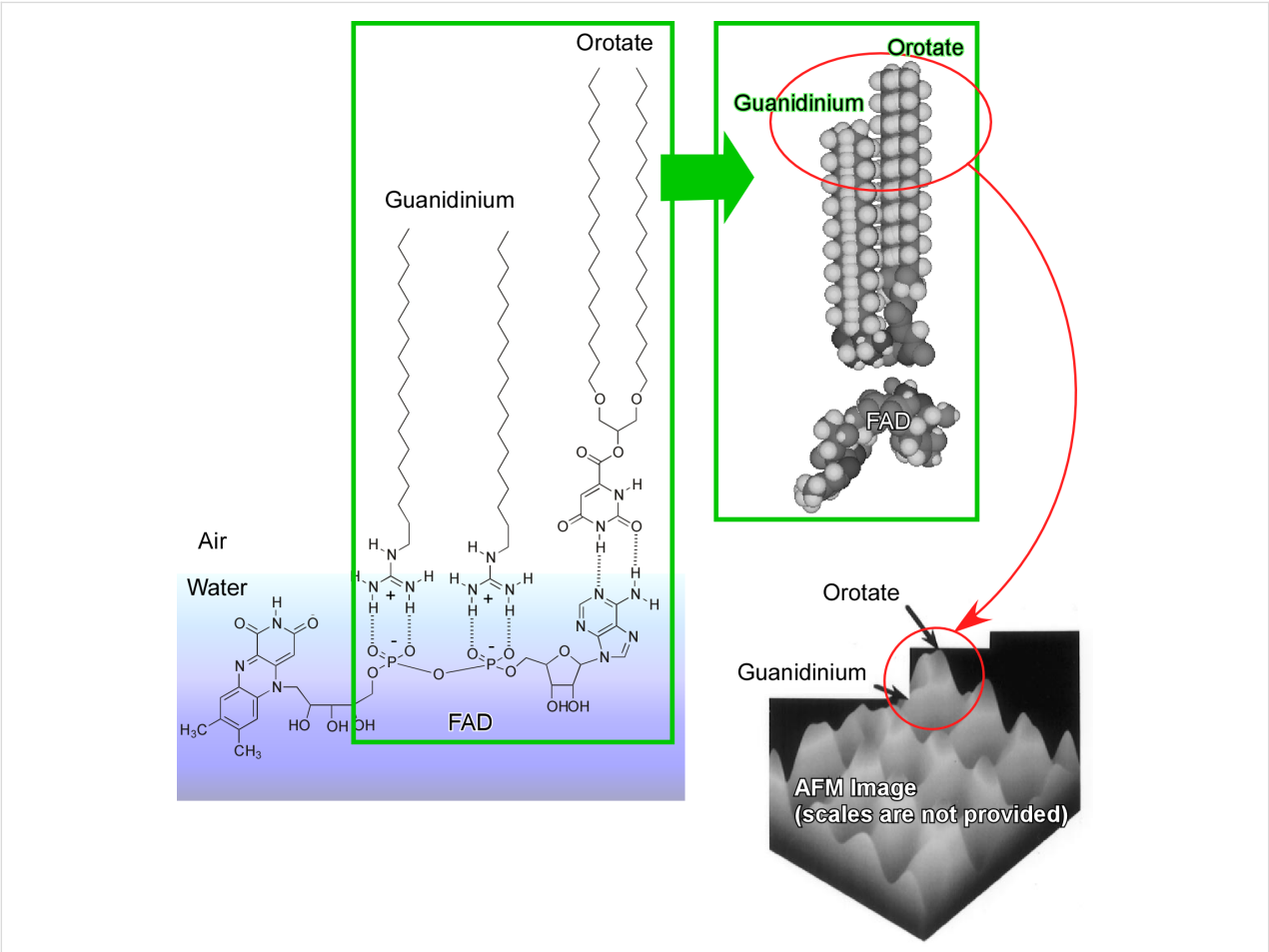

Figure 5: Formation of two-dimensional patterned structures using flavin adenine dinucleotide (FAD), which can bind site-specifically to two monolayer components, a guanidinium lipid or an orotate lipid, with the phosphate moieties and adenosine part, respectively. Adapted with permission from [195], copyright 1997 American Chemical Society.

related molecules (molecules consisting of two blocks, a fluorocarbon block and a hydrocarbon block, in a single chain) at the air–water interface is discussed. They expect possible applications of these two-dimensional nanodomains in sensors, nanoelectronics and nanophotonics.

Pellerin, Bazuin, and co-workers investigated the mechanisms of formation and transformation of zero-dimensional structures within two-dimensional media (dot-dispersed monolayers of block copolymers) [200]. Self-assembled monolayers of polystyrene-*b*-poly(4-vinylpyridine) and its supramolecular complex with 3-*n*-pentadecylphenol at the air–water interface alter their assembly patterns from hexagonal to squared upon applying lateral pressure. The transition is caused by the entropically driven molecular folding of the poly(4-vinylpyridine) moieties, in which the polymer transforms from a two-dimensional motif to a three-dimensional motif. The proposed mechanism might be generalized for zero-dimensional dot-dispersed monolayers of block-copolymers. Wen and co-workers reported the drastic modification of two-dimensionally patterned Langmuir–Blodgett (LB) films of polystyrene-*b*-poly(2-vinylpyridine) transferred from the air–water interface through acetone vapour annealing [201]. Complicated morphology shifts such as swelling, coalescing of aggregates, bicontinuous pattern formation, one-dimensional droplet formation, and the periodic evolution of the droplets were observed.

Mori et al. reported the formation of two-dimensional arrays of disk-shaped nano-assemblies at the air–water interface yielding a monolayer that was successively transferred onto solid surfaces via the contacting method (Figure 6) [202]. Unlike two-dimensional molecular patterning though molecular recognition, which has been described in the previous parts, a rather ambiguous interaction between amphiphilic triimide with three alkyl chains, a monolayer component, and 1,4,7,10-tetraazacyclododecane (cyclen), a subphase template, was used to regulate the formation of hydrogen bonds between the imide functional groups as hydrogen-bond acceptors and the secondary amine moieties of cyclen as hydrogen-bond donors. The two-dimensional quick dewetting process on a Langmuir–Schaefer-type surface can induce a good dispersion of nanodisks. Although the heights of nanodisks reported so far are within a narrow range between 2.6 and 2.9 nm, their diameters can widely range from 46 to 73 nm depending on their lateral surface pressure at the air–water interface. The fabricated array structures of nanodisks can be also transferred to metal surfaces such as platinum surfaces. The examples demonstrated that the combination of rather ambiguous molecular interactions and transfer processes can create precise patterns, which are one of the main concept of nanoarchitectonics.

Small gelation molecules often form one-dimensional assembled structures [203-207]. The inner structures of these one-

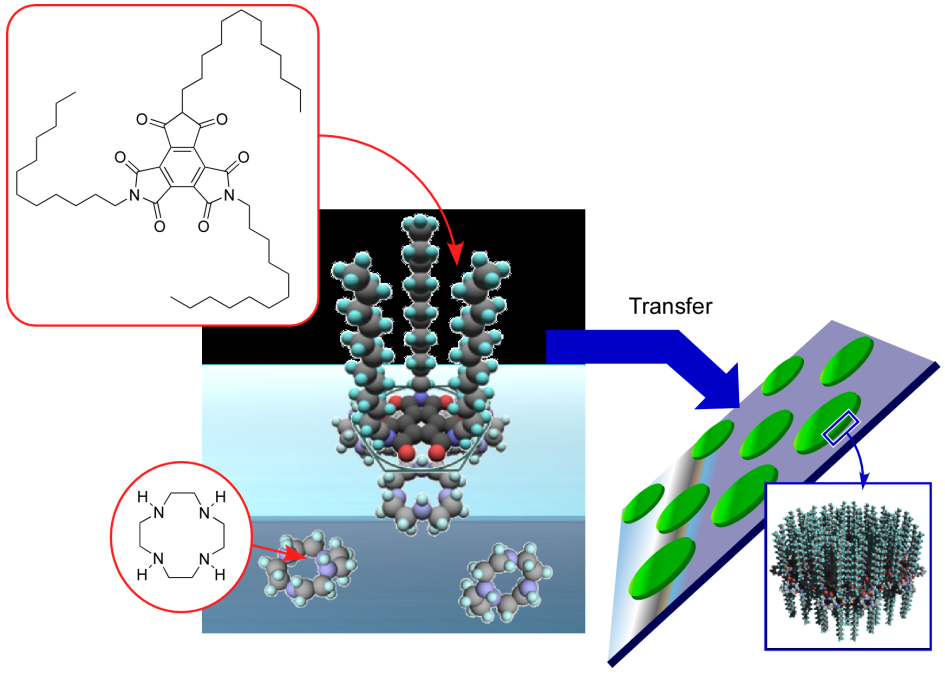

Figure 6: Formation of two-dimensional arrays of nanodisk-like assemblies via touching transfer of a monolayer of amphiphilic tri-*n*-dodecylmellitic triimide with three alkyl chains as a monolayer component and 1,4,7,10-tetraazacyclododecane (cyclen) as a subphase template. Adapted from [75], copyright 2019 The Authors.

dimensional objects can be significantly altered through the surrounding media such as organic solutions and the air–water interface. Sakakibara et al. investigated the morphological change of one-dimensional assemblies of oligo(*p*-phenylenevinylene) induced by different media (Figure 7) [208]. In entangled fibre structures, formed in toluene solution and successively transferred on a solid surface by drop-casting, the long axis of oligo(*p*-phenylenevinylene) molecules is arranged perpendicularly to the substrate. Intra-fiber energy transfer efficiently occurs in the entangled nanofibers. Long-range excitation energy transfers are advantageous for excitation energy transfer. In contrast, the oligo(*p*-phenylenevinylene) molecular units are oriented in parallel to the long axis of the aligned rods that were formed at the air–water interface from its homogeneous solution in chloroform. The excitation preferences between inter- and intra-fiber can be altered by controlling the arrangement of the aligned rods. In environments of closely packed nanorods (when the inter-rod distance was less than ca. 70 nm), enhanced excitation transfer was observed, indicating that fluorescence would be efficiently enhanced within well-aligned nanorods prepared at the air–water interface.

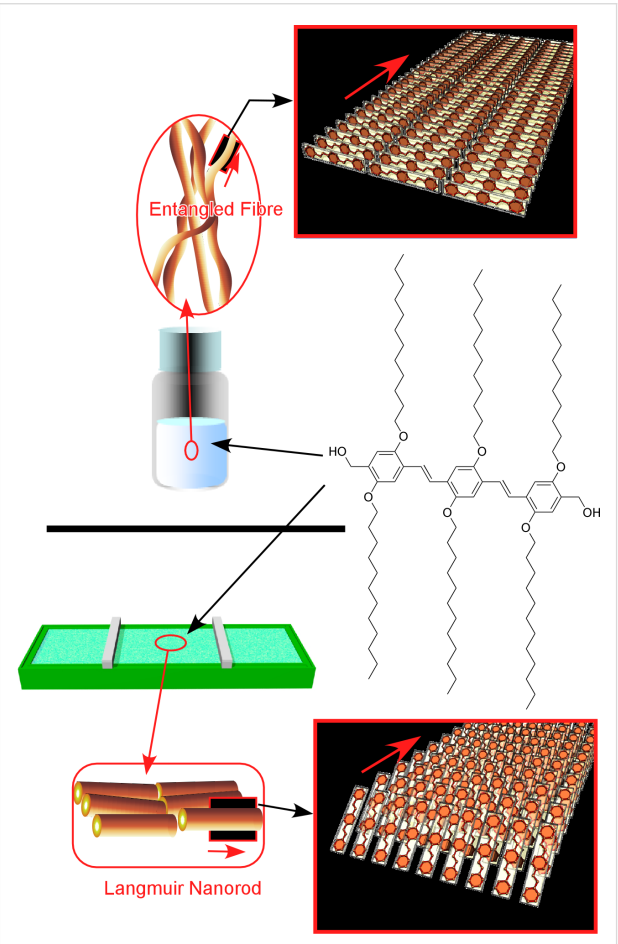

Figure 7: Difference of one-dimensional assemblies of an oligo(*p*-phenylenevinylene) derivative formed in different media: (top) entangled fibre structures formed in toluene solution and drop-cast on a solid surface; (bottom) aligned rods formed at the air–water interface. Adapted from [75], copyright 2019 The Authors.

Inorganic low-dimensional nanomaterials often exhibit interesting properties [209-215]. Such materials can be also nano-engineered at liquid interfaces. Niederberger and co-workers successfully fabricated two-dimensionally aligned arrays of one-dimensional $W_{18}O_{49}$ nanowires and used them for H_2-sensing at room temperature [216]. The diameters of the used nanowires are less than 2 nm and their aspect ratios exceed 100. The synthesized nanowires are dispersible in organic solvents and can be fabricated in large-area aligned arrays at the air–water interface. The films were transferred onto Si/SiO_2 substrates patterned with platinum interdigitated electrodes. An excellent sensor capability for H_2 gas in humid air at room temperature was observed for a film of 10 layers of the aligned one-dimensional $W_{18}O_{49}$ nanowires. Various additional techniques to fabricate two-dimensional structures have been proposed. Advincula and co-workers demonstrated two-dimensional co-patterned structures of carbazole-based conductive polymers and gold by nanosphere lithography [217]. Huang and co-workers proposed a high-yield LB method for nanoparticle films through electrospray techniques to significantly reduce the spreading of droplets and used a subphase-miscible solvent [218]. The modified method may become a powerful method to fabricate two-dimensional thin films of zero-dimensional nanoparticles at liquid interface.

The lateral degree of motional freedom of the liquid interfaces can promote associations of molecules and materials for the fabrication of two-dimensionally structures. As depicted in Figure 8, Yonamine et al. successfully demonstrated the one-dimensional supramolecular polymerization of DNA origami pieces upon repeated mechanical compression and expansion of the two-dimensional air–water interface [219]. The used DNA origami pieces had a rectangle shape with 90×65 nm^2, according to theoretical calculations, and were complexed with counter-cationic lipids to be soluble in organic solvents. The resulting organic solution of the DNA origami pieces was then spread on the air–water interface to form a Langmuir monolayer. Although the spread DNA origami pieces initially remained in the monomer form, the repeated mechanical compression and expansion of the Langmuir monolayer induced the interconnection of the rectangle pieces into one-dimensional polymer motifs. The origami–origami connections were formed only at the shorter sides of the rectangle pieces where dangling DNA chains remained. The enhanced capability of hydrogen-bond formation at the air–water interface resulted in one-dimensional supramolecular polymers through inter-piece connections at the specific sides. Interestingly,

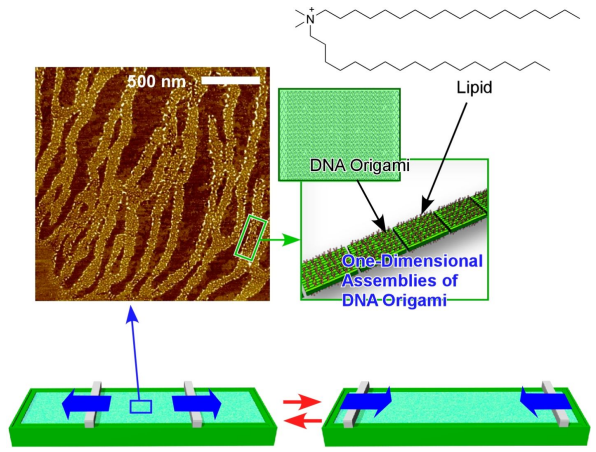

Figure 8: Formation of one-dimensional supramolecular polymerization of DNA origami pieces upon repeated mechanical compressions and expansions of two-dimensional air-water interface. An AFM image was reprinted with permission from [144], copyright 2019 American Chemical Society.

dynamic motion is indispensable for the formation of these supramolecular polymers of DNA origami. A simple application of high pressure is not enough to obtain supramolecular polymerization of DNA origami pieces at the air–water interface.

3 Interfacial nanoarchitectonics for MOF and COF

Interfaces are attractive platforms to synthesize two-dimensional materials. The recent developments of synthetic two-dimensional crystalline polymers (2DCPs), such as two-dimensional metal-organic frameworks (MOFs) and two-dimensional covalent organic frameworks (COFs), have unveiled their intriguing chemistry and properties, and have shown their potential for wide-ranging applications, such as electronics, sensing, catalysis, separation, and energy storage and conversion. However, most reported two-dimensional MOFs and COFs have been synthesised as powders, which are not easily processed into more useful forms due to their nature as cross-linked polymers. Thus, their adaption for technological applications is still challenging. Recently, liquid interfaces have been considered to be useful platforms to form thin 2DCP films, and the number of examples showing interfacially grown 2DCP films for potential applications is increasing [220].

The air–water interface is the most commonly used liquid interface to grow 2DCP films. In 2002, Culp et al. reported a reaction of a Langmuir monolayer of an amphiphilic pentacyanoferrate complex with Ni^{2+} ions from the subphase (Figure 9) [221]. This reaction resulted in the formation of a two-dimensional iron–nickel cyanide-bridged network at the air–water interface. A small amount of the amphiphilic pentacyanoferrate complex

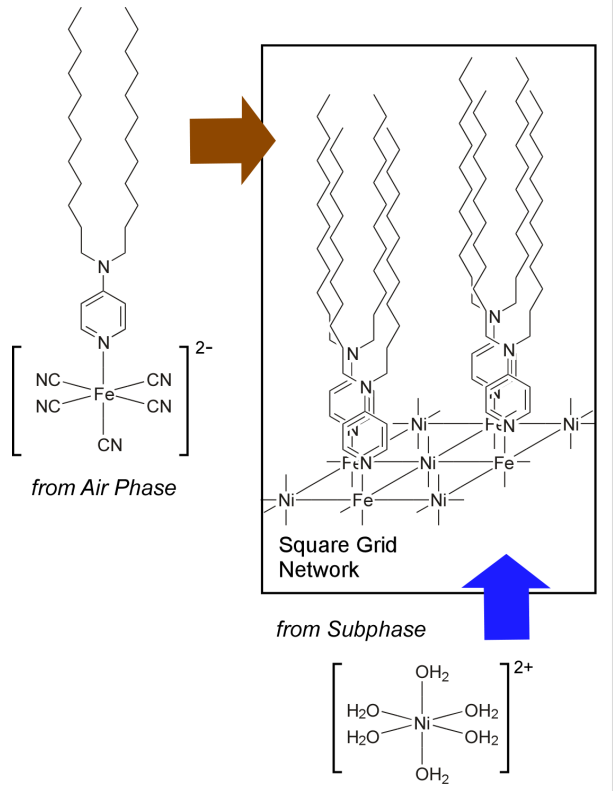

Figure 9: Formation of a two-dimensional iron–nickel cyanide-bridged network at the air–water interface through reaction of a Langmuir monolayer of an amphiphilic pentacyanoferrate complex with Ni^{2+} ions from the subphase.

monomer was spread from a chloroform solution to form a monolayer in a LB trough, and was subsequently connected by introducing an aqueous solution of nickel nitrate into the water phase, yielding a monolayer sheet of the two-dimensional nickel–iron cyanide grid network. Characterizations of the extended network by X-ray photoelectron spectroscopy (XPS), FTIR spectroscopy, SQUID magnetometry, X-ray absorption fine structure (XAFS), and grazing incidence synchrotron X-ray diffraction (GIXD) revealed a face-centred square grid structure with an average domain size of 3600 $Å^2$.

Makiura et al. employed a similar method to form multilayers of an oriented porphyrin-based MOF film on top of substrates by repeating transfer and washing of interfacially grown MOF layers (Figure 10) [222]. Interestingly, the proposed structural model incorporates metal-coordinated pyridine molecules projected from the two-dimensional sheets that allow each further layer to dock in a highly ordered interdigitated manner in the growth of multilayer structures. Ni_3(2,3,6,7,10,11-hexaiminotriphenylene)$_2$, Ni_3(HITP)$_2$, is a conjugated MOF films of which were prepared by interfacial polymerization at the air–water interface. Wu et al. prepared a Ni_3(HITP)$_2$ MOF film

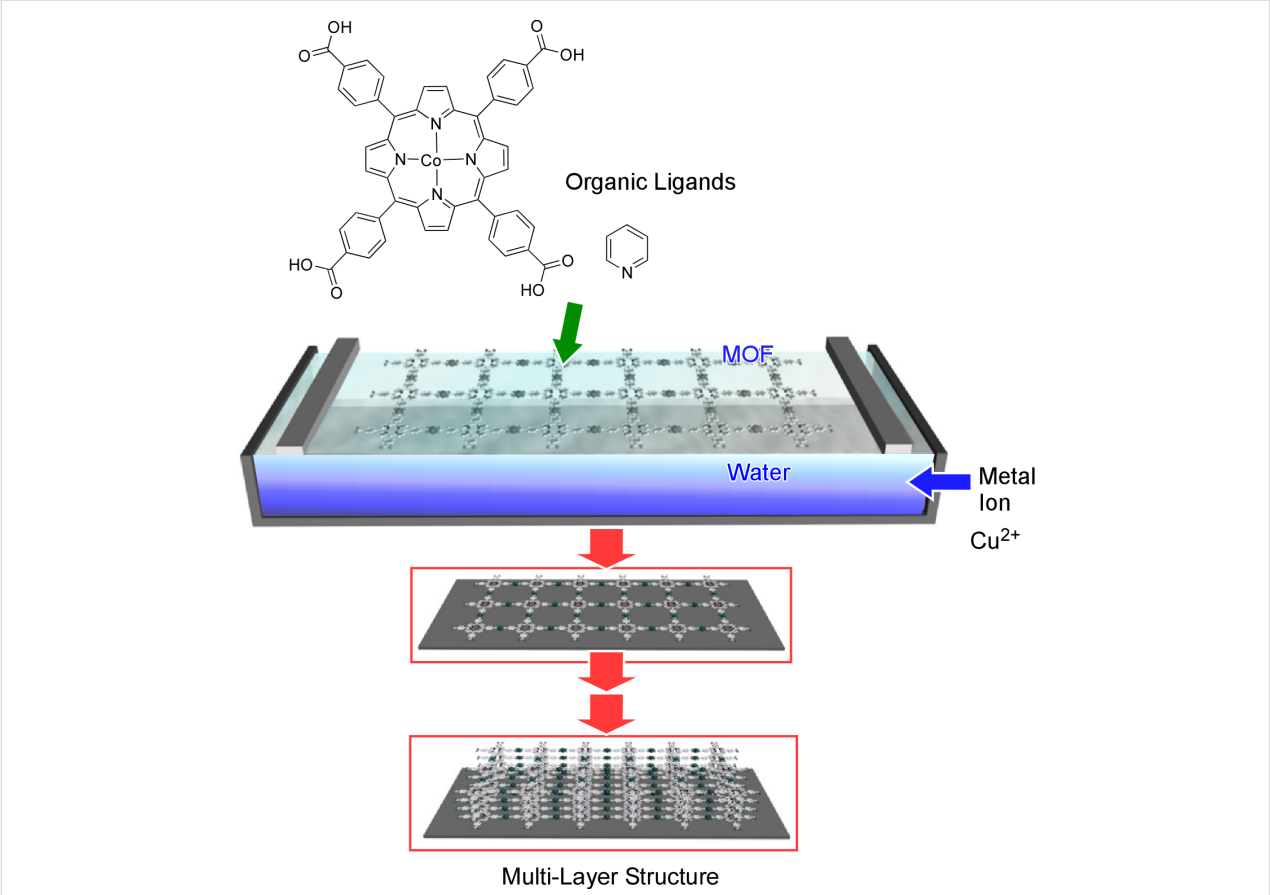

Figure 10: Fabrication of a multilayer of oriented porphyrin-based MOF films by repeatingly transferring and washing interfacially grown MOF layers.

and incorporated the resulting film into field-effect transistor (FET) devices, exhibiting p-type semiconductive behaviour, distinguishable on/off ratios, and excellent field-effect hole mobility values as high as 48.6 $cm^2 \cdot V^{-1} \cdot s^{-1}$ [223].

A COF film interfacially grown at a liquid–gas interface was also incorporated into a FET device and examined. Feldblyum et al. found an imine-linked COF film growing at the interface of air and a *N*,*N*-dimethylformamide (DMF) solution of COF precursors consisting of benzothiophene and triphenylamine moieties [224]. The interfacially grown film was transferred onto Si substrates in order to fabricate FET devices. The COF-film FET device also exhibited p-type behaviour, an average mobility of 3.0 10^{-6} $cm^2 \cdot V^{-1} \cdot s^{-1}$, and an on/off ratio of 850. Imine-linked COF films were also fabricated with the common interfacial polymerization method using LB troughs. Dai et al. newly designed a trisubstituted amine monomer bearing three *n*-hexyl groups [225]. These aliphatic chains are helpful to fix the orientation of the amine monomer when deposited on an air–water interface together with a dialdehyde monomer. The monomers compressed with an LB trough were polymerized with acetic acid as catalyst in the water phase.

Liquid–liquid interfaces are another class of interfaces used for the interfacial polymerization of 2DCPs. Because of the relatively dynamic nature of two liquids, the liquid–liquid interfaces are, in general, less well-defined than liquid-gas interfaces. Hence, the interfacial polymerizations tend to afford thicker films [220]. π-conjugated nickel bis(dithiolene) complex nanosheets reported by Kambe and co-workers [226] were one of the first representative examples for interfacially polymerized MOF films at the liquid–liquid interface. Two immiscible phases of water and dichloromethane spatially segregate nickel acetate, a metal node precursor, from benzenehexathiol (BHT, a coordinating linker) and confine the MOF formation to the liquid interface. The interfacially grown BHT–Ni network film of 1–2 μm thickness exhibited X-ray diffraction patterns corresponding to a crystalline network structure.

Takada et al. adopted a similar technique to form electrochromic bis(terpyridine)metal complex nanosheets (Figure 11) [227]. The demonstrated network structures are connected by the coordination of terpyridine moieties to either cobalt or iron ions, and the synthesized films change their colour depending on the oxidation levels of the cobalt and iron

ions. The colours of those MOF films can be modulated through electrochemical processes.

The interfacial formation of COFs at the liquid–liquid interfaces is more complicated because of the necessity of water-soluble COF precursors. Sahabudeen et al. have overcome this issue by using a hydrophilic dialdehyde monomer, 2,5-dihydroxyterephthalaldehyde (DHTPA) [228]. DHTPA was dissolved in water, and the resulted aqueous solution was layered on top of a chloroform solution of a tetra-substituted amine monomer containing porphyrin. The segregation of the monomers confined the imine formation to the interface and yielded wafer-size multilayer imine-linked COF films. The films grown from the amine monomer containing cobalt porphyrin exhibited catalytic activity for the electrochemical hydrogen generation from water. Dey et al. have dissolved one COF monomer into the aqueous phase by forming amine salts (Figure 12) [229]. Various multi-amino-substituted monomers were treated with *p*-toluene sulfonic acid (PTSA) forming [amine-PTSA] salts, and dissolved into aqueous phases. Each aqueous solution was layered on a dichloromethane solution containing 1,3,5-triformylphloroglucinol (Tp), an aldehyde-derivative COF monomer, yielding large COF films of sub-100 nm thickness. The prepared materials were capable of selective permeation.

In contrast to the two previous reports in which one of the COF monomers was dissolved into the aqueous phase, Matsumoto et al. confined the polymerization to the interface by segregating the catalyst from the COF monomers (Figure 13) [230]. Scandium triflate, one of the catalysts forming imine-linked COFs [231] in the aqueous phase was isolated from both amine and aldehyde COF monomers dissolved into an organic phase. The

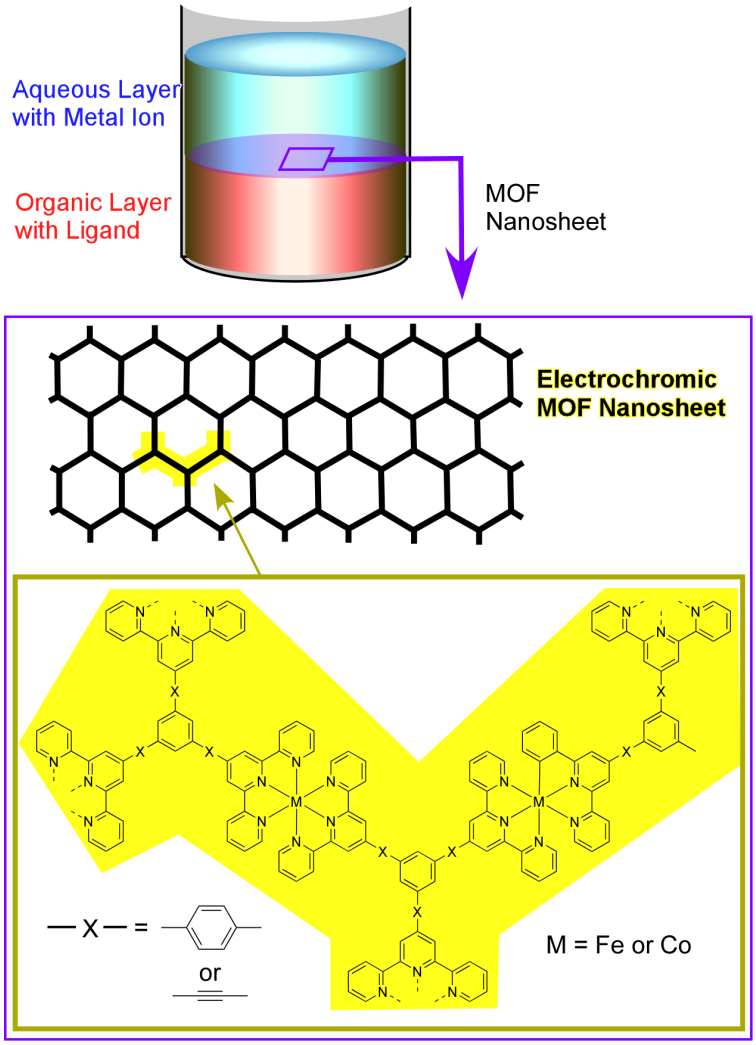

Figure 11: Electrochromic bis(terpyridine)metal complex MOF nanosheets formed through coordination of terpyridine moieties to either cobalt or iron ions. The synthesized films change their colour depending on the oxidation levels of the cobalt and iron ions.

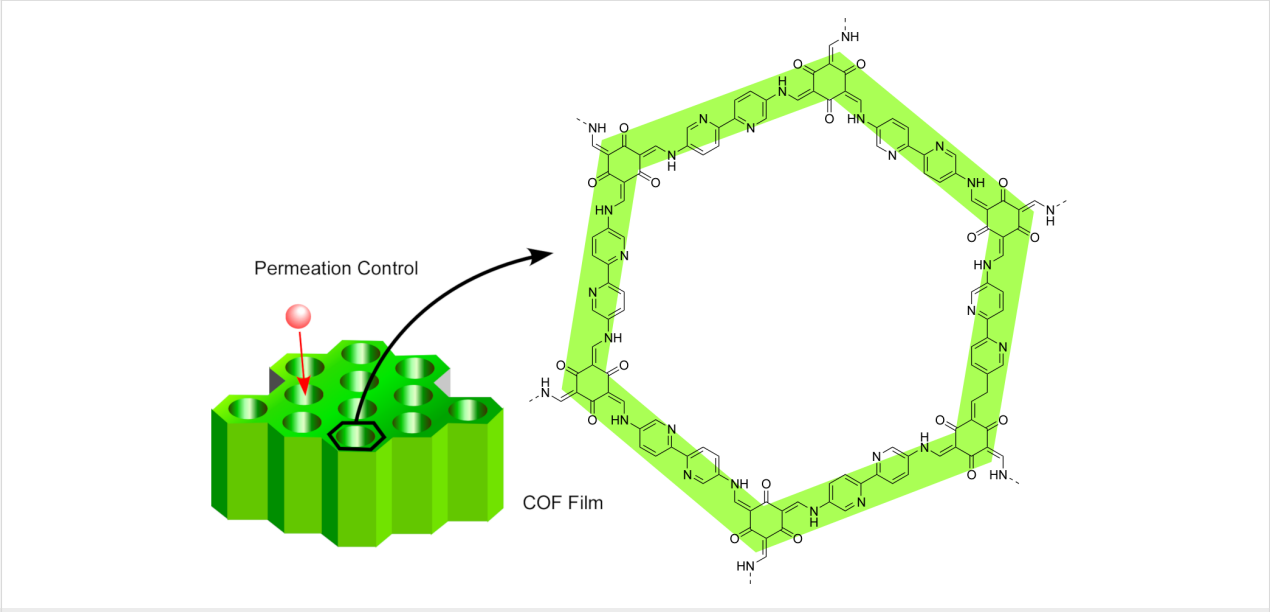

Figure 12: Aqueous solutions of multi-amino-substituted monomers with *p*-toluene sulfonic acid were layered on a dichloromethane solution containing 1,3,5-triformylphloroglucinol to yield large COF films of sub-100 nm thickness.

two phases in contact with each other induced the COF formation at the interface, forming large-area, continuous COF films (several square centimetres). Depending on the monomer concentrations, the film thickness was tuned from 100 μm to a few nanometres. The COF films made from the methods reported by Dey et al. and Matsumoto et al. were separately examined as separation membranes and exhibited high rejections of water pollutant surrogates from water [229-231]. Considering the high tuning capability of pore-size and functional groups decorating the inner pores of COFs, the separation membranes made out of COFs are promising for water purification technologies including desalination [232].

Interfacial polymerization at liquid interfaces is an already industrialized technique to produce conventional cross-linked polymer films/membranes. Interfacial polymerization of 2DCP films still remains in its infant stage in terms of controlling crystallinity, domain sizes, and generalities. However, the developments on interfacial polymerization of 2DCPs at liquid interfaces will be an important breakthrough for industrializing 2DCP materials.

4 Interfacial nanoarchitectonics for nanocarbon materials

4.1 Bottom-up production of nanocarbon materials

Low-dimensional carbon materials, such as carbon nanotubes and graphene derivatives, are now widely used especially in energy and environmental research fields [233]. A lot of attention has also been paid on the creation of novel nanocarbon materials from molecular units and structurally well-defined assemblies from nanocarbon units. Regarding the latter, liquid interfaces often provide important anisotropic fabrication media to synthesize novel types of low-dimensional carbon materials.

Recently, Mori et al. successfully demonstrated the fabrication of two-dimensional nanocarbon films from a designed molecular unit, the carbon nanoring molecule (9,9′,10,10′-tetrabutoxycyclo[6]paraphenylene[2]-3,6-phenanthrenylene), by using newly developed vortex LB method at a liquid interface with dynamic flow (Figure 14) [234]. For this bottom-up fabrication, the chloroform solution of the carbon nanoring was dripped at the air–water interface under rotating vortex flow. Appropriate flow rates yielded two-dimensional films of the carbon nanoring molecule with uniform thickness of a few nanometres. The monolayer films were transferred from the water surface to a solid substrate by hand. Further heat treatment under inert gas atmosphere led to the formation of uniform two-dimensional nanocarbon films, so-called carbon nanosheets, with ca. 10 nm thickness with dispersed nanopore structural motifs. The electrical conductivity of the transferred film was significantly increased after the thermal carbonization process. Nitrogen-doping was carried out simply by mixing nitrogen-containing compounds such as pyridine into the original solution of the carbon nanoring molecule. The prepared nitrogen-doped carbon nanosheets exhibited a higher electrical conductivity than the non-doped ones did. It should be noted that these nanomaterial fabrications can be conducted by using solely very common apparatuses such as beaker, stirrer, and tweezers. Therefore, the proposed method can be more generalized and extended even to industrial applications.

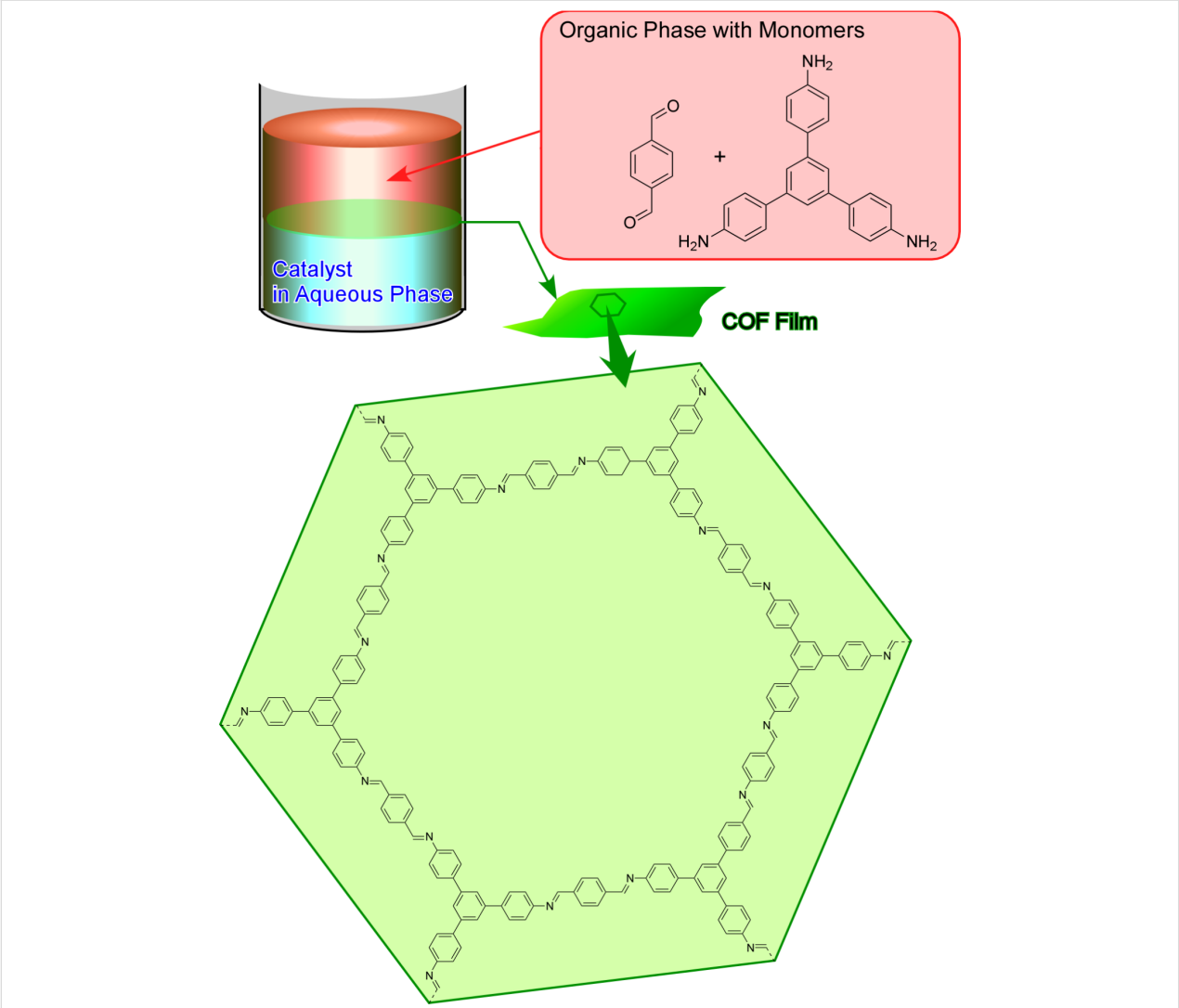

Figure 13: Confined polymerization at the interface by spatially segregating a catalyst from the COF monomers. The formation of imine at the interface of aqueous and organic layer yielded large-area, continuous COF films.

For the bottom-up fabrication of nanocarbon materials through self-assembly processes, the use of fullerene (especially, C_{60}) molecules as assembling components are both technically and scientifically attractive [235]. In addition to the technical importance of fullerene in many applications including physical devices and biomedical usages, assembly processes from completely symmetrical zero-dimensional objects with single elemental composition (carbon) are an intriguing fundamental topic in supramolecular chemistry [236]. Miyazawa and co-workers initiated a simple but highly useful method, i.e., liquid–liquid interfacial precipitation, to fabricate fullerene assemblies (crystals) with various morphologies (Figure 15) [237-239]. Fullerene molecules, such as C_{60} and C_{70}, are dissolved in a liquid phase (good solvent) that contacts an immiscible liquid phase in which the molecules are poorly soluble (poor solvent). The formation of crystalline assemblies of fullerene molecules is induced by supersaturation at the liquid–liquid interface. For example, C_{60} rods or needles can be obtained at the interface between a saturated solution of C_{60} in toluene and isopropyl alcohol as poor solvent.

4.2 One-dimensional fullerene assembly materials

Shrestha and co-workers have extended the research on dimensionally controlled assemblies of fullerene molecules through liquid–liquid interfacial precipitation [240]. For example, the conversion from one-dimensional structures to three-dimensional morphologies of C_{60} rods and tubes was carried out via a surfactant-assisted process in liquid–liquid interfacial precipitation [241]. At the interface between butanol and benzene, C_{60} typically assembles into one-dimensional superstructures (rods and tubes). However, by adding surfactants to those interfacial systems, the morphology of the assemblies can be altered to

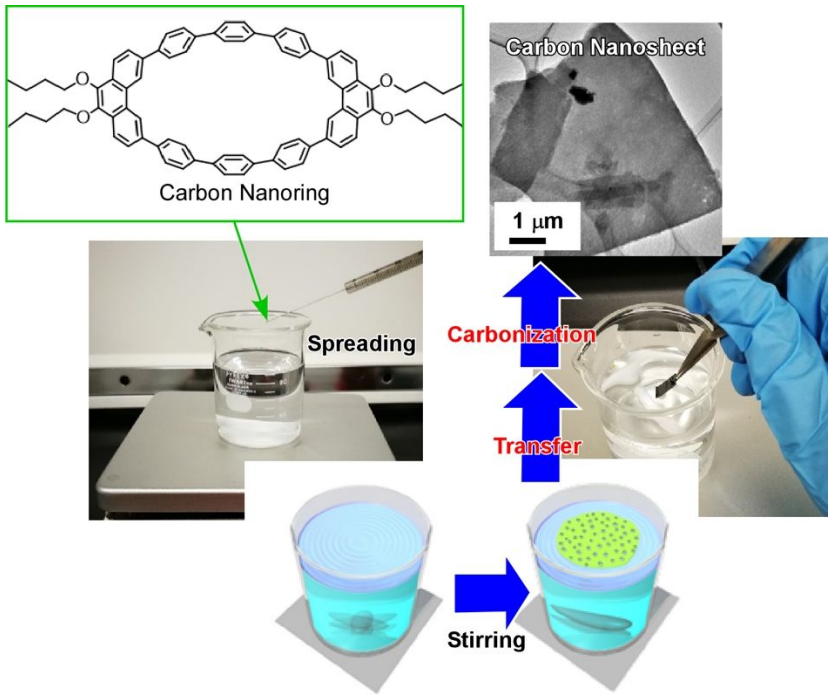

Figure 14: Fabrication of two-dimensional nanocarbon films from a carbon nanoring molecule (9,9′,10,10′-tetrabutoxycyclo[6]paraphenylene[2]-3,6-phenanthrene) via a newly developed vortex LB method at a liquid interface with dynamic flow followed by heat treatment under inert gas atmosphere. Both photographs were reproduced with permission from [68], copyright 2019 The Royal Society of Chemistry; the TEM image was reproduced from [75], copyright The authors.

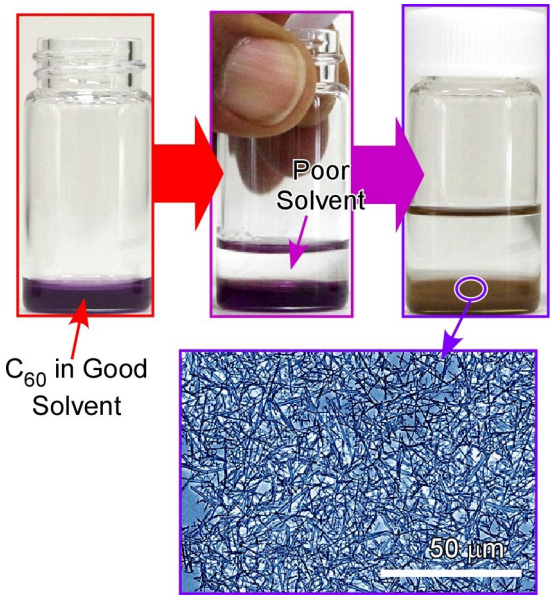

Figure 15: Liquid–liquid interfacial precipitation to fabricate fullerene assemblies (crystals) with various morphologies (in this case, assembly of one-dimensional nanowhiskers). Fullerene molecules, such as C_{60} and C_{70}, are dissolved in a liquid phase (good solvent) that contacts an immiscible liquid phase in which the molecules are poorly soluble (poor solvent).

three-dimensional objects. The final morphology highly depends on type and concentration of the surfactants. When the non-ionic surfactant diglycerol monolaurate was added to butanol (0.01%), flower-like three-dimensional objects were precipitated at the interface with benzene. Detailed morphological analyses with electron microscopy techniques revealed that the surfactants did not basically alter primarily the one-dimensional structures of the formed assemblies. Instead, they seemed to promote super-lattice formation constructing three-dimensional flowers form the same one-dimensional rods observed in non-surfactant systems (tubes).

The thermal conversion of one-dimensional fullerene crystalline assemblies at extremely high temperatures resulted in highly graphitic one-dimensional carbon materials as demonstrated by Shrestha and co-workers [242]. One-dimensional C_{60} nanorods and nanotubes precipitated at liquid–liquid interface were fully carbonized at 2000 °C in vacuum, resulting in morphology-preserved one-dimensional carbon materials with sp^2-hybridised π-electron-rich robust frameworks (Figure 16). Due to their highly aromatic nature, microbalance sensors with the synthesized one-dimensional carbon materials on a quartz crystal microbalance plate exhibited superior sensing properties for aromatic toxic gasses. In addition, these graphitic carbon

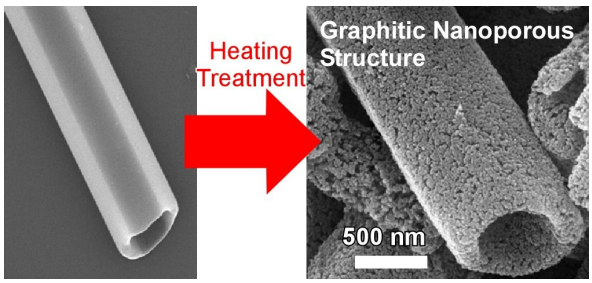

Figure 16: Conversion of one-dimensional C_{60} nanotubes precipitated at liquid-liquid interface to one-dimensional carbon materials having sp^2-carbon-based π-electron-rich robust mesoporous frameworks through carbonization at 2000 °C in vacuum.

materials exhibit excellent electrochemical capacitance, suggesting possible usages in electrochemical and electrical applications. A similar nanoarchitectonics strategy was adopted to C_{70} molecules. The one-dimensional carbon materials prepared through high-temperature carbonization of C_{70} crystalline assemblies showed high specific capacitances at a high current density and scan rate [243]. These nano-engineered one-dimensional carbon materials might be useful as electrode materials for supercapacitors.

Shrestha, Acharya, and co-workers investigated the optoelectronic properties of one-dimensional C_{60} nanorods prepared in ultra-rapid (5 s) processes of liquid–liquid interfacial precipitation at room temperature [244]. Dominant excitonic charge transfer transitions within the nanorods was confirmed by steady-state optical spectroscopy. Photovoltaic cells with one-dimensional C_{60} nanorods as active layer sandwiched by an indium tin oxide anode and an aluminium cathode exhibited enhanced photovoltaic capabilities. It also led to a significant enhancement of photogenerated charge carriers as compared to similar cells prepared with pristine C_{60} molecules. C_{60} molecules in a one-dimensional van der Waals solid preserve the electronic structure of C_{60}, but they crystallise in a hexagonal close-packed structure that is different from the cubic crystal structure of pristine C_{60} molecular crystals. This fact suggests that crystal lattice and molecular packing within low-dimensional fullerene assemblies significantly modify the optoelectronic properties. The rapid synthesis with the possibility to scale-up and the enhanced optoelectronic properties make the above-mentioned nanoarchitectonics strategy for one-dimensional fullerene nanorods a promising approach for applications in photosensitive devices.

Ji, Shrestha, and co-workers investigated the effects of the intercalation of polycyclic aromatic compounds, such as naphthalene, anthracene, and pyrene, on the formation of one-dimensional C_{60} nanowhiskers in liquid–liquid interfacial precipitation processes [245]. The intercalation of polycyclic aromatic compounds generally modifies the growth of fullerene one-dimensional crystals depending on intercalation species. While anthracene and pyrene led to an increased porosity of the structures, the structural characteristics of those without intercalator compounds were preserved in the presence of naphthalene. In addition, intercalation of the polycyclic molecules significantly modified the spectral emissions of the fullerene assemblies probably due to effects of molecular packing on the electron transfer within the assembled structures.

Acharya, Shrestha, and co-workers decorated one-dimensional C_{60} nanorods with zero-dimensional Ag nanoparticles that were used as substrates for surface-enhanced Raman scattering (SERS) to detect model targets such as rhodamine 6G with high sensitivity [246]. This system provides dispersed SERS substrates that can be evaluated by confocal Raman imaging. The nanoarchitectonic materials work as freestanding efficient plasmonic substrates for molecular detection.

Nanoporous bitter-melon-shaped C_{60} crystals with face-centred cubic lattice were fabricated through liquid–liquid interfacial precipitation from 2-propanol and C_{60} solution in dodecylbenzene as reported by Shrestha and co-workers (Figure 17) [247]. Quartz crystal microbalance sensors coated with the bitter-melon-shaped objects exhibited excellent sensing properties for aromatic vapours with sensitivities in the order of aniline > toluene > benzene > ethanol > hexane > cyclohexane > methanol > water. The obtained nanoporous low-dimensional C_{60} assemblies provide advantageous features of easy diffusion and promoted π–π interactions for facile sensing.

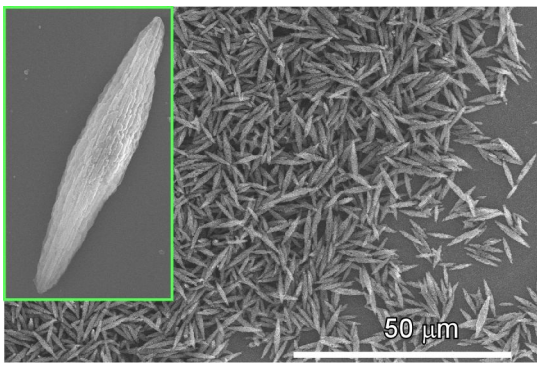

Figure 17: Nanoporous bitter-melon-shaped C_{60} crystals with face-centered cubic lattice fabricated through liquid-liquid interfacial precipitation methods between isopropyl alcohol and C_{60} solution in dodecylbenzene.

Saran and Curry reported the use of one-dimensional C_{60} crystals prepared through liquid–liquid interfacial precipitation between *m*-xylene and isopropyl alcohol for visible-spectrum

photodetectors [248]. Additional materials or two metal contacts are not necessary in the fabricated photodetectors. These devices made solely from carbon can be used as an alternative to commercial photodetector devices with CdS and CdSe. Enhanced photoluminescence and photoelectrochemical properties of one-dimensional $Lu_2@C_{82}$ nanorods prepared through liquid–liquid interfacial precipitation between carbon disulfide and 2-propanol were demonstrated by Lu and co-workers [249]. Photoluminescence of the one-dimensional $Lu_2@C_{82}$ nanorods was remarkably enhanced compared to the pristine $Lu_2@C_{82}$ powder. The increased charge carrier transport would be also useful for applications with photoelectric purposes such as photodetectors.

4.3 Two- and three-dimensional, and hierarchic fullerene assembly materials

One of the biggest advantages of liquid–liquid interfacial precipitation is the capability of creating nanomaterials with different dimensionalities just by changing the combination of liquids to form the interface. For example, Shrestha and co-workers successfully prepared two-dimensional C_{60} hexagonal nanosheets with hierarchic pore structures of macropores and mesopores just by changing the solvent combination (Figure 18) [250]. Liquid–liquid interfacial precipitation processes with isopropyl alcohol/benzene and isopropyl alcohol/carbon tetrachloride provided one-dimensional rods and two-dimensional hexagon nanosheets, respectively. While these objects do not possess porous interior structures, the use of good solvents (benzene and carbon tetrachloride) with isopropyl alcohol as poor solvent yielded nanosheets with pores depending on the mixing ratio between benzene and carbon tetrachloride. Incorporation of 30% carbon tetrachloride changes the morphology from one-dimensional rods to two-dimensional hexagonal sheets by preventing the sheets from rolling up to rods. Carbon tetrachloride contents of more than 50% yielded porous structures of two-dimensional hexagon nanosheets. At 90% carbon tetrachloride content, the average pore size became ca. 400 nm. These integrated two-dimensional structures would be nanoarchitectonics pieces for the fabrication of sensitive sensors, organic solar cells, and miniaturized organic superconductors.

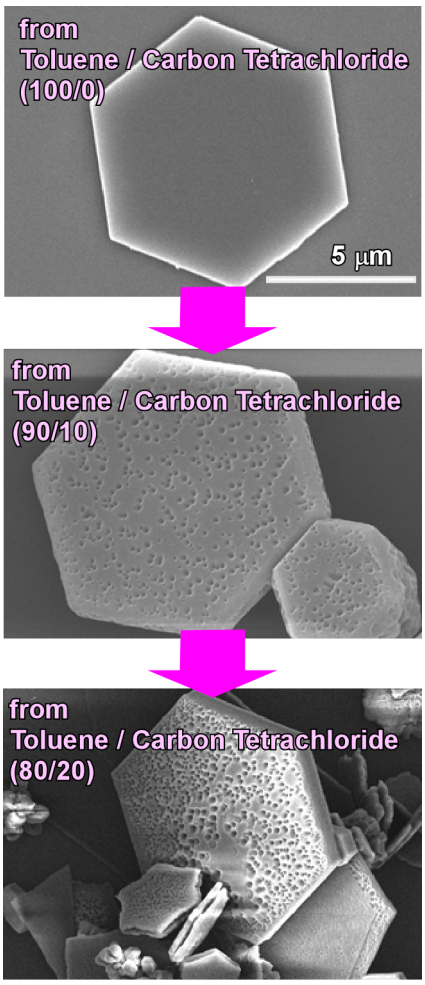

Figure 18: Two-dimensional C_{60} hexagonal nanosheets with hierarchic pore systems of macropores and mesopores prepared by liquid–liquid interfacial precipitation from isopropyl alcohol and mixtures of benzene and carbon tetrachloride. The porosity can be tuned through the mixing ratio between benzene and carbon tetrachloride. SEM images were reproduced with permission from [68], copyright 2019 The Royal Society of Chemistry.

As a functional development of two-dimensional fullerene objects, Ji, Shrestha, and co-workers reported the synthesis of two-dimensional mesoporous carbon microbelts and demonstrated their usage as electrode material for electrochemical supercapacitors (Figure 19) [251]. Two-dimensional belt-like mesoporous structures can be fabricated from C_{60} molecules by liquid–liquid interfacial precipitation using a carbon disulfide solution of C_{60} and isopropyl alcohol. Under optimized conditions, these mesoporous C_{60} microbelts extended to lengths of the order of centimetres. Heat treatment of the obtained C_{60} microbelts converts them into two-dimensional amorphous carbon microbelts at 900 °C and their dense graphitic versions at 2000 °C. Especially the former carbon material exhibited excellent electrochemical supercapacitive performance due to the enhanced surface area and the robust mesoporous framework motifs. The hierarchical bimodal pore nature throughout the carbonaceous frameworks results in efficient charge storage and rapid ion transport. Superior cycling stability without any capacity losses even after 10000 charge/discharge cycles was also confirmed.

Furthermore, preparations of three-dimensional and hierarchic structures of fullerene assemblies through liquid–liquid interfacial precipitation have been successfully reported. Shrestha et

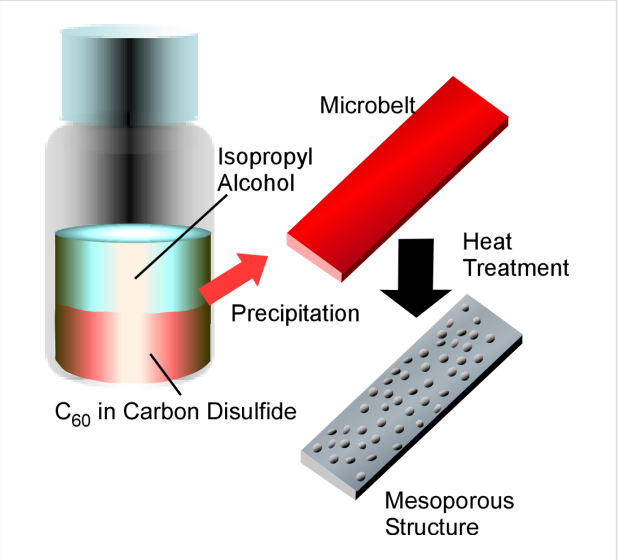

Figure 19: Synthesis of two-dimensional mesoporous C_{60}-based carbon microbelts by liquid–liquid interfacial precipitation using a carbon disulfide solution of C_{60} and isopropyl alcohol followed by high-temperature heat treatment.

al. reported the synthesis of highly integrated three-dimensional Bucky cubes through liquid–liquid interfacial precipitation and structural transformation by post-solvent treatment (Figure 20) [252]. Three-dimensional cubic structures were precipitated as Olmstead's crystalline C_{60}–Ag(I) organometallic hetero-nanostructures $[C_{60}\{AgNO_3\}_5]$ at the interface between a saturated benzene solution of C_{60} and an ethanol solution of silver(I) nitrate. The formed cubic structures underwent structural transformation upon exposing them to aliphatic alcohols of low molecular weight. The transformation of smooth-faced crystals to interpenetrated networks of one-dimensional needle crystals occurred while preserving the cubic shape. Several potential applications based on their electronic and optical properties can be expected for the obtained highly integrated fullerene assemblies.

As reported by Shrestha and co-workers, three-dimensional cubic structures can be fabricated from C_{70} molecules through an ultrasound-assisted liquid–liquid interfacial precipitation from *tert*-butyl alcohol and mesitylene [253]. In this modified method, mild sonication was applied for a short period of time after appropriate incubation time. The resulting C_{70} cubic objects were further transformed into needle-on-cube (one-dimensional structure on the surface of three-dimensional object) structures simply by washing with isopropyl alcohol at room temperature (Figure 21). The growth directions and diameters of the nanorod-like C_{70} one-dimensional structures can be tuned through the washing conditions. Interestingly, the formed nanorod structures possess mesoporous features, which makes the entire structure fully hierarchic. Quartz crystal microbal-

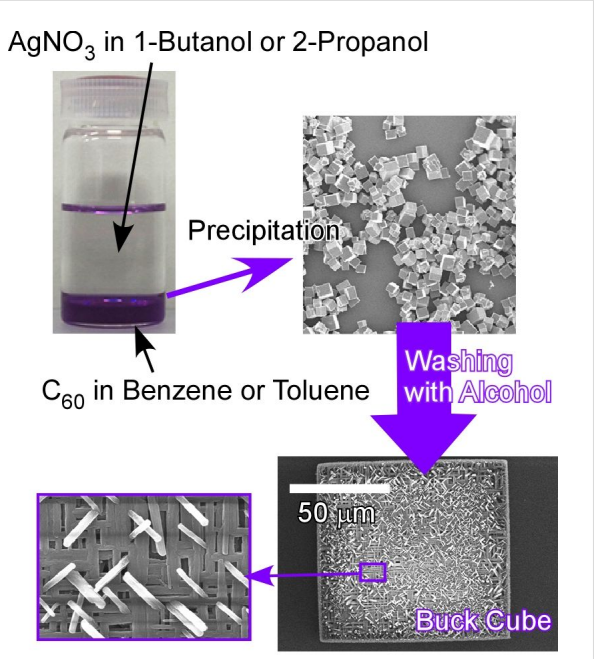

Figure 20: Highly integrated three-dimensional Bucky cubes synthesized by liquid–liquid interfacial precipitation of Olmstead's crystalline C_{60}–Ag(I) organometallic heteronanostructure and the subsequent structural transformation upon post-solvent treatment.

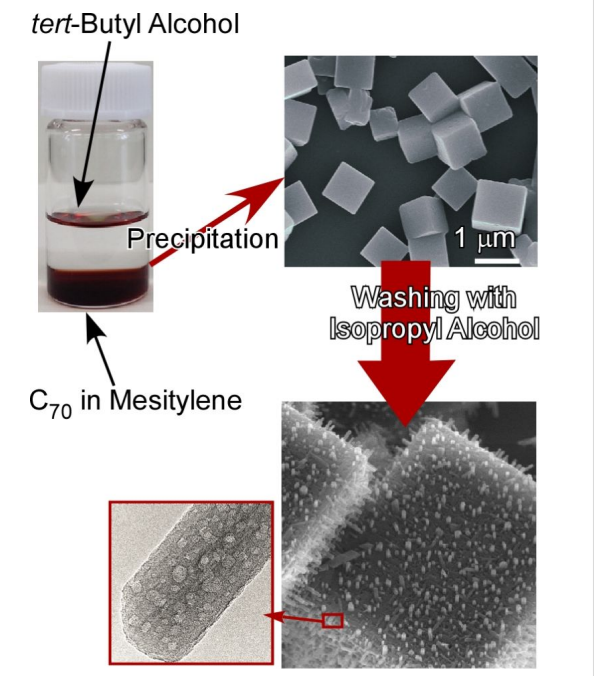

Figure 21: Three-dimensional cubic structures can be fabricated from C_{70} molecules through an ultrasound-assisted liquid–liquid interfacial precipitation from *tert*-butyl alcohol and mesitylene. The formed cubes can be further transformed into needle-on-cube (one-dimensional structure on the surface of three-dimensional object) structures simply by washing with isopropyl alcohol at room temperature. Reproduced from [75], copyright 2019 The authors.

ance sensors modified with these hierarchic C_{70} assemblies exhibited an excellent sensitivity to aromatic molecules in their vapour phase probably due to facile diffusion through the porous structure, high surface-area contact and advantageous π–π interaction. The formation of low-dimensional objects from a flat surface efficiently increases the surface area. This strategy of converting low-dimensional structures is beneficial for certain application such as sensing and drug delivery where contact of materials to external media is crucial.

Shrestha and co-workers demonstrated the manipulation of microscopic hole structures on the surface of cubic assemblies of C_{70} molecules leading to hole-in-cube structures (Figure 22) [254]. Open-hole cubes, in which microscopic holes are formed at center of every face, were fabricated through dynamic liquid–liquid interfacial precipitation from *tert*-butyl alcohol and mesitylene. In the dynamic procedure, a mesitylene solution of C_{70} molecules was rapidly added into *tert*-butyl alcohol and the resulting mixture was further incubated. The closing and re-opening of holes can be controlled through addition of excess C_{70} molecules and local electron beam irradiation, respectively. Interestingly, the fabricated holes have the capability to discriminate macro-size particles. The holes selectively accommodate graphitic carbon particles instead of resorcinol–formaldehyde resin particles of similar shape and size. Favourable π–π interactions at the sp^2-rich interior surface of the open holes are responsible for this selective capture of microscopic particles.

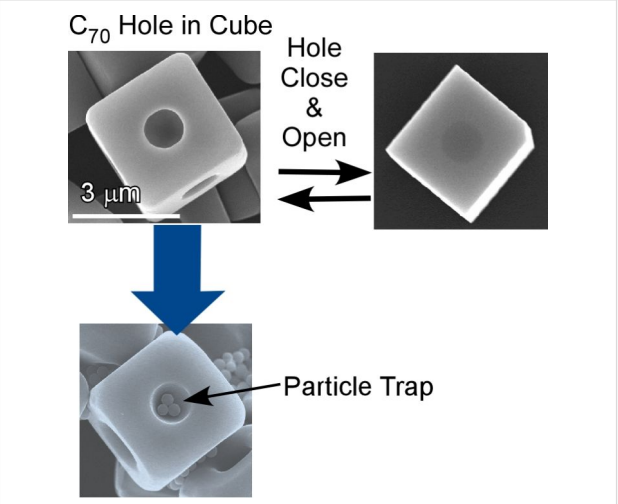

Figure 22: Hole-in-cube structures made from C_{70} molecules with hole closing and re-opening and particle-trap capability. Reproduced from [75], copyright 2019 The authors.

The preparation of mesoporous crystalline cubes of C_{70} molecules with unusually enhanced photoluminescence has been recently reported by Shrestha and co-workers [255]. The mesoporous C_{70} cubes can be prepared by applying a mild heat treatment process to the liquid–liquid interfacial precipitation from *tert*-butyl alcohol and mesitylene. Initially formed crystalline C_{70} cubes were transformed into mesoporous C_{70} cubes via intermediate one-dimensional structures. The resulting mesoporous C_{70} cubes showed enhanced photoluminescence probably due to their highly crystalline framework structures. In addition, these materials exhibited superior electrochemical supercapacitance over pristine C_{70} because of their increased electrochemically active surface areas.

Shrestha et al. also reported a modified method of liquid–liquid interfacial precipitation for fullerene nanoarchitectonics using non-ionic surfactants such as diglycerol monolaurate and diglycerol monomyristate [256]. The liquid–liquid precipitation from isopropyl alcohol and ethylbenzene usually provided one-dimensional structures. These were, however, transformed into Konpeito candy-like three-dimensional crystalline structures in the presence of the above surfactants in the ethylbenzene phase. Furthermore, the fabricated three-dimensional objects can be graphitized by heat treatment at 2000 °C. The obtained carbon materials show a high potential for applications in energy storage supercapacitor devices.

Liquid–liquid interfacial precipitation methods with the strategies of mixing components and conjugating molecules also create interesting results. Lu, Guldi, and co-workers investigated the co-crystallization of C_{70} and (metallo)porphyrins through liquid–liquid interfacial precipitation to give two-dimensional nanosheet structures [257]. Single crystal X-ray diffraction studies on the fabricated objects confirmed equimolar fractions of these two components. As indicated by steady-state absorption spectroscopy and fluorescence spectroscopy, a strong charge transfer interaction resulted in the charge separation with one-electron reduced C_{70} and one-electron oxidized (metallo)porphyrins. Li and co-workers reported the formation of superstructures of a C_{60}–adamantane conjugate through liquid–liquid interfacial precipitation with chloroform as the good solvent [258]. Diverse morphological structures with various dimensionalities such as spheres, fibers, plates, nanoflowers, cubes and microparticles were obtained.

As an interesting example of two-component fullerene assemblies at liquid–liquid interfaces, Minami, Shrestha, and co-workers demonstrated time-dependent shape shifts of co-assemblies of two fullerene derivatives, pentakis(phenyl)fullerene and pentakis(4-dodecylphenyl)fullerene (Figure 23) [259]. Structural shifts from egg-like structures to tadpole-like structures are regarded as supramolecular differentiation. At the interface of isopropyl alcohol and toluene, egg-like structures were first formed from the mixture of these two components.

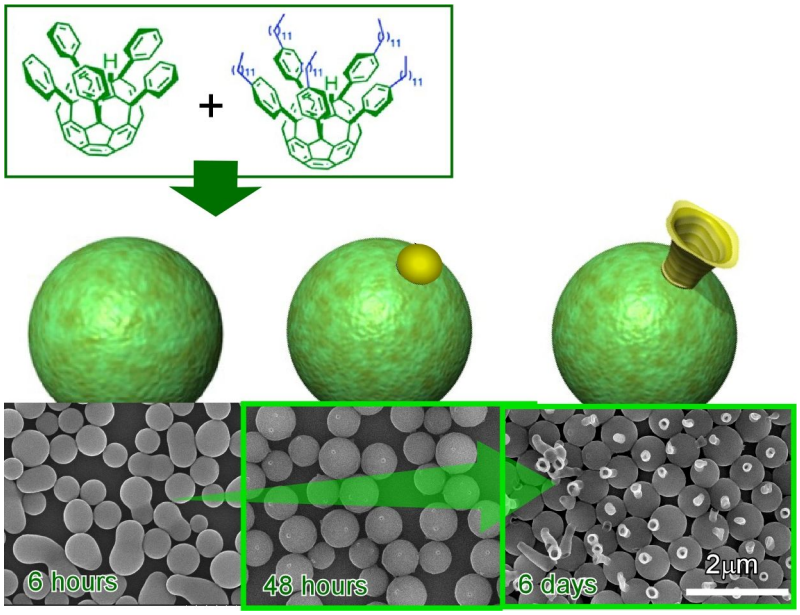

Figure 23: Time-dependent shape shift of co-assemblies of two fullerene derivatives, pentakis(phenyl)fullerene and pentakis(4-dodecylphenyl)fullerene from egg-like structures to tadpole-like structure regarded as supramolecular differentiation. Reproduced from [75], copyright 2019 The Authors.

One or multiple domains of pentakis(4-dodecylphenyl)fullerene appeared on the spherical assemblies of pentakis(phenyl)fullerene using appropriate mixing ratios and appropriate incubation times. From the phase-separated domains, one-dimensional tubular structures of pentakis(4-dodecylphenyl)fullerene preferentially growth as tails upon gentle sonication. The observed supramolecular differentiation can be regarded as the materials-science-based analogue of embryonic development.

5 Interfacial nanoarchitectonics for biomaterials

Well-designed biomolecular units should be powerful tools for nanoarchitectonics of low-dimensional materials [260-262]. Asymmetric motifs of biomolecular units can be well designed in many cases and the synthesized asymmetric units are often assembled into low-dimensional structures. As summarized in a recent review article by Matsuura [263], assembled structures of various shapes can be nanoengineered from well-designed biomolecular units such as carbohydrate-conjugated oligodeoxyribonucleotides and three-way junctions of DNA assemblies and oligopeptides. Uses of the assembled low-dimensional materials for drug carriers, ligand-displaying scaffolds, and platform for platforms are anticipated. Sawada and Serizawa explained in their recent review the use of M13 phages for asymmetrical assemblies [264]. Although M13 phages are generally known as useful scaffold for phage-display technology, they utilized the M13 phages as one-dimensional building block for novel liquid crystalline materials. These unique approaches can open a new avenue for phage-based soft materials. He and Xu reported a novel concept, namely, instructed assembly (iAssembly) [265], which can yield ordered low-dimensional assemblies as the consequence of at least one trigger event. The instructed assembly can be well related to molecular processes to control cell fate.

These examples strikingly indicate that biomaterials have a high potential as building blocks for nanoarchitectonics of functional low-dimensional structures. Restricting these assembly processes two low-dimensional media with certain degrees of motional freedom and diffusional restriction would result in functional low-dimensional materials with attractive biological functions. Liquid interfaces (especially aqueous interfaces) would be appropriate media for this purpose. However, the high surface tension at the air–water interface is disadvantageous for protein assembly because undesirable transformations of secondary structures might be induced by the high surface tension. One method to suppress surface denaturation during two-dimensional protein assembly was proposed by Fromherz. The adsorption of proteins from an underneath aqueous subphase to a lipid monolayer at the air–water interface in a multi-compartment trough can prevent undesirable denaturation of proteins [266,267].

Because the method by Fromherz may waste unused proteins in the subphase, it is not always suitable for the two-dimensional assembly of precious biomaterials. In order to overcome this drawback, Okahata and co-workers used lipid-coated proteins

for a LB process at the air–water interface [268,269]. Water-soluble biomolecules such as proteins were mixed with aqueous vesicles of appropriate lipid molecules, resulting in a water-insoluble lipid–biomolecule complex. For example, glucose oxidase was complexed with a cationic lipid to provide water-insoluble materials that were soluble in organic solvents. A benzene solution of the resulting complex was dripped at the air–water interface to give a monolayer film of glucose oxidase and the lipid. The, only the amount of glucose oxidase needed for monolayer formation is required and denaturation of glucose oxidase is avoided by lowering the surface tension through the presence of the lipid. The monolayers were transferred onto a surface of electrodes, leading to glucose detection sensors (Figure 24). Similarly, the presence of additional components such as lipids and polymers is advantageous for other methods of fabricating two-dimensional layered films, such as layer-by-layer assembly [270-273]. Single-enzyme and multi-enzyme reactors were successfully demonstrated [274-276].

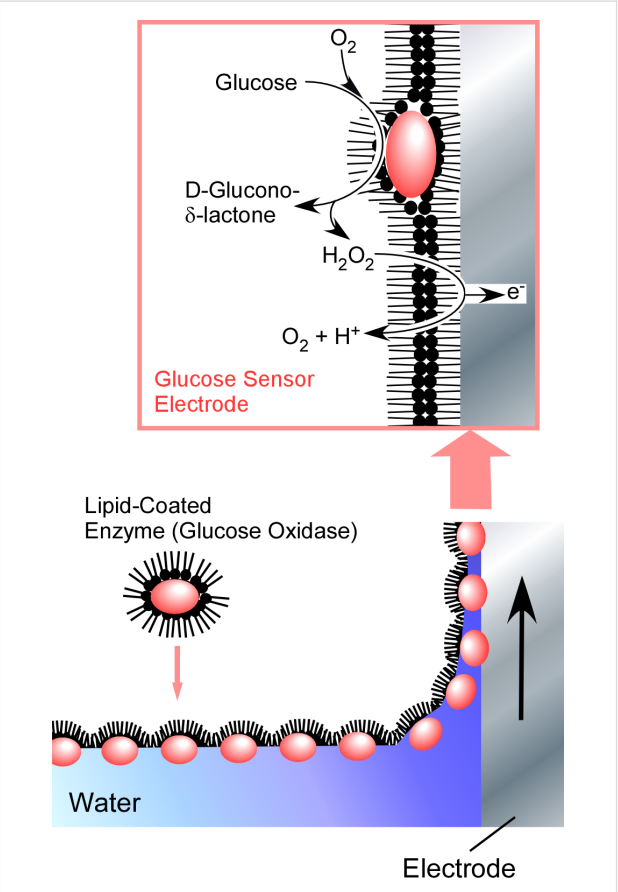

Figure 24: A monolayer of glucose oxidase complexed with a cationic lipid was transferred onto a surface of an electrode for glucose detection sensors.

In addition to the above-mentioned basic efforts in the nanoarchitectonics of bio-components through processes at liquid interfaces, there are more advanced strategies currently under research. For example, the culture, the organization, and the control over the differentiation of living cells have been investigated recently at liquid interfaces. Minami et al. pioneered in the cell differentiation control at a liquid–liquid interface (Figure 25) [277]. Several other research works [278-287] revealed that interfaces between perfluorocarbons and aqueous media are usable for the research of morphological changes, division, and the viability of cells. Minami et al. successfully demonstrated the regulation of myogenic differentiation of C2C12 myoblast cells at water–perfluorocarbon interfaces as fully fluidic microenvironments. While the expression of MyoD remained at the usual level, the expression of myogenic regulatory factors was remarkably attenuated. The observed unusual regulation of myogenic differentiation was attributed to the fluidic nature of the water–perfluorocarbon interfaces. These interfacial cell culture systems might provide good opportunities to study mechanobiological effects in cell science and tissue engineering.

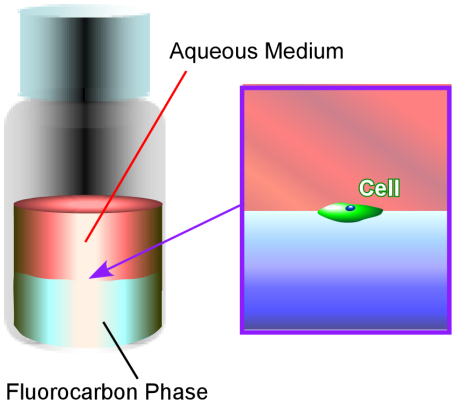

Figure 25: Cultures, organizations, and differentiation controls of living cells a liquid-liquid interface between aqueous media and fluorocarbon phase.

The formation of two-dimensional protein nanosheets and the modulation of stem cell mechanosensing at water–perfluorocarbon interfaces has been recently reported by Jia and co-workers [288]. At the water–perfluorocarbon interfaces, serum proteins were denatured to self-assemble into two-dimensional protein nanosheets. Their packing can be tuned through the selection of the perfluorocarbon compound, e.g., perfluorodecalin or perfluorotributylamine. Human mesenchymal stem cells are mechanically affected by the contact with the two-dimensional protein nanosheets. Spreading, adhesion growth, and yes-associated protein nuclear translocation of the cells were triggered by a greater stiffness of the two-dimensional protein nanosheets. The observed behaviour can be explained by a molecular clutch model (Figure 26). The underlying two-

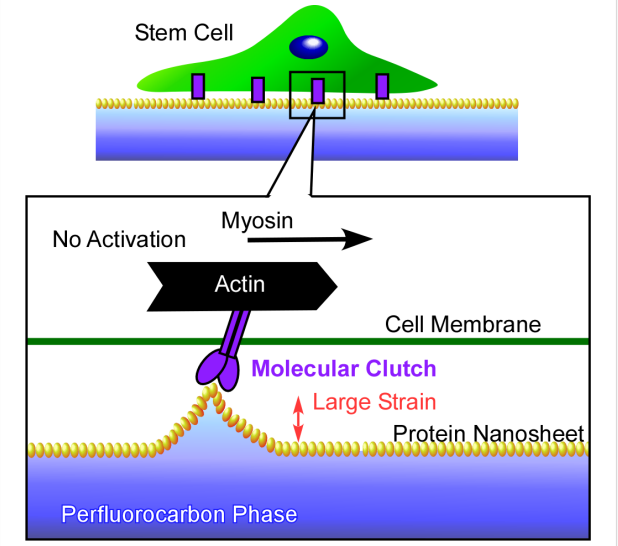

Figure 26: Human mesenchymal stem cells at the interface between aqueous medium and fluorocarbon phase with self-grown two-dimensional protein nanosheets at which the mechanical behaviour of cells can be explained by a molecular clutch model.

dimensional protein nanosheets are extremely flexible and exhibit a large strain upon traction by the cells, which is probably greater than the effect from solid surfaces. The obtained results are useful for the understanding of interactions between cells and materials at liquid interfacial media, as well as in the development of stem cell culture media, and regenerative therapies.

Yang and co-workers also demonstrated the fabrication of two-dimensional amyloid-like ultrathin two-dimensional protein membranes at the air–water interface [289]. The membranes are formed through fast aggregation of amyloid-like lysozyme molecules with controllable thickness from 30 to 250 nm accompanied by the formation of pores with diameters of 1.8 to 3.2 nm. While the two-dimensional membranes allow for a rather fast permeation of small substances, molecules and particles larger than 3 nm are retained at the membrane. Therefore, these two-dimensional materials exhibited an excellent hemodialysis capability to remove uremic toxins of medium molecular weight. The fabricated two-dimensional protein materials might be applied in pressure-driven filtration, size-directed forward osmosis, and large-scale dialysis systems.

Instead of spontaneously formed low-dimensional protein materials, low-dimensional fullerene materials artificially prepared at liquid interfaces have been used for the regulation of cell alignment and differentiation. Krishnan et al. applied a novel vortex LB method to align one-dimensional C_{60} nanowhiskers with controlled alignment and curvature (Figure 27) [290]. As described above, the vortex LB method utilizes the air–water interface with a vortex rotation of one subphase, which can

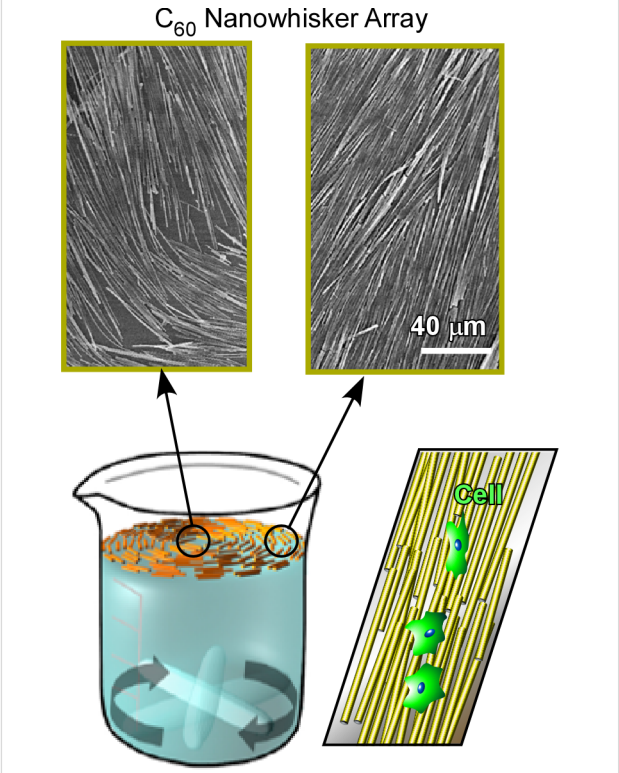

Figure 27: One-dimensional C_{60} nanowhiskers with controlled alignment and curvature fabricated by a vortex LB method for the culture of bone-forming human osteoblast MG63 cells.

align one-dimensional C_{60} nanowhiskers to the flow direction. The aligned nanowhiskers can be also transferred onto a solid substrate but their geometry can be regulated through the selection of the transfer position from the centre of vortex motion. While a transfer far from the centre resulted in almost parallel alignment, curved alignment can be obtained through transfer from near the vortex centre. The aligned C_{60} nanowhisker arrays were used as a scaffold for the culture of bone-forming human osteoblast MG63 cells. Cell growth occurred mostly along the axis of the aligned one-dimensional C_{60} nanowhiskers. In addition, the low toxicity of the C_{60} nanowhiskers was confirmed by cell proliferation test.

Minami et al. investigated the regulation of macroscopic cell orientation and differentiation of mouse skeletal myoblast C2C12 cells [291]. Highly aligned C_{60} nanowhisker arrays on a solid surface were fabricated via conventional LB transfer from the air–water interface. The culture of C2C12 cells on the aligned C_{60} nanowhiskers led to a significant enhancement of myotube formation with highly regulated directional growth. Hsu and co-workers proposed the fabrication of highly oriented and well-aligned arrays of one-dimensional C_{60} nanowhiskers through the modification of motion in a dynamic LB process [292]. Instead of vortex rotational motion, they used a recip-

rocal (shaking) motion in one direction for a monolayer of C_{60} nanowhiskers at the air–water interface, resulting in arrays of C_{60} nanowhiskers with a higher degree of alignment (Figure 28). The differentiation of neural stem cells on highly aligned C_{60} nanowhiskers was investigated to show their enhanced viability and their differentiation into mature neurons. Because of the biocompatibility of the used one-dimensional C_{60} nanowhiskers and the high potential for large-area fabrication, the presented C_{60} scaffolds might be a promising platform for patterned cell scaffolds for tissue engineering.

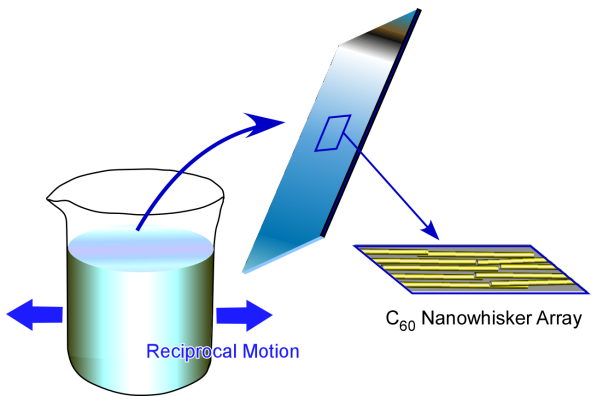

Figure 28: Highly aligned arrays of C_{60} nanowhiskers obtained by using a LB method with reciprocal motion in one direction for differentiation control of neural stem cells.

Highly expressible bacteriorhodopsin is known as a light-sensitive opsin with the potential capability of triggering neuronal activities through optogenetic modulation [293]. Optogenetic modulation and reprogramming of human fibroblasts transfected by highly expressible bacteriorhodopsin was investigated by Hsu and co-workers using tow-dimensional C_{60} nanosheets [294]. The transfected fibroblasts cultured on C_{60} nanosheets with controlled light illumination induced reprogramming and differentiation into neural cells. This approach may indicate the possibility to control cell differentiation by selective location (on two-dimensional C_{60} nanosheets) and timing (illumination time).

6 Conclusion and Perspectives

For designing advanced functions within a small space, the selective and anisotropic organization of materials, energy, electrons, and information is indispensable. One of the promising methods to obtain such a unique aggregated state would be using low-dimensional anisotropic systems and materials. Low-dimensional materials including nanoparticle, nanorods, and nanosheets have been paid much attention in science and technology in this context recently. In addition to conventional low-dimensional materials such as fullerene, carbon nanotubes, graphene and various two-dimensional materials, constructing novel low-dimensional materials from a wide range of nanomaterials precursors is an attractive research field. A novel concept called nanoarchitectonics in which functional materials are engineered from nanoscale components, might be the best methodology for this objective. Especially, the use of dynamic interfacial media providing a unique restriction the molecular motion is advantageous for the facile synthesis of anisotropic low-dimensional materials.

Based on these general considerations, this review described bottom-up syntheses of low-dimensional systems and materials using materials nanoarchitectonics at two-dimensional liquid interfaces. The contents of the review article range from the description of basic characteristics of interfacial media with specific features of molecular interactions to various materials systems including molecular patterns, two-dimensional MOF/COF, low-dimensional nanocarbons, and biomaterial assemblies including living cells at liquid interfaces. Methodologies to realize materials nanoarchitectonics at two-dimensional liquid interfaces make use of various aspects and functions of low-dimensional systems and materials including the control of fundamental molecular interactions that regulate complicated cell functions. A generality of nanoarchitectonics concepts at liquid interfaces for low-dimensional systems and materials can be found in the examples introduced in this review.

For future developments of the nanoarchitectonics strategy, two essential features need to be considered in more detail. The first is the control of functional component units within low-dimensional materials, especially in two-dimensional planes. Very advanced functions seen in biological systems such as energy conversion and signal transduction highly rely on sophisticated arrangements and organizations of functional elements within two-dimensional cell membranes. These sophisticated biological systems need to be studied more extensively as an ideal example of low-dimensional functional materials. The regulation of the organization of functional components within low-dimensional structures would be a key methodology to develop low-dimensional systems to the next stage. Another key requirement of nanoarchitectonics would be the development of large-scale production. Most of research efforts on nanoarchitectonics-based low-dimensional materials are still at the laboratory scale, which is not attractive for further industrial developments. The use of low-cost precursors and application examples that can be realized with simple technical procedures would be important. Upon technical development according to these required features, low-dimensional systems and materials might give more opportunities to design advanced functions for industrial applications.

Acknowledgements

This study was partially supported by JSPS KAKENHI Grant Number JP16H06518 (Coordination Asymmetry) and CREST JST Grant Number JPMJCR1665.

ORCID® iDs

Katsuhiko Ariga - https://orcid.org/0000-0002-2445-2955
Taizo Mori - https://orcid.org/0000-0002-6974-5137
Lok Kumar Shrestha - https://orcid.org/0000-0003-2680-6291

References

1. Silvestre, B. S.; Tîrcă, D. M. *J. Cleaner Prod.* **2019,** *208,* 325–332. doi:10.1016/j.jclepro.2018.09.244
2. Povie, G.; Segawa, Y.; Nishihara, T.; Miyauchi, Y.; Itami, K. *Science* **2017,** *356,* 172–175. doi:10.1126/science.aam8158
3. Wang, Y.; Michinobu, T. *Bull. Chem. Soc. Jpn.* **2017,** *90,* 1388–1400. doi:10.1246/bcsj.20170294
4. Takimiya, K.; Nakano, M. *Bull. Chem. Soc. Jpn.* **2018,** *91,* 121–140. doi:10.1246/bcsj.20170298
5. Sun, Z.; Matsuno, T.; Isobe, H. *Bull. Chem. Soc. Jpn.* **2018,** *91,* 907–921. doi:10.1246/bcsj.20180051
6. Sun, Z.; Ikemoto, K.; Fukunaga, T. M.; Koretsune, T.; Arita, R.; Sato, S.; Isobe, H. *Science* **2019,** *363,* 151–155. doi:10.1126/science.aau5441
7. Soloviev, I. I.; Klenov, N. V.; Bakurskiy, S. V.; Kupriyanov, M. Y.; Gudkov, A. L.; Sidorenko, A. S. *Beilstein J. Nanotechnol.* **2017,** *8,* 2689–2710. doi:10.3762/bjnano.8.269
8. Taniguchi, M. *Bull. Chem. Soc. Jpn.* **2017,** *90,* 1189–1210. doi:10.1246/bcsj.20170224
9. Su, V.-C.; Chu, C. H.; Sun, G.; Tsai, D. P. *Opt. Express* **2018,** *26,* 13148–13182. doi:10.1364/oe.26.013148
10. Huang, X.; Wang, J.; Li, T.; Wang, J.; Xu, M.; Yu, W.; El Abed, A.; Zhang, X. *Beilstein J. Nanotechnol.* **2018,** *9,* 30–41. doi:10.3762/bjnano.9.5
11. Nishizawa, M. *Bull. Chem. Soc. Jpn.* **2018,** *91,* 1141–1149. doi:10.1246/bcsj.20180064
12. Li, J.-F.; Zhang, Y.-J.; Ding, S.-Y.; Panneerselvam, R.; Tian, Z.-Q. *Chem. Rev.* **2017,** *117,* 5002–5069. doi:10.1021/acs.chemrev.6b00596
13. Mizutani, Y. *Bull. Chem. Soc. Jpn.* **2017,** *90,* 1344–1371. doi:10.1246/bcsj.20170218
14. Zrimsek, A. B.; Chiang, N.; Mattei, M.; Zaleski, S.; McAnally, M. O.; Chapman, C. T.; Henry, A.-I.; Schatz, G. C.; Van Duyne, R. P. *Chem. Rev.* **2017,** *117,* 7583–7613. doi:10.1021/acs.chemrev.6b00552
15. Ruiz-Hitzky, E.; Gómez-Avilés, A.; Darder, M.; Aranda, P. *Bull. Chem. Soc. Jpn.* **2018,** *91,* 608–616. doi:10.1246/bcsj.20170425
16. Einaga, Y. *Bull. Chem. Soc. Jpn.* **2018,** *91,* 1752–1762. doi:10.1246/bcsj.20180268
17. Hu, M.; Reboul, J.; Furukawa, S.; Torad, N. L.; Ji, Q.; Srinivasu, P.; Ariga, K.; Kitagawa, S.; Yamauchi, Y. *J. Am. Chem. Soc.* **2012,** *134,* 2864–2867. doi:10.1021/ja208940u
18. Chaikittisilp, W.; Torad, N. L.; Li, C.; Imura, M.; Suzuki, N.; Ishihara, S.; Ariga, K.; Yamauchi, Y. *Chem. – Eur. J.* **2014,** *20,* 4217–4221. doi:10.1002/chem.201304404
19. Malgras, V.; Ji, Q.; Kamachi, Y.; Mori, T.; Shieh, F.-K.; Wu, K. C.-W.; Ariga, K.; Yamauchi, Y. *Bull. Chem. Soc. Jpn.* **2015,** *88,* 1171–1200. doi:10.1246/bcsj.20150143
20. Wei, Q.; Xiong, F.; Tan, S.; Huang, L.; Lan, E. H.; Dunn, B.; Mai, L. *Adv. Mater. (Weinheim, Ger.)* **2017,** *29,* 1602300. doi:10.1002/adma.201602300
21. Gon, M.; Tanaka, K.; Chujo, Y. *Bull. Chem. Soc. Jpn.* **2017,** *90,* 463–474. doi:10.1246/bcsj.20170005
22. Jana, A.; Scheer, E.; Polarz, S. *Beilstein J. Nanotechnol.* **2017,** *8,* 688–714. doi:10.3762/bjnano.8.74
23. Yao, Q.; Yuan, X.; Chen, T.; Leong, D. T.; Xie, J. *Adv. Mater. (Weinheim, Ger.)* **2018,** *30,* 1802751. doi:10.1002/adma.201802751
24. Kobayashi, Y. *Bull. Chem. Soc. Jpn.* **2018,** *91,* 467–485. doi:10.1246/bcsj.20170374
25. Chaikittisilp, W.; Hu, M.; Wang, H.; Huang, H.-S.; Fujita, T.; Wu, K. C.-W.; Chen, L.-C.; Yamauchi, Y.; Ariga, K. *Chem. Commun.* **2012,** *48,* 7259–7261. doi:10.1039/c2cc33433j
26. Torad, N. L.; Hu, M.; Ishihara, S.; Sukegawa, H.; Belik, A. A.; Imura, M.; Ariga, K.; Sakka, Y.; Yamauchi, Y. *Small* **2014,** *10,* 2096–2107. doi:10.1002/smll.201302910
27. Guo, D.; Shibuya, R.; Akiba, C.; Saji, S.; Kondo, T.; Nakamura, J. *Science* **2016,** *351,* 361–365. doi:10.1126/science.aad0832
28. Kumar, S.; Kumar, A.; Bahuguna, A.; Sharma, V.; Krishnan, V. *Beilstein J. Nanotechnol.* **2017,** *8,* 1571–1600. doi:10.3762/bjnano.8.159
29. Stauss, S.; Honma, I. *Bull. Chem. Soc. Jpn.* **2018,** *91,* 492–505. doi:10.1246/bcsj.20170325
30. Miyasaka, T. *Bull. Chem. Soc. Jpn.* **2018,** *91,* 1058–1068. doi:10.1246/bcsj.20180071
31. Watanabe, M.; Dokko, K.; Ueno, K.; Thomas, M. L. *Bull. Chem. Soc. Jpn.* **2018,** *91,* 1660–1682. doi:10.1246/bcsj.20180216
32. Egorova, K. S.; Gordeev, E. G.; Ananikov, V. P. *Chem. Rev.* **2017,** *117,* 7132–7189. doi:10.1021/acs.chemrev.6b00562
33. Saptiama, I.; Kaneti, Y. V.; Suzuki, Y.; Suzuki, Y.; Tsuchiya, K.; Sakae, T.; Takai, K.; Fukumitsu, N.; Alothman, Z. A.; Hossain, M. S. A.; Ariga, K.; Yamauchi, Y. *Bull. Chem. Soc. Jpn.* **2017,** *90,* 1174–1179. doi:10.1246/bcsj.20170184
34. Chou, K.-C. *Curr. Top. Med. Chem.* **2017,** *17,* 2337–2358. doi:10.2174/1568026617666170414145508
35. Asanuma, H.; Murayama, K.; Kamiya, Y.; Kashida, H. *Bull. Chem. Soc. Jpn.* **2018,** *91,* 1739–1748. doi:10.1246/bcsj.20180278
36. Zheng, K.; Setyawati, M. I.; Leong, D. T.; Xie, J. *Coord. Chem. Rev.* **2018,** *357,* 1–17. doi:10.1016/j.ccr.2017.11.019
37. Saptiama, I.; Kaneti, Y. V.; Oveisi, H.; Suzuki, Y.; Tsuchiya, K.; Takai, K.; Sakae, T.; Pradhan, S.; Hossain, M. S. A.; Fukumitsu, N.; Ariga, K.; Yamauchi, Y. *Bull. Chem. Soc. Jpn.* **2018,** *91,* 195–200. doi:10.1246/bcsj.20170295
38. Kiguchi, M.; Fujii, S. *Bull. Chem. Soc. Jpn.* **2017,** *90,* 1–11. doi:10.1246/bcsj.20160229
39. Yamamura, A.; Watanabe, S.; Uno, M.; Mitani, M.; Mitsui, C.; Tsurumi, J.; Isahaya, N.; Kanaoka, Y.; Okamoto, T.; Takeya, J. *Sci. Adv.* **2018,** *4,* eaao5758. doi:10.1126/sciadv.aao5758
40. Acharya, S.; Hill, J. P.; Ariga, K. *Adv. Mater. (Weinheim, Ger.)* **2009,** *21,* 2959–2981. doi:10.1002/adma.200802648
41. Wang, R.; Lu, K.-Q.; Tang, Z.-R.; Xu, Y.-J. *J. Mater. Chem. A* **2017,** *5,* 3717–3734. doi:10.1039/c6ta08660h
42. Lodahl, P.; Mahmoodian, S.; Stobbe, S.; Rauschenbeutel, A.; Schneeweiss, P.; Volz, J.; Pichler, H.; Zoller, P. *Nature* **2017,** *541,* 473–480. doi:10.1038/nature21037

43. Nakano, K.; Honda, T.; Yamasaki, K.; Tanaka, Y.; Taniguchi, K.; Ishimatsu, R.; Imato, T. *Bull. Chem. Soc. Jpn.* **2018,** *91,* 1128–1130. doi:10.1246/bcsj.20180095
44. Ding, X.; Peng, F.; Zhou, J.; Gong, W.; Slaven, G.; Loh, K. P.; Lim, C. T.; Leong, D. T. *Nat. Commun.* **2019,** *10,* 41. doi:10.1038/s41467-018-07835-1
45. Datta, K. K. R.; Reddy, B. V. S.; Ariga, K.; Vinu, A. *Angew. Chem., Int. Ed.* **2010,** *49,* 5961–5965. doi:10.1002/anie.201001699
46. Shirai, H.; Nguyen, M. T.; Čempel, D.; Tsukamoto, H.; Tokunaga, T.; Liao, Y.-C.; Yonezawa, T. *Bull. Chem. Soc. Jpn.* **2017,** *90,* 279–285. doi:10.1246/bcsj.20160333
47. Huang, R.; Chen, H.; Xia, Z. *Bull. Chem. Soc. Jpn.* **2017,** *90,* 754–759. doi:10.1246/bcsj.20170016
48. Choukourov, A.; Pleskunov, P.; Nikitin, D.; Titov, V.; Shelemin, A.; Vaidulych, M.; Kuzminova, A.; Solař, P.; Hanuš, J.; Kousal, J.; Kylián, O.; Slavínská, D.; Biederman, H. *Beilstein J. Nanotechnol.* **2017,** *8,* 2002–2014. doi:10.3762/bjnano.8.200
49. Bhattacharyya, K.; Mukherjee, S. *Bull. Chem. Soc. Jpn.* **2018,** *91,* 447–454. doi:10.1246/bcsj.20170377
50. Kani, K.; Zakaria, M. B.; Lin, J.; Alshehri, A. A.; Kim, J.; Bando, Y.; You, J.; Hossain, M. S. A.; Bo, J.; Yamauchi, Y. *Bull. Chem. Soc. Jpn.* **2018,** *91,* 1333–1336. doi:10.1246/bcsj.20180129
51. Yonezawa, T.; Čempel, D.; Nguyen, M. T. *Bull. Chem. Soc. Jpn.* **2018,** *91,* 1781–1798. doi:10.1246/bcsj.20180285
52. Zhang, R.; Zhang, Y.; Wei, F. *Chem. Soc. Rev.* **2017,** *46,* 3661–3715. doi:10.1039/c7cs00104e
53. Kharlamova, M. V. *Beilstein J. Nanotechnol.* **2017,** *8,* 826–856. doi:10.3762/bjnano.8.85
54. Clancy, A. J.; Anthony, D. B.; Fisher, S. J.; Leese, H. S.; Roberts, C. S.; Shaffer, M. S. P. *Nanoscale* **2017,** *9,* 8764–8773. doi:10.1039/c7nr00734e
55. Chen, R.; Kang, J.; Kang, M.; Lee, H.; Lee, H. *Bull. Chem. Soc. Jpn.* **2018,** *91,* 979–990. doi:10.1246/bcsj.20180042
56. Ji, Q.; Honma, I.; Paek, S.-M.; Akada, M.; Hill, J. P.; Vinu, A.; Ariga, K. *Angew. Chem., Int. Ed.* **2010,** *49,* 9737–9739. doi:10.1002/anie.201004929
57. Anasori, B.; Lukatskaya, M. R.; Gogotsi, Y. *Nat. Rev. Mater.* **2017,** *2,* 16098. doi:10.1038/natrevmats.2016.98
58. Khan, A. H.; Ghosh, S.; Pradhan, B.; Dalui, A.; Shrestha, L. K.; Acharya, S.; Ariga, K. *Bull. Chem. Soc. Jpn.* **2017,** *90,* 627–648. doi:10.1246/bcsj.20170043
59. Manzeli, S.; Ovchinnikov, D.; Pasquier, D.; Yazyev, O. V.; Kis, A. *Nat. Rev. Mater.* **2017,** *2,* 17033. doi:10.1038/natrevmats.2017.33
60. Ariga, K.; Watanabe, S.; Mori, T.; Takeya, J. *NPG Asia Mater.* **2018,** *10,* 90–106. doi:10.1038/s41427-018-0022-9
61. Maeda, K.; Mallouk, T. E. *Bull. Chem. Soc. Jpn.* **2019,** *92,* 38–54. doi:10.1246/bcsj.20180258
62. Ulaganathan, R. K.; Chang, Y.-H.; Wang, D.-Y.; Li, S.-S. *Bull. Chem. Soc. Jpn.* **2018,** *91,* 761–771. doi:10.1246/bcsj.20180016
63. Sakamoto, R. *Bull. Chem. Soc. Jpn.* **2017,** *90,* 272–278. doi:10.1246/bcsj.20160304
64. Liu, J.; Chen, Q.-W.; Wu, K. *Chin. Chem. Lett.* **2017,** *28,* 1631–1639. doi:10.1016/j.cclet.2017.04.022
65. Ariga, K.; Mori, T.; Shrestha, L. K. *Chem. Rec.* **2018,** *18,* 676–695. doi:10.1002/tcr.201700070
66. Cao, L.; Wang, T.; Wang, C. *Chin. J. Chem.* **2018,** *36,* 754–764. doi:10.1002/cjoc.201800144
67. Wang, Y.; Mayorga-Martinez, C. C.; Pumera, M. *Bull. Chem. Soc. Jpn.* **2017,** *90,* 847–853. doi:10.1246/bcsj.20170076
68. Ariga, K.; Jia, X.; Shrestha, L. K. *Mol. Syst. Des. Eng.* **2019,** *4,* 49–64. doi:10.1039/c8me00094h
69. Seki, T. *Bull. Chem. Soc. Jpn.* **2018,** *91,* 1026–1057. doi:10.1246/bcsj.20180076
70. Vinu, A.; Miyahara, M.; Ariga, K. *J. Nanosci. Nanotechnol.* **2006,** *6,* 1510–1532. doi:10.1166/jnn.2006.253
71. Katagiri, K.; Hashizume, M.; Ariga, K.; Terashima, T.; Kikuchi, J.-i. *Chem. – Eur. J.* **2007,** *13,* 5272–5281. doi:10.1002/chem.200700175
72. Ariga, K.; Hill, J. P.; Lee, M. V.; Vinu, A.; Charvet, R.; Acharya, S. *Sci. Technol. Adv. Mater.* **2008,** *9,* 014109. doi:10.1088/1468-6996/9/1/014109
73. Ariga, K.; Hill, J. P.; Ji, Q. *Macromol. Biosci.* **2008,** *8,* 981–990. doi:10.1002/mabi.200800102
74. Haketa, Y.; Maeda, H. *Bull. Chem. Soc. Jpn.* **2018,** *91,* 420–436. doi:10.1246/bcsj.20170434
75. Ariga, K.; Nishikawa, M.; Mori, T.; Takeya, J.; Shrestha, L. K.; Hill, J. P. *Sci. Technol. Adv. Mater.* **2019,** *20,* 51–95. doi:10.1080/14686996.2018.1553108
76. Hiraoka, S. *Bull. Chem. Soc. Jpn.* **2018,** *91,* 957–978. doi:10.1246/bcsj.20180008
77. Dhiman, S.; George, S. J. *Bull. Chem. Soc. Jpn.* **2018,** *91,* 687–699. doi:10.1246/bcsj.20170433
78. Shimizu, T. *Bull. Chem. Soc. Jpn.* **2018,** *91,* 623–668. doi:10.1246/bcsj.20170424
79. Komiyama, M.; Mori, T.; Ariga, K. *Bull. Chem. Soc. Jpn.* **2018,** *91,* 1075–1111. doi:10.1246/bcsj.20180084
80. Akamatsu, M.; Komatsu, H.; Matsuda, A.; Mori, T.; Nakanishi, W.; Sakai, H.; Hill, J. P.; Ariga, K. *Bull. Chem. Soc. Jpn.* **2017,** *90,* 678–683. doi:10.1246/bcsj.20170046
81. Suda, M. *Bull. Chem. Soc. Jpn.* **2018,** *91,* 19–28. doi:10.1246/bcsj.20170283
82. Abdullayev, E.; Sakakibara, K.; Okamoto, K.; Wei, W.; Ariga, K.; Lvov, Y. *ACS Appl. Mater. Interfaces* **2011,** *3,* 4040–4046. doi:10.1021/am200896d
83. Vinokurov, V. A.; Stavitskaya, A. V.; Chudakov, Y. A.; Ivanov, E. V.; Shrestha, L. K.; Ariga, K.; Darrat, Y. A.; Lvov, Y. M. *Sci. Technol. Adv. Mater.* **2017,** *18,* 147–151. doi:10.1080/14686996.2016.1278352
84. Glotov, A.; Stavitskaya, A.; Chudakov, Y.; Ivanov, E.; Huang, W.; Vinokurov, V.; Zolotukhina, A.; Maximov, A.; Karakhanov, E.; Lvov, Y. *Bull. Chem. Soc. Jpn.* **2019,** *92,* 61–69. doi:10.1246/bcsj.20180207
85. Zhong, S.; Xu, Q. *Bull. Chem. Soc. Jpn.* **2018,** *91,* 1606–1617. doi:10.1246/bcsj.20180227
86. Sengottaiyan, C.; Jayavel, R.; Bairi, P.; Shrestha, R. G.; Ariga, K.; Shrestha, L. K. *Bull. Chem. Soc. Jpn.* **2017,** *90,* 955–962. doi:10.1246/bcsj.20170092
87. Li, B. L.; Setyawati, M. I.; Chen, L.; Xie, J.; Ariga, K.; Lim, C.-T.; Garaj, S.; Leong, D. T. *ACS Appl. Mater. Interfaces* **2017,** *9,* 15286–15296. doi:10.1021/acsami.7b02529
88. Ariga, K.; Ji, Q.; Hill, J. P.; Bando, Y.; Aono, M. *NPG Asia Mater.* **2012,** *4,* e17. doi:10.1038/am.2012.30
89. Ariga, K.; Ji, Q.; Nakanishi, W.; Hill, J. P.; Aono, M. *Mater. Horiz.* **2015,** *2,* 406–413. doi:10.1039/c5mh00012b
90. Ariga, K.; Yamauchi, Y.; Aono, M. *APL Mater.* **2015,** *3,* 061001. doi:10.1063/1.4922549
91. Ariga, K.; Aono, M. *Jpn. J. Appl. Phys.* **2016,** *55,* 1102A6. doi:10.7567/jjap.55.1102a6
92. Ariga, K.; Li, M.; Richards, G.; Hill, J. *J. Nanosci. Nanotechnol.* **2011,** *11,* 1–13. doi:10.1166/jnn.2011.3839

93. Ariga, K.; Li, J.; Fei, J.; Ji, Q.; Hill, J. P. *Adv. Mater. (Weinheim, Ger.)* **2016,** *28,* 1251–1286. doi:10.1002/adma.201502545
94. Shirai, Y.; Minami, K.; Nakanishi, W.; Yonamine, Y.; Joachim, C.; Ariga, K. *Jpn. J. Appl. Phys.* **2016,** *55,* 1102A2. doi:10.7567/jjap.55.1102a2
95. Aono, M.; Ariga, K. *Adv. Mater. (Weinheim, Ger.)* **2016,** *28,* 989–992. doi:10.1002/adma.201502868
96. Ariga, K. *Mater. Chem. Front.* **2017,** *1,* 208–211. doi:10.1039/c6qm00240d
97. Ariga, K.; Vinu, A.; Yamauchi, Y.; Ji, Q.; Hill, J. P. *Bull. Chem. Soc. Jpn.* **2012,** *85,* 1–32. doi:10.1246/bcsj.20110162
98. Govindaraju, T.; Avinash, M. B. *Nanoscale* **2012,** *4,* 6102–6117. doi:10.1039/c2nr31167d
99. Ramanathan, M.; Shrestha, L. K.; Mori, T.; Ji, Q.; Hill, J. P.; Ariga, K. *Phys. Chem. Chem. Phys.* **2013,** *15,* 10580–10611. doi:10.1039/c3cp50620g
100. Zerkoune, L.; Angelova, A.; Lesieur, S. *Nanomaterials* **2014,** *4,* 741–765. doi:10.3390/nano4030741
101. Ariga, K.; Ji, Q.; Nakanishi, W.; Hill, J. P. *J. Inorg. Organomet. Polym. Mater.* **2015,** *25,* 466–479. doi:10.1007/s10904-015-0179-4
102. Shrestha, L. K.; Strzelczyk, K. M.; Shrestha, R. G.; Ichikawa, K.; Aramaki, K.; Hill, J. P.; Ariga, K. *Nanotechnology* **2015,** *26,* 204002. doi:10.1088/0957-4484/26/20/204002
103. Hecht, S. *Angew. Chem., Int. Ed.* **2003,** *42,* 24–26. doi:10.1002/anie.200390045
104. Ariga, K.; Lee, M. V.; Mori, T.; Yu, X.-Y.; Hill, J. P. *Adv. Colloid Interface Sci.* **2010,** *154,* 20–29. doi:10.1016/j.cis.2010.01.005
105. Ramanathan, M.; Hong, K.; Ji, Q.; Yonamine, Y.; Hill, J. P.; Ariga, K. *J. Nanosci. Nanotechnol.* **2014,** *14,* 390–401. doi:10.1166/jnn.2014.8766
106. Wakayama, Y. *Jpn. J. Appl. Phys.* **2016,** *55,* 1102AA. doi:10.7567/jjap.55.1102aa
107. Ariga, K.; Malgras, V.; Ji, Q.; Zakaria, M. B.; Yamauchi, Y. *Coord. Chem. Rev.* **2016,** *320-321,* 139–152. doi:10.1016/j.ccr.2016.01.015
108. Sangian, D.; Ide, Y.; Bando, Y.; Rowan, A. E.; Yamauchi, Y. *Small* **2018,** *14,* 1800551. doi:10.1002/smll.201800551
109. Ishihara, S.; Labuta, J.; Van Rossom, W.; Ishikawa, D.; Minami, K.; Hill, J. P.; Ariga, K. *Phys. Chem. Chem. Phys.* **2014,** *16,* 9713–9746. doi:10.1039/c3cp55431g
110. Ariga, K.; Yamauchi, Y.; Ji, Q.; Yonamine, Y.; Hill, J. P. *APL Mater.* **2014,** *2,* 030701. doi:10.1063/1.4868177
111. Ariga, K.; Minami, K.; Shrestha, L. K. *Analyst* **2016,** *141,* 2629–2638. doi:10.1039/c6an00057f
112. Jackman, J. A.; Cho, N.-J.; Nishikawa, M.; Yoshikawa, G.; Mori, T.; Shrestha, L. K.; Ariga, K. *Chem. – Asian J.* **2018,** *13,* 3366–3377. doi:10.1002/asia.201800935
113. Rajendran, R.; Shrestha, L. K.; Minami, K.; Subramanian, M.; Jayavel, R.; Ariga, K. *J. Mater. Chem. A* **2014,** *2,* 18480–18487. doi:10.1039/c4ta03996c
114. Rajendran, R.; Shrestha, L. K.; Kumar, R. M.; Jayavel, R.; Hill, J. P.; Ariga, K. *J. Inorg. Organomet. Polym. Mater.* **2015,** *25,* 267–274. doi:10.1007/s10904-014-0102-4
115. Chen, R.; Zhao, T.; Zhang, X.; Li, L.; Wu, F. *Nanoscale Horiz.* **2016,** *1,* 423–444. doi:10.1039/c6nh00016a
116. Kim, J.; Kim, J. H.; Ariga, K. *Joule* **2017,** *1,* 739–768. doi:10.1016/j.joule.2017.08.018
117. Shrestha, L. K.; Shrestha, R. G.; Joshi, S.; Rajbhandari, R.; Shrestha, N.; Adhikari, M. P.; Pradhananga, R. R.; Ariga, K. *J. Inorg. Organomet. Polym. Mater.* **2017,** *27* (Suppl. 1), 48–56. doi:10.1007/s10904-017-0548-2
118. Ariga, K.; Ishihara, S.; Abe, H.; Li, M.; Hill, J. P. *J. Mater. Chem.* **2012,** *22,* 2369–2377. doi:10.1039/c1jm14101e
119. Puscasu, C. M.; Carja, G.; Zaharia, C. *Int. J. Mater. Prod. Technol.* **2015,** *51,* 228–240. doi:10.1504/ijmpt.2015.072239
120. Ariga, K.; Ishihara, S.; Abe, H. *CrystEngComm* **2016,** *18,* 6770–6778. doi:10.1039/c6ce00986g
121. Wang, H.; Yin, S.; Eid, K.; Li, Y.; Xu, Y.; Li, X.; Xue, H.; Wang, L. *ACS Sustainable Chem. Eng.* **2018,** *6,* 11768–11774. doi:10.1021/acssuschemeng.8b02015
122. Ariga, K.; Ji, Q.; Mori, T.; Naito, M.; Yamauchi, Y.; Abe, H.; Hill, J. P. *Chem. Soc. Rev.* **2013,** *42,* 6322–6345. doi:10.1039/c2cs35475f
123. Nakanishi, W.; Minami, K.; Shrestha, L. K.; Ji, Q.; Hill, J. P.; Ariga, K. *Nano Today* **2014,** *9,* 378–394. doi:10.1016/j.nantod.2014.05.002
124. Ariga, K.; Kawakami, K.; Ebara, M.; Kotsuchibashi, Y.; Ji, Q.; Hill, J. P. *New J. Chem.* **2014,** *38,* 5149–5163. doi:10.1039/c4nj00864b
125. Pandey, A. P.; Girase, N. M.; Patil, M. D.; Patil, P. O.; Patil, D. A.; Deshmukh, P. K. *J. Nanosci. Nanotechnol.* **2014,** *14,* 828–840. doi:10.1166/jnn.2014.9014
126. Ariga, K.; Naito, M.; Ji, Q.; Payra, D. *CrystEngComm* **2016,** *18,* 4890–4899. doi:10.1039/c6ce00432f
127. Nayak, A.; Unayama, S.; Tai, S.; Tsuruoka, T.; Waser, R.; Aono, M.; Valov, I.; Hasegawa, T. *Adv. Mater. (Weinheim, Ger.)* **2018,** *30,* 1703261. doi:10.1002/adma.201703261
128. Yan, Y.; Ye, J.; Wang, K.; Yao, J.; Zhao, Y. S. *Small* **2018,** *14,* 1702698. doi:10.1002/smll.201702698
129. Stulz, E. *Acc. Chem. Res.* **2017,** *50,* 823–831. doi:10.1021/acs.accounts.6b00583
130. Pandeeswar, M.; Senanayak, S. P.; Govindaraju, T. *ACS Appl. Mater. Interfaces* **2016,** *8,* 30362–30371. doi:10.1021/acsami.6b10527
131. Zhang, L.; Wang, T.; Shen, Z.; Liu, M. *Adv. Mater. (Weinheim, Ger.)* **2016,** *28,* 1044–1059. doi:10.1002/adma.201502590
132. Zhao, L.; Zou, Q.; Yan, X. *Bull. Chem. Soc. Jpn.* **2019,** *92,* 70–79. doi:10.1246/bcsj.20180248
133. Abe, H.; Liu, J.; Ariga, K. *Mater. Today* **2016,** *19,* 12–18. doi:10.1016/j.mattod.2015.08.021
134. Osada, M.; Sasaki, T. *Dalton Trans.* **2018,** *47,* 2841–2851. doi:10.1039/c7dt03719h
135. Xu, J.; Zhang, J.; Zhang, W.; Lee, C.-S. *Adv. Energy Mater.* **2017,** *7,* 1700571. doi:10.1002/aenm.201700571
136. Mathesh, M.; Liu, J.; Barrow, C. J.; Yang, W. *Chem. – Eur. J.* **2017,** *23,* 304–311. doi:10.1002/chem.201604348
137. Ariga, K.; Yamauchi, Y.; Mori, T.; Hill, J. P. *Adv. Mater. (Weinheim, Ger.)* **2013,** *25,* 6477–6512. doi:10.1002/adma.201302283
138. Ariga, K.; Mori, T.; Nakanishi, W. *Chem. – Asian J.* **2018,** *13,* 1266–1278. doi:10.1002/asia.201800225
139. Ariga, K.; Ishihara, S.; Izawa, H.; Xia, H.; Hill, J. P. *Phys. Chem. Chem. Phys.* **2011,** *13,* 4802–4811. doi:10.1039/c0cp02040k
140. Ariga, K.; Hill, J. P. *Chem. Rec.* **2011,** *11,* 199–211. doi:10.1002/tcr.201100004
141. Ariga, K.; Mori, T.; Hill, J. P. *Soft Matter* **2012,** *8,* 15–20. doi:10.1039/c1sm06832f
142. Ariga, K.; Kunitake, T. *Acc. Chem. Res.* **1998,** *31,* 371–378. doi:10.1021/ar970014i

143. Ariga, K.; Ito, H.; Hill, J. P.; Tsukube, H. *Chem. Soc. Rev.* **2012,** *41,* 5800–5835. doi:10.1039/c2cs35162e
144. Ariga, K.; Mori, T.; Li, J. *Langmuir* **2019,** *35,* 3585–3599. doi:10.1021/acs.langmuir.8b01434
145. Kurihara, K.; Ohto, K.; Tanaka, Y.; Aoyama, Y.; Kunitake, T. *Thin Solid Films* **1989,** *179,* 21–26. doi:10.1016/0040-6090(89)90160-0
146. Kurihara, K.; Ohto, K.; Tanaka, Y.; Aoyama, Y.; Kunitake, T. *J. Am. Chem. Soc.* **1991,** *113,* 444–450. doi:10.1021/ja00002a010
147. Cha, X.; Ariga, K.; Onda, M.; Kunitake, T. *J. Am. Chem. Soc.* **1995,** *117,* 11833–11838. doi:10.1021/ja00153a003
148. Cha, X.; Ariga, K.; Kunitake, T. *J. Am. Chem. Soc.* **1996,** *118,* 9545–9551. doi:10.1021/ja961526f
149. Ariga, K.; Kamino, A.; Cha, X.; Kunitake, T. *Langmuir* **1999,** *15,* 3875–3885. doi:10.1021/la981047p
150. Ikeura, Y.; Kurihara, K.; Kunitake, T. *J. Am. Chem. Soc.* **1991,** *113,* 7342–7350. doi:10.1021/ja00019a035
151. Kurihara, K.; Ohto, K.; Honda, Y.; Kunitake, T. *J. Am. Chem. Soc.* **1991,** *113,* 5077–5079. doi:10.1021/ja00013a063
152. Kawahara, T.; Kurihara, K.; Kunitake, T. *Chem. Lett.* **1992,** *21,* 1839–1842. doi:10.1246/cl.1992.1839
153. Taguchi, K.; Ariga, K.; Kunitake, T. *Chem. Lett.* **1995,** *24,* 701–702. doi:10.1246/cl.1995.701
154. Ariga, K.; Kamino, A.; Koyano, H.; Kunitake, T. *J. Mater. Chem.* **1997,** *7,* 1155–1161. doi:10.1039/a700081b
155. Onda, M.; Yoshihara, K.; Koyano, H.; Ariga, K.; Kunitake, T. *J. Am. Chem. Soc.* **1996,** *118,* 8524–8530. doi:10.1021/ja960991+
156. Springs, B.; Haake, P. *Bioorg. Chem.* **1977,** *6,* 181–190. doi:10.1016/0045-2068(77)90019-0
157. Sasaki, D. Y.; Kurihara, K.; Kunitake, T. *J. Am. Chem. Soc.* **1991,** *113,* 9685–9686. doi:10.1021/ja00025a051
158. Sasaki, D. Y.; Kurihara, K.; Kunitake, T. *J. Am. Chem. Soc.* **1992,** *114,* 10994–10995. doi:10.1021/ja00053a065
159. Sakurai, M.; Tamagawa, H.; Furuki, T.; Inoue, Y.; Ariga, K.; Kunitake, T. *Chem. Lett.* **1995,** *24,* 1001–1002. doi:10.1246/cl.1995.1001
160. Sakurai, M.; Tamagawa, H.; Inoue, Y.; Ariga, K.; Kunitake, T. *J. Phys. Chem. B* **1997,** *101,* 4810–4816. doi:10.1021/jp9700591
161. Tamagawa, H.; Sakurai, M.; Inoue, Y.; Ariga, K.; Kunitake, T. *J. Phys. Chem. B* **1997,** *101,* 4817–4825. doi:10.1021/jp9700600
162. Ariga, K. *ChemNanoMat* **2016,** *2,* 333–343. doi:10.1002/cnma.201600053
163. Ariga, K.; Mori, T.; Hill, J. P. *Adv. Mater. (Weinheim, Ger.)* **2012,** *24,* 158–176. doi:10.1002/adma.201102617
164. Ariga, K.; Mori, T.; Hill, J. P. *Langmuir* **2013,** *29,* 8459–8471. doi:10.1021/la4006423
165. Ariga, K.; Mori, T.; Ishihara, S.; Kawakami, K.; Hill, J. P. *Chem. Mater.* **2014,** *26,* 519–532. doi:10.1021/cm401999f
166. Ariga, K. *Anal. Sci.* **2016,** *32,* 1141–1149. doi:10.2116/analsci.32.1141
167. Ariga, K.; Terasaka, Y.; Sakai, D.; Tsuji, H.; Kikuchi, J.-i. *J. Am. Chem. Soc.* **2000,** *122,* 7835–7836. doi:10.1021/ja000924m
168. Ariga, K.; Nakanishi, T.; Terasaka, Y.; Tsuji, H.; Sakai, D.; Kikuchi, J.-i. *Langmuir* **2005,** *21,* 976–981. doi:10.1021/la0477845
169. Mori, T.; Komatsu, H.; Sakamoto, N.; Suzuki, K.; Hill, J. P.; Matsumoto, M.; Sakai, H.; Ariga, K.; Nakanishi, W. *Phys. Chem. Chem. Phys.* **2018,** *20,* 3073–3078. doi:10.1039/c7cp04256f
170. Mori, T.; Chin, H.; Kawashima, K.; Ngo, H.; Cho, N.-J.; Nakanishi, W.; Hill, J. P.; Ariga, K. *ACS Nano* **2019,** *13,* 2410–2419. doi:10.1021/acsnano.8b09320
171. Ishikawa, D.; Mori, T.; Yonamine, Y.; Nakanishi, W.; Cheung, D. L.; Hill, J. P.; Ariga, K. *Angew. Chem., Int. Ed.* **2015,** *54,* 8988–8991. doi:10.1002/anie.201503363
172. Mori, T.; Ishikawa, D.; Yonamine, Y.; Fujii, Y.; Hill, J. P.; Ichinose, I.; Ariga, K.; Nakanishi, W. *ChemPhysChem* **2017,** *18,* 1470–1474. doi:10.1002/cphc.201601144
173. Sakakibara, K.; Joyce, L. A.; Mori, T.; Fujisawa, T.; Shabbir, S. H.; Hill, J. P.; Anslyn, E. V.; Ariga, K. *Angew. Chem., Int. Ed.* **2012,** *51,* 9643–9646. doi:10.1002/anie.201203402
174. Michinobu, T.; Shinoda, S.; Nakanishi, T.; Hill, J. P.; Fujii, K.; Player, T. N.; Tsukube, H.; Ariga, K. *J. Am. Chem. Soc.* **2006,** *128,* 14478–14479. doi:10.1021/ja066429t
175. Michinobu, T.; Shinoda, S.; Nakanishi, T.; Hill, J. P.; Fujii, K.; Player, T. N.; Tsukube, H.; Ariga, K. *Phys. Chem. Chem. Phys.* **2011,** *13,* 4895–4900. doi:10.1039/c0cp01990a
176. Mori, T.; Okamoto, K.; Endo, H.; Hill, J. P.; Shinoda, S.; Matsukura, M.; Tsukube, H.; Suzuki, Y.; Kanekiyo, Y.; Ariga, K. *J. Am. Chem. Soc.* **2010,** *132,* 12868–12870. doi:10.1021/ja106653a
177. Mori, T.; Okamoto, K.; Endo, H.; Sakakibara, K.; Hill, J. P.; Shinoda, S.; Matsukura, M.; Tsukube, H.; Suzuki, Y.; Kanekiyo, Y.; Ariga, K. *Nanoscale Res. Lett.* **2011,** *6,* 304. doi:10.1186/1556-276x-6-304
178. Ariga, K.; Minami, K.; Ebara, M.; Nakanishi, J. *Polym. J.* **2016,** *48,* 371–389. doi:10.1038/pj.2016.8
179. Ariga, K.; Mori, T.; Nakanishi, W.; Hill, J. P. *Phys. Chem. Chem. Phys.* **2017,** *19,* 23658–23676. doi:10.1039/c7cp02280h
180. Shrestha, L. K.; Mori, T.; Ariga, K. *Curr. Opin. Colloid Interface Sci.* **2018,** *35,* 68–80. doi:10.1016/j.cocis.2018.01.007
181. Lehn, J.-M. *Angew. Chem., Int. Ed. Engl.* **1988,** *27,* 89–112. doi:10.1002/anie.198800891
182. Cram, D. J. *Angew. Chem., Int. Ed. Engl.* **1988,** *27,* 1009–1020. doi:10.1002/anie.198810093
183. Pedersen, C. J. *Angew. Chem., Int. Ed. Engl.* **1988,** *27,* 1021–1027. doi:10.1002/anie.198810211
184. Shinkai, S.; Ogawa, T.; Nakaji, T.; Kusano, Y.; Nanabe, O. *Tetrahedron Lett.* **1979,** *20,* 4569–4572. doi:10.1016/s0040-4039(01)86651-x
185. Ueda, A. *Bull. Chem. Soc. Jpn.* **2017,** *90,* 1181–1188. doi:10.1246/bcsj.20170239
186. Gropp, C.; Quigley, B. L.; Diederich, F. *J. Am. Chem. Soc.* **2018,** *140,* 2705–2717. doi:10.1021/jacs.7b12894
187. Irie, M.; Morimoto, M. *Bull. Chem. Soc. Jpn.* **2018,** *91,* 237–250. doi:10.1246/bcsj.20170365
188. Park, J. S.; Sessler, J. L. *Acc. Chem. Res.* **2018,** *51,* 2400–2410. doi:10.1021/acs.accounts.8b00308
189. Stoddart, J. F. *Angew. Chem., Int. Ed.* **2017,** *56,* 11094–11125. doi:10.1002/anie.201703216
190. Feringa, B. L. *Angew. Chem., Int. Ed.* **2017,** *56,* 11060–11078. doi:10.1002/anie.201702979
191. Sauvage, J.-P. *Angew. Chem., Int. Ed.* **2017,** *56,* 11080–11093. doi:10.1002/anie.201702992
192. Ariga, K. *J. Nanosci. Nanotechnol.* **2004,** *4,* 23–34. doi:10.1166/jnn.2004.048
193. Ariga, K. *J. Photopolym. Sci. Technol.* **2008,** *21,* 553–558. doi:10.2494/photopolymer.21.553
194. Oishi, Y.; Torii, Y.; Kuramori, M.; Suehiro, K.; Ariga, K.; Taguchi, K.; Kamino, A.; Kunitake, T. *Chem. Lett.* **1996,** *25,* 411–412. doi:10.1246/cl.1996.411

195. Oishi, Y.; Torii, Y.; Kato, T.; Kuramori, M.; Suehiro, K.; Ariga, K.; Taguchi, K.; Kamino, A.; Koyano, H.; Kunitake, T. *Langmuir* **1997,** *13,* 519–524. doi:10.1021/la960112x
196. Oishi, Y.; Kato, T.; Kuramori, M.; Suehiro, K.; Ariga, K.; Kamino, A.; Koyano, H.; Kunitake, T. *Chem. Commun.* **1997,** 1357–1358. doi:10.1039/a702880f
197. Koyano, H.; Yoshihara, K.; Ariga, K.; Kunitake, T.; Oishi, Y.; Kawano, O.; Kuramori, M.; Suehiro, K. *Chem. Commun.* **1996,** 1769–1770. doi:10.1039/cc9960001769
198. Oishi, Y.; Kato, T.; Narita, T.; Ariga, K.; Kunitake, T. *Langmuir* **2008,** *24,* 1682–1685. doi:10.1021/la7036372
199. Liu, X.; Riess, J. G.; Krafft, M. P. *Bull. Chem. Soc. Jpn.* **2018,** *91,* 846–857. doi:10.1246/bcsj.20170431
200. Richard-Lacroix, M.; Borozenko, K.; Pellerin, C.; Bazuin, C. G. *Macromolecules* **2016,** *49,* 9089–9099. doi:10.1021/acs.macromol.6b01980
201. Wu, T.; Wen, G.; Huang, C. *J. Polym. Sci., Part B: Polym. Phys.* **2016,** *54,* 825–830. doi:10.1002/polb.23979
202. Mori, T.; Sakakibara, K.; Endo, H.; Akada, M.; Okamoto, K.; Shundo, A.; Lee, M. V.; Ji, Q.; Fujisawa, T.; Oka, K.; Matsumoto, M.; Sakai, H.; Abe, M.; Hill, J. P.; Ariga, K. *Langmuir* **2013,** *29,* 7239–7248. doi:10.1021/la304293z
203. Das, T.; Häring, M.; Haldar, D.; Díaz Díaz, D. *Biomater. Sci.* **2018,** *6,* 38–59. doi:10.1039/c7bm00882a
204. Hanabusa, K.; Nakashima, M.; Funatsu, E.; Kishi, S.; Suzuki, M. *Bull. Chem. Soc. Jpn.* **2018,** *91,* 1176–1185. doi:10.1246/bcsj.20180072
205. Ganta, S.; Chand, D. K. *Chem. – Asian J.* **2018,** *13,* 3777–3789. doi:10.1002/asia.201801161
206. Sasaki, J.; Suzuki, M.; Hanabusa, K. *Bull. Chem. Soc. Jpn.* **2018,** *91,* 538–547. doi:10.1246/bcsj.20170409
207. Cherumukkil, S.; Vedhanarayanan, B.; Das, G.; Praveen, V. K.; Ajayaghosh, A. *Bull. Chem. Soc. Jpn.* **2018,** *91,* 100–120. doi:10.1246/bcsj.20170334
208. Sakakibara, K.; Chithra, P.; Das, B.; Mori, T.; Akada, M.; Labuta, J.; Tsuruoka, T.; Maji, S.; Furumi, S.; Shrestha, L. K.; Hill, J. P.; Acharya, S.; Ariga, K.; Ajayaghosh, A. *J. Am. Chem. Soc.* **2014,** *136,* 8548–8551. doi:10.1021/ja504014k
209. Vinu, A.; Srinivasu, P.; Sawant, D. P.; Mori, T.; Ariga, K.; Chang, J.-S.; Jhung, S.-H.; Balasubramanian, V. V.; Hwang, Y. K. *Chem. Mater.* **2007,** *19,* 4367–4372. doi:10.1021/cm070657k
210. Ariga, K.; Ji, Q.; McShane, M. J.; Lvov, Y. M.; Vinu, A.; Hill, J. P. *Chem. Mater.* **2012,** *24,* 728–737. doi:10.1021/cm202281m
211. Chaikittisilp, W.; Ariga, K.; Yamauchi, Y. *J. Mater. Chem. A* **2013,** *1,* 14–19. doi:10.1039/c2ta00278g
212. Zhang, J.; Yang, X.; Deng, H.; Qiao, K.; Farooq, U.; Ishaq, M.; Yi, F.; Liu, H.; Tang, J.; Song, H. *Nano-Micro Lett.* **2017,** *9,* 36. doi:10.1007/s40820-017-0137-5
213. Jeevanandam, J.; Barhoum, A.; Chan, Y. S.; Dufresne, A.; Danquah, M. K. *Beilstein J. Nanotechnol.* **2018,** *9,* 1050–1074. doi:10.3762/bjnano.9.98
214. Smith, M. D.; Karunadasa, H. I. *Acc. Chem. Res.* **2018,** *51,* 619–627. doi:10.1021/acs.accounts.7b00433
215. Ogawa, S.; Wakayama, T.; Watanabe, H.; Hayashi, K.; Ogata, S.; Oaki, Y.; Hasegawa, M.; Imai, H. *Bull. Chem. Soc. Jpn.* **2018,** *91,* 87–91. doi:10.1246/bcsj.20170291
216. Cheng, W.; Ju, Y.; Payamyar, P.; Primc, D.; Rao, J.; Willa, C.; Koziej, D.; Niederberger, M. *Angew. Chem., Int. Ed.* **2015,** *54,* 340–344. doi:10.1002/anie.201408617
217. Tiu, B. D. B.; Pernites, R. B.; Foster, E. L.; Advincula, R. C. *J. Colloid Interface Sci.* **2015,** *459,* 86–96. doi:10.1016/j.jcis.2015.08.004
218. Nie, H.-L.; Dou, X.; Tang, Z.; Jang, H. D.; Huang, J. *J. Am. Chem. Soc.* **2015,** *137,* 10683–10688. doi:10.1021/jacs.5b06052
219. Yonamine, Y.; Cervantes-Salguero, K.; Minami, K.; Kawamata, I.; Nakanishi, W.; Hill, J. P.; Murata, S.; Ariga, K. *Phys. Chem. Chem. Phys.* **2016,** *18,* 12576–12581. doi:10.1039/c6cp01586g
220. Wang, L.; Sahabudeen, H.; Zhang, T.; Dong, R. *npj 2D Mater. Appl.* **2018,** *2,* 26. doi:10.1038/s41699-018-0071-5
221. Culp, J. T.; Park, J.-H.; Stratakis, D.; Meisel, M. W.; Talham, D. R. *J. Am. Chem. Soc.* **2002,** *124,* 10083–10090. doi:10.1021/ja026312e
222. Makiura, R.; Motoyama, S.; Umemura, Y.; Yamanaka, H.; Sakata, O.; Kitagawa, H. *Nat. Mater.* **2010,** *9,* 565–571. doi:10.1038/nmat2769
223. Wu, G.; Huang, J.; Zang, Y.; He, J.; Xu, G. *J. Am. Chem. Soc.* **2017,** *139,* 1360–1363. doi:10.1021/jacs.6b08511
224. Feldblyum, J. I.; McCreery, C. H.; Andrews, S. C.; Kurosawa, T.; Santos, E. J. G.; Duong, V.; Fang, L.; Ayzner, A. L.; Bao, Z. *Chem. Commun.* **2015,** *51,* 13894–13897. doi:10.1039/c5cc04679c
225. Dai, W.; Shao, F.; Szczerbiński, J.; McCaffrey, R.; Zenobi, R.; Jin, Y.; Schlüter, A. D.; Zhang, W. *Angew. Chem., Int. Ed.* **2016,** *55,* 213–217. doi:10.1002/anie.201508473
226. Kambe, T.; Sakamoto, R.; Hoshiko, K.; Takada, K.; Miyachi, M.; Ryu, J.-H.; Sasaki, S.; Kim, J.; Nakazato, K.; Takata, M.; Nishihara, H. *J. Am. Chem. Soc.* **2013,** *135,* 2462–2465. doi:10.1021/ja312380b
227. Takada, K.; Sakamoto, R.; Yi, S.-T.; Katagiri, S.; Kambe, T.; Nishihara, H. *J. Am. Chem. Soc.* **2015,** *137,* 4681–4689. doi:10.1021/ja510788b
228. Sahabudeen, H.; Qi, H.; Glatz, B. A.; Tranca, D.; Dong, R.; Hou, Y.; Zhang, T.; Kuttner, C.; Lehnert, T.; Seifert, G.; Kaiser, U.; Fery, A.; Zheng, Z.; Feng, X. *Nat. Commun.* **2016,** *7,* 13461. doi:10.1038/ncomms13461
229. Dey, K.; Pal, M.; Rout, K. C.; Kunjattu H, S.; Das, A.; Mukherjee, R.; Kharul, U. K.; Banerjee, R. *J. Am. Chem. Soc.* **2017,** *139,* 13083–13091. doi:10.1021/jacs.7b06640
230. Matsumoto, M.; Valentino, L.; Stiehl, G. M.; Balch, H. B.; Corcos, A. R.; Wang, F.; Ralph, D. C.; Mariñas, B. J.; Dichtel, W. R. *Chem* **2018,** *4,* 308–317. doi:10.1016/j.chempr.2017.12.011
231. Matsumoto, M.; Dasari, R. R.; Ji, W.; Feriante, C. H.; Parker, T. C.; Marder, S. R.; Dichtel, W. R. *J. Am. Chem. Soc.* **2017,** *139,* 4999–5002. doi:10.1021/jacs.7b01240
232. Valentino, L.; Matsumoto, M.; Dichtel, W. R.; Mariñas, B. J. *Environ. Sci. Technol.* **2017,** *51,* 14352–14359. doi:10.1021/acs.est.7b04056
233. Sarikhani, Z.; Manoochehri, M. *Bull. Chem. Soc. Jpn.* **2017,** *90,* 746–753. doi:10.1246/bcsj.20160407
234. Mori, T.; Tanaka, H.; Dalui, A.; Mitoma, N.; Suzuki, K.; Matsumoto, M.; Aggarwal, N.; Patnaik, A.; Acharya, S.; Shrestha, L. K.; Sakamoto, H.; Itami, K.; Ariga, K. *Angew. Chem., Int. Ed.* **2018,** *57,* 9679–9683. doi:10.1002/anie.201803859
235. Nakanishi, T.; Michinobu, T.; Yoshida, K.; Shirahata, N.; Ariga, K.; Möhwald, H.; Kurth, D. G. *Adv. Mater. (Weinheim, Ger.)* **2008,** *20,* 443–446. doi:10.1002/adma.200701537
236. Shrestha, L. K.; Shrestha, R. G.; Hill, J. P.; Ariga, K. *J. Oleo Sci.* **2013,** *62,* 541–553. doi:10.5650/jos.62.541
237. Miyazawa, K.; Kuwasaki, Y.; Hamamoto, K.; Nagata, S.; Obayashi, A.; Kuwabara, M. *Surf. Interface Anal.* **2003,** *35,* 117–120. doi:10.1002/sia.1506

238. Shrestha, L. K.; Ji, Q.; Mori, T.; Miyazawa, K.; Yamauchi, Y.; Hill, J. P.; Ariga, K. *Chem. – Asian J.* **2013,** *8,* 1662–1679. doi:10.1002/asia.201300247
239. Miyazawa, K. *Sci. Technol. Adv. Mater.* **2015,** *16,* 013502. doi:10.1088/1468-6996/16/1/013502
240. Shrestha, L. K.; Hill, J. P.; Miyazawa, K.; Ariga, K. *J. Nanosci. Nanotechnol.* **2012,** *12,* 6380–6384. doi:10.1166/jnn.2012.6220
241. Shrestha, L. K.; Hill, J. P.; Tsuruoka, T.; Miyazawa, K.; Ariga, K. *Langmuir* **2013,** *29,* 7195–7202. doi:10.1021/la304549v
242. Shrestha, L. K.; Shrestha, R. G.; Yamauchi, Y.; Hill, J. P.; Nishimura, T.; Miyazawa, K.; Kawai, T.; Okada, S.; Wakabayashi, K.; Ariga, K. *Angew. Chem., Int. Ed.* **2015,** *54,* 951–955. doi:10.1002/anie.201408856
243. Bairi, P.; Shrestha, R. G.; Hill, J. P.; Nishimura, T.; Ariga, K.; Shrestha, L. K. *J. Mater. Chem. A* **2016,** *4,* 13899–13906. doi:10.1039/c6ta04970b
244. Shrestha, R. G.; Shrestha, L. K.; Khan, A. H.; Kumar, G. S.; Acharya, S.; Ariga, K. *ACS Appl. Mater. Interfaces* **2014,** *6,* 15597–15603. doi:10.1021/am5046235
245. Tang, Q.; Zhang, S.; Liu, X.; Sumita, M.; Ishihara, S.; Fuchs, H.; Ji, Q.; Shrestha, L. K.; Ariga, K. *Phys. Chem. Chem. Phys.* **2017,** *19,* 29099–29105. doi:10.1039/c7cp04553k
246. Kumar, G. S.; Shrestha, R. G.; Ji, Q.; Hill, J. P.; Ariga, K.; Acharya, S.; Shrestha, L. K. *Phys. Chem. Chem. Phys.* **2018,** *20,* 18873–18878. doi:10.1039/c8cp02779j
247. Furuuchi, N.; Shrestha, R.; Yamashita, Y.; Hirao, T.; Ariga, K.; Shrestha, L. *Sensors* **2019,** *19,* 267. doi:10.3390/s19020267
248. Saran, R.; Curry, R. J. *Small* **2018,** *14,* 1703624. doi:10.1002/smll.201703624
249. Shen, W.; Zhang, L.; Zheng, S.; Xie, Y.; Lu, X. *ACS Appl. Mater. Interfaces* **2017,** *9,* 28838–28843. doi:10.1021/acsami.7b05180
250. Shrestha, L. K.; Yamauchi, Y.; Hill, J. P.; Miyazawa, K.; Ariga, K. *J. Am. Chem. Soc.* **2013,** *135,* 586–589. doi:10.1021/ja3108752
251. Tang, Q.; Bairi, P.; Shrestha, R. G.; Hill, J. P.; Ariga, K.; Zeng, H.; Ji, Q.; Shrestha, L. K. *ACS Appl. Mater. Interfaces* **2017,** *9,* 44458–44465. doi:10.1021/acsami.7b13277
252. Shrestha, L. K.; Sathish, M.; Hill, J. P.; Miyazawa, K.; Tsuruoka, T.; Sanchez-Ballester, N. M.; Honma, I.; Ji, Q.; Ariga, K. *J. Mater. Chem. C* **2013,** *1,* 1174–1181. doi:10.1039/c2tc00449f
253. Bairi, P.; Minami, K.; Nakanishi, W.; Hill, J. P.; Ariga, K.; Shrestha, L. K. *ACS Nano* **2016,** *10,* 6631–6637. doi:10.1021/acsnano.6b01544
254. Bairi, P.; Minami, K.; Hill, J. P.; Ariga, K.; Shrestha, L. K. *ACS Nano* **2017,** *11,* 7790–7796. doi:10.1021/acsnano.7b01569
255. Bairi, P.; Tsuruoka, T.; Acharya, S.; Ji, Q.; Hill, J. P.; Ariga, K.; Yamauchi, Y.; Shrestha, L. K. *Mater. Horiz.* **2018,** *5,* 285–290. doi:10.1039/c7mh00954b
256. Shrestha, L. K.; Shrestha, R. G.; Hill, J. P.; Tsuruoka, T.; Ji, Q.; Nishimura, T.; Ariga, K. *Langmuir* **2016,** *32,* 12511–12519. doi:10.1021/acs.langmuir.6b01378
257. Wang, B.; Zheng, S.; Saha, A.; Bao, L.; Lu, X.; Guldi, D. M. *J. Am. Chem. Soc.* **2017,** *139,* 10578–10584. doi:10.1021/jacs.7b06162
258. Zhou, S.; Wang, L.; Chen, M.; Liu, B.; Sun, X.; Cai, M.; Li, H. *Nanoscale* **2017,** *9,* 16375–16385. doi:10.1039/c7nr06112a
259. Bairi, P.; Minami, K.; Hill, J. P.; Nakanishi, W.; Shrestha, L. K.; Liu, C.; Harano, K.; Nakamura, E.; Ariga, K. *ACS Nano* **2016,** *10,* 8796–8802. doi:10.1021/acsnano.6b04535
260. Komiyama, M.; Yoshimoto, K.; Sisido, M.; Ariga, K. *Bull. Chem. Soc. Jpn.* **2017,** *90,* 967–1004. doi:10.1246/bcsj.20170156
261. Ariga, K.; Leong, D. T.; Mori, T. *Adv. Funct. Mater.* **2018,** *28,* 1702905. doi:10.1002/adfm.201702905
262. Ariga, K.; Jackman, J. A.; Cho, N.-J.; Hsu, S.-h.; Shrestha, L. K.; Mori, T.; Takeya, J. *Chem. Rec.*, in press. doi:10.1002/tcr.201800103
263. Matsuura, K. *Bull. Chem. Soc. Jpn.* **2017,** *90,* 873–884. doi:10.1246/bcsj.20170133
264. Sawada, T.; Serizawa, T. *Bull. Chem. Soc. Jpn.* **2018,** *91,* 455–466. doi:10.1246/bcsj.20170428
265. He, H.; Xu, B. *Bull. Chem. Soc. Jpn.* **2018,** *91,* 900–906. doi:10.1246/bcsj.20180038
266. Fromherz, P. *Biochim. Biophys. Acta, Biomembr.* **1971,** *225,* 382–387. doi:10.1016/0005-2736(71)90235-5
267. Fromherz, P. *Rev. Sci. Instrum.* **1975,** *46,* 1380–1385. doi:10.1063/1.1134025
268. Okahata, Y.; Tsuruta, T.; Ijiro, K.; Ariga, K. *Langmuir* **1988,** *4,* 1373–1375. doi:10.1021/la00084a030
269. Okahata, Y.; Tsuruta, T.; Ijiro, K.; Ariga, K. *Thin Solid Films* **1989,** *180,* 65–72. doi:10.1016/0040-6090(89)90055-2
270. Ariga, K.; Hill, J. P.; Ji, Q. *Phys. Chem. Chem. Phys.* **2007,** *9,* 2319–2340. doi:10.1039/b700410a
271. Ariga, K.; Lvov, Y. M.; Kawakami, K.; Ji, Q.; Hill, J. P. *Adv. Drug Delivery Rev.* **2011,** *63,* 762–771. doi:10.1016/j.addr.2011.03.016
272. Ariga, K.; Yamauchi, Y.; Rydzek, G.; Ji, Q.; Yonamine, Y.; Wu, K. C.-W.; Hill, J. P. *Chem. Lett.* **2014,** *43,* 36–68. doi:10.1246/cl.130987
273. Rydzek, G.; Ji, Q.; Li, M.; Schaaf, P.; Hill, J. P.; Boulmedais, F.; Ariga, K. *Nano Today* **2015,** *10,* 138–167. doi:10.1016/j.nantod.2015.02.008
274. Onda, M.; Lvov, Y.; Ariga, K.; Kunitake, T. *J. Ferment. Bioeng.* **1996,** *82,* 502–506. doi:10.1016/s0922-338x(97)86992-9
275. Onda, M.; Lvov, Y.; Ariga, K.; Kunitake, T. *Biotechnol. Bioeng.* **1996,** *51,* 163–167. doi:10.1002/(sici)1097-0290(19960720)51:2<163::aid-bit5>3.0.co;2-h
276. Onda, M.; Ariga, K.; Kunitake, T. *J. Biosci. Bioeng.* **1999,** *87,* 69–75. doi:10.1016/s1389-1723(99)80010-3
277. Minami, K.; Mori, T.; Nakanishi, W.; Shigi, N.; Nakanishi, J.; Hill, J. P.; Komiyama, M.; Ariga, K. *ACS Appl. Mater. Interfaces* **2017,** *9,* 30553–30560. doi:10.1021/acsami.7b11445
278. Giaever, I.; Keese, C. R. *Proc. Natl. Acad. Sci. U. S. A.* **1983,** *80,* 219–222. doi:10.1073/pnas.80.1.219
279. Keese, C. R.; Giaever, I. *Proc. Natl. Acad. Sci. U. S. A.* **1983,** *80,* 5622–5626. doi:10.1073/pnas.80.18.5622
280. Keese, C. R.; Giaever, I. *Exp. Cell Res.* **1991,** *195,* 528–532. doi:10.1016/0014-4827(91)90406-k
281. Shiba, Y.; Ohshima, T.; Sato, M. *Kagaku Kogaku Ronbunshu* **1998,** *24,* 343–345. doi:10.1252/kakoronbunshu.24.343
282. Shiba, Y.; Ohshima, T.; Sato, M. *Biotechnol. Bioeng.* **1998,** *57,* 583–589. doi:10.1002/(sici)1097-0290(19980305)57:5<583::aid-bit10>3.0.co;2-d
283. Sato, M.; Shinozawa, T.; Ueno, H.; Sadakata, M. *Kagaku Kogaku Ronbunshu* **1991,** *17,* 671–673. doi:10.1252/kakoronbunshu.17.671
284. Ando, J.; Albelda, S. M.; Levine, E. M. *In Vitro Cell. Dev. Biol.: Anim.* **1991,** *27,* 525–532. doi:10.1007/bf02631282

285. Pilarek, M.; Grabowska, I.; Ciemerych, M. A.; Dąbkowska, K.; Szewczyk, K. W. *Biotechnol. Lett.* **2013,** *35,* 1387–1394. doi:10.1007/s10529-013-1218-2
286. Kong, D.; Megone, W.; Nguyen, K. D. Q.; Di Cio, S.; Ramstedt, M.; Gautrot, J. E. *Nano Lett.* **2018,** *18,* 1946–1951. doi:10.1021/acs.nanolett.7b05339
287. Kong, D.; Peng, L.; Di Cio, S.; Novak, P.; Gautrot, J. E. *ACS Nano* **2018,** *12,* 9206–9213. doi:10.1021/acsnano.8b03865
288. Jia, X.; Minami, K.; Uto, K.; Chang, A. C.; Hill, J. P.; Ueki, T.; Nakanishi, J.; Ariga, K. *Small* **2019,** *15,* 1804640. doi:10.1002/smll.201804640
289. Yang, F.; Tao, F.; Li, C.; Gao, L.; Yang, P. *Nat. Commun.* **2018,** *9,* 5443. doi:10.1038/s41467-018-07888-2
290. Krishnan, V.; Kasuya, Y.; Ji, Q.; Sathish, M.; Shrestha, L. K.; Ishihara, S.; Minami, K.; Morita, H.; Yamazaki, T.; Hanagata, N.; Miyazawa, K.; Acharya, S.; Nakanishi, W.; Hill, J. P.; Ariga, K. *ACS Appl. Mater. Interfaces* **2015,** *7,* 15667–15673. doi:10.1021/acsami.5b04811
291. Minami, K.; Kasuya, Y.; Yamazaki, T.; Ji, Q.; Nakanishi, W.; Hill, J. P.; Sakai, H.; Ariga, K. *Adv. Mater. (Weinheim, Ger.)* **2015,** *27,* 4020–4026. doi:10.1002/adma.201501690
292. Hsieh, F.-Y.; Shrestha, L. K.; Ariga, K.; Hsu, S.-h. *Chem. Commun.* **2017,** *53,* 11024–11027. doi:10.1039/c7cc06395d
293. Deisseroth, K. *Nat. Methods* **2011,** *8,* 26–29. doi:10.1038/nmeth.f.324
294. Luo, P.-W.; Han, H.-W.; Yang, C.-S.; Shrestha, L. K.; Ariga, K.; Hsu, S.-h. *Adv. Biosyst.* **2019,** *3,* 1800254. doi:10.1002/adbi.201800254

License and Terms

BEILSTEIN JOURNAL OF NANOTECHNOLOGY

TiO_2/GO-coated functional separator to suppress polysulfide migration in lithium–sulfur batteries

Ning Liu[1], Lu Wang[1], Taizhe Tan[2], Yan Zhao[*1] and Yongguang Zhang[*1]

Full Research Paper

Open Access

Address:
[1]School of Materials Science and Engineering, Hebei University of Technology, Tianjin 300130, China and [2]Synergy Innovation Institute of GDUT, Heyuan 517000, China

Email:
Yan Zhao[*] - yanzhao1984@hebut.edu.cn; Yongguang Zhang[*] - yongguangzhang@hebut.edu.cn

* Corresponding author

Keywords:
dealloying; functional separator; lithium–sulfur batteries; TiO_2/GO composite

Beilstein J. Nanotechnol. **2019,** *10,* 1726–1736.
doi:10.3762/bjnano.10.168

Received: 26 February 2019
Accepted: 30 July 2019
Published: 19 August 2019

This article is part of the thematic issue "Low-dimensional materials and systems".

Guest Editor: S. Walia

Abstract

Lithium–sulfur batteries render a high energy density but suffer from poor cyclic performance due to the dissolution of intermediate polysulfides. Herein, a lightweight nanoporous TiO_2 and graphene oxide (GO) composite is prepared and utilized as an interlayer between a Li anode and a sulfur cathode to suppress the polysulfide migration and improve the electrochemical performance of Li/S batteries. The interlayer can capture the polysulfides due to the presence of oxygen functional groups and formation of chemical bonds. The hierarchically porous TiO_2 nanoparticles are tightly wrapped in GO sheets and facilitate the polysulfide storage and chemical absorption. The excellent adhesion between TiO_2 nanoparticles and GO sheets resulted in enhanced conductivity, which is highly desirable for an efficient electron transfer process. The Li/S battery with a TiO_2/GO-coated separator exhibited a high initial discharge capacity of 1102.8 mAh g^{-1} and a 100th cycle capacity of 843.4 mAh g^{-1}, which corresponds to a capacity retention of 76.48% at a current rate of 0.2 C. Moreover, the Li/S battery with the TiO_2/GO-coated separator showed superior cyclic performance and excellent rate capability, which shows the promise of the TiO_2/GO composite in next-generation Li/S batteries.

Introduction

The portability of handheld electronic products and successful realization of next-generation electric vehicles urgently require advanced energy storage devices with higher storage capacity and excellent service life. Li-ion batteries have successfully demonstrated their promise for a wide range of small-scale applications. However, the large-scale utilization of Li-ion batteries is limited by the energy density [1-5]. Recently, lithium–sulfur batteries (Li/S batteries) have been widely investigated as an alternative energy storage system due to their distinct advantages, such as high theoretical capacity (1675 mAh g^{-1}) and high energy density (2600 Wh kg^{-1}). Furthermore, the abundance and nontoxic nature of elemental sulfur favors the

large-scale utilization of Li/S batteries [6-10]. However, the development and widespread utilization of Li/S batteries is hindered by (i) the poor electronic/ionic conductivity of sulfur, causing a low reaction rate and electrochemical polarization, (ii) dissolution and the shuttle effect of intermediate polysulfides, resulting in the deposition of Li_2S and Li_2S_2 at the electrode/electrolyte interface, shortening the service life and rendering poor coulombic efficiency, and (iii) large volumetric changes during charge/discharge, destroying the conductive network of the electrode and causing capacity decay [11-15].

To overcome these issues, researchers have adopted various techniques, such as optimization of the cathode material [16-18], incorporation of electrolyte additives [19], and protection of the anode [20]. Recently, much attention has been directed to the development of a functional separator, which serves as an intermediate layer and plays an important role in enhancing the electrochemical performance of Li/S batteries. It has been demonstrated that the polysulfide shuttle can be effectively suppressed by modifying the separator or incorporating an interlayer at the cathode/separator interface [21,22]. For instance, the performance of Li/S batteries has been significantly enhanced by using carbon-modified separators due to the superior conductivity, adjustable pore structure and high specific surface area [23-26]. However, only physical adsorption occurs between carbonaceous materials and polysulfides, and nonpolar carbon-based materials offer weak interactions with polar polysulfides [27,28]. On the other hand, metal oxides can form chemical bonds with sulfur to trap sulfur species. As a result, sulfur species are confined at the cathode/separator interface and the shuttle effect is minimized. Hence, the carbon/metal-oxide hybrid interlayer combines the advantages of carbon and metal oxides and exhibits superior performance over monolithic materials. Recently, the inclusion of V_2O_5/CNT [29], MoO_3@CNT [30], TiO_2@CNF [31], TiO_2/graphene [32] interlayers has been shown to suppress the shuttle effect and the Li/S batteries with these functional interlayers deliver high gravimetric energy density and superior cyclic performance.

Two-dimensional graphene oxide (GO) has excellent thermal stability, an ultrahigh specific surface area, and good electrical conductivity. The polysulfide shuttle can be suppressed due to the presence of oxygen functional groups on the surface of GO, electrostatic repulsion and steric exclusion [33,34]. However, as far as we know, no study has been reported applying TiO_2/GO composites as a functional interlayer in Li/S batteries. Herein, a three-dimensional TiO_2/GO-coated separator was introduced between the Li anode and sulfur cathode as a highly efficient polysulfide absorber. The TiO_2/GO composite was prepared by dealloying, as reported elsewhere [35], and subsequent spray drying. It has been demonstrated that the utilization of the TiO_2/GO composite interlayer enhanced the cycling stability and charge storage capacity of Li/S batteries due to excellent conductivity of graphene oxide and strong chemical interactions between nanoporous TiO_2 and polysulfides.

Results and Discussion

Figure 1 presents a schematic of a Li/S battery with a TiO_2/GO-coated separator, which is sandwiched between a sulfur cathode and Li metal and prevents the diffusion of polysulfides. Thereby, the separator inhibits the polysulfide shuttle during the charge/discharge process. At the same time, the coating layer provides an unimpeded pathway for the transmission of Li ions, which guarantees the excellent cyclic stability and desirable rate performance of Li/S batteries.

Figure 2a shows X-ray diffraction (XRD) patterns of the as-spun and as-dealloyed sample. The TiAl foil exhibits Al_3Ti

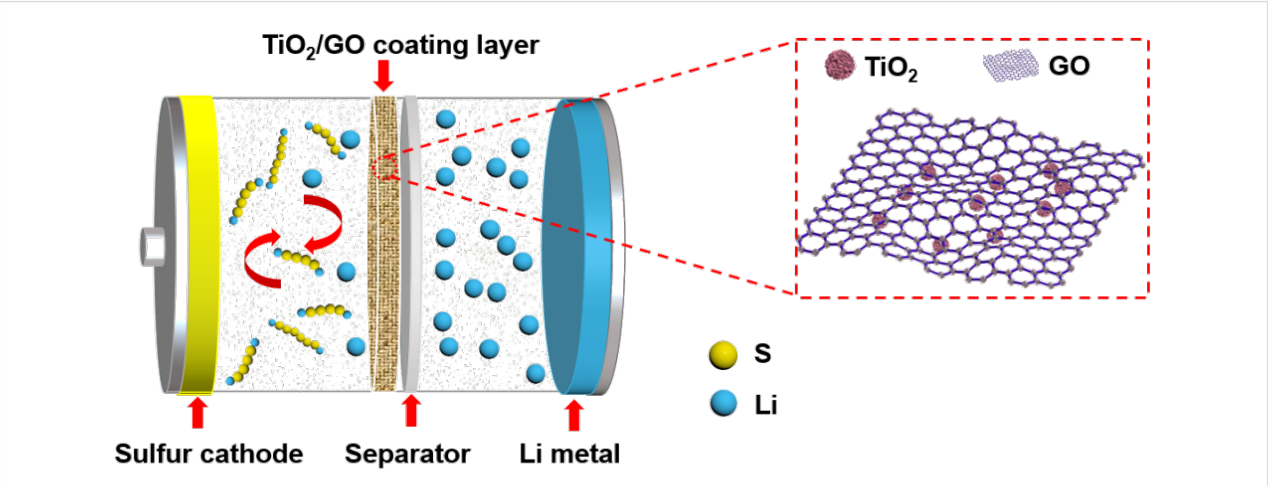

Figure 1: Schematic illustration of a Li/S battery with a TiO_2/GO-coated functional separator.

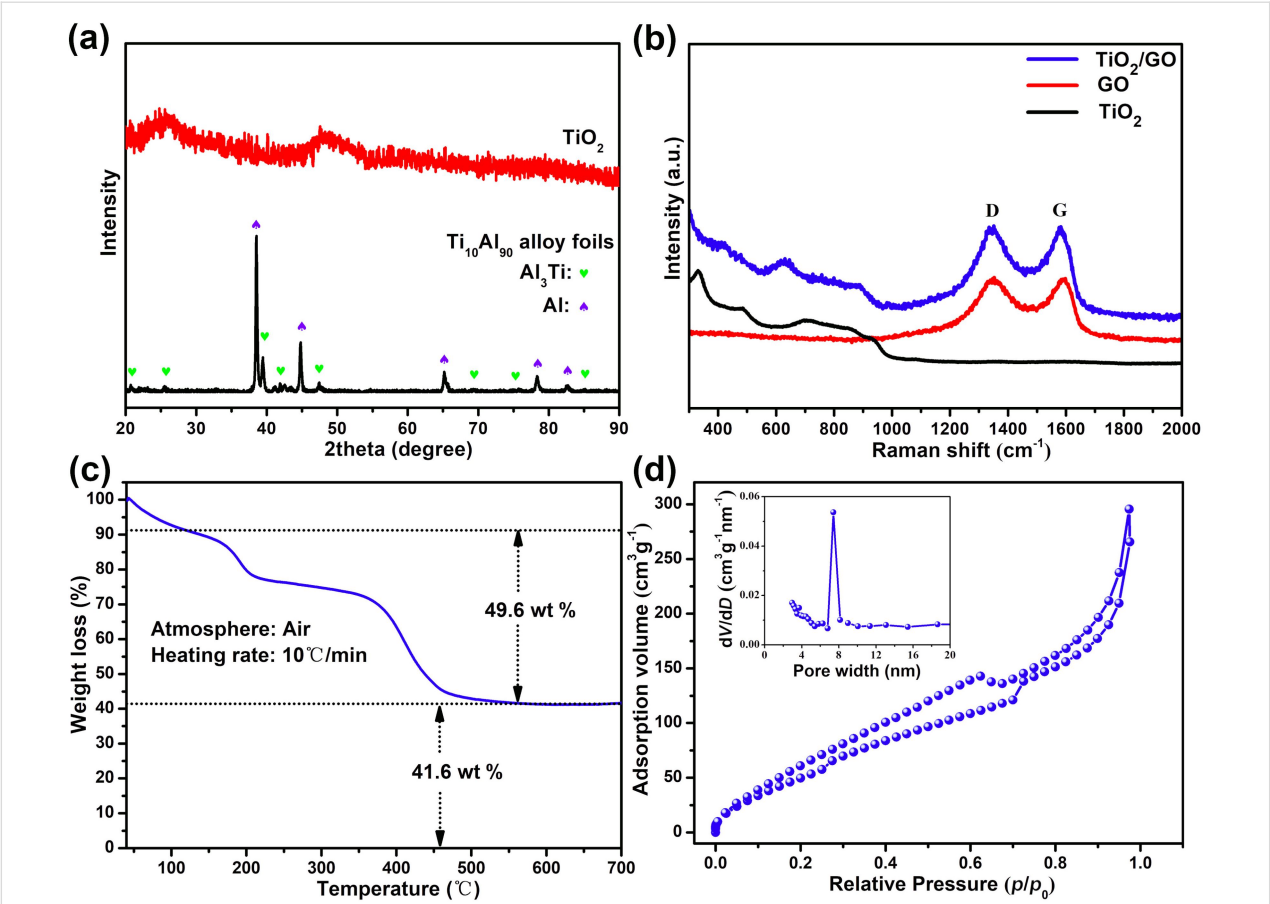

Figure 2: (a) XRD patterns of the as-spun and as-dealloyed $Ti_{10}Al_{90}$ alloy foils. (b) Raman spectra of TiO_2, GO and the TiO_2/GO composite. (c) TGA curve and (d) N_2 adsorption–desorption isotherms and pore size distribution of the TiO_2/GO composite.

(JCPDS 65-2667) and Al (JCPDS 65-2869) phases. After dealloying, the specimen shows a typical amorphous state with two weak diffraction peaks at about 25° and 48°, and the peaks of the Al_3Ti and Al phases were absent, indicating almost complete dissolution of Al and the formation of amorphous TiO_2. Figure 2b shows the Raman spectra of TiO_2, GO and the TiO_2/GO composite. The Raman spectrum of as-dealloyed TiO_2 is featureless due to its amorphous nature [36], and the GO alone shows the typical D- and G-bands at ≈1350 cm^{-1} and 1592 cm^{-1}. Meanwhile, the composite displays the spectral characteristics of GO with two distinct peaks at ≈1343 cm^{-1} and 1580 cm^{-1}. The slight shift in the position of the D- and G-band of the TiO_2/GO composite can be ascribed to the interaction between TiO_2 and GO and the formation of Ti–O–C bonds [37]. In addition, the TiO_2/GO composite shows a new, weak peak at 628 cm^{-1} that corresponds to the E_g mode of the anatase TiO_2 [38], suggesting that the TiO_2 is crystallized with a low degree of crystallinity after spray drying. Thermogravimetric analysis (TGA) of the TiO_2/GO composite is presented in Figure 2c. When the temperature was increased from room temperature to 120 °C, a weight decrease of 8.8% was noticed due to the elimination of a small amount of adsorbed water. The remainder after the heating process was regarded as the TiO_2, which accounts for 45.6 wt % of the whole. The N_2 adsorption–desorption isotherm of the TiO_2/GO composite is shown in Figure 2d. A distinct hysteresis loop can be identified, indicating the microporous structure of the TiO_2/GO composite. The BET specific surface area of the TiO_2/GO composite was determined to be 155.2 m^2 g^{-1}. Through the Barrett–Joyner–Halenda (BJH) analysis, the pore size distribution of TiO_2/GO shows that the majority of the pores are around 2.9 and 7.4 nm. The rich porosity not only provides abundant pore structure to accommodate sulfur, but also supplies numerous adsorption and catalytic sites for the polysulfides, thus significantly improving both the specific capacity and cycling performance of Li/S batteries.

Figure 3a shows a scanning electron microscopy (SEM) image of as-prepared TiO_2, which has been synthesized by selectively dissolving Al atoms from a $Ti_{10}Al_{90}$ alloy. It can be readily observed that the abundant nanowires and uniform nanopores, with a pore size of ≈40 nm, formed a sea-urchin-like structure.

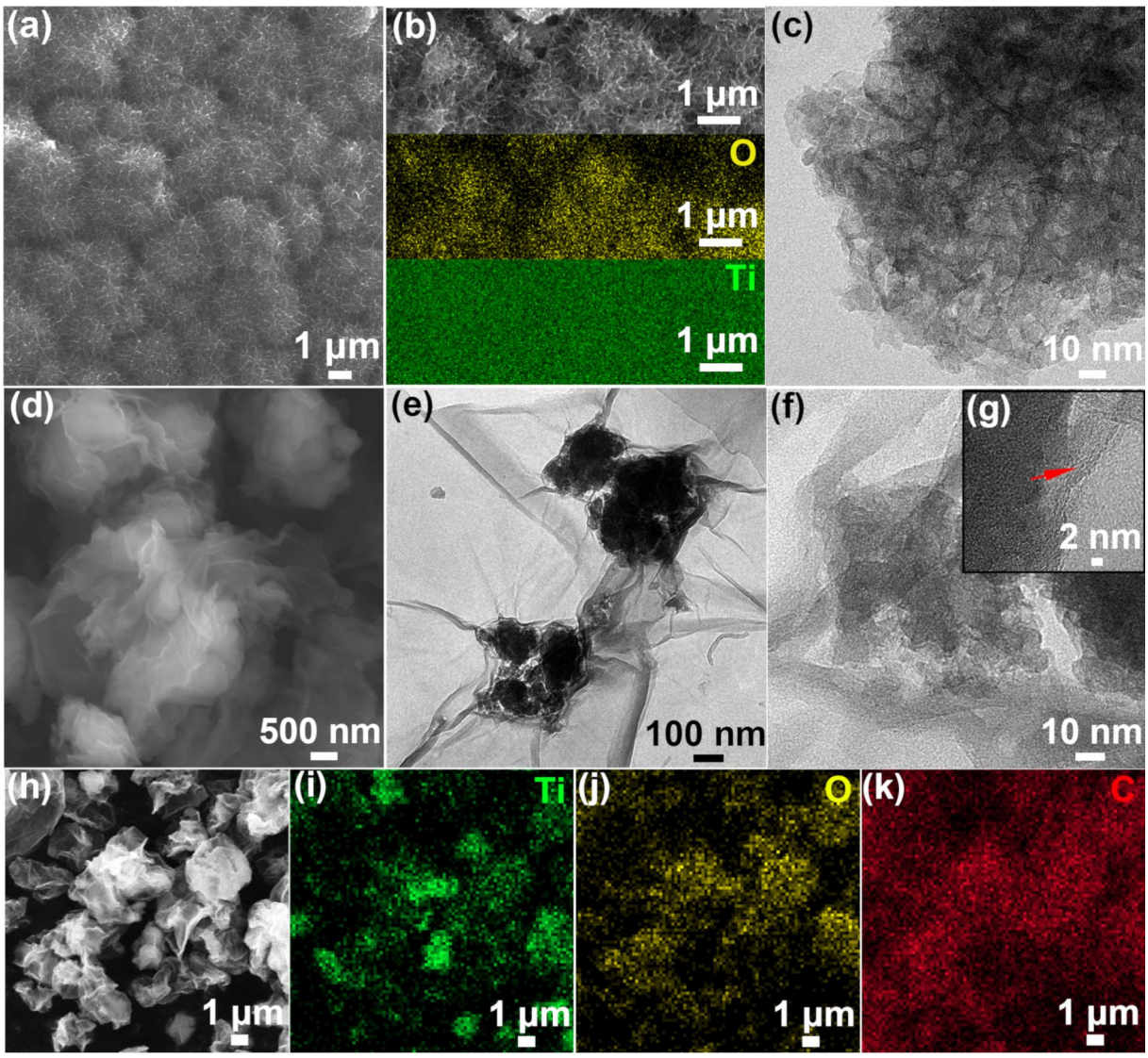

Figure 3: (a) SEM image, (b) element maps and (c) TEM image of the as-prepared nanoporous TiO_2 particles. (d) SEM image, (e) TEM image, (f, g) HRTEM images and (h–k) EDS mapping of the as-prepared TiO_2/GO composite.

Furthermore, the energy-dispersive X-ray spectroscopy (EDS) analysis confirms the homogenous distribution of Ti and O elements (Figure 3b). In addition, the transmission electron microscopy (TEM) image of TiO_2 shows the nanoporous architecture with dark nanowires and bright nanopores (Figure 3c). On the other hand, the SEM and TEM images of the as-prepared TiO_2/GO composite show that the surface of nanoporous TiO_2 has been completely wrapped by wrinkled GO nanosheets (Figure 3d and 3e). As displayed in the high-resolution TEM (HRTEM) images (Figure 3f and 3g), the TiO_2/GO composite reveals no clear lattice fringe for TiO_2, indicating poor crystallinity. It is clear that the GO sheets have a flake-like structure with wrinkles and folds, which is in line with previous works [39]. The EDS elemental mapping of titanium, oxygen and carbon provide additional evidence to further show the GO uniform distribution on the TiO_2 particle, as shown in Figure 3i–k. Moreover, based on the Raman and TEM results, the TiO_2 and GO sheets exhibit excellent adhesion, which ensures efficient electron transfer from the GO sheet to nanoporous TiO_2. The use of TiO_2/GO composites as an interlayer can greatly suppress the migration of polysulfides due to their physical and chemical interactions with dissolved polysulfides. Therefore, the as-prepared TiO_2/GO composite is expected to exhibit enhanced conductivity and render excellent rate performance [40].

Figure 4 displays the SEM images of the pristine and TiO_2/GO-coated separator. The pristine separator shows abundant pores

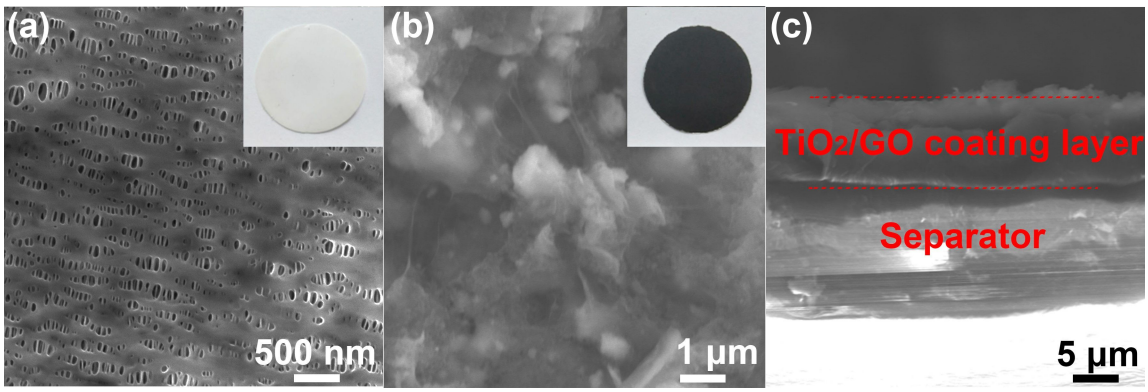

Figure 4: Surface SEM images of (a) a pristine separator, (b) a TiO_2/GO-coated separator and (c) the TiO_2/GO-coated separator as a cross-sectional view. Insets in panel (a) and (b) are the digital photographs of the pristine and the TiO_2/GO-coated separator, respectively.

with an average diameter of 100 nm (Figure 4a). Meanwhile, the TiO_2/GO-coated separator confirms that TiO_2 particles are tightly wrapped with GO sheets, indicating the strong interaction between nanoporous TiO_2 and GO (Figure 4b). The cross-sectional morphology of the TiO_2/GO-coated separator shows that the thickness of the TiO_2/GO composite layer was ≈5 μm (Figure 4c). Furthermore, the interface does not contain any cracks, suggesting the excellent adhesion of the TiO_2/GO composite layer with a pristine separator.

Figure 5 compares the cycle voltammetry (CV) curves of the Li/S batteries with pristine, GO-coated and TiO_2/GO-coated separators at a scan rate of 0.1 mV s^{-1}. All the CV curves exhibit two cathodic peaks, which can be ascribed to the transformation of elemental sulfur, S_8, into soluble high-order polysulfides and then into Li_2S and Li_2S_2 [41]. On the other hand, the anodic peaks can be assigned to the reversible transformation of Li_2S and Li_2S_2 into the high valence state Li_2S_{4-8} [42-44]. One should note that the Li/S batteries with a pristine separator and those with a GO-coated separator exhibit much broader redox peaks than that of the Li/S batteries with TiO_2/GO-coated separator due to the high polarization and poor reversibility. Moreover, compared with Figure 5a, the position and shape of redox for the 2nd and 3rd cycles remain unchanged in Figure 5c. In addition, the batteries with the TiO_2/GO-coated separator exhibit sharper and more symmetric redox peaks than the batteries with a pristine separator or a GO-coated separator. These observations indicate the stable electrochemical performance and high reversibility of the Li/S batteries with the TiO_2/GO-coated separator.

The discharge–charge cyclic performance was assessed at 0.2 C in the voltage range of 1.5 to 3 V (vs Li/Li^+). Figure 6a shows that the Li/S batteries with the TiO_2/GO-coated separator delivered a high initial discharge capacity of 1102.8 mAh g^{-1} and a 100th cycle capacity of 843.4 mAh g^{-1}, which corresponds to a capacity retention of 76.48%. On the other hand, the initial discharge capacity of Li/S batteries with a pristine and GO-coated separator were only 757.7 and 907.9 mAh g^{-1}, respectively. After 100 cycles, the capacity decreased to 467.1 and 652.7 mAh g^{-1}, respectively, which corresponds to a capacity retention of 61.65% and 71.89%. In addition, the TiO_2/GO-coated separator Li/S batteries rendered a stable coulombic efficiency during charge/discharge process. The enhanced cyclic

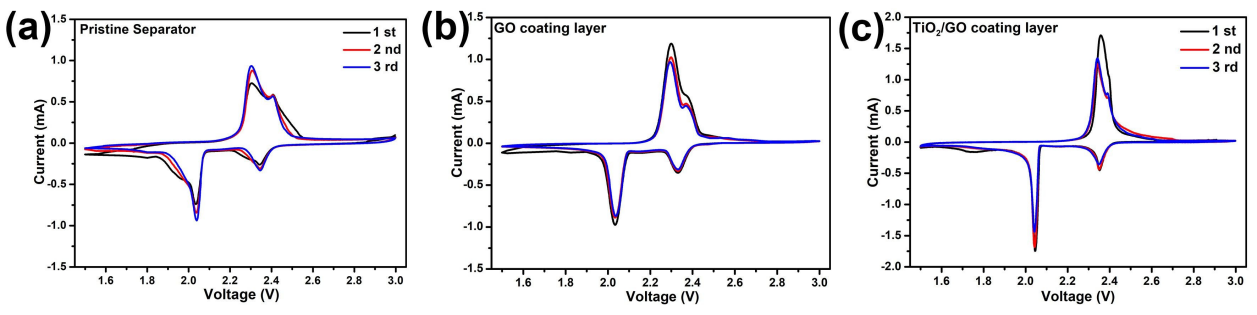

Figure 5: CV curves of the Li/S batteries with a (a) pristine separator, (b) GO-coated separator and (c) TiO_2/GO-coated separator.

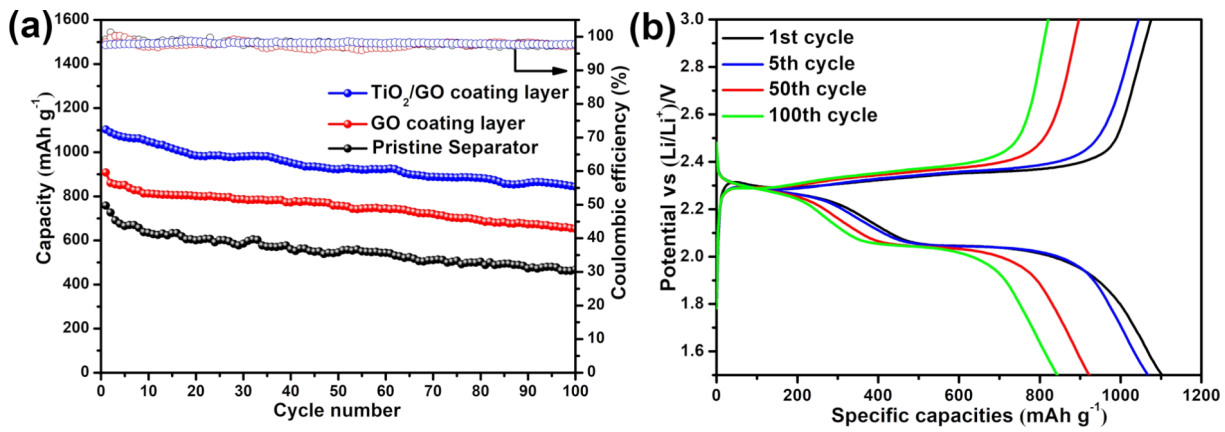

Figure 6: (a) Cyclic performance and coulombic efficiency of the Li/S batteries with pristine, GO-coated and TiO_2/GO-coated separators at a c-rate of 0.2 C and (b) corresponding discharge–charge profiles of the Li/S batteries with a TiO_2/GO-coated separator.

performance of the TiO_2/GO-coated separator batteries can be attributed to the outstanding physical and chemical absorption between the TiO_2/GO composite and the dissolved polysulfide. In addition, the TiO_2/GO composite forms a three-dimensional structure, which can improve the active material utilization and mitigate the "shuttle effect".

Figure 6b presents the galvanostatic discharge–charge curves of the TiO_2/GO-coated separator batteries for the 1st, 5th, 50th and 100th cycles at a c-rate of 0.2 C. The discharge–charge curves exhibit two pairs of reduction and oxidation peaks, corresponding to the redox reactions of typical Li/S batteries. These observations are consistent with the CV curves. In addition, the plateaus in the discharge–charge profiles are almost overlapped even after the 100th cycle, indicating a stable electrochemical performance of the Li/S batteries with a TiO_2/GO-coated separator.

Figure 7a shows the rate capability of Li/S batteries with pristine, GO-coated and TiO_2/GO-coated separators at various current rates. Over the entire discharge–charge process, the TiO_2/GO-coated separator batteries delivered a much higher capacity than the Li/S batteries with a pristine separator. When the c-rate was increased from 0.2 to 0.5, 1 and 2 C, the TiO_2/GO-coated separator batteries delivered a high reversible capacity of 889.7, 685.9, 546.4 and 419.7 mAh g^{-1}, respectively. Even at a high c-rate of 3 C, a reasonably high reversible capacity of ≈320.8 mAh g^{-1} was delivered by the TiO_2/GO-coated separator batteries. Moreover, once the current density was restored to a low rate (0.5 C), the TiO_2/GO-coated separator batteries exhibited a capacity of 655 mAh g^{-1}, which corresponds to a recovery of 95.5%. On the other hand, the Li/S batteries with the pristine and GO-coated separator exhibited a low capacity of ≈179.6 and 266.2 mAh g^{-1}, respectively, at 3 C, which are quite lower than the Li/S batteries with the TiO_2/GO-coated separator. For the Li/S batteries with a pristine and GO-coated separator, when the c-rate was restored to 0.5 C, only a capacity of 400.5 and 553.7 mAh g^{-1} could be restored, which indicates the poor rate capability of the Li/S batteries with a pristine separator and GO-coated separator. Figure 7b presents the discharge–charge profiles of the Li/S batteries with the TiO_2/GO-coated separator at different current rates from 0.2

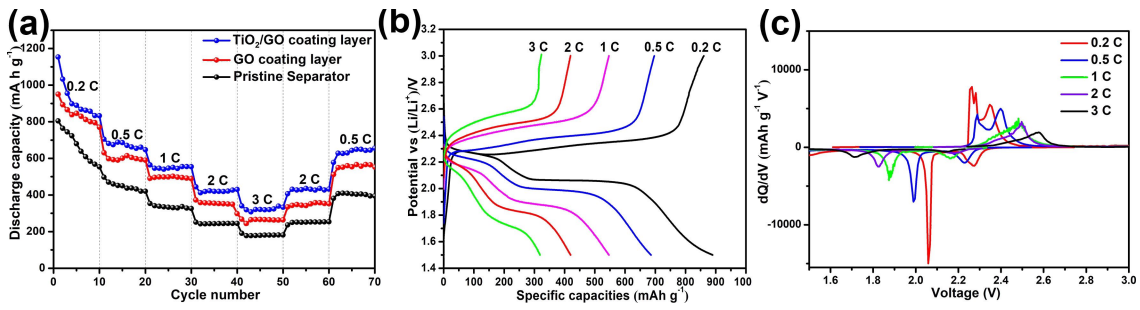

Figure 7: (a) Rate capability of the Li/S batteries with pristine, GO-coated and TiO_2/GO-coated separators. (b) Charge/discharge curves and (c) corresponding d*Q*/d*V* curves of the Li/S batteries with a TiO_2/GO-coated separator at different c-rates.

to 3 C. One should note that the shape of the voltage curves remained the same even under high current rates, such as 2 C and 3 C. Figure 7c shows the differential capacity versus voltage (dQ/dV) obtained from the discharge–charge profiles in Figure 8b. There were some shifts of the redox peaks with the increase in the current rate. However, the peak separation at a high current rate of 3 C still exhibits pronounced peaks. The excellent rate capability of the Li/S batteries with the TiO_2/GO coated separator suggests that the migration of polysulfides has been effectively restrained due to the introduction of the separator. Moreover, the adsorption advantages of GO with oxygen functional groups and TiO_2 with chemical bonds results in an increase in the sulfur utilization and leads to an enhanced rate stability of the Li/S batteries.

Furthermore, we have carried out electrochemical impedance spectroscopy (EIS) analysis to analyze the charge transfer kinetics in Li/S batteries with pristine and TiO_2/GO-coated separators. Figure 8 presents the Nyquist plots of Li/S batteries with pristine and TiO_2/GO-coated separators before and after cycling. As shown in Figure 8a, the charge transfer resistance (R_{ct}) of the TiO_2/GO-coated separator battery was ≈15.7 Ω, which is smaller than the Li/S battery with a pristine separator (19.2 Ω) or GO-coated separator (17.4 Ω). The lower charge transfer resistance can be ascribed to the higher conductivity of the TiO_2/GO layer. After cycling, the R_{ct} of the Li/S batteries with the TiO_2/GO-coated separator decreased to 12.6 Ω, whereas the R_{ct} of the Li/S batteries with the pristine and GO-coated separator reduced to 18.3 and 14.8 Ω, respectively. The lower R_{ct} after cycling can be ascribed to the chemical activation and redistribution of the active material [45]. In addition, an additional semicircle emerged in the EIS spectra of the Li/S batteries with the pristine separator after cycling, which suggests the dissolution of polysulfides and their deposition on the surface of the sulfur cathode. The absence of an additional semicircle in the EIS spectra of the TiO_2/GO-coated separator batteries indicates that the presence of the TiO_2/GO interlayer hindered the movement of polysulfides and thereby enhanced the utilization of the active material by reducing the shuttle effect.

The permeability of polysulfides through both membranes was visually analyzed by separating two compartments with either the pristine or the TiO_2/GO-coated separator, as shown in Figure 9. The left side of the test tube was filled with anhydrous tetrahydrofuran (THF) and 1 M Li_2S_6 solution and the right side was filled with anhydrous THF. As shown in Figure 9a, the color of the THF solution, on the right side, changed to dark yellow with prolonged diffusion up to 12 h due to the diffusion of polysulfides from the pristine separator. On the other hand, the TiO_2/GO-coated separator hindered the diffusion of polysulfides and exhibited a much slower color change even after 12 hours. Hence, the TiO_2/GO-coated separator effectively adsorbed and blocked the transportation of Li_2S_6.

Raman and Fourier-transform infrared spectroscopy (FTIR) analysis was carried out to understand the interaction between TiO_2/GO and polysulfides (Figure 10). The TiO_2/GO composite was treated with a Li_2S_6 electrolyte (1.0 M/0.1 M LiTFSI/$LiNO_3$ in DOL and DME (1:1 v/v)) via immersion for 12 h; the Li_2S_6-treated TiO_2/GO material was then obtained after centrifugal separation and vacuum drying. Raman and FTIR studies of the Li_2S_6-treated TiO_2/GO material clearly show the existence of an S–S stretching band at 470 cm^{-1}, indicating that Li_2S_6 was absorbed on the surfaces of the TiO_2/GO composite [46]. The Raman band at 745 cm^{-1} relates to a typical characteristic feature of LiTFSI in electrolyte [47]. A band that appeared at 801 cm^{-1} in the FTIR spectrum can be attributed to the S–O–C stretching, suggesting that the C of the TiO_2/GO

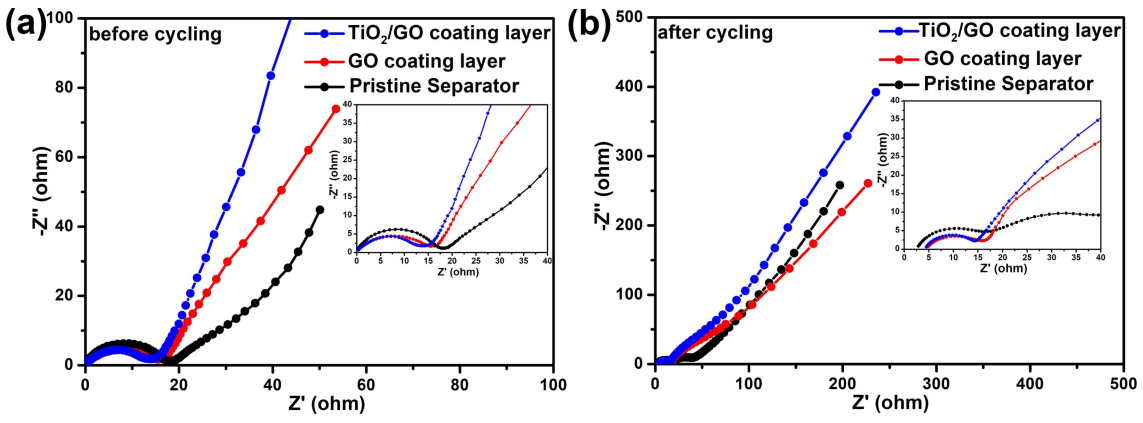

Figure 8: Nyquist plots of the Li/S batteries with pristine, GO-coated and TiO_2/GO-coated separators (a) before cycling and (b) after cycling.

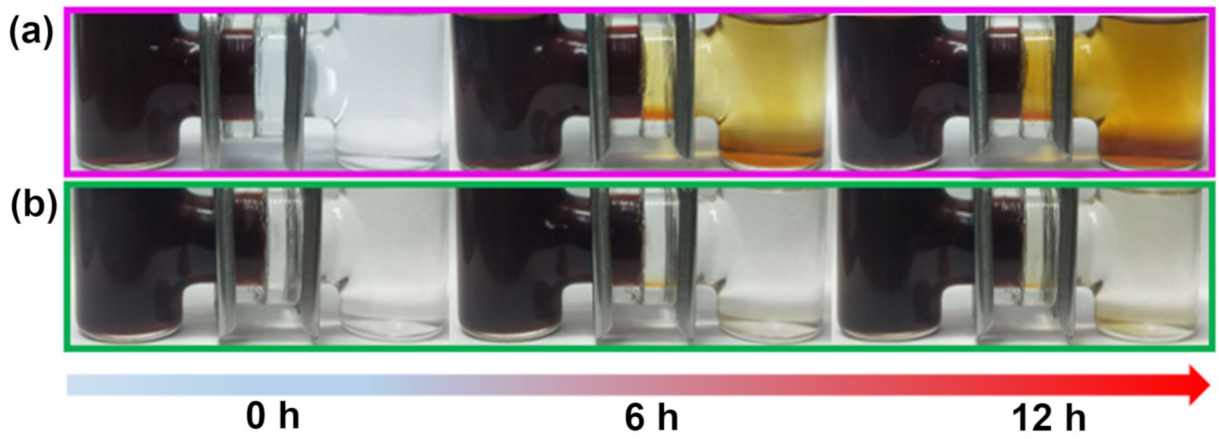

Figure 9: Optical images of the diffusion process of the polysulfides through the (a) pristine separator and the (b) TiO_2/GO-coated separator.

composite is chemically bonded to the polysulfides [48]. The FTIR spectrum of Li_2S_6–TiO_2/GO revealed that the peaks at 576, 597 and 740 cm^{-1} were attributed to the asymmetric bending mode of CF_3, the Li–O stretching and the S–N stretching of LiTFSI [49-51].

To further investigate the interaction between TiO_2 and the polysulfides during the charge/discharge process, the XPS spectra of the Li/S batteries with the TiO_2/GO-coated separator were recorded before and after 100 cycles, as shown in Figure 11. A broadened Ti $2p_{1/2}$ peak at ≈464 eV after cycling can be attributed to the presence of Ti–S interaction [32], indicating that TiO_2 interacts with S during the charge/discharge process. The combination of TiO_2 and sulfur effectively prevents the loss of active sulfur and improves the cyclic performance of the Li/S batteries. Based on the above results, it can be concluded that the TiO_2/GO composite has the synergetic effects of physical

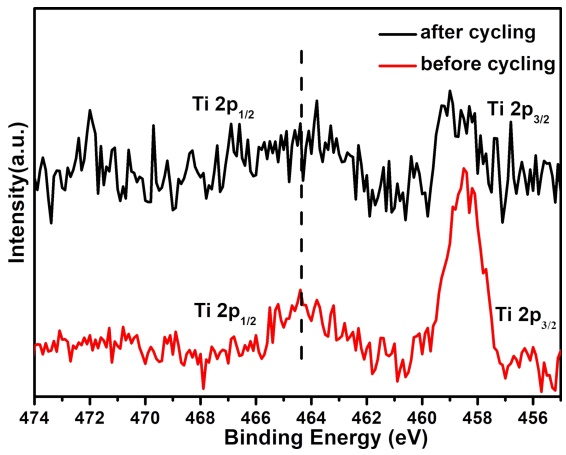

Figure 11: XPS spectra (Ti 2p) of the battery with a TiO_2/GO-coated separator before and after charge/discharge cycling.

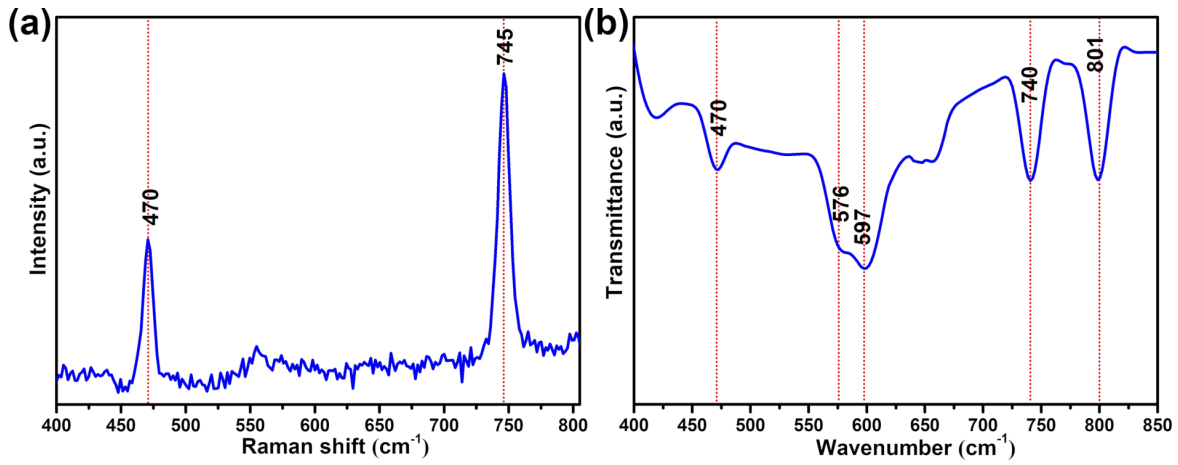

Figure 10: (a) Raman and (b) FTIR spectra of the Li_2S_6-treated TiO_2/GO composite.

and chemical interaction in inhibiting the shuttling of polysulfides. The increase of the active material utilization contributes to improvement of the cyclic performance and rate performance of Li/S batteries.

Conclusion

In summary, a lightweight TiO_2/GO coating, applied as an interlayer for Li/S batteries, has been prepared by using a simple method. The hierarchically porous TiO_2 nanoparticles are tightly wrapped in GO sheets and formed a 3D network structure, which can capture the polysulfides by physical and chemical adsorption and buffer the volumetric change of the sulfur cathode during the charge/discharge process. As a result, the Li/S batteries with the TiO_2/GO-coated separator exhibited a higher capacity, excellent rate performance and superior cyclic stability as compared to the Li/S batteries with a pristine or GO-coated separator. With the TiO_2/GO-coated separator, the Li/S batteries still exhibited a high specific capacity of 843.4 mAh g^{-1} after 100 cycles. Additionally, the discharge capacity of ≈320.8 mAh g^{-1} can be obtained even at a high current density of 3 C. The present study demonstrates the potential of the TiO_2/GO functional interlayer in next-generation Li/S batteries and presents a novel approach to prepare metal oxide based hybrid coatings for energy storage applications.

Experimental

Preparation of TiO_2/GO composite

$Ti_{10}Al_{90}$ alloy ribbons were fabricated by refining pure Al (99.9 wt %) and Ti (99.9 wt %) in an arc furnace, followed by melt spinning under an argon-protected atmosphere. The $Ti_{10}Al_{90}$ alloy ribbons were immersed in a 2 M NaOH solution for 72 h to prepare nanoporous TiO_2 particles at ambient temperature. The resulting powder was washed several times by using deionized (DI) water (18.2 MΩ cm) and ethyl alcohol. Then, the powder was vacuum dried (−0.08 MPa) for 8 h. To synthesize the TiO_2/GO composites, 1 g of nanoporous TiO_2 (≈40 nm) and 100 mL of graphene oxide (GO) solution were dispersed into 100 mL of deionized water and ultrasonically mixed for 2 h, followed by continuous stirring for 12 h to obtain a stable and uniform mixture. Then, the mixture was spray-dried at a flow rate of 5 mL min^{-1}, which resulted in the TiO_2/GO composite. The inlet temperature of the spray dryer was 200 °C.

Fabrication of TiO_2/GO-coated separator

The coating layer was fabricated by mixing TiO_2/GO composites (90 wt %) and poly(vinylidene fluoride) (PVDF, 10 wt %) in ultrapure water and milling for 40 min. The as-prepared slurry was coated onto the separator and dried at 60 °C in a vacuum oven for 8 h. Then, the TiO_2/GO-coated separator was sectioned in the form of circular discs with a diameter of 18 mm. For reference, a pure GO-modified separator was fabricated using the same process.

Synthesis of sulfur cathode

The sulfur cathode was prepared by mixing 70 wt % of elemental sulfur, 10 wt % PVDF and 20 wt % Ketjen black in *N*-methyl-2-pyrrolidone (NMP) solvent to form a slurry, which was coated onto an aluminum foil and vacuum-dried at 60 °C for 8 h. Finally, the cathodes were cut into a round shape with a diameter of 9 mm for coin-cell fabrication.

Material characterization

The crystalline structure of the samples was examined using XRD (Rigaku-TTRIII) with a step rate of 3° min^{-1}. The morphology and microstructure were observed by SEM (JEOL JSM-7100F) and TEM (JEOL JEM-2100F) with an accelerating voltage of 15 kV and 200 kV, respectively. The Raman spectra were recorded on a Raman spectrometer (Renishaw RM 2000) by using a laser with an excitation wavelength of 632.8 nm. Thermogravimetric analysis (SDTQ600) was taken under air flow (RT to 800 °C, 10 °C min^{-1}). The N_2 adsorption/desorption tests were analyzed using Brunauer–Emmett–Teller (BET) theory on a Micromeritics ASAP 2020 device. The surface composition was analyzed by XPS (VG ESCALAB MK II USA). The binding energies of all the elements were calibrated using C 1s (284.5 eV) as a reference. The FTIR spectra of the samples were recorded on a Bruker VERTEX 80 infrared spectrometer.

Electrochemical characterization

The 2032-type coin-cells were assembled in an argon-filled glove box (MBraun). In a half-cell configuration, Li metal served as a reference electrode, TiO_2/GO hybrid and GO membranes as separators, 1.0 M/0.1 M LiTFSI/$LiNO_3$ in DOL and DME (1:1 v/v) as an electrolyte and sulfur as a cathode. The charge–discharge measurements were carried out in the voltage range of 1.5–3 V (vs Li/Li^+) by using a multichannel Neware battery tester. CV and EIS were carried out on an electrochemical workstation (Princeton Applied Research, PARSTAT 2273). The CV scans were collected at a scanning rate of 0.1 mV s^{-1} between the voltage range of 1.5–3 V. EIS was performed in the frequency range of 100 kHz to 0.01 Hz with an amplitude of 5 mV.

Acknowledgements

This work was supported by the National Natural Science Foundation of China [Grant number 51505122]; Program for the Outstanding Young Talents of Hebei Province, China; Cultivation project of National Engineering Technology Center, China [Grant No. 2017B090903008].

ORCID® iDs

Lu Wang - https://orcid.org/0000-0002-1060-2684
Yongguang Zhang - https://orcid.org/0000-0001-6584-9062

References

1. Manthiram, A.; Fu, Y.; Chung, S.-H.; Zu, C.; Su, Y.-S. *Chem. Rev.* **2014,** *114,* 11751–11787. doi:10.1021/cr500062v
2. Mahmood, N.; Tang, T.; Hou, Y. *Adv. Energy Mater.* **2016,** *6,* 1600374. doi:10.1002/aenm.201600374
3. Jiang, J.; Feng, Y.; Mahmood, N.; Liu, F.; Hou, Y. *Sci. Adv. Mater.* **2013,** *5,* 1667–1675. doi:10.1166/sam.2013.1626
4. Mahmood, N.; De Castro, I. A.; Pramoda, K.; Khoshmanesh, K.; Bhargava, S. K.; Kalantar-Zadeh, K. *Energy Storage Mater.* **2019,** *16,* 455–480. doi:10.1016/j.ensm.2018.10.013
5. Jian, X.; Wang, H.; Rao, G.; Jiang, L.; Wang, H.; Subramaniyam, C. M.; Mahmood, A.; Zhang, W.; Xiang, Y.; Dou, S. X.; Zhou, Z.; Hui, D.; Kalantar-Zadeh, K.; Mahmood, N. *Chem. Eng. J.* **2019,** *364,* 578–588. doi:10.1016/j.cej.2019.02.003
6. Bruce, P. G.; Freunberger, S. A.; Hardwick, L. J.; Tarascon, J.-M. *Nat. Mater.* **2012,** *11,* 19–29. doi:10.1038/nmat3191
7. Lin, Z.; Liu, Z.; Fu, W.; Dudney, N. J.; Liang, C. *Adv. Funct. Mater.* **2013,** *23,* 1064–1069. doi:10.1002/adfm.201200696
8. Ding, B.; Yuan, C.; Shen, L.; Xu, G.; Nie, P.; Zhang, X. *Chem. – Eur. J.* **2013,** *19,* 1013–1019. doi:10.1002/chem.201202127
9. Gu, X.; Wang, Y.; Lai, C.; Qiu, J.; Li, S.; Hou, Y.; Martens, W.; Mahmood, N.; Zhang, S. *Nano Res.* **2015,** *8,* 129–139. doi:10.1007/s12274-014-0601-1
10. Rehman, S.; Gu, X.; Khan, K.; Mahmood, N.; Yang, W.; Huang, X.; Guo, S.; Hou, Y. *Adv. Energy Mater.* **2016,** *6,* 1502518. doi:10.1002/aenm.201502518
11. Lin, Z.; Liang, C. *J. Mater. Chem. A* **2015,** *3,* 936–958. doi:10.1039/c4ta04727c
12. Cui, Y.; Abouimrane, A.; Sun, C.-J.; Ren, Y.; Amine, K. *Chem. Commun.* **2014,** *50,* 5576–5579. doi:10.1039/c4cc00934g
13. Kim, J. H.; Fu, K.; Choi, J.; Sun, S.; Kim, J.; Hu, L.; Paik, U. *Chem. Commun.* **2015,** *51,* 13682–13685. doi:10.1039/c5cc04103a
14. Wei Seh, Z.; Li, W.; Cha, J. J.; Zheng, G.; Yang, Y.; McDowell, M. T.; Hsu, P.-C.; Cui, Y. *Nat. Commun.* **2013,** *4,* 1331. doi:10.1038/ncomms2327
15. Seh, Z. W.; Yu, J. H.; Li, W.; Hsu, P.-C.; Wang, H.; Sun, Y.; Yao, H.; Zhang, Q.; Cui, Y. *Nat. Commun.* **2014,** *5,* 5017. doi:10.1038/ncomms6017
16. Jia, X.; Zhang, C.; Liu, J.; Lv, W.; Wang, D.-W.; Tao, Y.; Li, Z.; Zheng, X.; Yu, J.-S.; Yang, Q.-H. *Nanoscale* **2016,** *8,* 4447–4451. doi:10.1039/c5nr08839a
17. Yin, F.; Liu, X.; Zhang, Y.; Zhao, Y.; Menbayeva, A.; Bakenov, Z.; Wang, X. *Solid State Sci.* **2017,** *66,* 44–49. doi:10.1016/j.solidstatesciences.2017.02.009
18. Li, H.; Sun, L.; Zhao, Y.; Tan, T.; Zhang, Y. *Electrochim. Acta* **2019,** *295,* 822–828. doi:10.1016/j.electacta.2018.11.012
19. Xiong, S.; Xie, K.; Diao, Y.; Hong, X. *J. Power Sources* **2013,** *236,* 181–187. doi:10.1016/j.jpowsour.2013.02.072
20. Zhang, X.; Wang, W.; Wang, A.; Huang, Y.; Yuan, K.; Yu, Z.; Qiu, J.; Yang, Y. *J. Mater. Chem. A* **2014,** *2,* 11660–11665. doi:10.1039/c4ta01709a
21. Yang, Y.; Sun, W.; Zhang, J.; Yue, X.; Wang, Z.; Sun, K. *Electrochim. Acta* **2016,** *209,* 691–699. doi:10.1016/j.electacta.2016.05.092
22. Liu, M.; Li, Q.; Qin, X.; Liang, G.; Han, W.; Zhou, D.; He, Y.-B.; Li, B.; Kang, F. *Small* **2017,** *13,* 1602539. doi:10.1002/smll.201602539
23. Sun, F.; Wang, J.; Chen, H.; Li, W.; Qiao, W.; Long, D.; Ling, L. *ACS Appl. Mater. Interfaces* **2013,** *5,* 5630–5638. doi:10.1021/am400958x
24. Schuster, J.; He, G.; Mandlmeier, B.; Yim, T.; Lee, K. T.; Bein, T.; Nazar, L. F. *Angew. Chem., Int. Ed.* **2012,** *51,* 3591–3595. doi:10.1002/anie.201107817
25. Zhang, B.; Qin, X.; Li, G. R.; Gao, X. P. *Energy Environ. Sci.* **2010,** *3,* 1531–1537. doi:10.1039/c002639e
26. Guo, J.; Xu, Y.; Wang, C. *Nano Lett.* **2011,** *11,* 4288–4294. doi:10.1021/nl202297p
27. Sun, J.; Sun, Y.; Pasta, M.; Zhou, G.; Li, Y.; Liu, W.; Xiong, F.; Cui, Y. *Adv. Mater. (Weinheim, Ger.)* **2016,** *28,* 9797–9803. doi:10.1002/adma.201602172
28. Guo, P.; Liu, D.; Liu, Z.; Shang, X.; Liu, Q.; He, D. *Electrochim. Acta* **2017,** *256,* 28–36. doi:10.1016/j.electacta.2017.10.003
29. Liu, F.; Xiao, Q.; Wu, H. B.; Sun, F.; Liu, X.; Li, F.; Le, Z.; Shen, L.; Wang, G.; Cai, M.; Lu, Y. *ACS Nano* **2017,** *11,* 2697–2705. doi:10.1021/acsnano.6b07603
30. Luo, L.; Qin, X.; Wu, J.; Liang, G.; Li, Q.; Liu, M.; Kang, F.; Chen, G.; Li, B. *J. Mater. Chem. A* **2018,** *6,* 8612–8619. doi:10.1039/c8ta01726c
31. Liang, G.; Wu, J.; Qin, X.; Liu, M.; Li, Q.; He, Y.-B.; Kim, J.-K.; Li, B.; Kang, F. *ACS Appl. Mater. Interfaces* **2016,** *8,* 23105–23113. doi:10.1021/acsami.6b07487
32. Xiao, Z.; Yang, Z.; Wang, L.; Nie, H.; Zhong, M.; Lai, Q.; Xu, X.; Zhang, L.; Huang, S. *Adv. Mater. (Weinheim, Ger.)* **2015,** *27,* 2891–2898. doi:10.1002/adma.201405637
33. Dreyer, D. R.; Park, S.; Bielawski, C. W.; Ruoff, R. S. *Chem. Soc. Rev.* **2010,** *39,* 228–240. doi:10.1039/b917103g
34. Huang, J.-Q.; Zhuang, T.-Z.; Zhang, Q.; Peng, H.-J.; Chen, C.-M.; Wei, F. *ACS Nano* **2015,** *9,* 3002–3011. doi:10.1021/nn507178a
35. Liu, N.; Wang, L.; Zhao, Y.; Tan, T.; Zhang, Y. *J. Alloys Compd.* **2018,** *769,* 678–685. doi:10.1016/j.jallcom.2018.08.027
36. Yin, H.; Wada, Y.; Kitamura, T.; Kambe, S.; Murasawa, S.; Mori, H.; Sakata, T.; Yanagida, S. *J. Mater. Chem.* **2001,** *11,* 1694–1703. doi:10.1039/b008974p
37. Lavanya, T.; Satheesh, K.; Dutta, M.; Victor Jaya, N.; Fukata, N. *J. Alloys Compd.* **2014,** *615,* 643–650. doi:10.1016/j.jallcom.2014.05.088
38. Chattopadhyay, S.; Maiti, S.; Das, I.; Mahanty, S.; De, G. *Adv. Mater. Interfaces* **2016,** *3,* 1600761. doi:10.1002/admi.201600761
39. Zhang, X.-Y.; Li, H.-P.; Cui, X.-L.; Lin, Y. *J. Mater. Chem.* **2010,** *20,* 2801–2806. doi:10.1039/b917240h
40. Li, N.; Zhou, G.; Fang, R.; Li, F.; Cheng, H.-M. *Nanoscale* **2013,** *5,* 7780–7784. doi:10.1039/c3nr01349a
41. Elazari, R.; Salitra, G.; Garsuch, A.; Panchenko, A.; Aurbach, D. *Adv. Mater. (Weinheim, Ger.)* **2011,** *23,* 5641–5644. doi:10.1002/adma.201103274
42. Xiao, L.; Cao, Y.; Xiao, J.; Schwenzer, B.; Engelhard, M. H.; Saraf, L. V.; Nie, Z.; Exarhos, G. J.; Liu, J. *Adv. Mater. (Weinheim, Ger.)* **2012,** *24,* 1176–1181. doi:10.1002/adma.201103392
43. Ma, J.; Fang, Z.; Yan, Y.; Yang, Z.; Gu, L.; Hu, Y.-S.; Li, H.; Wang, Z.; Huang, X. *Adv. Energy Mater.* **2015,** *5,* 1500046. doi:10.1002/aenm.201500046
44. Li, C.; Li, Z.; Li, Q.; Zhang, Z.; Dong, S.; Yin, L. *Electrochim. Acta* **2016,** *215,* 689–698. doi:10.1016/j.electacta.2016.08.044

45. Xie, J.; Yang, J.; Zhou, X.; Zou, Y.; Tang, J.; Wang, S.; Chen, F. *J. Power Sources* **2014,** *253,* 55–63. doi:10.1016/j.jpowsour.2013.12.074
46. Li, G.; Cai, W.; Liu, B.; Li, Z. *J. Power Sources* **2015,** *294,* 187–192. doi:10.1016/j.jpowsour.2015.06.083
47. Lassegues, J.-C.; Grondin, J.; Aupetit, C.; Johansson, P. *J. Phys. Chem. A* **2009,** *113,* 305–314. doi:10.1021/jp806124w
48. Tang, H.; Yao, S.; Xue, S.; Liu, M.; Chen, L.; Jing, M.; Shen, X.; Li, T.; Xiao, K.; Qin, S. *Electrochim. Acta* **2018,** *263,* 158–167. doi:10.1016/j.electacta.2018.01.066
49. Kumar, R.; Sharma, J. P.; Sekhon, S. S. *Eur. Polym. J.* **2005,** *41,* 2718–2725. doi:10.1016/j.eurpolymj.2005.05.010
50. Etacheri, V.; Geiger, U.; Gofer, Y.; Roberts, G. A.; Stefan, I. C.; Fasching, R.; Aurbach, D. *Langmuir* **2012,** *28,* 6175–6184. doi:10.1021/la300306v
51. Ramesh, S.; Lu, S.-C. *J. Power Sources* **2008,** *185,* 1439–1443. doi:10.1016/j.jpowsour.2008.07.055

License and Terms